



The
University
Of
Sheffield.

**The Effect of Direct Laser Deposition Process Parameters on Microstructure
and Mechanical Properties of Ti-6Al-2Sn-4Zr-6Mo**

Emily Sarah Davison

A thesis submitted in partial fulfilment of the requirements for the degree of
Doctor of Philosophy

The University of Sheffield
Faculty of Engineering
Department Materials Science & Engineering

14th October 2019

Abstract

Blown powder Direct Laser Deposition (DLD) is a type of Additive Manufacturing (AM) that is of interest to the aerospace industry as a method of performing high-integrity repairs of critical components. The properties of the deposited material are largely influenced by process parameters such as beam power, velocity, hatch spacing, beam radius and powder feed rate. It is critical for a high-quality repair, that the effect of these process parameters on the solidification microstructure and hence the mechanical properties are fully understood.

The work presented here focuses on quantifying the effect of process parameters on DLD of the $\alpha+\beta$ titanium alloy Ti-6Al-2Sn-4Zr-6Mo (Ti-6246). This alloy demonstrates high strength and good corrosion resistance and is a suitable replacement for Ti-6Al-4V in aerospace applications. This is due to its ability to perform at higher temperatures which is important as gas turbine engines push towards higher efficiencies and hence elevated operating temperatures.

A Design of Experiment (DoE) was used to map a potential process window that would be suitable for Ti-6246 DLD repair of compressor bladed disks (Blisks). The aim was to identify combinations of process parameters that resulted in a fully-dense defect-free build that produced repeatable mechanical properties comparable to the parent Ti-6246 blisk material.

Ten deposits were built with five different parameter sets using an RPM 557 laser deposition machine. Tensile specimens were machined from the build for uniaxial tensile testing. Small sections of each build were also retained for microstructural analysis, with the aim to correlate process parameters with the size of the resultant $\alpha+\beta$ lamellar microstructure. The α -lath width was found to generally increase with decreasing line energy density (beam power divided by velocity), although the effects of additional process parameters such as powder feed rate is also important and the influence of this is also explored.

The results from this work were used to determine response surfaces relating process inputs such as energy density to process outputs such as 0.2% yield stress. These were then used to provide recommendations for future work with the aim of optimizing the DLD process window for Ti-6246 as a suitable repair method.

The experimental work was supported by the development of a thermal model. This helped to inform how process parameters influenced the laser deposition conditions. The thermal model was calibrated against a thin-wall aerofoil-type build and reasonable agreement was found between predicted and measured melt depths for a range of process parameters. The thermal model also can help to provide

Abstract

predictions about the how further optimisation of the process window may affect mechanical properties.

Some of the key findings and outcomes of this work are:

- Development of an automated process to measure the size of Ti-6246 $\alpha+\beta$ lamellar microstructure produced by DLD. This automated process was validated using manual measurement techniques and was found to be a robust and trustworthy method that significantly decreases the time to gather microstructural data.
- Size of the α -laths were generally found to be $<1\mu\text{m}$, apart from a dendritic zone at the top of each of the builds which has remained fine due to lack of coarsening from repeated thermal cycles.
- Definition of a process window for the DLD of Ti-6246 which can produce dense builds with minimal defects (as revealed by both SEM and XCT analysis).
- Testing of Ti-6246 DLD builds showed mechanical properties (tensile strength, 0.2% yield stress and elongation) comparable to parent forged material and within requirements set by Rolls-Royce for repair purposes.
- Linear regression and response surface analysis showed that laser beam velocity (v) had the most effect on mechanical properties, particularly the 0.2% yield stress. Hatch spacing had little to no quantifiable effect on the mechanical properties.
- Recommendations for process optimisation and productivity gains include increasing the hatch spacing and/or beam velocity to increase productivity.
- Development of a Gaussian-based thermal model used to define a new parameter – melt pool saturation level (MPSL), this being the ratio between melting capacity of the laser and the actual amount of material being melted during the DLD process.
- The MPSL was used to calculate an upper limit to the PFR and DLD process inputs were used to define a lower limit or “aspirational” PFR. Hence, the model developed in this work is useful in an industrial setting as it can reduce the number of test deposits needed to down-select the best process parameters and therefore define a suitable process window.

Contents

Abstract.....	2
List of figures.....	8
List of Tables	13
Nomenclature	14
Acknowledgements.....	16
1 Introduction	17
2 Literature Review.....	20
2.1 Titanium alloys.....	20
2.1.1 Crystal structure.....	20
2.1.2 Classification of Titanium alloys.....	21
2.1.3 $\alpha+\beta$ alloys and Ti-6246	22
2.1.4 Use of Titanium alloys in aerospace industry	24
2.2 Phase transformation	25
2.2.1 $\beta \rightarrow \alpha$ transformation	25
2.2.2 Lamellar microstructure and properties.....	27
2.3 Additive Manufacturing	29
2.3.1 Background and history	29
2.3.2 Powder Bed.....	30
2.4 Blown powder direct laser deposition.....	31
2.4.1 Process parameters.....	32
2.4.2 Applications of blown powder DLD.....	34
2.5 Modelling the AM process.....	42
2.5.1 Introduction	42
2.5.2 Point heat source vs. diffuse heat source.....	42
2.5.3 Melt pool size and geometry	45
2.5.4 Blown powder	46
2.5.5 Limitations.....	48
2.6 Dimensionless process parameters	48
2.6.1 Background	48
2.6.2 Definitions.....	49
2.6.3 Normalised process maps	50
2.6.4 Advantages.....	53
3 Experimental techniques	54

Contents

3.1	Direct Laser Deposition & process parameters	54
3.2	Mini tensile builds.....	55
3.2.1	Normalised Process Parameters	56
3.2.2	Design of Experiments	57
3.3	Calibration build.....	58
3.4	Mechanical testing.....	59
3.4.1	Uniaxial tensile testing.....	59
3.4.2	Ti-6264 DLD tensile test pieces	59
3.5	Characterisation of microstructure and build quality.....	60
3.5.1	Scanning electron microscopy	60
3.5.2	CLEMEX automated measurement.....	61
3.5.3	ICP analysis.....	66
3.5.4	XCT	68
3.5.5	Mini Tensile samples.....	68
3.5.6	Reconstruction	70
3.5.7	Image Analysis.....	70
4	Microstructural analysis and build quality.....	71
4.1	Introduction	71
4.2	Typical solidification microstructure.....	71
4.3	Quantification of DLD Ti-6246 α -laths	75
4.3.1	Manual vs. automated microstructural assessment.....	75
4.4	CLEMEX results.....	80
4.5	Bulk vs. localised section.....	84
4.6	Effect of build height on microstructure.....	85
4.7	ICP-OES results	86
4.8	3-D analysis of build quality using X-ray Computed Tomography	88
4.8.1	Results & Discussion	88
4.9	Conclusions	90
5	Effect of process parameters on properties of Ti-6246 DLD	92
5.1	Introduction	92
5.2	Investigating process space	92
5.2.1	Design of Experiments for Ti-6246 mini tensile process window.....	94
5.3	Results & Discussion	95
5.3.1	Grubbs' Test	96
5.3.2	Response surfaces.....	97
5.3.3	0.2% YS model.....	100

Contents

5.3.4	%E model.....	101
5.3.5	UTS model.....	103
5.3.6	Optimisation.....	105
5.3.7	Effect of build height on mechanical results.....	106
5.3.8	Microstructural effects on mechanical properties.....	109
5.4	Conclusions.....	111
6	Modelling the DLD process.....	113
6.1	Introduction.....	113
6.2	Calibration build deposition.....	116
6.2.1	Optical microscopy of calibration build.....	117
6.2.2	Determining value of calibration factor “n”.....	120
6.3	Eagar & Tsai “Rosenthal” model.....	121
6.3.1	Calibration results.....	122
6.3.2	Effects of process parameters.....	124
6.3.3	Cooling rates.....	129
6.3.4	Assumptions and limitations of the point heat-source model.....	130
6.4	Development of Shercliff and Ashby Gaussian model.....	135
6.4.1	Calculating the value of characteristic length, z_0	136
6.4.2	Calibration results.....	139
6.4.3	Calculating melt depths for Ti-6246 DLD.....	140
6.5	Conclusions.....	142
7	Powder effects and Melt Pool Saturation.....	144
7.1	Investigating the effects of powder feed rate.....	144
7.1.1	Powder particle influences on beam power.....	144
7.1.2	Initial attenuation by powder particles in laser beam.....	146
7.2	Melt pool saturation.....	148
7.2.1	Laser melting capability.....	149
7.2.2	Calculating the MPSL.....	153
7.3	Aspirational powder feed rate.....	155
7.3.1	Effect of aspirational feed rate on mini tensile DoE.....	159
7.4	Conclusions.....	164
8	Conclusions & Future Work.....	165
8.1	Ti-6246 DLD Microstructure.....	165
8.2	Mechanical properties and response surfaces.....	166
8.3	Point heat source and Gaussian models.....	167
8.4	Powder effects and PFR limits.....	167

Contents

8.5	Further work	168
8.5.1	Testing conditions	168
8.5.2	Assessment of optimisation recommendations	169
8.5.3	Expansion of the thermal model for elevated temperatures	169
8.5.4	Quality assurance.....	169
8.5.5	Additional process parameters	170
	References	171
9	Appendix A: CLEMEX routine	185
10	Appendix B: Pareto Charts	186
11	Appendix C: MATLAB code.....	187
12	Appendix D: Master plot for validation	197

List of figures

Figure 2.1: Crystal structure for (a) α -phase - hexagonal close packed (HCP) and (b) β -phase - body centered cubic (BCC) [9]	20
Figure 2.2: Diagram to show the effect of different stabilizers on the Ti phase diagram [19].....	22
Figure 2.3: Generic $\alpha+\beta$ phase diagram indicating the location of the α and β phase fields with respect to temperature and concentration of β stabilizers [20]	23
Figure 2.4: Schematic showing typical material distribution within an aero-engine [26].....	25
Figure 2.5: Example of typical titanium alloy microstructure at different cooling rates (a) furnace cooled (b) air cooled showing colony α (c) air cooled showing basket-weave (d) air cooled showing Widmanstätten α [8].....	26
Figure 2.6: Micrograph of martensitic titanium formed due to (a) rapid quenching $525^{\circ}\text{Cs}^{-1}$ and (b) 15°Cs^{-1} [29]	27
Figure 2.7: Micrograph showing the typical Widmanstätten microstructure for direct laser fabricated Ti-6246. Note substrate material on left-hand side [33]	28
Figure 2.8: Effect of cooling rate on mechanical properties of common titanium alloys with fully lamellar microstructures [19,34]	28
Figure 2.9: Schematic of the main components during a powder bed AM process [52]	31
Figure 2.10: Schematic of a typical blown powder deposition process [2]	31
Figure 2.11: Microstructure of DLD 316L SS at using beam power and velocities of (a) $750\text{W} \ \& \ 300 \ \text{mmmin}^{-1}$ (b) $750\text{W} \ \& \ 450 \ \text{mmmin}^{-1}$ and (c) $900\text{W} \ \& \ 300 \ \text{mmmin}^{-1}$ [55]	32
Figure 2.12: Optical micrographs of AM Ti-6Al-4V revealing a reduction in grain size as the laser beam velocity and powder feed rate are increased (a) $200 \ \text{mmmin}^{-1}, \ 6 \ \text{gmin}^{-1}$ (b) $500 \ \text{mmmin}^{-1}, \ 15 \ \text{gmin}^{-1}$ (c) $800 \ \text{mmmin}^{-1}, \ 18 \ \text{gmin}^{-1}$ [48]	34
Figure 2.13: Example of part manufacture using DLD of AlSi10Mg for a fuselage [65]	35
Figure 2.14: SEM images of coating produced by plasma spray (left) and DLD (right)[73].....	37
Figure 2.15: Ni-alloy/WC coating on a H11 tool steel applied using laser cladding (DLD)[67].....	38
Figure 2.16: (a-c) V-shaped grooves (d-f) square shaped grooves repaired using DLD [81]	39
Figure 2.17: (a) Test geometry for DLD repair (b) Gas turbine burner with LMD repair and SLM substrate (IN718)[83].....	40
Figure 2.18: Schematic to show the position of the imaginary surface at a distance z_0 above the substrate surface [96]	44
Figure 2.19: Comparison between experimental and predicted melt depths for different laser modes as a function of beam velocity [96].....	46

List of figures

Figure 2.20: (a) Attenuation of the laser beam due to shading effect of powder particles (b) Graph showing amount of attenuated beam power as a function of powder feed rate [87]	47
Figure 2.21: Normalised process map for transformation hardening. Contours show constant normalised hardened depth [105]	50
Figure 2.22: Example of a master plot for case depth in transformation hardening. Contours show constant dimensionless beam power (q^*) [95]	51
Figure 2.23: Normalised process map with lines of constant energy density showing effects of changing parameters on microstructure of EBM Ti-6Al-4V [107]	52
Figure 3.1: RPM 557 [109]	55
Figure 3.2: Image of as-deposited mini tensile builds. Note scale is in inches	55
Figure 3.3: Contour and hatch scan strategy	56
Figure 3.4: Dimensionless process map showing the process window investigated by the mini tensile deposits	58
Figure 3.5: Schematic of tensile test specimens machined from DLD material. Note scale is in inches	59
Figure 3.6: Schematic diagram of a SEM showing how the electron beam is focused by a series of apertures and lenses [114]	61
Figure 3.7: Example SEM image to be put through CLEMEX routine	62
Figure 3.8: Example of grey thresholding being applied to SEM image in CLEMEX	63
Figure 3.9: SEM image after an exaggerated grey threshold (left) followed by applying Closing CIRC process (right)	64
Figure 3.10: Image after an exaggerated "Trap" has been applied to image in above figure	64
Figure 3.11: Image after an exaggerated separate function has been applied	65
Figure 3.12: Image after object measure has been performed. Features can be selected (see centre of image) in order to show their associated measurements (i.e. width etc.)	66
Figure 3.13: ICP-OES methodology [116]	66
Figure 3.14: Excitation from ground state to excited and back to ground state with photon emission	67
Figure 3.15: Schematic showing how a 3-D image is created using XCT [119]	68
Figure 3.16: 2-D slice before separation of the grip sections (left) and after identifying as separate materials (right)	70
Figure 4.1: SEM BSE micrograph showing typical DLD Ti-6246 microstructure	72
Figure 4.2: Micrograph showing the presence of secondary alpha within the beta phase	73

List of figures

Figure 4.3: BSE micrograph of DLD Ti-6246 showing grain boundary alpha (left) and side plates (right)	74
Figure 4.4: Position of bottom microscopy sample (red dashed line) with respect to tensile specimen. Primary ROI for microstructural analysis shown in orange	75
Figure 4.5: SEM micrograph with alpha laths indicating method A	76
Figure 4.6: SEM micrograph with alpha laths measured using method B.....	77
Figure 4.7: Manual measurement vs CLEMEX measurement.....	78
Figure 4.8: Histogram showing manual vs. automated (CLEMEX) measurements of alpha lath widths	79
Figure 4.9: Probability plot for the alpha lath widths for all DoE specimens	80
Figure 4.10: Probability plots for the five different parameter sets (a-e) showing alpha lath widths from the microscopy sections.....	83
Figure 4.11: Bulk microscopy sample	84
Figure 4.12: Normalised alpha lath widths in bulk sample.....	85
Figure 4.13: Probability plot showing the alpha lath widths as a function of build position	86
Figure 4.14: Al content as a function of energy density	87
Figure 4.15: Schematic showing the regions of interest for the high resolution (left) and low resolution (right) XCT scans	88
Figure 4.16: XCT reconstruction of pore detected in low resolution scans.....	89
Figure 4.17: XCT reconstruction of the high resolution scan of the gauge section. Fracture surface is at the top	89
Figure 5.1: Normalised process map for DLD of different alloys [107]	93
Figure 5.2: Pareto chart for 0.2%YS	100
Figure 5.3: Response surface with contours showing constant 0.2% yield stress for the process window. The yield stress values shown are $0.2\%YS/0.2\%YS_{req}$	101
Figure 5.4: Pareto chart for %E response	102
Figure 5.5: Response surface showing contours of constant %E for the process window. The elongation values shown are $\%E/\%E_{target}$. Blue circle indicates position of the $\%E/\%E_{target}=1$ contour line.....	103
Figure 5.6: Pareto chart for UTS response.....	104
Figure 5.7: Response surface showing contours of constant UTS for the process window. The UTS values are defined as UTS/UTS_{target}	104
Figure 5.8: Contour plot to show regions of optimised mechanical responses	105

List of figures

Figure 5.9: Contour plot showing "unexplored region" for potential Blisk repair process window with improved mechanical properties.....	106
Figure 5.10: Probability plots showing the elongation to failure, 0.2% yield stress and UTS results as a function of build position.....	108
Figure 5.11: Hall-Petch type graph showing relationship between the inverse square root of the alpha lath widths and the 0.2% yield stress for Ti-6246 DLD	110
Figure 6.1: Schematic (top) of the different process input parameter sets for the deposition of the aerofoil-type build (bottom) used to calibrate both the Rosenthal and Gaussian heat source models. Note the scale is in inches for the bottom image.....	116
Figure 6.2: Optical image of top section of the Ti-6-2-4-6 MA aerofoil-type build showing the last laser pass.....	117
Figure 6.3: Comparison between experimentally measured melt depths for a Ti-6246 DLD build compared to predictions made by the Rosenthal thermal model with $n=0.14$	123
Figure 6.4: Optical micrograph of the top of calibration build deposited using an energy density of 101245 Jm^{-1} (top) and 24987 Jm^{-1} (bottom)	124
Figure 6.5: Temperature field generated by a point-heat source in the x-y plane. Laser centre at (0,0) moving in the positive x-direction. Laser power (q) – 400W, laser velocity (v) – 0.01ms^{-1}	125
Figure 6.6: Temperature fields generated by the laser beam in the x-z plane. Laser beam moving in the positive x-direction. Laser power (q) – 400W, laser velocity (v) – 0.01ms^{-1}	125
Figure 6.7: Relationship between the aspect ratio of the melt pool and the velocity of the laser beam	126
Figure 6.8: Temperature distribution as a function of transverse (y) distance from laser centre for a range of depths (z)	128
Figure 6.9: Relationship between melt pool depth (blue) and beta transus depth (orange) and beam velocity for constant laser power	128
Figure 6.10: Cooling rates as a function of both depth below the surface (z) and transverse distance from laser centre (x) for the high velocity mini tensile builds.....	129
Figure 6.11: Cooling rates along the T_m contour using process parameters for mini tensile builds ..	130
Figure 6.12: Comparison between using room temperature thermophysical properties (top) and elevated temperature properties (bottom) for Ti-6Al-4V	132
Figure 6.13: Comparison between assuming build temperature is at room temperature (top) and at an elevated temperature (bottom)	134
Figure 6.14: Schematic to show the position of the imaginary surface at a distance z_0 above the substrate surface[96]	137

List of figures

Figure 6.15: Temperature profile of the laser beam using Shercliff and Ashby model.....	139
Figure 6.16: Comparison between melt depths predicted by the Gaussian and Rosenthal models and experimental results	140
Figure 6.17: Maximum melt pool depth predicted by a Gaussian laser beam as a function of dimensionless laser velocity (v^*) for different laser powers	141
Figure 7.1: Graph showing the relationship between powder feed rate and attenuated power as a function of laser power.....	147
Figure 7.2: Graph to show the relationship between powder feed rate and total workpiece absorption.....	147
Figure 7.3: Graph showing maximum mass of Ti-6246 that can be melted per second for different laser powers.....	150
Figure 7.4: Graph showing maximum mass of Ti-6246 raised to T_p per second for different laser powers	151
Figure 7.5: Powder capture area (yellow) bounded by the $T=T_m$ isotherm.....	152
Figure 7.6: Graph showing the relationship between q/v energy density and amount of material melted per second	153
Figure 7.7: Comparison between (a) low melt pool saturation (left) and (b) high melt pool saturation (right)	154
Figure 7.8: Melt pool saturation levels for mini tensile DoE parameter sets	155
Figure 7.9: 3-D process map for the Ti-6246 DLD mini tensile builds including the PFR.....	158
Figure 7.10: Percentage of "ideal" or required mass of powder delivered to the melt pool.....	158
Figure 7.11: Probability plot of alpha lath widths grouped by DoE parameter sets	159
Figure 7.12 (a-e): Typical micrographs showing the alpha laths for five different MPSSLs. (a) 23%, (b) 38%, (c) 48%, (d) 61% and (e) 74%	161
Figure 7.13: Relationship between the 0.2% Yield Stress and the fractional of aspirational PFR used	163
Figure 7.14: Relationship between fraction of aspirational PFR and ductility	163
Figure 10.1: Pareto Effect Chart for %E, UTS and 0.2% YS to show standardised effects of $q^*v^*l^*$ and $1/h^*$	186
Figure 12.1: Recreation of the master plot by Shercliff and Ashby.	197

List of Tables

Table 2.1: Typical composition of Ti-6246	23
Table 2.2: List of different types of powder-based Additive Manufacturing technologies and terminologies	30
Table 2.3: Typical process parameters used in DLD	33
Table 2.4: Description of the parameters in the Rosenthal equation	43
Table 3.1: Definition of main process parameters used during DLD	54
Table 3.2: Settings for the Nikon Custom 320kV Bay	69
Table 3.3: Settings for the Xradia Versa XCT.....	69
Table 4.1: Comparison between width measurements using methods A and B.....	77
Table 4.2: Statistics from probability plot.....	81
Table 4.3: Results from ICP-OES.....	86
Table 4.4: Effect of Al content on UTS properties	87
Table 5.1: DoE table showing experimental factors and the responses.....	95
Table 5.2: Results from non-DLD tensile specimens.....	96
Table 5.3: Table of inputs and calculated values for the Grubb's test.....	97
Table 5.4: ANOVA results from the response models	99
Table 6.1: Build parameters used for the deposition of the aerofoil thin build.....	117
Table 6.2: Optical microscopy images of the aerofoil-type build with measurements of the depth of the melt pool generated by the last laser pass.....	119
Table 6.3: Comparison between predicted and measured values for maximum melt pool depth for a Ti-6246 DLD build.....	121
Table 6.4: List of parameters used in the semi-infinite Rosenthal equation.....	122
Table 6.5: Thermophysical properties for Ti-6Al-4V at room and elevated temperatures	131
Table 6.6: Additional modelling parameters for Gaussian laser mode	135
Table 7.1: Table listing parameters used in calculating powder-laser beam interactions for Ti-6246 DLD	145

Nomenclature

SYMBOL	DEFINITION	UNITS
%E	Elongation to Failure	%
\bar{x}	Average of data points (Grubbs' test)	-
$\frac{\delta T}{\delta t} / CR$	Cooling rate	$Ks^{-1} / ^{\circ}C^{-1}$
A(L)M	Additive (Layer) Manufacturing	-
BCC	Body Centred Cubic	-
CAD	Computer Aided Design	-
CP	Commercially Pure	-
c_p	Specific heat capacity	$Jg^{-1}K^{-1}$
D(L)MD	Direct (Laser) Metal Deposition	-
DLD	Direct Laser Deposition	-
DLF	Direct Laser Fabrication	-
DoE	Design of Experiments	-
E_0^*	(Normalised) energy density	-
EBSD	Electron Back-scattered Diffraction	-
EDM	Electro Discharge Machine	-
G	Grubbs' test statistic	-
h^*	(Normalised) hatch spacing	-
HCP	Hexagonal Close Packed	-
HESXR	High Energy Synchrotron X- ray Radiation	-
IP	Intermediate Pressure	-
k	Thermal conductivity	$Wm^{-1}K^{-1}$
k_y	Strengthening coefficient	$MPamm^{1/2}$
l	Layer height	m
L	Latent heat of fusion	Jkg^{-1}
l^*	(Normalised) layer height	-
LENS	Laser Engineered Net Shape	-
MPSL	Melt Pool Saturation Level	%
M_s	Martensitic start temperature	K
N	Number of data points (Grubbs' test)	-
n, A, β_w	Workpiece absorptivity	%
n_p	Powder capture efficiency	%
$PFR / m_p / \overline{m_p}$	Powder Feed Rate	$kg s^{-1} / g min^{-1}$
q^*	(Normalised) beam power	-
q, P_l	Laser power	W
R	Distance from laser in cartesian co-ordinates	m
r_b, r_l	Beam radius	m

Nomenclature

r_j	Radius of powder jet	M
ROI	Region of Interest	-
RP	Rapid Prototyping	-
r_p	Powder radii	μm
s	Standard deviation	-
SDAS	Secondary Dendrite Arm-spacing	-
SEM	Scanning Electron Microscopy	-
SLM	Selective Laser Melting	-
t	Time	secs
T	Temperature	K
T_0	Build temperature	K
t_0	Heat flow time constant	secs
t_{crit}	Critical value of a t-distribution	-
T_m	Melting temperature	K
t_p^*	(Normalised) time to peak temperature	-
T_p^*	(Normalised) peak temperature	-
UTS	Ultimate Tensile Strength	MPa
v	Beam velocity	ms^{-1}
v^*	(Normalised) beam velocity	-
v_p	Powder velocity	ms^{-1}
x^*, y^*, z^*	(Normalised) position in cartesian co-ordinates	-
x, y, z	Position in cartesian co-ordinates	m
XCT	X-ray Computed Tomography	-
YS, σ_y	Yield Stress	MPa
z_0	Characteristic length	m
z_0^*	(Normalised) characteristic length	-
z_c^*	(Normalised) case depth	-
z_m	Maximum melt depth	m
z_m^*	(Normalised) maximum melt depth	-
α	Thermal diffusivity	m^2s^{-1}
α'	Hexagonal phase	-
α''	Orthorhombic phase	-
θ_j	Angle of powder jet	$^\circ$
ρ	Density	Kgm^{-3}

Acknowledgements

I would like to thank everyone who has helped me make it through to the end of my PhD. There have been a lot of people over the past four years who have helped me in some way and I'm so grateful to them all. In particular I would like to acknowledge and thank the following people.

Firstly I would like to thank my supervisor Professor Iain Todd who gave me the opportunity to do this project in the first place. The advice, support and technical knowledge he provided throughout the course of this project have been invaluable. I would also like to acknowledge the financial support from the EPSRC and Rolls-Royce plc who provided the funding for this project. In particular I thank my industrial supervisor Dr Gavin Baxter and also Martyn Jones for all of their important guidance and expertise.

I thank the staff in the Department of Materials Science and Engineering at the University of Sheffield who have been especially helpful in providing training during my project. I also thank my fellow colleagues and researchers at the University especially PRIMates for their help and support. In particular Dr Sam Tammam-Williams for his assistance with the XCT performed at the University of Manchester. I also thank Dr Meurig Thomas for his guidance and support as I first got to grips with my project and Dr Joanne Sharp for her tireless support and encouragement.

I thank the CDT staff for all of the hard-work and direction they provided throughout the past four years, particularly Dr Claire Hinchcliffe. I especially thank my CDT cohort for their constant support and for making these past four years so great.

Finally I would like to thank my family and friends for their care and support through all the hard times, and without whom this would all have been impossible.

1 Introduction

Modern-day aerospace components are often fabricated from high strength, creep and fatigue resistant alloys. Such materials are often expensive, both in terms of cost and energy to produce. This becomes problematic when critical components such as engine compressor blades are damaged during service and require repair. Whilst a conventionally designed blade and disk assembly allows for the easy removal of the damaged section, the integrated compressor bladed disk or “blisk” does not.

Conventionally, blades are mechanically fastened to the disk. A blisk design means that the blades and disk are one component, either being machined from solid or by friction welding the blades to the disk. This reduces the weight of the component and the absence of mechanical fastenings means that there is no longer an initiation site for fatigue cracks to grow [1]. This design, along with the economic implications of replacing an entire component, has led to the development of an additive manufacturing (AM) technology known as blown powder Direct Laser Deposition (DLD) as a means of repair. It is crucial that the quality of the repair is such that the mechanical properties match that of the parent component to avoid premature failure. Therefore, it is important that the effects of process parameters on microstructure and mechanical properties of the repaired part are understood.

There are already many studies to be found in literature on properties and process development for additively manufactured materials, including by DLD as detailed in Chapter 2. A lot of this work focuses on alloys that are already well-documented and very widely used in industry such as IN718 [2,3] and Ti-6Al-4V [4,5]. However, the aerospace industry requires new alloys which are lighter, stronger and can operate at higher temperatures than these traditional materials. This is especially true for gas turbine engines, where the drive to improve overall efficiency has resulted in increased gas compression in order to improve thermal efficiency and hence reduce the amount of fuel required for combustion [6,7]. To this end, the work presented here is based around Ti-6Al-2Sn-4Zr-6Mo (Ti-6246), an $\alpha+\beta$ titanium alloy, as a replacement for Ti-6Al-4V due to its suitability for elevated temperature environments. This alloy is already being used in the manufacture of some intermediate pressure (IP) compressor blisks for this reason.

In line with the above discussion, the first aim of this project is to investigate the fundamentals of DLD of Ti-6246 which is currently extremely limited in literature. This includes quantifying the effects process parameters have on the deposited microstructure and the mechanical properties of the material. This has been achieved by using a systematic approach to explore a potential process window via Design of Experiments (DoE). The DoE, in conjunction with linear regression analysis, provides a statistical model to describe the relationship between process inputs such as beam velocity

and process outputs such as 0.2% yield stress. In addition, a custom programme has been created for an automated method to measure size of the Ti-6246 microstructure.

The second aim was to develop an easily usable and understandable model which could be used to inform process parameter selection. Two different modelling approaches for the heat source were investigated (point-heat source and Gaussian). Both were validated against a real deposit with a geometry representative of the IP compressor blisks ear-marked for repair. The thermal models were used to develop and define the melt pool saturation level which compared the size of the molten area during the process to the full melting capabilities of the laser. This was then used to define upper and lower limits on the powder feed rate which is a critical and sometimes overlooked parameter during DLD.

To address these aims, the introduction here is followed by a review of the relevant literature relating to this work including a discussion of titanium alloys and microstructure, additive manufacturing (focussing on blown powder), industrial applications of DLD, aspects of thermal modelling and an introduction and discussion on normalised parameters and process maps. The chapters are then as follows:

- **Chapter 3:** Experimental techniques such as the methodology behind calibration of the thermal model and a discussion of the automated programme developed for the microstructural analysis.
- **Chapter 4:** This Chapter provides an overview of the typical microstructure of Ti-6246 produced by DLD which is not prevalent in literature. It also contains the results from the automated measurement technique using CLEMEX software and discusses the overall quality of the DLD builds by analysing the results from ICP-OES and XCT. The conclusions from both 2-D and 3-D analysis is presented here.
- **Chapter 5:** This chapter describes the set-up of the Design of Experiments for the DLD builds. Results from the uniaxial tensile tests are presented here. The response surfaces for key mechanical properties as a function of process inputs are presented as well as recommendations for further optimisation of the process window for repair. Response surfaces were produced to visualise how DLD process parameters alter important mechanical properties such as elongation to failure and 0.2% yield stress, with the ultimate goal of identifying and optimizing a process window for Ti-6246 DLD repair.
- **Chapter 6:** Chapter 6 discusses the set-up and calibration of the point heat source and Gaussian thermal models. The results for predicting melt depths are presented here as well as a discussion about the assumptions and limitations of the respective models.

- **Chapter 7:** This chapter discusses and quantifies the blown powder aspect of DLD such as power attenuation and effect of powder feed rate on the melt pool. It describes the calculation for determining the melt pool saturation level and the aspirational powder feed rate as a way for optimising the powder feed rate as a DLD input.
- **Chapter 8:** This chapter discusses the main conclusions from this work as well as suggestions for future work.

2 Literature Review

2.1 Titanium alloys

2.1.1 Crystal structure

The use of titanium alloys is dominated by the aerospace industry, from engine components to the landing gear. The metallurgical properties of titanium and its alloys are largely determined by the allotropic transformation which takes place at 882.5°C (for pure Ti). The transformation is from the body centred cubic (BCC) β -phase, to the hexagonal close packed (HCP) α -phase [8]. The two different crystal structures are depicted in Figure 2.1.

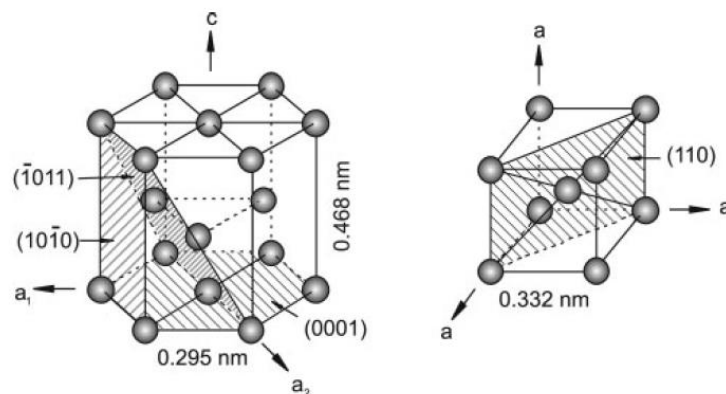


Figure 2.1: Crystal structure for (a) α -phase - hexagonal close packed (HCP) and (b) β -phase - body centered cubic (BCC) [9]

The presence of two different crystal structures means that titanium can have different mechanical properties depending upon which crystal structures are present. For example the HCP α -phase leads to highly anisotropic mechanical properties, depending upon whether the stress is applied parallel or perpendicular to the c-axis. In addition the number of easy slip systems in HCP is three, whereas there are twelve for BCC [9,10]. The slip systems are formed of the directions and planes for which plastic deformation is favoured. The limited number of planes available for the α -phase means that it does not plastically deform as well as the BCC β -phase.

In addition to the known differences in mechanical behaviour of the two crystal structures, there is also an orientation relationship between the two phases. This is known as the Burgers relationship

which was first observed in zirconium but was later found to occur in titanium as well [11,12]. Essentially, this relationship describes how from cooling through the β -transus temperature, up to twelve different orientations of α can form from a single β -crystal. This is also discussed by Stanford & Bate (2004) [13] where electron back-scattered diffraction (EBSD) revealed significant texture for the α -phase in Ti-6Al-4V which meant that instead of being random, there was a preferred orientation. This was concluded to be down to the influence of the crystallography of the prior- β grain boundaries where the α nucleates.

Rugg, Dixon & Dunne (2007) [14] also discuss the preferential orientation as a result of α -phase already present in the material or from mechanical or thermal stresses during cooling. The authors note however, that the diffusionless martensitic transformation from β to α may reduce the preferential orientation effect due to no nucleation from pre-existing alpha. However, they do not discuss how this rapid cooling may affect the thermal stresses during cooling which also leads to a preferential orientation[15].

However, both of these studies were not performed on additively manufactured titanium where variant selection of α is most likely influenced by the thermal stress within the material as opposed to nucleation effects [16]. Antonysamy, Meyer & Prangnell (2013) [17], found that although the prior- β grains in AM Ti-6Al-4V had a strong texture, the α -phase had a far weaker texture. This indicates that there was no preferred crystallographic orientation, which has also found to be true by other studies [18]. The implications of this is that the formation of the α -phase after cooling from the β -phase field, breaks up the initial strong texture and so reduces the anisotropy in mechanical properties that would otherwise be present. However, as noted by the authors, this does not necessarily mean all AM titanium builds will have weak texture. Instead it may be dependent upon the scan strategies used which in turn effect the amount of thermal stress in the material.

2.1.2 Classification of Titanium alloys

The transformation temperature is affected by the presence of alloying elements, known as α or β stabilizers depending on whether they raise or lower the transformation temperature.

As shown in Figure 2.2, typical α stabilizing elements such as Al, O, N and C broaden the α phase field up to higher temperatures. β stabilizing elements such as Mo, V and Ta move the β phase field to lower temperatures. As such, titanium alloys are categorized into α , $\alpha+\beta$ and β depending upon the contribution of the α and β phases. However, as noted by Lutjering (2007) [19], this is not necessarily

representative of the phases present in the alloy. For example, some α alloys do contain small fractions of β -phase. In line with this, the titanium alloys may be split into two further categories, namely near- α and near- β [8].

The group of α alloys comprises of the Commercially Pure (CP) titanium grades and the α alloys which contain around 2-5% of β -phase. In such alloys, oxygen is an interstitial that acts to increase the strength of the alloy, but also reduces the ductility [9]. This group of titanium alloys can't be age hardened but do generally have good corrosion behaviour. The near- α alloys, by comparison, contain elements that stabilize the α -phase but additionally they can contain up to 10% of β -stabilizers. They can be used at temperatures of up to 600°C and they demonstrate the good creep behaviour of α alloys and the high strength properties of the α + β alloys.

The near- β and β alloys have high enough levels of β stabilizing elements that the β -phase is stable (or metastable) at room temperature and does not transform upon quenching. The β stabilizing elements slow or prevent the nucleation and the growth of the α -phase. It should be noted that most of the commercial β alloys are metastable and not located in the single-phase field. Given enough ageing time, the α -phase will begin to grow.

The titanium alloy used in compressor Blisks, and that is the focus of this work is Ti-6246, which is an α + β alloy and so this group will be the focus of the following discussion.

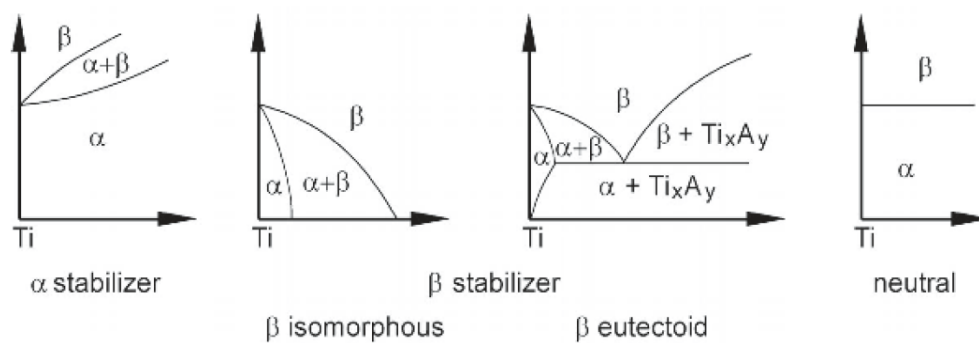


Figure 2.2: Diagram to show the effect of different stabilizers on the Ti phase diagram [19]

2.1.3 α + β alloys and Ti-6246

α + β alloys usually contain between 4 and 6% of β stabilizers, which results in a broad α + β phase field at room temperature and a notable amount of β -phase being retained after cooling [1, 3]. The

microstructure of $\alpha+\beta$ alloys depends on the cooling rates applied to the material. Fast cooling or quenching from the β -phase field results in a martensitic transformation.

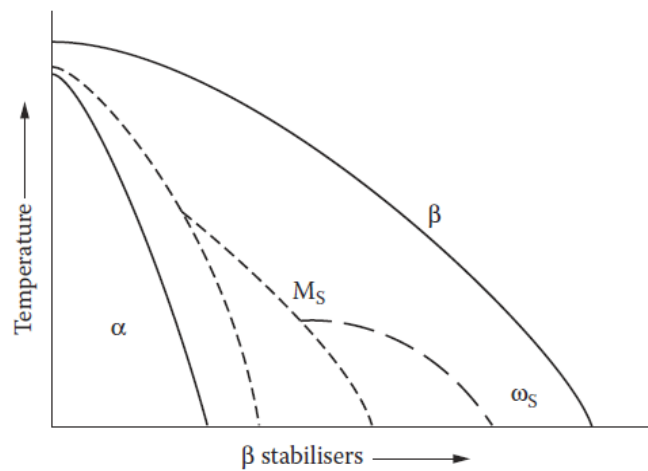


Figure 2.3: Generic $\alpha+\beta$ phase diagram indicating the location of the α and β phase fields with respect to temperature and concentration of β stabilizers [20]

The most widely used of the $\alpha+\beta$ alloys, and indeed the most widely used titanium alloy is Ti-6Al-4V. It is the most tested and developed of all the titanium alloys and is mostly used in aerospace components. Its usefulness is mainly due to its balance of mechanical properties including; ductility, strength and fracture resistance. However, it is only useful up to temperatures of 300°C [19].

Ti-6246 is a $\alpha+\beta$ alloy developed by TIMET whose high-strength, toughness and creep properties at elevated temperatures means that it is used for critical rotating components in aero-engines, such as intermediate pressure compressor Blisks [4, 5]. Its composition is given below in Table 2.1.

Table 2.1: Typical composition of Ti-6246

Element	Al	Fe	Mo	N	O	Sn	Zr	C	Ti
%	5.5-6.5	0.15	5.5-6.5	0.04	0.15	1.8-2.2	3.6-4.4	0.1	Bal.

Although, as stated above, Ti-6246 is often classified as an $\alpha+\beta$ alloy, it is also sometimes called a near- β alloy due to its high β stabilizer composition (namely 6% Mo). The lack of agreement arises because there is no absolute definition as to the separation between $\alpha+\beta$ and near- β alloys. Often, $\alpha+\beta$ alloys are defined as those that undergo a martensitic transformation when subject to rapid cooling from the β -phase field to room temperature. Near- β alloys have a high enough concentration of β stabilizing

elements such that the martensitic start and finish lines are below room temperature [8]. There is some evidence that observed martensite in Ti-6246 is produced during sample preparation steps [19] and not from quenching and hence should not be classed as an $\alpha+\beta$ alloy. However high energy synchrotron X-ray radiation (HESXR) revealed the presence of orthorhombic martensite in Ti-6246 that had been rapidly quenched from the β -phase field [23]. Ti-6246 contains both α and β stabilizing elements (Al and Mo respectively) and martensitic microstructures have been observed in the direct laser deposition (DLD) material used in this work. Therefore, it will be referred to as an $\alpha+\beta$ alloy in the following sections.

2.1.4 Use of Titanium alloys in aerospace industry

The driving force for materials in aero-engines is the requirement for reducing the weight of the components but also for them to operate at higher temperatures. For the compressor blades in particular, there is a need for good corrosion, impact and fatigue properties. Higher temperature sections of the aero-engine means that there is also a need for the materials to have good creep resistance [24]. It is for this reason that titanium alloys are commonly used in the aerospace industry, with 50% of the global titanium production in 2010 going to the aerospace sector [25]. Using titanium also leads to a reduction in the weight of aero-components when compared to using nickel or steel, which goes a long way to improving fuel efficiencies. Titanium alloys also have a high specific strength, good corrosion resistance and can be used at elevated temperatures [9]. Their temperature capabilities are limited however, and so titanium alloys are generally found in the lower temperature sections of aero-engines such as the intermediate pressure compressor (see Figure 2.4). Nickel superalloys are instead used in the high temperature areas such as the high pressure compressor.

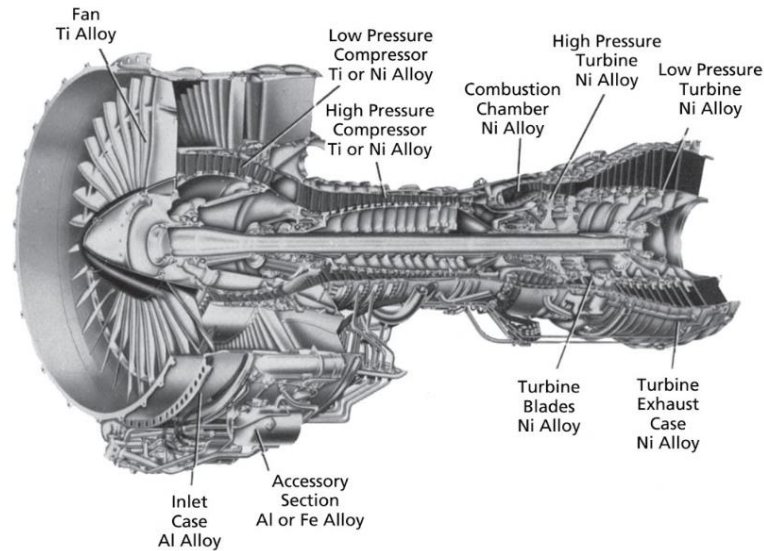


Figure 2.4: Schematic showing typical material distribution within an aero-engine [26]

For the most part, the $\alpha+\beta$ titanium alloys are used in the aero-engine such as Ti-6Al-4V which is a traditional and most widely used of the titanium alloys. Other $\alpha+\beta$ alloys include Ti-6242 and Ti-6246 [25,27,28], the latter of which is the material used in this body of work. Ti-6242 has a high creep resistance as well as good strength and toughness properties and can be used up to temperatures of approximately 425°C. Ti-6246 is stronger than and can be used at higher temperatures (480°C) than Ti-6Al-4V due to the presence of 2% Sn and 4% Zr which provides solid solution strengthening, and also due to the β stabilizer Mo (6%).

2.2 Phase transformation

2.2.1 $\beta \rightarrow \alpha$ transformation

The phase transformation from the BCC β -phase to the HCP α -phase is of importance because it determines the final microstructure and hence the mechanical properties of the material. This transformation is controlled by both the alloy composition and the cooling rate, the latter of which determines the mechanism of how the β -phase is transformed into α .

Cooling down from the β -phase region slowly results in nucleation and diffusional growth. At very slow cooling rates, the α -phase initially nucleates at the β grain boundaries, forming grain boundary α . Continued cooling results in α lamellar with a plate-like morphology to nucleate from the grain

boundary α and grow into the prior- β grain as shown in Figure 2.5a. Retained β -phase separates the individual α lamellar. Slightly faster cooling results in α plates growing parallel to one another to form colonies within the prior- β grain (Figure 2.5b), the slower the cooling rate the larger the colonies are. The size of the α colonies is important because slip is easily transferred across the individual lamellae (or laths) [8]. Different colonies have different orientations (up to 12 variants in total), and the interweaving of these colonies as they meet each other growing within the same grain leads to a basket-weave microstructure which is evident in Figure 2.5c.

At higher cooling rates, the lamellar microstructure becomes more refined and the α -colony size decreases. In this regime, new α colonies not only nucleate at the grain boundaries but also from pre-existing α colonies within the grain. This gives a fine basket-weave or a Widmanstätten microstructure (Figure 2.5d) commonly observed in titanium alloys such as Ti-6246 that have a high percentage of β stabilizing elements [9].

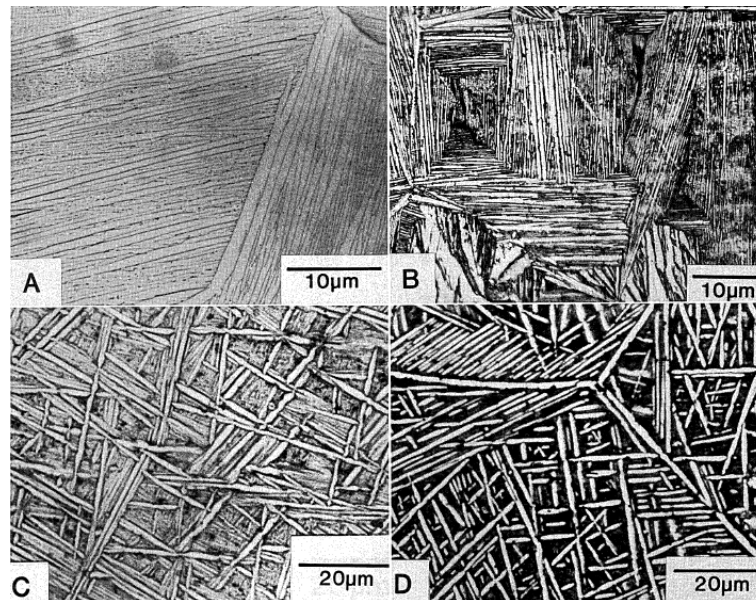


Figure 2.5: Example of typical titanium alloy microstructure at different cooling rates (a) furnace cooled (b) air cooled showing colony α (c) air cooled showing basket-weave (d) air cooled showing Widmanstätten α [8]

2.2.1.1 Diffusionless transformation

At high enough cooling rates from temperatures above the martensitic start temperature (M_s), the β -phase undergoes a diffusionless transformation. This gives an extremely fine meta-stable martensitic microstructure. For titanium this can be put into two categories; hexagonal (α') or orthorhombic (α'') which is formed by cooling from below 900°C [9]. The hexagonal α' phase produces a fine basket-

weave type microstructure made up of thin needles, not dissimilar to the basket-weave formed by slower cooling rates.

The effect of cooling rates on titanium microstructure was studied by Ahmed and Rack (1998) [29]. They performed a study using different cooling rates on a Ti-6Al-4V test piece and found that a high cooling rate of $525^{\circ}\text{C}\text{s}^{-1}$ resulted in a fully martensitic (α') microstructure (Figure 2.6a). This phenomenon has been observed in other studies [8-10], where high cooling rates and rapid solidification results in martensitic microstructures. Slower cooling rates within the same study showed much coarser microstructure as shown in Figure 2.6b (note the change in scale between the two micrographs). Here the typical basket-weave Widmanstätten microstructure can be seen.

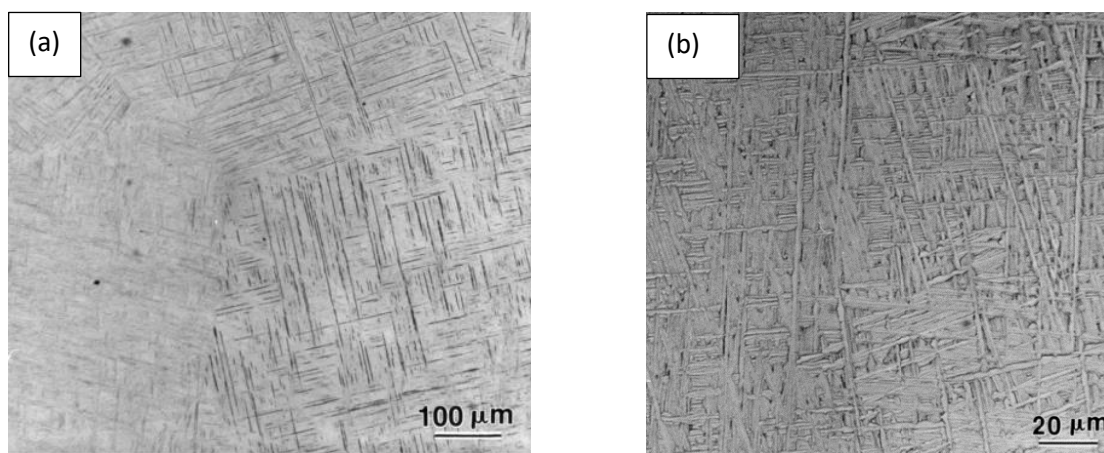


Figure 2.6: Micrograph of martensitic titanium formed due to (a) rapid quenching $525^{\circ}\text{C}\text{s}^{-1}$ and (b) $15^{\circ}\text{C}\text{s}^{-1}$ [29]

2.2.2 Lamellar microstructure and properties

In general, it has been observed that lamellar microstructures have a higher strength over equiaxed microstructure but lower ductility than an equiaxed microstructure [32]. The microstructure observed in DLD Ti-6246 in this study mostly consists of fine α lamellar separated by retained β -phase which is also observed by Blackwell & Wisbey (2005) [33] as shown in Figure 2.7. Here the presence of continuous grain boundary α is also very clear. Due to the high level of beta stabilizing elements in Ti-6246, the microstructure can also share some characteristics with beta annealed microstructures (of beta alloys). For instance, in Ti-6246, the formation of “side-plates” is fairly common, as well as the formation of a necklace microstructure. Discussion and examples of this are in Chapter 6.

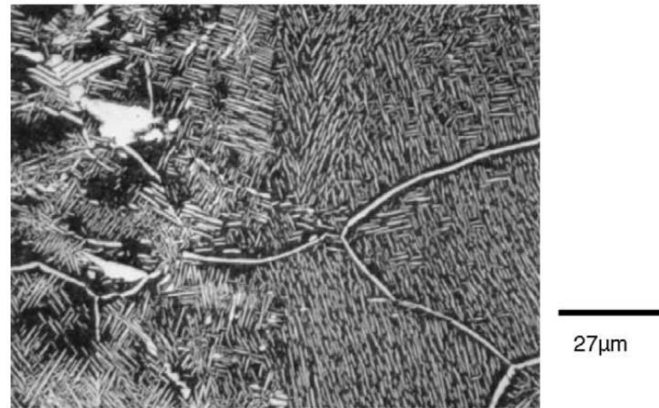


Figure 2.7: Micrograph showing the typical Widmanstätten microstructure for direct laser fabricated Ti-6246. Note substrate material on left-hand side [33]

The cooling rate is important in defining specific aspects of the lamellar microstructure such as the size of the α -laths, the size of the α colonies and the thickness of grain boundary α [19]. As the cooling rate increases, the size of these features decreases. As can be seen from Figure 2.8, as the cooling rate increases there is an overall increase in the strength of the material, with a rapid increase observed in the yield stress for cooling rates greater than $1000^{\circ}\text{C}\text{s}^{-1}$ due to the formation of martensitic microstructure. By contrast, the elongation to failure which is a measure of the ductility, remains fairly consistent as the cooling rate increases. At a critical cooling rate there is an initial increase in the ductility, followed by a fairly sharp decrease. This is attributed to a change in the fracture mode by Lutjering (1998) [34], from a ductile crystalline to a ductile intercrystalline fracture which is related to the grain boundary α .

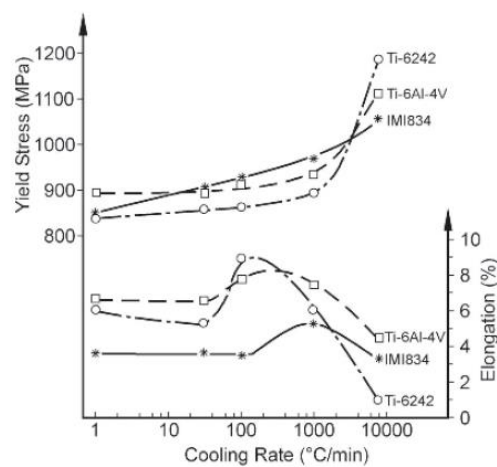


Figure 2.8: Effect of cooling rate on mechanical properties of common titanium alloys with fully lamellar microstructures [19,34]

2.3 Additive Manufacturing

2.3.1 Background and history

Additive Manufacturing (AM) started off as a Rapid Prototyping (RP) method. Parts could be fabricated in a layer-by-layer process very quickly but did not necessarily have desirable mechanical properties or geometrical accuracy. This made RP suitable for designing and creating rough models or prototypes of a final product but not as a serious manufacturing technology. However, as the technology developed, the RP process reached the point where the printed component had the required properties of the final product. The term Additive (Layer) Manufacturing (ALM) was coined as a more accurate representation of the technology.

The basic premise of AM is that components can be built up in layers in an additive process as opposed to subtractive processes such as CNC machining. The geometry of the layers are generally determined using computer aided design (CAD) software to segment a schematic of the component in thin sections [35].

There are many different manifestations of AM technology, with the distinction primarily stemming from how the layers of the component are formed. Table 2.2 shows a non-exhaustive list of the different types and naming conventions for powder-based additive manufacturing. As can be seen there are a large number of terminologies being used in the literature and in some cases there is little to no difference between them. However, when looking at metal powder, it is common to divide them into two main categories; powder bed and blown powder. The repair of compressor Blisks is performed using blown powder technology and so will be the main focus of discussion here. A brief description of powder bed will be given for comparison.

Table 2.2: List of different types of powder-based Additive Manufacturing technologies and terminologies

Name	Type	Examples/refs
Direct laser deposition (DLD)/ Direct laser additive manufacturing	Blown powder	[36,37]
Selective laser melting (SLM)	Powder bed	[31,38]
Laser engineered net shape (LENS)	Blown powder	[39]
Electron beam melting	Powder bed	[18,40–42]
Laser net shape manufacturing	Blown powder	[2]
Direct metal deposition (DMD)	Blown powder	[43–45]
Direct(ed) energy deposition	Blown powder	[4]
(Direct) Laser fabrication	Blown powder	[46]
Laser (powder) deposition	Blown powder	[47,48]
Laser rapid forming	Blown powder	[49]
Laser powder bed fusion	Powder bed	[50]

2.3.2 Powder Bed

As shown in Figure 2.9, powder bed technology comprises of a powder delivery system, powder spreader, build platform and a laser system. During the build process, the powder spreader is used to spread a thin layer of metal powder onto the build platform. The laser then selectively melts designated parts of the powder that correspond to the geometry of the final part. When this layer is complete, the build platform is lowered and the process start again by spreading over a new layer of powder. This type of AM technology is often used as a means to redesign and manufacture components to increase their performance by using complex geometries to reduce weight [51]. However, this process is quite slow and requires a flat substrate on which to spread the powder, as such it is not suitable as a repair technology.

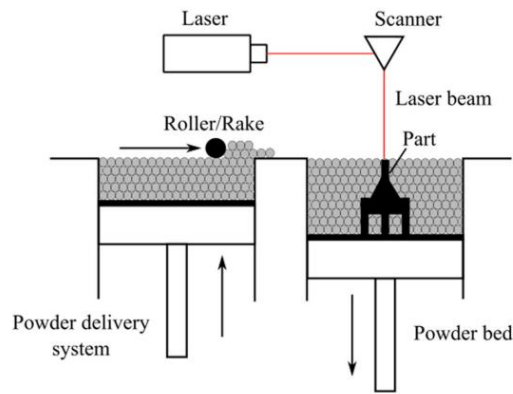


Figure 2.9: Schematic of the main components during a powder bed AM process [52]

2.4 Blown powder direct laser deposition

As discussed above, there are many different names given to the blown powder process, such as Laser Engineered Net Shaping (LENS), Direct (Laser) Metal Deposition (DLMD) and Direct Laser Fabrication (DLF). Direct Laser Deposition (DLD) will be used when referring to cases specific to this work.

A basic setup of a blown powder ALM machine is shown in Figure 2.10. Generally, blown powder DLD requires a laser beam, powder nozzles and an inert gas system. In the case of repair, the parent component will be used as the substrate upon which the additional layers will be built up with new material.

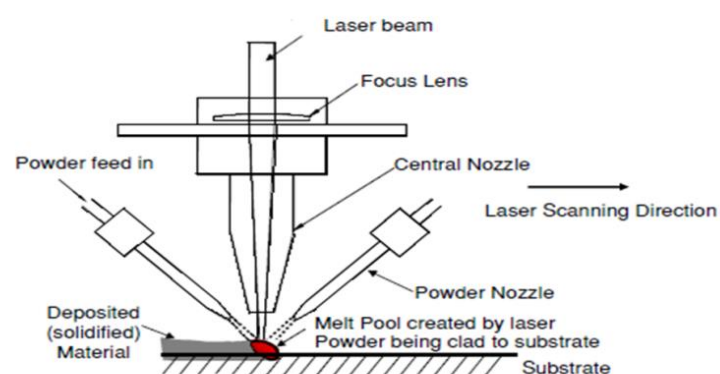


Figure 2.10: Schematic of a typical blown powder deposition process [2]

During the blown powder DLD process, a heat source (in this case a laser) is focussed on the workpiece and generates a pool of molten material. At the same time, metal powder is ejected or blown coaxially

into this melt pool via the powder nozzles. As the powder interacts with the laser beam and the melt pool it melts and then rapidly cools as the beam continues to traverse the workpiece [53].

2.4.1 Process parameters

It is known that there is an inherent relationship between process parameters used to build an AM part and the resultant microstructure and mechanical properties of the build [43,54,55]. Amine, Newkirk & Liou (2004) [55] investigated how changing parameters such as the laser beam power and velocity affected the deposition process of 316L SS. They found that increasing the beam power resulted in a significant increase in the size of the microstructure (secondary dendrite arm spacing) as shown in Figure 2.11. This was linked to a decrease in the cooling rate as the power increased. It should be noted that the micrographs shown in Figure 2.11 were deposited with increasing beam power and velocity. The authors have not attempted to quantify the effects of these two parameters in combination in the results. Several authors have used a combination of parameters such as power, velocity, layer height and hatch spacing together to form a type of line energy density [31].

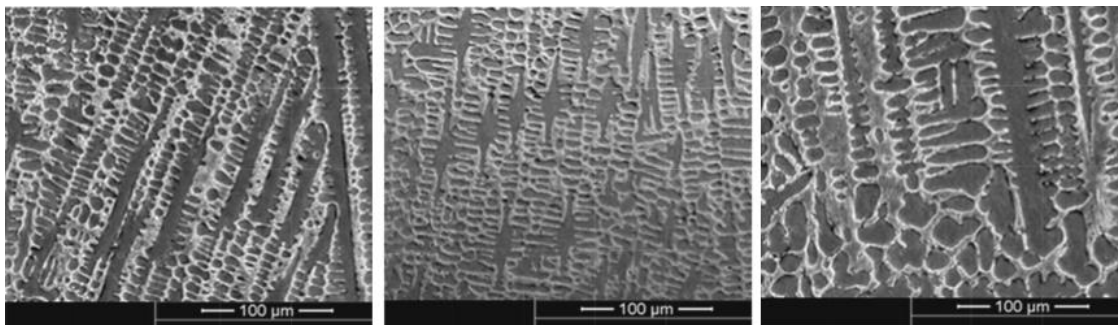


Figure 2.11: Microstructure of DLD 316L SS at using beam power and velocities of (a) 750W & 300 mmmin^{-1} (b) 750W & 450 mmmin^{-1} and (c) 900W & 300 mmmin^{-1} [55]

There is not a lot of information to be found in literature concerning the DLD of Ti-6246 (or indeed any other AM technology). Blackwell and Wisbey (2005) [33] however, investigated the effects of using two different heat sources on the mechanical properties of Ti-6246. As discussed previously, they found that both the CO₂ laser and the Nd-YAG laser produced fine Widmanstätten microstructure, although the microstructure for the CO₂ laser was slightly coarser, although this appears to be qualitative rather than quantitative. The coarser microstructure corresponded to a lower tensile strength than the finer microstructure. In both cases, the ductility of the material was found to be very poor. However, as noted by the authors, no attempt was made to optimize the parameters before deposition. As such comparison between the two different laser types is mostly valid, but comparison

to other titanium alloys or conventionally fabricated Ti-6246 is not. This study is therefore not a good example of the properties of DLD of Ti-6246.

Other than the aforementioned study, there is extremely limited information about DLD of Ti-6246. However, there are studies in literature about DLD process parameters in general that highlight the general trends for microstructural and mechanical properties of DLD materials. Table 2.3 provides a list of the most common process parameters that can be controlled in some way for the DLD process.

Table 2.3: Typical process parameters used in DLD

Parameter	Units
Beam Power	W
Beam velocity	ms^{-1}
Beam Radius	m
Powder feed rate	gmin^{-1}
Hatch spacing	m
Layer height	m

As discussed above, changing one or more of the parameters can have a quantifiable effect on the final solidification microstructure within the build [46]. An example of this is described in the work on AM of Ti-6Al-4V by Wu et al. (2004) [48], whereby an increase in the powder feed rate and the beam velocity was found to result in the formation of small equiaxed grains instead of the more common columnar prior- β grains. This change in the solidification microstructure was attributed to an increase in the number of nucleation sites within the melt due to the reduced melting of powder particles. This has important implications for DLD processing since the morphology and orientation of the prior- β grains is known to affect mechanical properties [4]. Additionally, although not noted by Wu et al., the changes in microstructure with respect to process parameters does place limitations on the upper (and lower) values of these parameters and hence on the deposition time for each build. It may be desirable to use a fast beam velocity to decrease the deposition time but clearly this has repercussions for the microstructure. However, as noted by the authors, the exact effect of each of the parameters is not straightforward to quantify, so defining these upper and lower limits is not trivial.

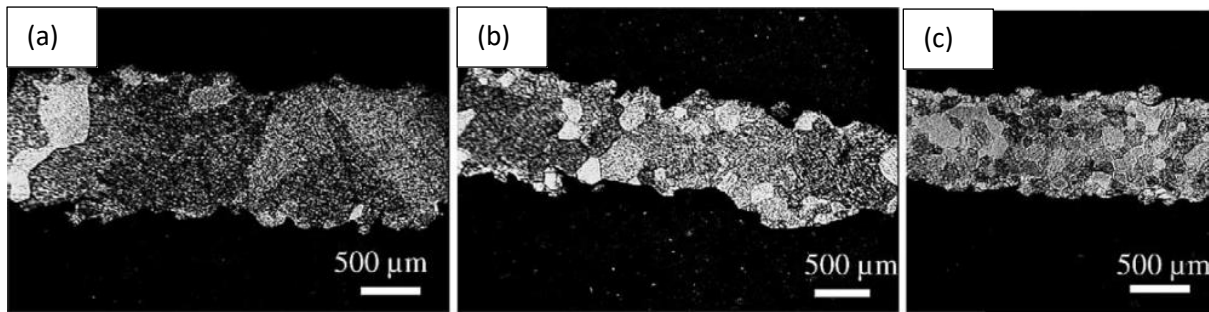


Figure 2.12: Optical micrographs of AM Ti-6Al-4V revealing a reduction in grain size as the laser beam velocity and powder feed rate are increased (a) 200 mmmin^{-1} , 6 gmin^{-1} (b) 500 mmmin^{-1} , 15 gmin^{-1} (c) 800 mmmin^{-1} , 18 gmin^{-1} [48]

A large portion of the studies found in literature are for the powder bed process, although the findings are very similar. Hrabec and Quinn (2013) [56,57] performed a fairly extensive study into the effects of variables such as energy input, orientation and the build height (distance from the substrate). Much as the study undertaken by Carroll, Palmer and Beese (2015) [4], they found that the AM builds were subject to anisotropic mechanical properties due to the orientation of the prior- β grains. Similar studies cited by Carroll. The issue with all of these studies however, is that there is a large range of specimen geometries, process parameters and testing methodologies. As such, it is not straightforward to compare one study with another and so there is a difficulty in precisely quantifying what the exact effects are. This is highlighted in the anisotropic behaviour found in the aforementioned studies. Whereas Carroll et al. found that the elongation to failure was higher in the transverse specimens, Hrabec and Quinn found the longitudinal specimens had the higher elongation to failures. It is unclear if this difference arises due to the differences between powder bed and blown powder processes or whether there is another mechanism causing this.

2.4.2 Applications of blown powder DLD

Direct laser deposition, much like AM in general, opens a lot of new possibilities within manufacturing across a number of different industries including aerospace, automotive, medical and oil & gas. Reviews of the AM literature reveal a general consensus of three main applications for the DLD process: near-net shape manufacturing, laser cladding and component repair [58–61]. Other applications also build on these three areas and include rapid prototyping and functionally graded components. Many different metal alloys including but not limited to; Ti-alloys such as Ti-6Al-4V, Ni-based superalloys (IN625, IN718, Hastelloy X and Waspaloy) and stainless steels including 316L and 304 [52] are all key areas of interest within the literature.

Near-net shape manufacturing using DLD covers multi-layer deposition to fabricate a fully-functional component at, or near to, the final required geometry, in a one-step process [62]. Rapid prototyping may also fall into this category, although in this case mechanical properties may not be representative of the final part. DLD has many advantages over more conventional subtractive processes as it significantly reduces the buy-to-fly ratio and allows components to be manufactured from difficult to machine materials. In their review, authors Liu et al (2017) [63], discuss the suitability of DLD for more complex part geometries. However, the limitations of this are not discussed and consideration of the material being processed, feedstock characteristics, laser beam radius, deposition rate, part size and number of machine axes available needs to be considered. More complex and detailed geometries are often achieved using L-PBF instead [64]. This highlights an issue within literature around a lack of understanding or distinction between powder-bed and blown powder processes.

In any case, the manufacture of parts using DLD is already being demonstrated in the aerospace industry. For example, Heilemann et al (2018) [65] performed a study to investigate the possibility of using DLD of AlSi10Mg to manufacture a light-weight fuselage (Figure 2.13).

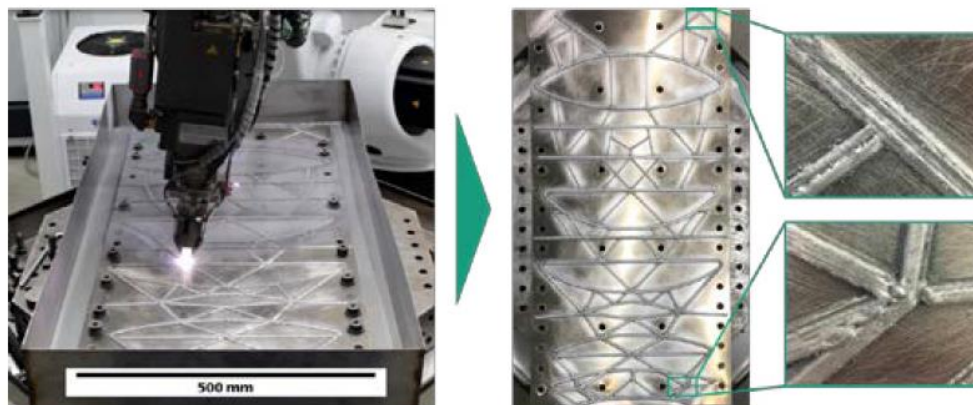


Figure 2.13: Example of part manufacture using DLD of AlSi10Mg for a fuselage [65]

The authors took advantage of the design flexibility this process offers and performed topology optimisation on the part before deposition. As was noted, optimisation should consider the limitations of the process in question to ensure that the geometry is still realistic to achieve. Overall, the authors concluded that the selected geometry was feasible but that the process had to be carefully monitored and controlled to avoid deformation due to the material selected.

Other applications can be found in the biomedical industry. Xue et al (2007) [66] demonstrated how the DLD process could be used to create porous bone implants using titanium. The authors found that the mechanical properties of the porous DLD material were a close match to actual bone tissue. There are currently other techniques to manufacture porous titanium components, but this either introduces additional chemicals in the form of foaming agents or limits the size of the pores that can

be generated. The ability to control the level of porosity in a structure simply by altering DLD process parameters makes this technology a good fit.

One of the key things missing in the literature is that the use of functional DLD products in service is limited to a certain degree by the need for confidence in the process and the ability to manufacture consistent parts. Although the general design and mechanical property advantages of DLD make it a desirable choice in the manufacturing industry, integration of DLD components into the aerospace sector (for example) requires quality assurance and certification which appears to be somewhat overlooked. To achieve this would require more extensive studies, both experimental and model-based and it therefore may take a long time before DLD overtakes conventional manufacturing routes.

The second main DLD application is laser cladding. This is the process of depositing material onto a substrate or component, normally in one or a few layers typically up to 1mm thick [67]. This may be done before the component goes into service to protect the substrate and/or to increase service-life. Laser cladding may also be used as a type of repair strategy to enable a component to return to service after wear.

An overview by Quintino (2012) [68] discussing a variety of different coating techniques provides four main applications: hard-facing, surface cladding, build-up (repair) and buttering for joining incompatible or dissimilar materials. Although these are for surfacing technologies in general, they are all applicable for DLD coatings, highlighting the potential reach of this technology. This is especially true when considering the variety of coating materials for DLD. A review of the literature shows this includes; high-entropy alloys such as AlCoCrFeNi [69] or FeCoNiCrCu_xSi_{0.5} [70], Co-alloys such as Stellite-6 or Stellite-21 [71] and meta-stable alloys such as Fe-Cr-Mn-C and Ni-Cr-Al-Hf [72].

A coherent understanding of the deposition process is just as important for thin coatings as it is for large net-shape components. The quality of a coating is dependent on reducing any defects such as pores or cracks which would otherwise lead to failure of the coating and exposure of the more susceptible substrate material. DLD has advantages over more typical coating or deposition techniques including TIG or MIG welding and plasma or thermal spray due to a smaller resultant heat affected zone and hence low dilution levels, as well as its geometric precision. Reviews of different coating techniques also discuss how the metallurgical bond achieved between coating and substrate using DLD is far stronger than the mechanical bond produced by methods such as plasma spraying. DLD also results in a better surface finish ($R_a \sim 1.3\text{-}2.8\mu\text{m}$) compared to an R_a of $4\text{-}5\mu\text{m}$ for plasma spray which is represented in Figure 2.14 [73].

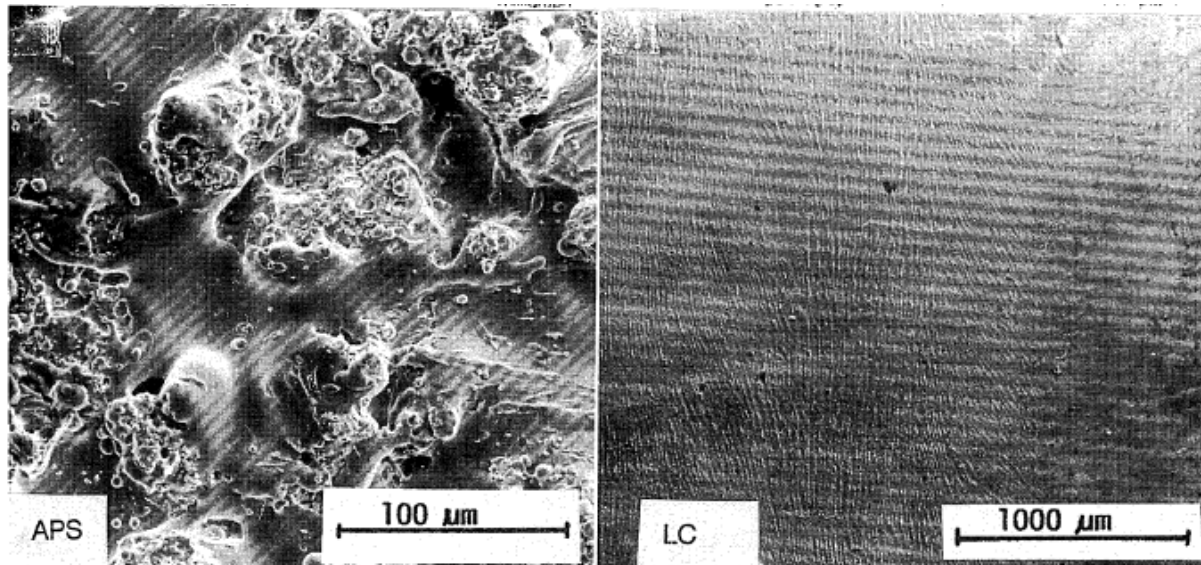


Figure 2.14: SEM images of coating produced by plasma spray (left) and DLD (right)[73]

DLD allows coatings using dissimilar materials, so that a component may be manufactured primarily from a cheaper alloy than the coating material, which has superior corrosion or wear resistance properties [59,74]. For example, in a review by Khanna et al (2009) [75] comparing thermal spray and laser cladding, they revealed that laser cladding of low carbon steel using WC/Co + Ni-Cr produces coatings with superior hardness as well as wear and friction resistance compared to both a conventional hard-chrome plating method and by plasma spraying.

DLD as a coating method is particularly advantageous in the tooling industry, where components regularly become worn during service. DLD can be used to deposit a thin layer of a hard-facing coating onto the surface in order to increase the lifetime of the component. For example, DLD has been used to coat a H11 tool steel, used for pressing tools, with a Ni-alloy/WC material as an alternative to conventional nitriding [67]. The coating (Figure 2.15) underwent wear testing which revealed that it had significantly higher wear resistance than a traditional nitrided surface under identical conditions, and indicated a potential x6 increase in service-life for the tool.

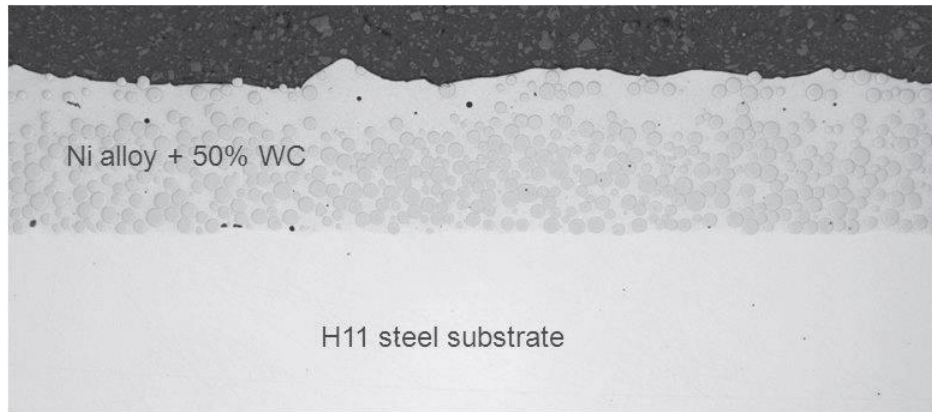


Figure 2.15: Ni-alloy/WC coating on a H11 tool steel applied using laser cladding (DLD)[67]

Repair is the third major application of DLD and the process of returning a component to its original state may also be known as re-manufacturing [76–78]. A review of the current state-of-the-art in DLD technology by Dass and Moridi (2019) [59] clearly identifies the ability to extend a component's life either if it fails prematurely or beyond what would normally be expected as major advantage of DLD. This is backed-up in a review by Birger et al (2011) [79], which quantifies the potential savings gained by using DLD for re-manufacturing at an American naval base as up to \$1.15 million every year.

DLD as a repair technology is also useful for legacy parts [80]. In this case, the flexibility of DLD is useful since these are generally one-offs and it would be uneconomical to manufacture a new component especially if the original drawings are unavailable or if the part is manufactured from an alloy no longer in common-use. Another application for DLD repair is for components that have manufacturing or machining defects. In this case, DLD can be used to prevent the component from being scrapped before it has even been in service.

DLD isn't the only technology used to repair or re-manufacture components. However, methods such as TIG are problematic due to the high heat input which causes distortion of the original part. Identical to the benefits found in coatings, DLD allows for more precise application of material compared to methods such as high velocity oxygen fuel (HVOF) as well as a strong metallurgical rather than mechanical bond to the parent material [63].

Wilson et al (2014) [76] investigated the process of re-manufacturing of a turbine blade. Their work focused on creating a model for the repair section as well as simulating a repair scenario during deposition of a tensile sample. Testing of the tensile specimens showed good mechanical properties compared to parent material and the region of failure was away from the repair-parent interface. Although these are both good indicators that the DLD process and material properties are suitable for repair, this type of experiment needs to be extended significantly before being validated as a repair strategy for aerospace components. This would include but not be limited to systematic down-

selection of parameters as well as intensive testing of microstructural and mechanical properties not just ultimate tensile strength and yield stress. It's also unclear from this study whether the tensile specimens were deposited with geometries representative of turbine blades which is an important consideration for industrial uptake.

A lot of the work reported in literature focuses on repairing groove-like defects such as that conducted by Pinkerton, Wang & Li (2008) [81] and Liu et al (2016) [82]. In the later study, the authors investigated repair of TC17, an $\alpha+\beta$ titanium alloy commonly used by the aerospace industry. Wrought TC17 with pre-machined grooves was used as the substrate and DLD of TC17 powder was used to fill or repair U-shaped grooves. The deposited material showed low levels of porosity and corresponding tensile specimens achieved comparable strength and ductility to forged TC17, showing this process and material may be suitable for repairing groove-like features. The study undertaken by Pinkerton also looked at groove repair, this time using H13 tool steel as a substrate and powder. The authors expanded on U-shaped grooves and instead machined V-type and square-type geometries into the substrate as shown in Figure 2.16.

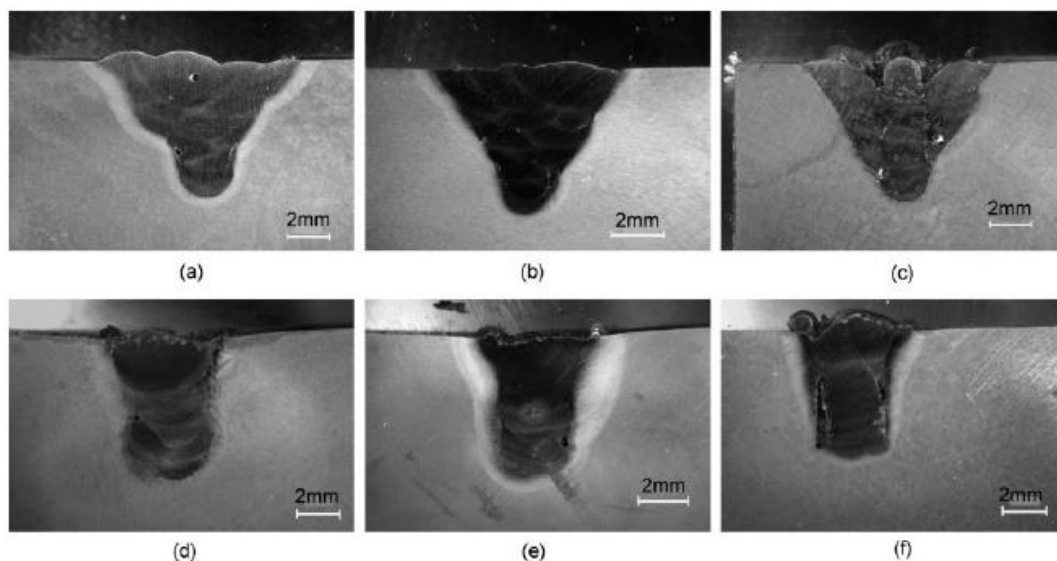


Figure 2.16: (a-c) V-shaped grooves (d-f) square shaped grooves repaired using DLD [81]

Petrat et al (2016) [83] investigated a more 3-D application by using DLD to repair a gas turbine burner using Ni-base superalloy IN718. Interestingly, the full burner component was manufactured using L-PBF and material was then removed to allow for a DLD repair as shown in Figure 2.17. The difficulty with this repair was that the cylindrical section required deposition with three different wall thicknesses, diameters and build heights which required three different process parameter sets. However, despite these difficulties the final repair showed relatively low levels of porosity and only a

slight drop in hardness compared to L-PBF material. It's likely that with further exploration of the process window, these properties could be improved if the application required it.

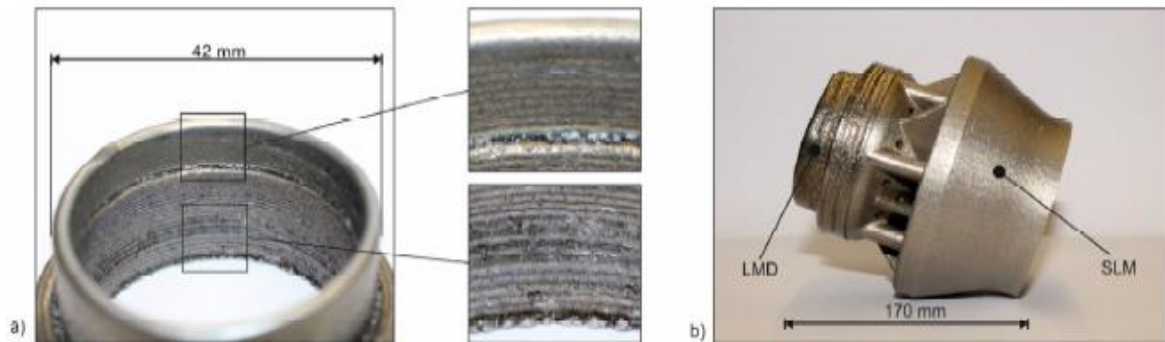


Figure 2.17: (a) Test geometry for DLD repair (b) Gas turbine burner with LMD repair and SLM substrate (IN718)[83]

In conclusion, the literature discussing the above applications agree that DLD has the potential to be an extremely disruptive technology. In contrast to the general understanding about AM, these disruptions may be just as, if not more likely, to come in the form of coatings or repairs rather than full-scale manufacturing. A lot of discussion around using AM technologies for near-net shape manufacture appears to collate L-PBF and blown powder technologies under one umbrella. It is important therefore, to provide a clear distinction about the potentials of blown powder DLD in order to see its uptake in industry. Additionally, a fuller understanding about the scope of DLD is required as different industry sectors, for example, do not equate laser cladding with DLD or even AM/3-D printing. This is also hindered by the many different naming conventions used; direct laser deposition, laser engineered net shape, laser cladding, direct energy deposition and laser metal deposition to name a few.

However, for all these applications, there is a consensus that a fundamental understanding of the process is necessary in order to fully exploit DLD. Still though, many reviews and studies investigate bulk microstructural and mechanical properties which are not necessarily representative of the final geometry being explored. In addition, although there are some real-world examples to found in literature where DLD is already being used, there is surprisingly little considering the interest surrounding AM in general. The main barrier that stands in the way of large-scale adoption of DLD, is that, in comparison to methods such as casting, forging or even traditional welding, DLD is still relatively new. The means that there is far less understanding of the process and how changes will affect build quality. Confidence in the quality of a component is paramount, especially for critical components and especially in the aerospace industry. This means that there is still a long way to go

before DLD parts have the necessary quality assurance and certification required to go into service on a large scale.

A review of the literature also shows that there is still a big focus on traditional alloys such as Ti-6Al-4V and IN718 even though the potential for new alloys is highlighted as an advantage of this technology. However, coatings and repairs provide the most obvious application for using new or more expensive high-performance alloys since only small quantities of the material may be required.

Therefore, the investigation into less traditional alloys, such as Ti-6246, is important as it establishes the groundwork for this material and process to gain traction in repair applications. It also starts to provide important fundamental information about process parameters, microstructure and mechanical properties that are not currently available in literature. This lack of information hinders the acceptance of such new alloys into the industry as well as hinders the uptake of this technology and material.

2.5 Modelling the AM process

2.5.1 Introduction

In order to fully understand how DLD, or AM in general, process parameters affect the microstructure and mechanical properties of a build, it is crucial that the fundamentals behind this technology is understood. Modelling of the AM process can focus on many different aspects such as the effect of process parameters on melt pool shape, solidification and cooling rate conditions and the solidification microstructure [18,84].

2.5.2 Point heat source vs. diffuse heat source

There are a large amount of studies to be found in literature that describe various ways of modelling different AM techniques. These include using relatively straightforward heat-flow models that can easily be coded into a programme such as MATLAB to finite element modelling [85–88].

In the case of Eagar & Tsai (1983) [88] and Pinkerton & Li (2004) [86] the starting point has been the work done by Rosenthal [89,90] to describe a moving heat source. This work is commonly referred to in any study looking at modelling laser-based processes. A common form of the Rosenthal equation is given below in equation 1. The equation describes the temperature field for a point heat source with power, q , that is travelling with a velocity, v .

$$T_m - T_0 = \frac{nq}{2\pi kR} e^{-\frac{v(x+R)}{2\alpha}} \quad (1)$$

The parameters along with a description and typical values for Ti-6246 are given in Table 2.4. The thermal diffusivity, α , can be calculated using equation 2 [91]. The parameter k is defined in Table 2.4, ρ is the density of Ti-6246 (4650 kgm^{-3}) and c_p is the specific heat capacity of Ti-6246 ($0.5 \text{ Jg}^{-1}\text{K}^{-1}$).

$$\alpha = \frac{k}{\rho c_p} \quad (2)$$

Table 2.4: Description of the parameters in the Rosenthal equation

Parameter	Description	Value
T_m	Melting temperature of the material [K]	1948[21,92]
T_0	Build temperature [K]	298
q	Beam power [W]	-
n	Absorptivity of workpiece	-
k	Thermal conductivity [$Wm^{-1}K^{-1}$]	7.7[21,92]
v	Beam velocity [ms^{-1}]	-
α	Thermal diffusivity [m^2s^{-1}]	3.31×10^{-6}
R	Distance between laser and point on workpiece in Cartesian co-ordinates (x, y, z)	$\sqrt{x^2 + y^2 + z^2}$

The assumptions made by Rosenthal when developing this heat source equation are that;

- The thermophysical properties of the material such as thermal conductivity and thermal diffusivity are fixed, i.e. they are not temperature dependent.
- The heat source speed and power remain constant
- There is no convective or radiative heat flow

Although in many cases this approach is shown to have good agreement with experimental work, the Rosenthal equation gives a very simplistic description of the laser beam as a point heat source. This equation is useful for determining the temperature of the workpiece away from the centre of the heat source [93], but becomes more and more inaccurate as $R \rightarrow 0$. At the centre of the heat source, the temperature field tends to infinity which is clearly not a realistic prediction. It is for this reason that many authors adapt the Rosenthal equation to make it more representative of a real-world laser.

Shercliff and Ashby (1984) [94] define a Gaussian line source equation which can be used to model the laser beam in the Gaussian mode. The equation is given below, where T_0 , n , q , k , v , x , y , z and α

have been previously defined in Table 2.4. The additional parameters are time (t), heat flow time constant (t_0) defined as $r_b^2/4\alpha$ where r_b is the beam radius and the characteristic length (z_0).

$$T - T_0 = \frac{nq}{2\pi kv\sqrt{t(t+t_0)}} e^{-\frac{1}{4\alpha}\left(\frac{(z+z_0)^2}{t} + \frac{y^2}{t+t_0}\right)} \quad (3)$$

This equation to describe a laser beam was used by the authors in their initial study looking at the laser hardening of steel surfaces.

Later work by Shercliff and Ashby (1991) [95] built upon this equation but instead used normalised process parameters. The definitions and equations for calculating these normalised parameters is discussed in detail in Chapter 6. They utilised a parameter defined as the characteristic length (z_0) which prevents the temperature field from reaching infinity as it does when using the Rosenthal equation. This is achieved by assuming that the heat source (laser beam for this study) is incident on an imaginary surface that is a distance (z_0) above the actual substrate surface [96]. The value of z_0 is dependent on the process parameters such as laser power and velocity and must be calculated each time one of these is changed. The method for determining the characteristic length is described in Chapter 6.

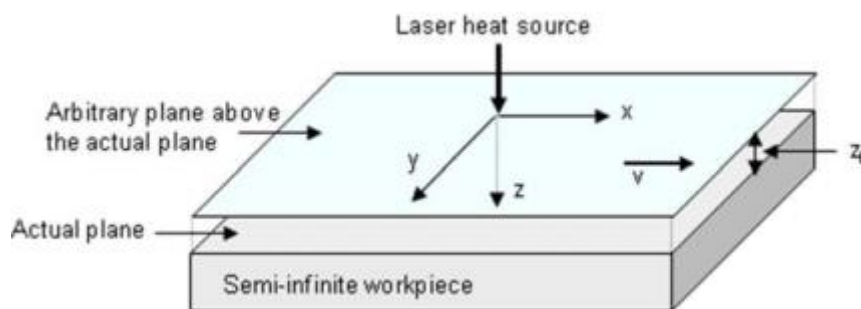


Figure 2.18: Schematic to show the position of the imaginary surface at a distance z_0 above the substrate surface [96]

Cline & Anthony (1977) [85] also use a Gaussian heat source in their study. In this case the model was found to have good agreement with experimental results. It was also noted by the authors that changing the laser profile from a point heat source did not overly complicate the model whilst still removing the tendency to infinite temperatures which is a major issue of the models based on the

Rosenthal equation. For this reason, and due to the rapid improvement in personal computers since the 1970's, much of the work now done on modelling laser-based processes is based upon a Gaussian or other non-point heat source laser profile. Gaumann et al. (2001) [54] used the Gaussian approach to help determine potential processing windows for single-crystal repair by linking processing parameters to solidification conditions. The ability to link experimental work to predictions made by robust models is a very powerful tool and highly significant to the work detailed in this report.

Other more complex models have been developed in recent years which involve more intensive mathematics [97] or use Finite Element Modelling [98–100]. For example, Baykasoglu et al. (2018) [98] created a complex model, that combined a finite element thermal model with a phase transformation kinetic model. This allowed the authors to model the thermal history of a multi-layer build as well as predict likely microstructures as a function of build height based upon the heating and cooling cycles. The model was validated against experimental results and was found to be effective in predicting Ti-6Al-4V deposited microstructure. However, as noted by the authors, the work did not include the effects of changing process parameters which as discussed previously is an important aspect of blown powder DLD.

Kelly and Kampe (2004) [101] used a finite difference technique to model the effect of laser velocity on the thermal history of a single-track build. The advantage of this model over a more simplistic thermal model, is that it can be used to predict possible microstructures as a function of build height. Although this model is far less complex than the one developed by Baykasoglu et al. Overall, the authors found that the model predicted the formation of a “characteristic layer” which was comprised of two layers of the previously deposited material due to the cyclical heating and cooling nature of the process. However, the position of this layer with respect to the top layer was not in agreement with experimental results. Additionally, the model incorrectly predicted a martensitic region in the bottom two layers of the deposit which was not observed in experimental builds. Although, the authors note that additional analysis should be performed on the experimental builds since this region might have been missed in optical or secondary electron microscopy.

2.5.3 Melt pool size and geometry

The geometry and size of the melt pool is an important part of understanding the final microstructure and hence is an important aspect of the modelling [41,102]. This approach to process modelling has been to use a thermal model to determine how processing parameters, such as beam velocity and power, affect melt pool geometry. This has been described in some detail by Shercliff and Ashby (1991)

[95] where an adapted form of a Gaussian line source was used to predict case depths for laser hardening.

This can be adapted to model melt pool depths as in the case of Ahmed, Voisey & McCartney (2010) [96]. The authors re-worked the model described by Shercliff and Ashby, to create a model that explored a variety of different laser beam profiles and the effect that this had on predicted maximum melt pool depths. These predicted depths were also compared to experimental results, and much like in previous work, were found to be in good agreement as shown in Figure 2.19.

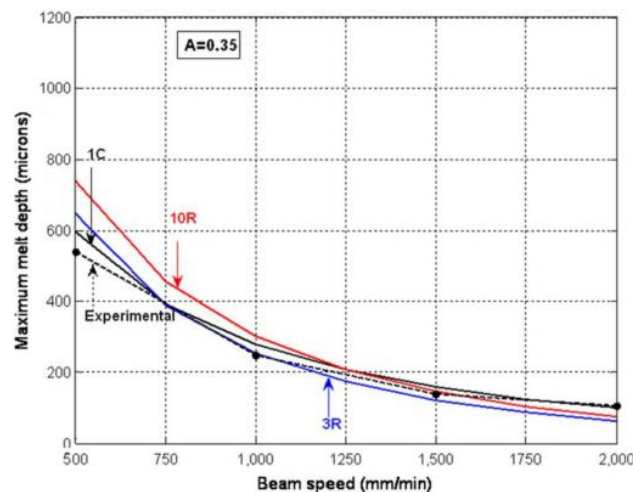


Figure 2.19: Comparison between experimental and predicted melt depths for different laser modes as a function of beam velocity [96]

Shah et al. (2011) [45] took a slightly different approach and used image analysis of experimental builds to correlate process parameters with melt pool geometry for DLD. They found that higher powder feed rates resulted in a larger (area) melt pool. They also looked at how melt pool characteristics affected the quality of the final build. An increased melt pool disturbance (a measure of how uniform the melt pool limits are) gave a better surface finish. Although the authors did not model this work and instead only plotted experimental results, a predictive model for surface roughness based on process parameters such as powder feed rate could be developed.

2.5.4 Blown powder

Most of the models discussed above have either been for laser-hardening, welding or for the powder bed process and so the blown powder aspect has not been included. However, in the case of DLD, the powder feed rate is an important parameter to include in the model. This has been explored by Picasso

et al. (1994) [87] for a laser cladding process. Here the focus is not just on the laser beam parameters such as power and speed, instead the effect of powder feed rate, size of powder particles and the speed of the powder jet is explored. This numerical model has attempted to consider the interactions of the powder jet stream with the laser beam and the melt pool which many models exclude for simplicity. Including these interactions is of benefit as the effects of these additional parameters on the workpiece absorption and the melt pool geometry are important aspects of the DLD process and have consequences on the microstructure of the build.

Powder feed rate (PFR) is often overlooked as many of the models focus on the laser beam mode and the resultant melt pool. This is useful for powder bed processes but not for DLD. The addition of powder to the path of the laser beam will affect the amount of power that reaches the substrate. As shown in Figure 2.20, as the powder feed rate increases the amount of power that is attenuated due to the shading effect of the particles increases. This means that less power is incident on the workpiece and so lowers the overall efficiency of the process.

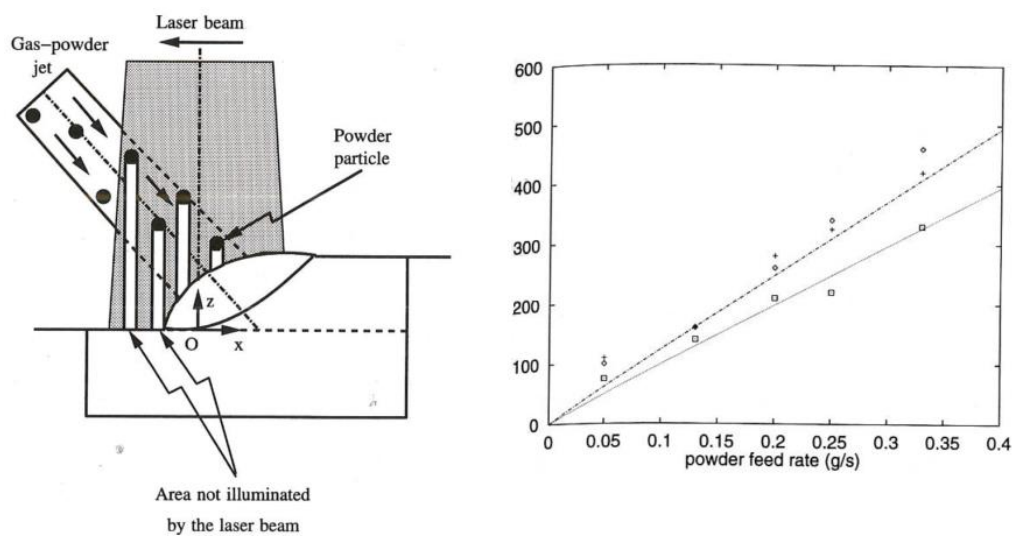


Figure 2.20: (a) Attenuation of the laser beam due to shading effect of powder particles (b) Graph showing amount of attenuated beam power as a function of powder feed rate [87]

Picasso et al. have only considered the effect of PFR on the amount of power incident on the workpiece. The focus of this study was not particularly on the effect the powder parameters would have on the shape of the melt pool and since this was for a laser cladding process the implications for microstructure have not been discussed.

2.5.5 Limitations

There are still many assumptions even in these more intensive models which are inherent in any of the models described regardless of the method used. In addition, the laser deposition process has a lot of different variables and as a result the solidification conditions and the final build can be highly variable. Trying to determine the effect of one process parameter in isolation is difficult and is ultimately not useful when trying to optimize the deposition process.

Although complex FEM models have been shown to provide reasonable predictive results when compared to experiment, the time taken to set-up the models and to compute the results can be long. The complexity of the models means that changing any one of the process variables may result in far less accurate results and will need to be validated against experiment again which is costly. Simpler thermal models allow for predictions of aspects such as cooling rates for a large range of process parameters very quickly. These results can then be used to help inform or predict experimental results.

2.6 Dimensionless process parameters

2.6.1 Background

Due to the large number of process parameters that can be varied in laser-based processes including additive manufacturing, it makes sense to combine certain parameters together. This resulted in normalising parameters such as beam power against material dependent properties to define the parameters in a dimensionless form. Overall, this simplifies analysis of parameter effects on microstructure and mechanical properties. Swift-Hook and Gick (1973) [103] performed this type of approach by normalising laser velocity and power for a laser welding process. A similar approach was performed by a number of authors in the 1980's for laser hardening in the case of Davis, Kapadia & Dowden (1986) [104] and Ion, Shercliff & Ashby (1992) [105] to develop processing diagrams for laser-based processes.

2.6.2 Definitions

Ion et al. [105] defined the following dimensionless groups of dimensionless beam power (q^*) and dimensionless beam velocity (v^*):

Dimensionless power:

$$q^* = \frac{nq}{r_b k (T_m - T_0)} \quad (4)$$

Dimensionless velocity:

$$v^* = \frac{vr_b}{\alpha} \quad (5)$$

Dimensionless temperature:

$$T^* = \frac{T - T_0}{T_m - T_0} \quad (6)$$

Dimensionless co-ordinates (relative to beam centre):

$$x^* = \frac{x}{r_b}; \quad y^* = \frac{y}{r_b}; \quad z^* = \frac{z}{r_b} \quad (7)$$

Dimensionless time:

$$t^* = \frac{t}{t_0} \quad (8)$$

In creating the dimensionless processing diagrams, the thermophysical properties such as k and α were taken by the authors at $0.6T_m$ rather than at room temperature. When using these equations in the work in the following sections, the values were taken at room temperature but using the same

assumption as Ion et al. that the values are independent of temperature. Additionally, the parameter n which is defined as the surface absorptivity is assumed to remain constant by Ion et al., although in reality this is likely to be dependent upon the temperature and will also depend upon the type of heat-source being used. For example, electron beam processes are generally more efficient than laser-based process with typical values of 0.6-0.55 [5] and 0.35 [39,46] respectively.

2.6.3 Normalised process maps

One of the main uses of the groups of normalised process parameters is that they can be used to create normalised process maps such as the one produced by Ion et al. (1992) [105] shown in Figure 2.21. Here contour lines for constant hardened depth have been plotted as a function of q^* and v^* . The map shows which combinations of parameters result in no hardening of the material and also when surface melting occurs. Hence, the map shows the limits of the process as defined by the melting temperature of the material. Since q and v have been normalised against material dependent properties, different materials such as cast iron and martensitic stainless steel can be plotted on the same graph.

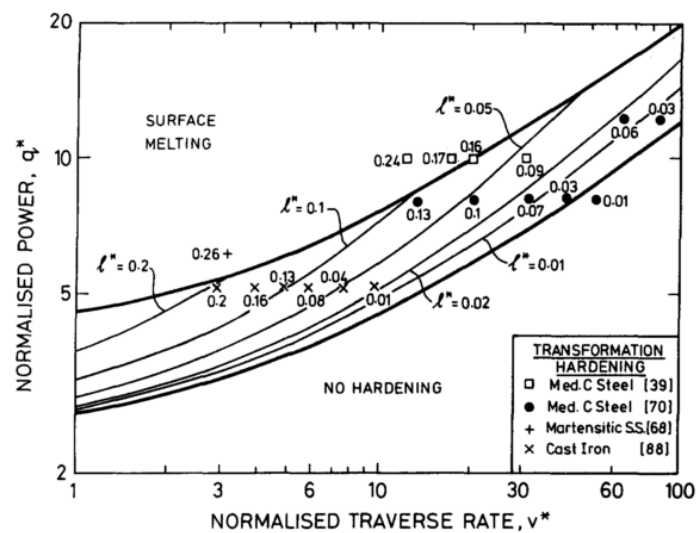


Figure 2.21: Normalised process map for transformation hardening. Contours show constant normalised hardened depth [105]

Shercliff and Ashby (1991) [95] used the normalised approach to produce “master” plots for both Gaussian and non-Gaussian heat sources for laser transformation hardening. In this case, the normalised map plotted a process output in the form of normalised case depth (z_c^*) against a process input, normalised beam velocity. An example of this master plot is shown in Figure 2.22 where contour

lines of constant laser power (q^*) are also plotted. The lines are stopped at the dashed line since this represents surface melting of the material. This type of process map using the empirical data from the dimensionless groups allows for the easy selection of process parameters for a required case depth (z_c^*). Alternatively, the maps provide a predicted case depth for a given combination of process inputs.

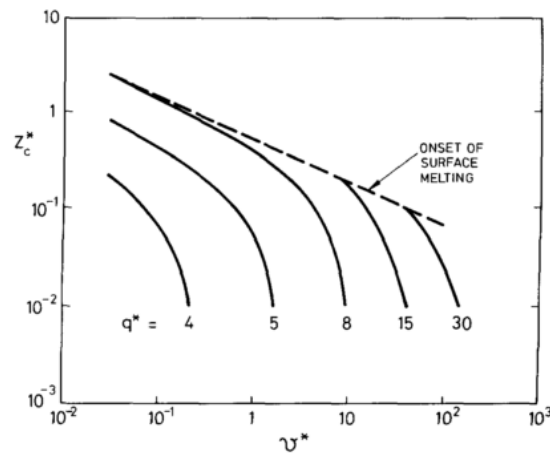


Figure 2.22: Example of a master plot for case depth in transformation hardening. Contours show constant dimensionless beam power (q^*) [95]

The above examples have been for laser-based processes such as laser welding and laser transformation hardening, but the same approach can be applied to additive manufacturing. Vasinonta, Beuth & Griffith (2001) [106] applied the dimensionless variable approach to a Laser Engineered Net Shaping (LENS) process which is analogous to DLD. The authors took a slightly different approach to those discussed previously and modelled the laser beam as a point heat source (using the Rosenthal equation) rather than as a Gaussian source. The authors used the dimensionless groups to create a generalised process map relating the effect of changing power, speed, wall height and amount of preheating on the melt pool length. Although the authors used the Rosenthal equation as the basis for their work, the predicted results for the melt pool length were found to be in good agreement with experimental measurements. However, the effect of powder addition on the size and morphology of the melt pool was not considered in this case.

Thomas, Baxter & Todd (2016) [107] built on the method of Ion et al. by defining additional process parameters to put into dimensionless form. Much like Vasinonta et al. who introduced a dimensionless wall height, Thomas et al. defined dimensionless layer height (l^*) and hatch spacing (h^*) to tailor the Ion et al. approach to AM. The normalised map created by the authors then plotted $1/h^*$ against q^*/v^*l^* as shown in Figure 2.23. Here the x-axis characterises the total amount of energy needed to melt the material within a single laser scan, this can be denoted by E^* . The dashed lines on the plot in

Figure 2.23, correspond to lines of constant normalised energy density (E_0^*) which can be defined as $q^*/(v^*l^*h^*)$. The higher the E_0^* value (moving to the right on the process map), the more energy is put into the material per unit volume. As noted by the authors, deposits of the same material with the same E_0^* values will not necessarily have the same microstructural features. This is because changes to power and/or velocity, for example, will result in different melt pool morphologies even if the overall E_0^* is identical. The changes in melt pool geometry will affect the solidification conditions and hence the microstructure of the material.

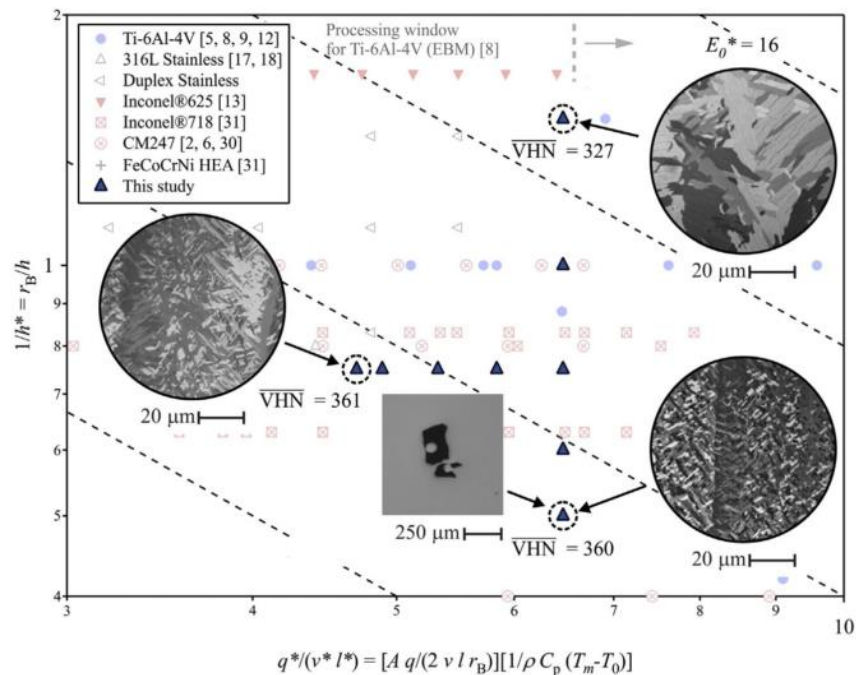


Figure 2.23: Normalised process map with lines of constant energy density showing effects of changing parameters on microstructure of EBM Ti-6Al-4V [107]

Wang et al. (2018) [108] made use of the normalised energy density approach in order to compare microstructural response of 316L SS with respect to processing parameters. As noted previously, identical values of normalized energy density does not result in the same microstructural or mechanical response. In the case of this study, the thermophysical properties of the material, namely thermal conductivity and diffusivity, were treated as temperature dependent. This removes the assumption made by both Ion et al. and Thomas et al. in the formation of their process maps that the thermophysical properties are constant. This improves the accuracy of the normalized parameters, but the surface absorptivity was still assumed to be constant at 0.35 when in reality this will also be dependent on temperature.

2.6.4 Advantages

The advantages of creating normalised process maps and diagrams such as the ones presented here is that it is possible to plot data for a wide array of different processes and materials on the same map. They have proved useful in determining and optimizing process windows for specific materials such as steel, nickel, titanium or techniques such as laser hardening, laser AM and EBM. These process windows are formed of optimized parameters and include the effect of parameters in combination with one another rather than in isolation. As noted by Thomas et al. (2016) this avoids the necessity of complex computational models which can reduce time and the costs associated with developing and validating the models. This approach has been used in this work to help define and narrow down a possible process window for Blisk repair using DLD of Ti-6264.

3 Experimental techniques

This chapter summarises the experimental and characterisation techniques used for this project. The set-up of the Ti-6246 direct laser deposition (DLD) builds deposits is described, including the different process parameters. The main characterisation techniques used to analyse the deposits, and the mechanical test parameters are also outlined.

3.1 Direct Laser Deposition & process parameters

For this study, the builds were deposited on a RPM 557 at Rolls-Royce Corp., USA. The key process parameters used during blown powder (DLD) terms used are the same and are defined below in Table 3.1.

Table 3.1: Definition of main process parameters used during DLD

Parameter	Typical Units	Description
Power	W	The power of the laser beam during the deposition process.
Beam velocity	m/s or mm/s	This is the speed at which the laser beam traverses the workpiece.
Powder feed rate	g/min	This is the total mass of metal powder being delivered by the nozzles per unit time. This parameter is often altered simply as a means to keep the layer height constant.
Hatch width	m or mm	This is width of each individual melt track (or the distance between the centre of two neighbouring tracks)
Beam radius	m or mm	The distance between the centre of the focussed laser beam and the point at which the laser power has decreased to $1/e^2$

3.2 Mini tensile builds

The mini tensile builds were deposited using a custom-built RPM 557 laser metal deposition machine manufactured by RPM Innovations Inc. (Figure 3.1). The system operates using a “blown powder” approach whereby powder is delivered coaxially into the path of a 3kW fibre laser.

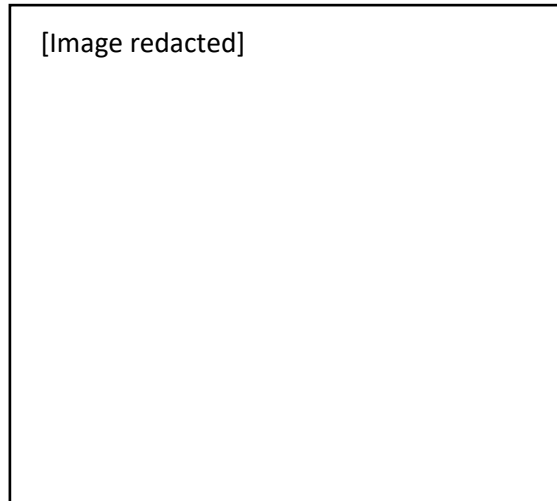


Figure 3.1: RPM 557 [109]

The builds were deposited using an Argon atmosphere to reduce the likelihood of oxidation of the material. Argon gas was also used within the powder nozzles to deliver the metal powder into the path of the laser beam at a gas flow rate of 4 L/min. A layer thickness of 0.254mm and laser spot size of 0.1mm was used to deposit builds of approximately 30 mm x 56 mm x 2.5 mm using a contour and hatch scan strategy as shown in Figure 3.3.

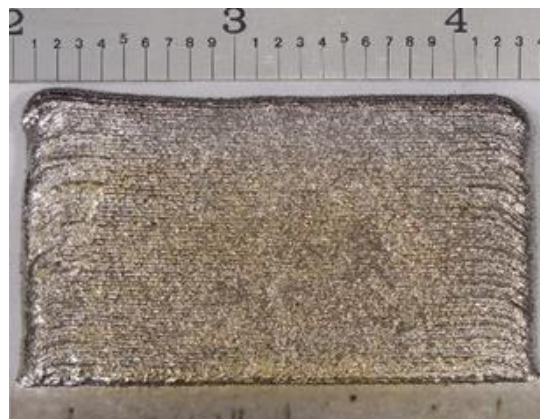


Figure 3.2: Image of as-deposited mini tensile builds. Note scale is in inches

Experimental techniques

In this type of strategy, a single contour pass (blue) is used to deposit material around the parameter of the shape. The central region of the shape is then filled by using a hatch scan strategy (red), which is comprised of a series of melt tracks placed adjacent to one another.

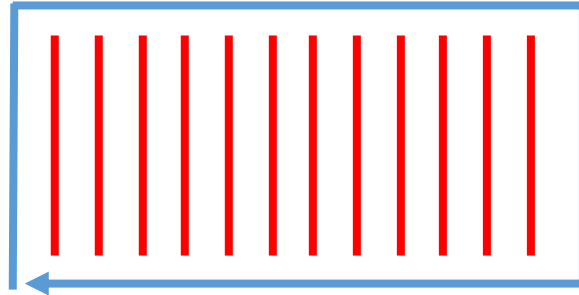


Figure 3.3: Contour and hatch scan strategy

In order to investigate a possible process window that would be suitable for Blisk repair, five different parameter sets were used, with the beam velocity and hatch spacing being the two main variables. The laser power remained constant throughout the builds.

For the purposes of commercial sensitivity, the process parameters have been converted into dimensionless forms according to the definitions set out by Ion et al [105] and in section 2.6. For ease, the main definitions are also given below.

3.2.1 Normalised Process Parameters

The dimensionless process parameters are defined as follows:

Dimensionless power

$$q^* = \frac{Aq}{r_b k (T_m - T_0)} \quad (9)$$

Dimensionless velocity

$$v^* = \frac{vr_b}{\alpha} \quad (10)$$

Dimensionless hatch spacing

$$h^* = \frac{h}{r_b} \quad (11)$$

Similarly, dimensionless layer height (l^*) can be calculated by substituting “h” in Eq. 11 with “l” and multiplying by 2. The five parameter sets form the process window shown on the dimensionless process map in Figure 3.4. The dashed lines are isopleths of constant energy density (E^*) which is defined as q^*/v^*l^* . In this investigation there are three different energy densities. Builds 2-4 have equivalent energy densities, though they have been deposited using different hatch spacings and beam velocities. The parameters were determined using a Design of Experiments (DoE) which is discussed in the following section.

3.2.2 Design of Experiments

The main objective of an experiment is to determine the response of a system (which could be e.g. a biological system, a material or a chemical solution) when it is subjected to changes in variables such as temperature, pressure or chemical concentrations. Experimental results can quite easily be subjected to human bias or error and systematic errors. A DoE is a way to limit the effect of these sources of error, for example by introducing an element of randomisation [110].

In addition to the sources of error in any experiment, it is often of interest to study the effect of multiple different variables both independently and in conjunction with one another. These different variables can be labelled as factors and used to create a factorial DoE. Each of these factors will have a number of different values or levels and a comprehensive factorial DoE can be used to investigate the effects of combinations of factors and levels.

Design of Experiments is used by industry to identify critical process parameters that have the most effect on the quality of products. The results can then be used to optimise the parameters in order to improve the efficiency, robustness and quality of the process. Within an industrial process (such as Additive Manufacturing) there are a lot of variables that can be investigated. Ordinarily, these variables may be varied one at a time and the results of each change recorded. However this type of approach is inefficient in terms of time and resources [111] which is not beneficial to the business. The advantage of the factorial DoE approach is that it reduces the number of experiments that need to be performed by varying the different factors and levels simultaneously.

Experimental techniques

The DoE process window being explored in this work is shown below in Figure 3.4. The diagonal on which parameter sets 2, 3 and 4 sit defines a specific value of $q^*/v^*l^*h^*$ or energy density (E^*).

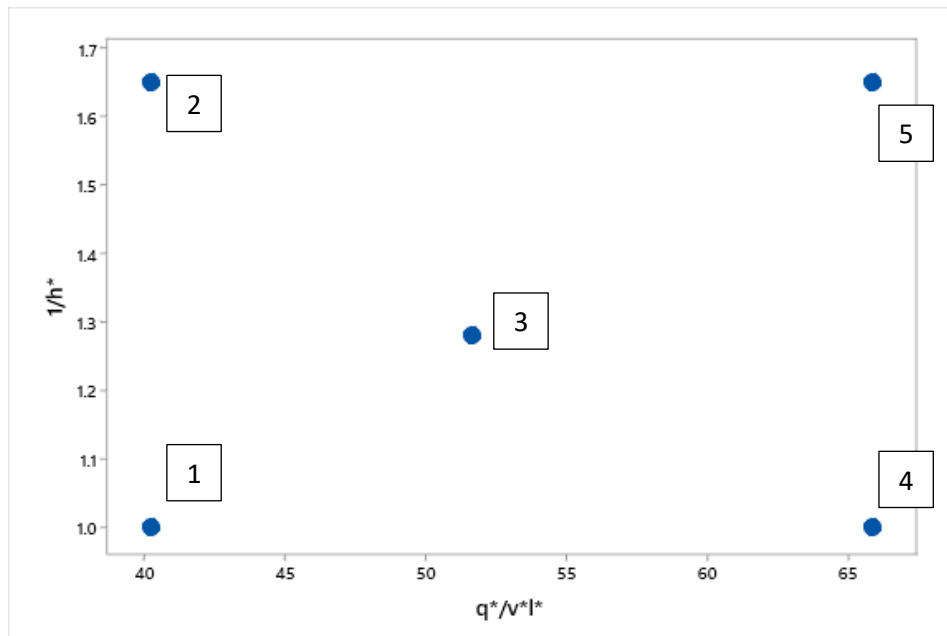


Figure 3.4: Dimensionless process map showing the process window investigated by the mini tensile deposits

3.3 Calibration build

A thin-walled aero-foil type build was deposited using the same system described above. This was fabricated using a series of different build parameters (see Chapter 6.2) and was then used to help calibrate a thermal model.

Due to the size of geometry the scan strategy used was contour-only (i.e. no hatch), as this was sufficient to build up the specimen. The spot size, layer thickness and gas flow was the same as for the mini tensile deposits. The calibration build is discussed in further detail in section 6.2.

3.4 Mechanical testing

3.4.1 Uniaxial tensile testing

In its simplest form, a tensile test is performed by gripping both ends of the test piece and then applying a tensile force parallel to the specimen gauge. This results in the elongation of the specimen, followed by it fracturing into two. During this process, a number of different mechanical properties can be determined such as the Young's modulus, a measure of the elasticity of the material, the ductility and the yield stress and ultimate tensile strength.

The yield stress can be defined as the maximum amount of stress that can be applied to the material before plastic deformation can occur. The ultimate tensile strength is the maximum stress that can be applied before the material fractures.

3.4.2 Ti-6264 DLD tensile test pieces

The five parameter sets laid out in Figure 3.4 each had a repeat build, resulting in ten builds in total. From these builds, two dog-bone type tensile test pieces, perpendicular to build direction, were machined from the DLD material using Electro Discharge Machining (EDM). Additionally, a non-DLD test piece was machined from the baseplate, one for each of the five parameter sets. The non-DLD test pieces were to use as a comparison of mechanical properties achieved by DLD.

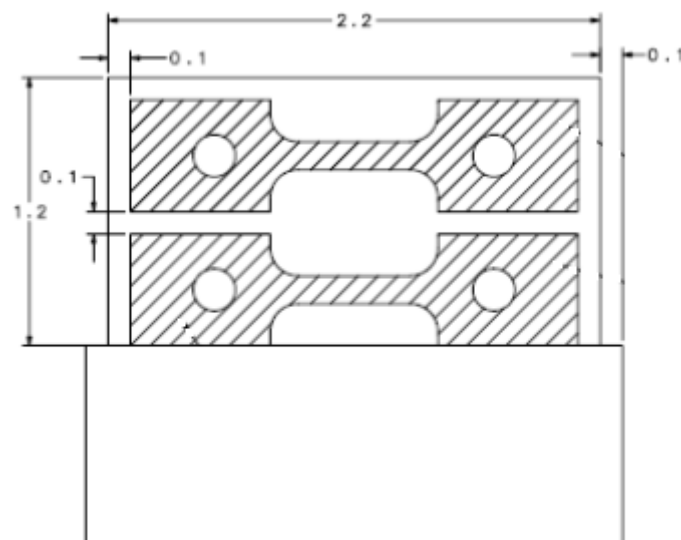


Figure 3.5: Schematic of tensile test specimens machined from DLD material. Note scale is in inches

Experimental techniques

The 20 DLD and 5 non-DLD test pieces underwent uniaxial tensile testing according to ASTM E-8(11) [112] with an initial strain of 0.13mm/min and then a second strain of 0.69mm/min to failure. The testing was performed by Exova plc. The Young's Modulus, elongation to failure, 0.2% yield stress and the ultimate tensile strength were all recorded.

Sections of the build were also retained for microstructural analysis. These were removed from the top, middle and bottom sections of the deposit so that any build height effects could also be investigated.

3.5 Characterisation of microstructure and build quality

The DLD sections retained from the tensile builds were prepared for scanning electron microscopy (SEM) using a Struers Tegramin preparation system. The first step was to grind down the as-deposited surface using resin bonded diamond discs for 2-3 mins with water coolant. The initial grinding stage used a disc equivalent to 500 grit paper followed by 1200 grit, at 200 and 150 rpm respectively. This was then followed by polishing using a 9µm diamond solution for 10 mins, and then polishing with OP-S for 6 mins. Finally the samples were flushed with water and polished for a further 4-5 mins to remove any excess OP-S. The samples were then washed using isopropanol and dried using hot air. This method produced a consistent mirror finish that was suitable for microscopic analysis using the SEM.

3.5.1 Scanning electron microscopy

A scanning electron microscope (SEM) allows for the imaging of features on the microscopic scale. It works by generating and then focusing a beam of electrons onto a sample as shown in Figure 3.6. This is achieved by accelerating the electrons through a series of apertures and magnetic or electrostatic lenses before it reaches the sample [113].

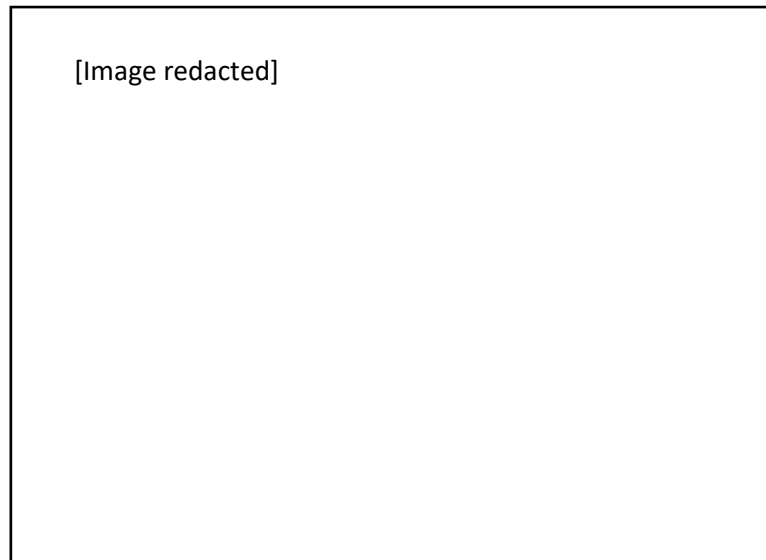


Figure 3.6: Schematic diagram of a SEM showing how the electron beam is focused by a series of apertures and lenses [114]

The sample itself is placed inside a chamber which is then put under vacuum. As the electron beam passes over the sample, the electrons interact with it and produce a series of different responses. The response primarily used for this work concerns the backscattered electrons. In this case, the backscattered electrons are produced by interactions with the nucleus of the atoms in the sample. Heavier elements or atoms cause the electrons to scatter more than lighter ones which produces a contrast which can then be used to create an image of the sample. In the case of Ti-6246 the contrast between the α -phase and the β -phase is used to produce a BSE of the microstructure.

Scanning electron microscopy was performed using a FEI Sirion FEG microscope primarily in the BSE mode in order to reveal the lamellar $\alpha+\beta$ lath structure. An accelerating voltage of 20kV, a working distance of approximately 10 mm and a magnification of between 10,000x and 20,000x was found to be suitable.

3.5.2 CLEMEX automated measurement

Once BSE micrographs of the Ti-6246 DLD samples were obtained, it was necessary to quantify the size of the α -laths. Initially, the micrographs are fed into the image analysis package, ImageJ. The software is used to apply a threshold to the image, to increase the contrast between the α and β -phases.

Experimental techniques

These images can then be loaded into another image analysis package, CLEMEX. This package allows the user to apply a wide range of different techniques and adjustments to the images it is given such as thresholding, volume measurements, object tracking and object characterisation such as length, area and aspect ratio. For the purposes of this study, the software was used to first create a routine that was then applied to the micrographs for all the samples. The tasks in the routine are detailed below. At each stage, a *pause* can be added so the user can check that the operations are being applied appropriately. The routine as it is set out in the CLEMEX software is written out in Appendix A: CLEMEX routine.

1. Load image

Here a specific folder can be identified for processing using the following routine so that individual images do not have to be loaded manually one at a time. Figure 3.7 shows a typical SEM image that can be loaded into the CLEMEX software.

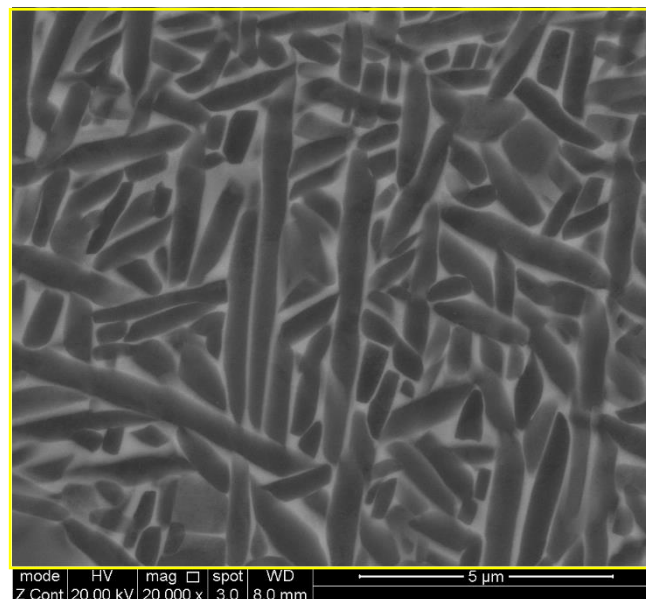


Figure 3.7: Example SEM image to be put through CLEMEX routine

2. Set process frame

The dimensions of the micrograph are set. Anything outside this defined area will not be affected by the following routine. The process frame used in this routine is depicted by the yellow box in Figure 3.7.

3. Grey threshold

A thresholding technique on the grey-scale image in order to fully separate the α -laths from the background. This is shown in Figure 3.8, where the software has separated the lath features from the background and shaded them in blue. Any feature which is highlighted in blue is now added to “bitplane 1”. The blue highlighting has not been applied to the image information bar at the bottom of the image due to the application of the process frame in a previous step.

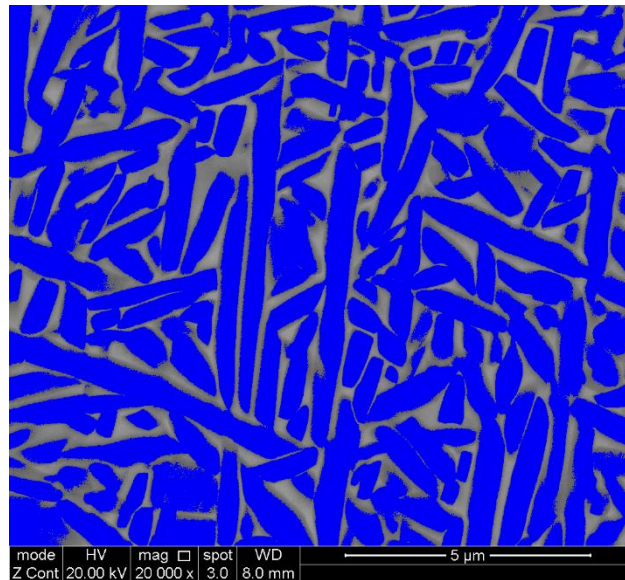


Figure 3.8: Example of grey thresholding being applied to SEM image in CLEMEX

4. Closing CIRC

This fills any small holes that are present in larger features that had therefore been previously counted as part of the background (in this case the β -phase). An example of this is shown below in Figure 3.9. In this an exaggerated grey threshold has been applied to more fully show the effects of “Closing CIRC” process. Some of the more speckled features have been filled to produce more complete laths within the bitplane. The process can be repeated multiple times in order to fill in any holes or voids still remaining in the bitplane.

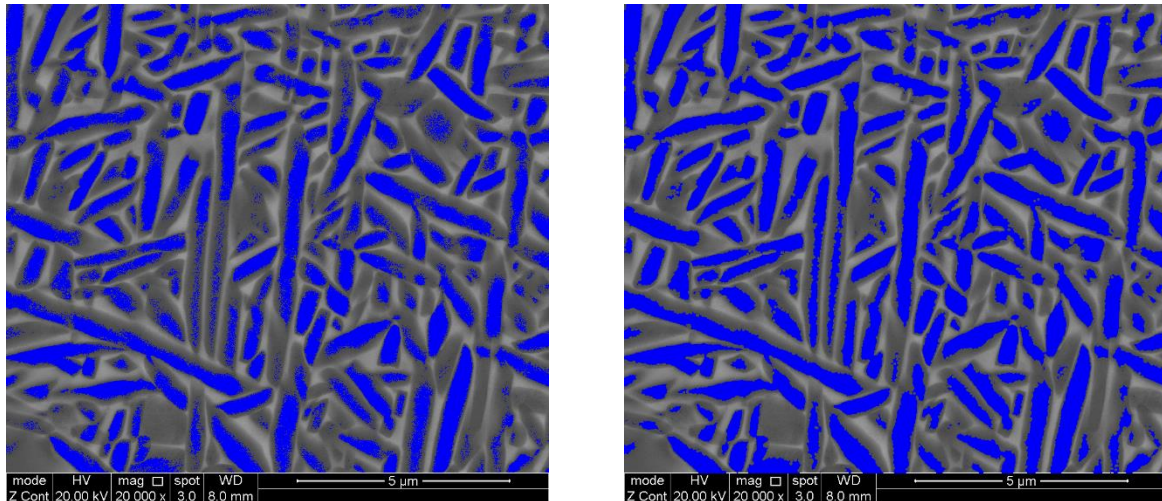


Figure 3.9: SEM image after an exaggerated grey threshold (left) followed by applying Closing CIRC process (right)

5. Trap

This identifies or “traps” any objects within the defined bitplane (i.e. anything highlighted in blue) and then performs a selected operation. In this case any feature less than 10x10 pixels was “trapped” and then removed from the bitplane. See Appendix A: CLEMEX routine. This helps to reduce any noise within the image that would skew the results, and is especially beneficial when the laths are not so easily distinguishable from the background.

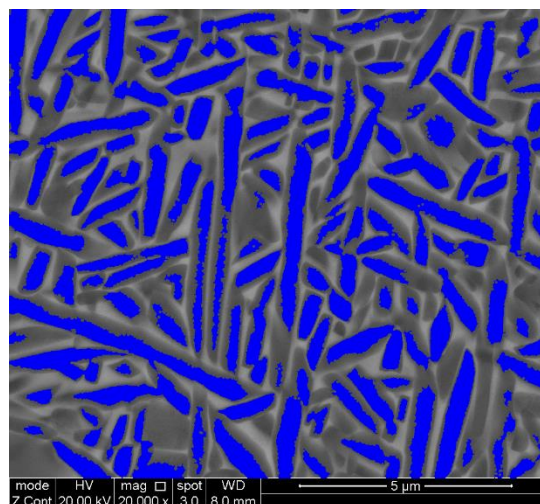


Figure 3.10: Image after an exaggerated "Trap" has been applied to image in above figure

Figure 3.10 shows this process applied after the image shown in Figure 3.9. Some of the smaller features included in the blue bitplane have now been removed and so won't be included in the

Experimental techniques

measurements at the end of the routine. This step can be easily adjusted to trap different sized objects depending on the image and the results from the previous steps in the routine.

6. *Separate SQR => BPL1*

The separate function can be used to separate overlapping features or to break up longer features. Again, a slightly exaggerated version of this has been applied to Figure 3.10 to show the results of applying this process to the image (see Figure 3.11). Due to the exaggerated threshold applied there are few overlapping features and so this function has split up the longer laths into smaller features. A similar function *split long objects* can be used instead which produces a similar result.

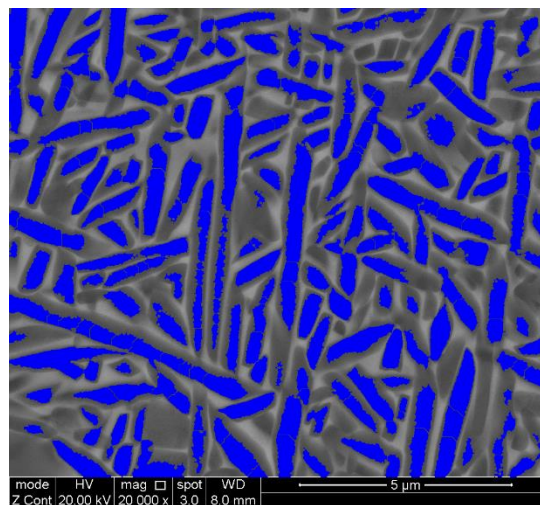


Figure 3.11: Image after an exaggerated separate function has been applied

7. *Object measure – width*

This is performed on any features within the process frame that is not part of the background (β -phase). Once this function has been performed, any feature highlighted in blue may be selected (see central feature in Figure 3.12) and the resulting measurement will be shown in the spreadsheet produced by CLEMEX software.

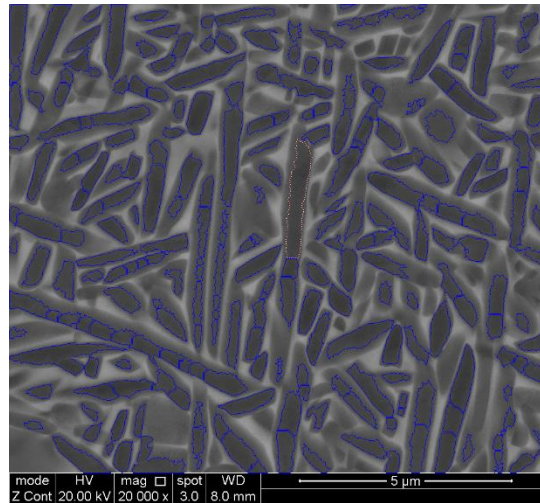


Figure 3.12: Image after object measure has been performed. Features can be selected (see centre of image) in order to show their associated measurements (i.e. width etc.)

3.5.3 ICP analysis

Inductively coupled plasma optical emission spectroscopy (ICP-OES) is an analytical technique to quantitatively determine the amount of either alloying or trace elements within a material. Other techniques such as atomic absorption spectroscopy (AAS) can also be used but the advantage of ICP-OES is that it is capable of detecting a wide range of elements instead of being restricted to just one. The technique is also flexible and can be used to accurately determine elemental composition for both high and low (trace) concentrations up to parts per billion [115]. To perform this type of analysis, a small sample of the material is dissolved in an acid and then nebulized to turn the solution into an aerosol.



Figure 3.13: ICP-OES methodology [116]

Experimental techniques

The resulting solution is introduced to and heated in an argon plasma which causes the molecules in the solution to separate into individual atoms. Due to the high temperatures (~10,000K) from the plasma, the electrons associated with these atoms are excited from their ground state into higher energy states. When the electrons return to the ground state they emit photons (see Figure 3.14).

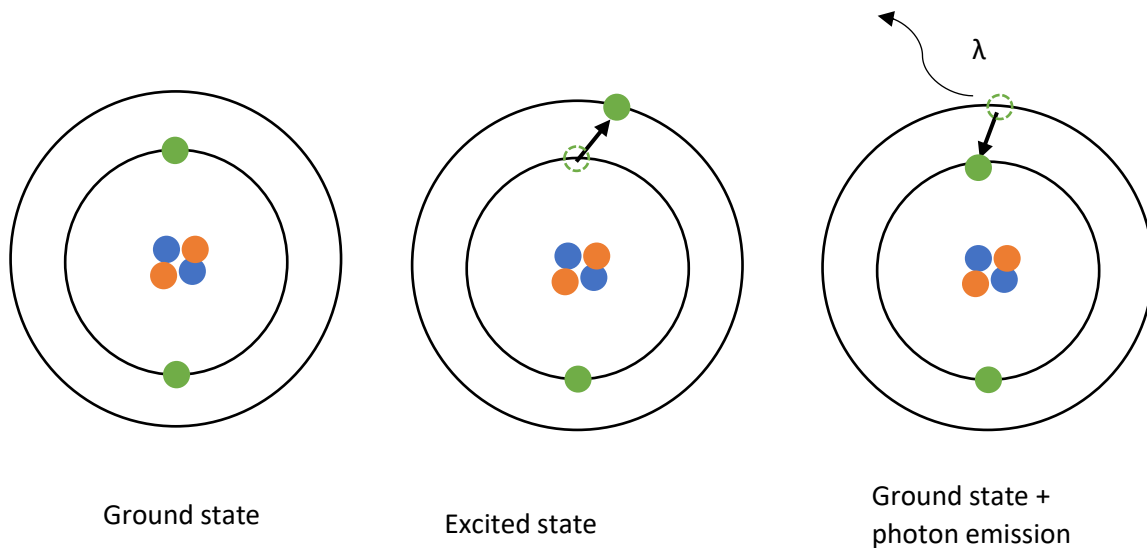


Figure 3.14: Excitation from ground state to excited and back to ground state with photon emission

The photons have wavelengths that are unique to each element, and so the different elements making up the material can be determined qualitatively. An optical emission spectrometer can then be used to measure the intensity of the photon emissions to determine the concentration of each element [115].

ICP-OES is used by many different industries and applications. These can range from simple analysis of iron content in metal samples [117] to environmental applications for the analysis of soil [118]. This later study highlights the wide range of elements that can be detected using the ICP-OES technique (e.g. Zn, Cd, Sb and Pb).

The ICP-OES approach was used by AMG Analytical in Rotherham to analyse the concentration of aluminium within Ti-6246 DLD specimens. This was done to compare to the baseline value of 6wt%. The results are given and discussed in Chapter 4.

3.5.4 XCT

X-ray computed tomography (XCT) is a non-destructive method that can be used to create a 3-D image of a sample in order to characterise any internal features. The 3-D image is built up by taking a number of 2-D images of the sample as it is rotated about its axis. These 2-D images are generated by directing a X-ray beam from a source to the sample which is fixed on a rotating stage as shown in Figure 3.15. As the X-rays pass through the sample, some of the photons are absorbed decreasing the intensity of the beam which hits the detector on the other side of the sample. The rotation step size between each 2-D projection can be chosen by the user. These individual 2-D images are combined to reconstruct a 3-D representation of the sample.

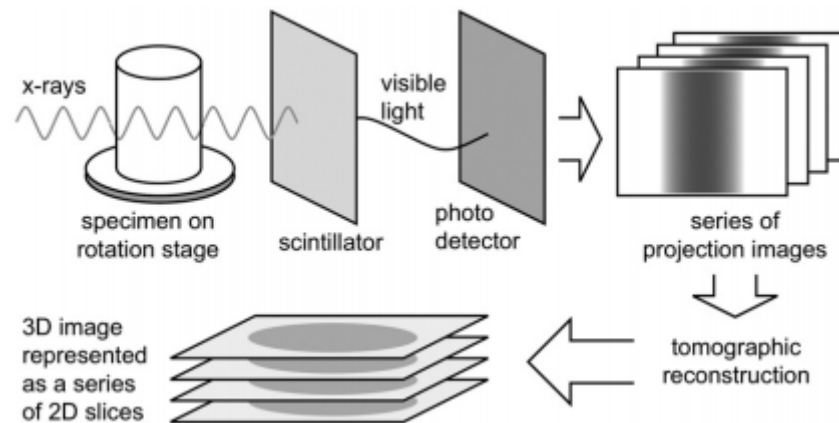


Figure 3.15: Schematic showing how a 3-D image is created using XCT [119]

3.5.5 Mini Tensile samples

XCT was used to investigate the presence of any defects within the mini tensile build that may have influenced the mechanical properties of the tensile specimens.

The first set of scans was performed on the grip sections of the 20 DLD tensile specimens. The Nikon Custom 320kV Bay machine at The University of Manchester was used for these scans. Due to the low resolution nature of the scans, multiple grip sections could be scanned at the same time. Four grip sections were stuck together using double-sided tape per scan, the sample numbers had been pre-machined onto the surface of the grips, which would be visible for identification in the 3-D

reconstruction for identification. The main settings used for these low resolution scans is given in Table 3.2.

Table 3.2: Settings for the Nikon Custom 320kV Bay

Setting	Value
Voltage (kV)	140
Exposure time (s)	3
Power (W)	10
Optical magnification	4x
Binning	2

A higher resolution scan was performed on the gauge section of one of the tensile specimens using the Xradia Versa XCT also at The University of Manchester. This was to investigate the presence of smaller defects (around 10-20 μ m) that may be within the build due to gas porosity. Unlike the low resolution scans where the field of view was allowed for multiple samples to be scanned at once, the Versa has a much smaller field of view. For this reason, the gauge had to be sectioned so that only a small portion from the fracture surface down was put into the machine. The main settings used for the high resolution Versa scan is given in Table 3.3.

Table 3.3: Settings for the Xradia Versa XCT

Setting	Value
Voltage (kV)	140
Exposure time (s)	4
Power (W)	10
Optical magnification	4x
Binning	2

3.5.6 Reconstruction

The software CT Pro 3D was used to reconstruct the 2-D slices into a 3-D image of the scanned samples. The first step was to find the centre of rotation which can be done automatically by the software. The next step was to correct for beam hardening and noise reduction. Beam hardening is an effect where the lower energy photons are more readily absorbed by the sample resulting in only the higher energy photons passing through and being picked up by the detector. This results in the beam energy being increased or “hardened”, this often shows up in the images as the central regions of the sample appearing darker than the outside. To account for this, it is common for a thin plate of either copper or aluminium to be placed between the X-rays and the sample to reduce the number of lower energy photons reaching the sample [120]. As in the case of CT Pro 3D, the software used for reconstruction often contains an option for correcting for beam hardening. To do this, a value between 1 and 6 was chosen manually, where 1 had the lowest correction effect and 6 the highest. The value chosen was the one which resulted in the highest quality image. A value of 2 was chosen for both the beam hardening and the noise reduction.

3.5.7 Image Analysis

The software package Avizo was used to analyse the reconstructed 3-D images of the samples. A threshold was applied to the 2-D slices that made up the 3-D image in order to segment the solid material and the surrounding air. In the case of the grip scans, each grip was segmented and labelled as a separate material so that they could be treated individually.

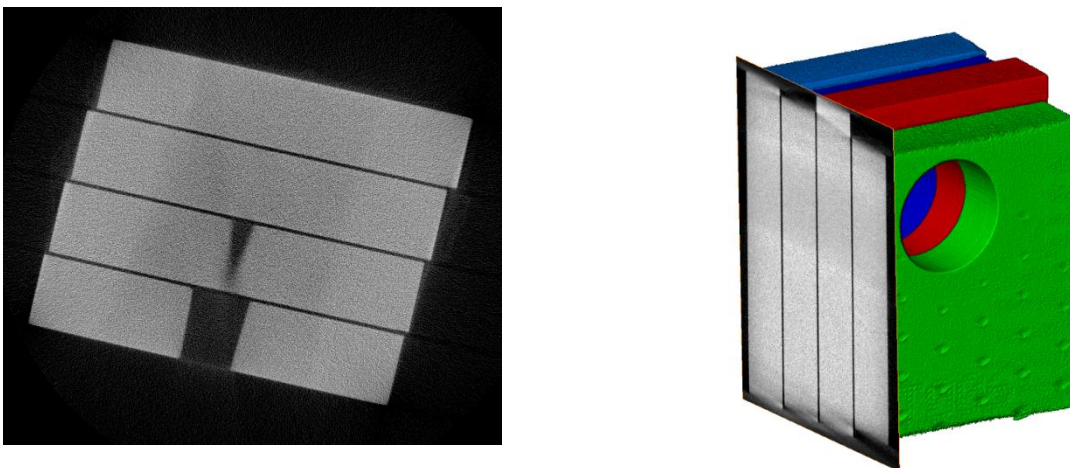


Figure 3.16: 2-D slice before separation of the grip sections (left) and after identifying as separate materials (right)

4 Microstructural analysis and build quality

4.1 Introduction

The literature on titanium microstructure is often dominated by Ti-6Al-4V since this is the most commonly used alloy especially within the aerospace industry. This is also true for literature regarding titanium that has been processed using additive manufacturing (AM). Research on the $\alpha+\beta$ alloy Ti-6246 is limited in general and has not been quantified as a function of direct laser deposition (DLD) process parameters. Due to the high cooling rates present during DLD, the microstructure of material that has been manufactured using this process may not resemble nor be easily categorised or compared to microstructure of a material that has been conventionally produced.

The mechanical properties of a DLD component are largely determined by the microstructure so it is important to be able to characterise it. In the case of Ti-6246, the microstructure takes the form of $\alpha+\beta$ lamellae. An overview of the typical Ti-6246 solidification microstructure is presented in this chapter. Additionally, the size of the α -laths are influenced by the process parameters such as velocity and hatch spacing and this will be explored in this section by providing quantification not just qualification as it relates to the process parameters. By understanding a quantifying the link between these it can be possible to control the final properties of a build by selecting appropriate combinations of process parameters.

In addition, it is important that the process window explored in this work allows for a stable DLD process that is capable of consistently producing fully-dense and defect-free builds. This is assessed by performing X-ray computed tomography (XCT) on the manufactured DLD builds.

4.2 Typical solidification microstructure

There is a lot of information in literature about the general appearance and formation of titanium microstructure depending upon whether it is classed as an α , $\alpha+\beta$ or β alloy [8,34]. Recently there has also been an interest in the specifics of titanium AM microstructure [48,121–123] which has its own characteristics features due to the extremely high cooling rates. Much of this literature focuses on Ti-6Al-4V and Ti-6246 is less well documented or quantified.

The final solidification microstructure for DLD Ti-6246 most typically consists of α -laths separated by fine β -phase as shown in Figure 4.1. However, the very top of the deposits showed evidence of

martensitic transformation, resulting in a microstructure too fine to be detected by the secondary electron microscope.

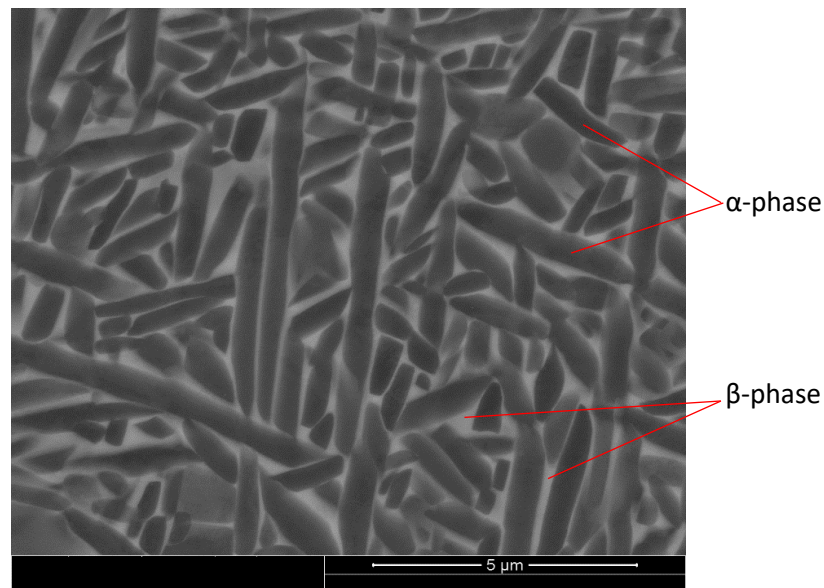


Figure 4.1: SEM BSE micrograph showing typical DLD Ti-6246 microstructure

Additionally, in some regions of the deposits, the amount of the β -phase separating the α -laths was quite large up to 47% compared to an average of around 27%. In some cases this β -phase contained secondary α (Figure 4.2), which is much like an aged β -phase [124]. This was often not observed in the main bulk of the deposit but in a transition region between the microstructure shown in Figure 4.1 and the extra-fine microstructure regions (martensitic) at the very top of the build. This microstructure can be described as bi-lamellar [19] and it would be expected to improve the strength of the material due to the reduction in slip length. However, this type of microstructure was not observed near where the tensile specimens were taken in the deposit and so it is unlikely that the formation of this bi-lamellar microstructure had an effect on the results presented in this chapter. Additionally, in the case of DLD Blisk repair, the final part will undergo machining and there will be a degree of “over build” which would be removed. Therefore, this bi-lamellar and the very fine martensitic microstructure would not be present in the final repaired component.

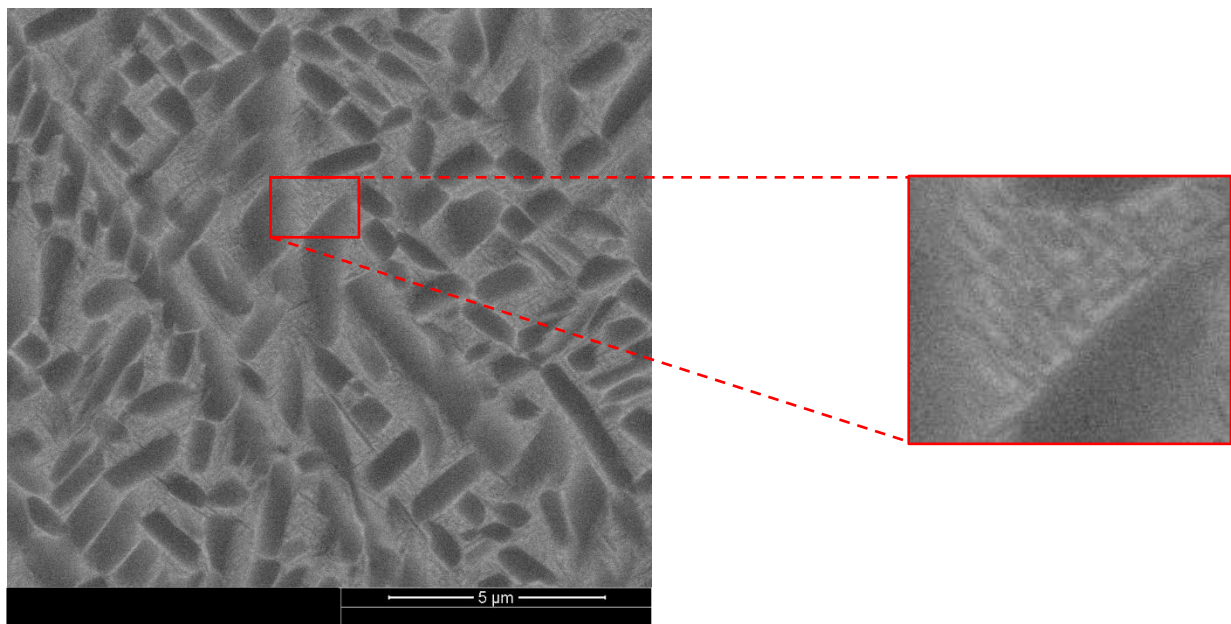


Figure 4.2: Micrograph showing the presence of secondary alpha within the beta phase

Common microstructural features that were present in the bulk of DLD Ti-6246 microstructure were (continuous) grain boundary α and “side plates” which are discussed as common to $\alpha+\beta$ by Lutjering. Example micrographs of these features as seen in the DLD Ti-6246 builds are shown below in Figure 4.3. [19]. Interestingly the presence of grain boundary α is in contrast with findings by Neikter et al. (2017) [121], though the authors used Ti-6Al-4V instead and likely used different process parameters which would have affected the cooling rate. Higher cooling rates reduce the extent of the grain boundary α [34]. The α side-plates are more commonly found in β alloys, though since Ti-6246 can be classed as near- β due to its high content of β -stabilisers (6% Mo) it is possible for this to form.

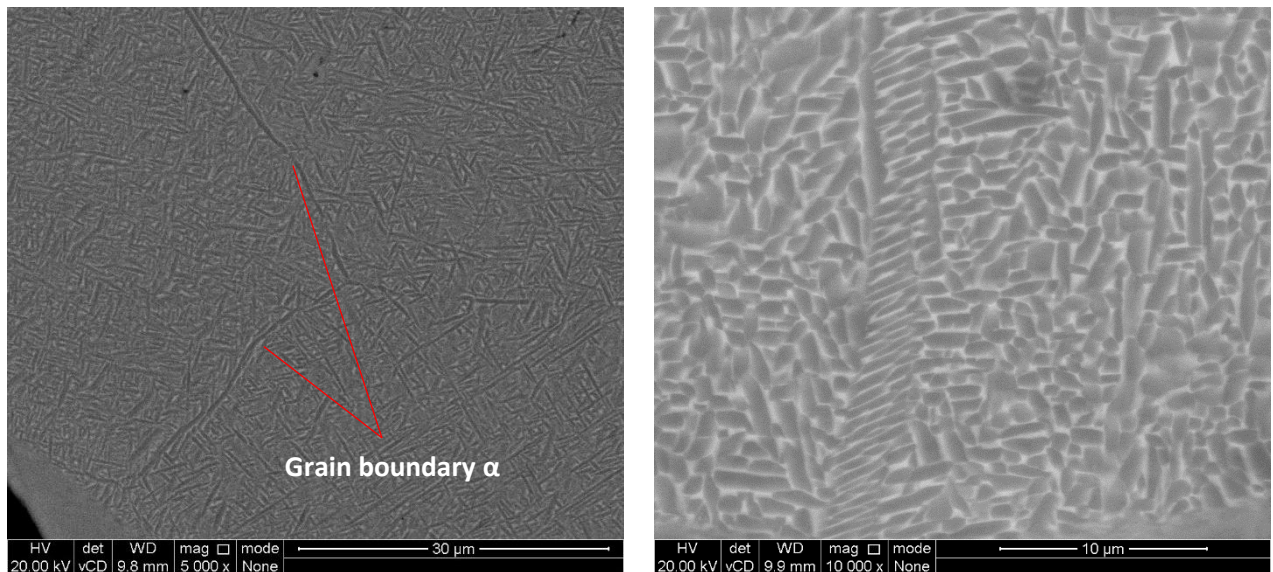


Figure 4.3: BSE micrograph of DLD Ti-6246 showing grain boundary alpha (left) and side plates (right)

The appearance of specific types of features such as grain boundary α and the “side plates” is down to local solidification rates and local composition. However, on a more macro-scale, the average size of the α -laths is dependent on the cooling rates during the deposition, which are in themselves dependent upon the processing parameters. In literature there is a lot of work linking the size and/or morphology of microstructural features to cooling rates in processes such as casting. For example, secondary dendrite arm spacing (SDAS) can be related to cooling rates. However, there is very little evidence in literature of the quantification of Ti-6246 DLD microstructure and how it relates to process inputs, cooling rates or build location. Since the size and morphology of the solidification microstructure has consequences for the mechanical properties of the material, it is important to understand how the deposition process affects it.

In light of this, microscopy specimens were taken from the ten Ti-6246 DLD deposits. High magnification back-scatter SEM images were obtained for each of the microscopy specimens for microstructural quantification such as the ones in Figure 4.1 & Figure 4.2.

4.3 Quantification of DLD Ti-6246 α -laths

Two sections were removed and retained from each deposit for microstructural analysis, one from the top and one from the bottom of the build. The sections were adjacent to the position of the gauge of the tensile specimens (shown in red in Figure 4.4), to get a good indication of the bulk microstructure. The microscopy was performed using an FEI Sirion FEG secondary electron microscope in the BSE mode as discussed in Chapter 3. All samples were imaged in the same plane for consistency. Primarily, the regions of interest for microstructural analysis were along and near to the shared edge with the tensile specimens (shown in orange). Four regions of interest (ROI) were chosen per microscopy sample for microstructural quantification.

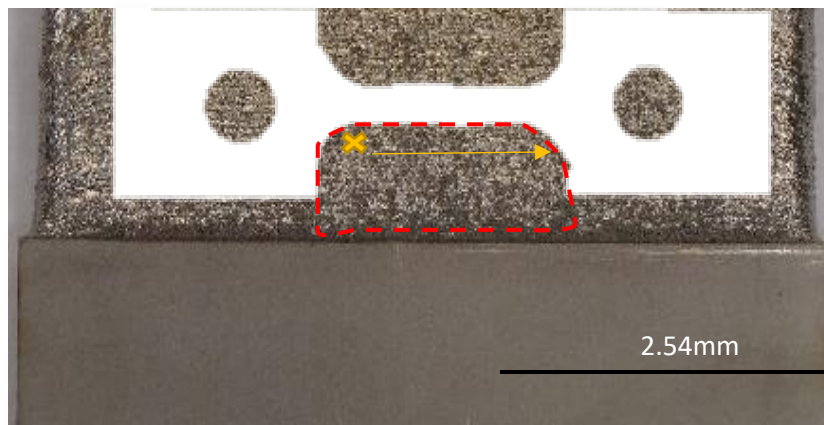


Figure 4.4: Position of bottom microscopy sample (red dashed line) with respect to tensile specimen. Primary ROI for microstructural analysis shown in orange

4.3.1 Manual vs. automated microstructural assessment

Microstructural assessment, namely the quantification of the alpha lath widths was ultimately achieved using an image analysis software package called CLEMEX. The details of the routine are described in Chapter 3 (and Appendix A: CLEMEX routine) but the primary processes were to apply a threshold to the image, separate the two phases, remove any noise and then measure the width of the laths. When measuring widths of features, the CLEMEX software is best suited for well-defined features (clear contrast with the background) with little overlap especially for elongated features like the alpha laths. It was found that the CLEMEX software often could not separate out laths that were overlapped multiple times and also struggled with images with a lot of noise. Therefore, the raw data often contained many “outliers” both at the top end and bottom end where the software had not separated the laths appropriately. To correct this, the d_{10} and d_{90} were calculated for each of the data sets. All measurements below the d_{10} value and all measurements above the d_{90} value were removed.

To ensure that this was a robust and reliable method for determining the microstructure for all the Ti-6246 DLD builds, the results were compared to measurements performed manually.

ImageJ, an image analysis package, was used to threshold all the SEM images acquired to clearly define the boundaries of the alpha laths and ensure more accurate measurements. Two different manual measurement techniques were compared and the most robust was selected to provide baseline results to validate the CLEMEX routine.

4.3.1.1 *Manual Method A: Individual lath measurements*

The first method was performed using the line drawing tool in ImageJ. The length of the line was calibrated for measuring in microns instead of pixels using the scale bar on the SEM micrograph. For each region of interest (ROI), a line was drawn across the width of each lath as shown in Figure 4.5. with the width defined (as in the CLEMEX software) to be at 90° to the longest axis.

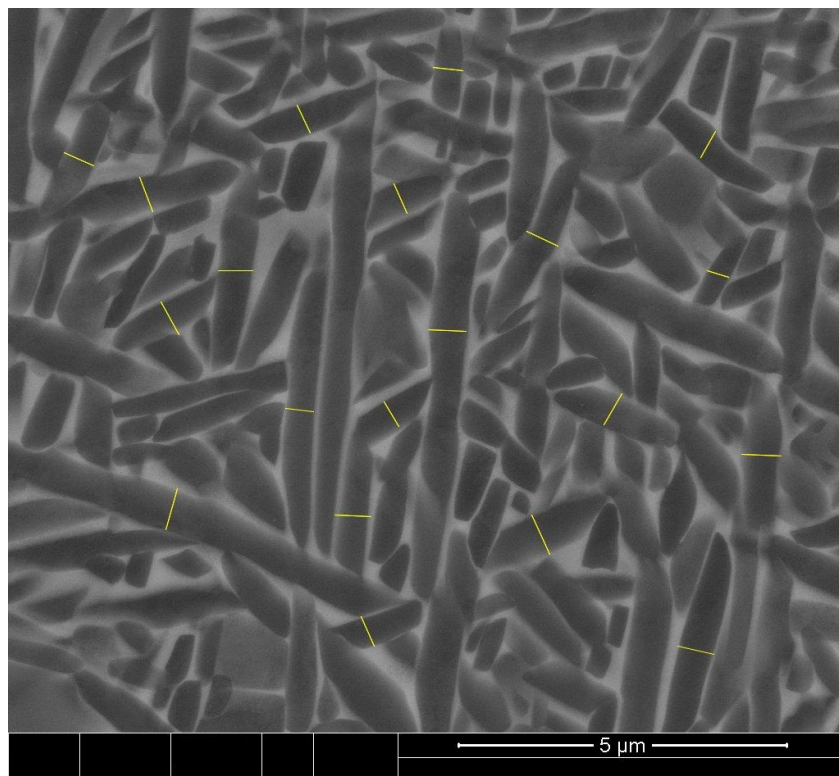


Figure 4.5: SEM micrograph with alpha laths indicating method A

4.3.1.2 *Manual method B: Linear intercept*

Due to the amount of time required to perform individual measurements, a second method was investigated. This employed the line draw tool in ImageJ to draw a line across the micrographs at a number of orientations (Figure 4.6). As with method A, the line was calibrated using the scale bar to give its length in microns. A marker was placed along the line, each time it crossed a boundary between

the alpha laths. The length of the line in microns was divided by the number of markers to give an average lath width, similar to the method used by Collins et al. (2009) [125].

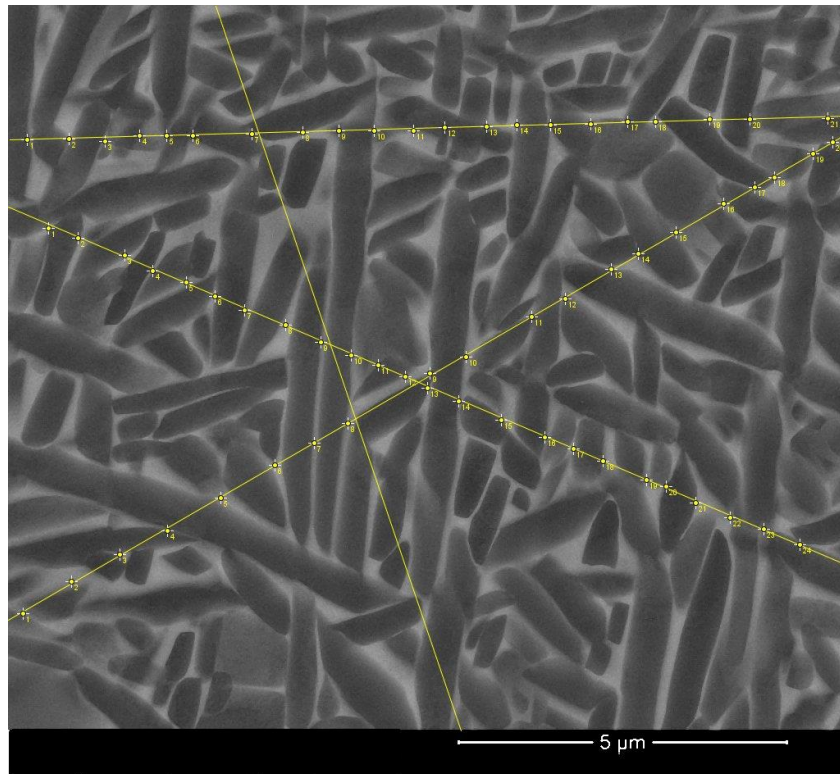


Figure 4.6: SEM micrograph with alpha laths measured using method B

However, as shown in Table 4.1, the average measurement using method B resulted in a significant over-estimate of the lath widths. At certain orientations, the intercept lines are close to the orientation of the laths, reducing the number of times the line crosses a boundary between the laths, skewing the results. Therefore, method A was chosen to provide the baseline measurements to calibrate the CLEMEX routine.

Table 4.1: Comparison between width measurements using methods A and B

Method A: Individual widths	Method B: Linear intercept
0.42	0.66

4.3.1.3 Validation of CLEMEX routine

To check the validity of the created CLEMEX routine (see Chapter 3.5.2 and Appendix A: CLEMEX routine for full details), the alpha lath widths output by the automated routine were compared to manual measurements. The ROI depicted in Figure 4.5 was used for the initial validation due to the clear and sharp delineation between α -laths as well as the high density of α -laths.

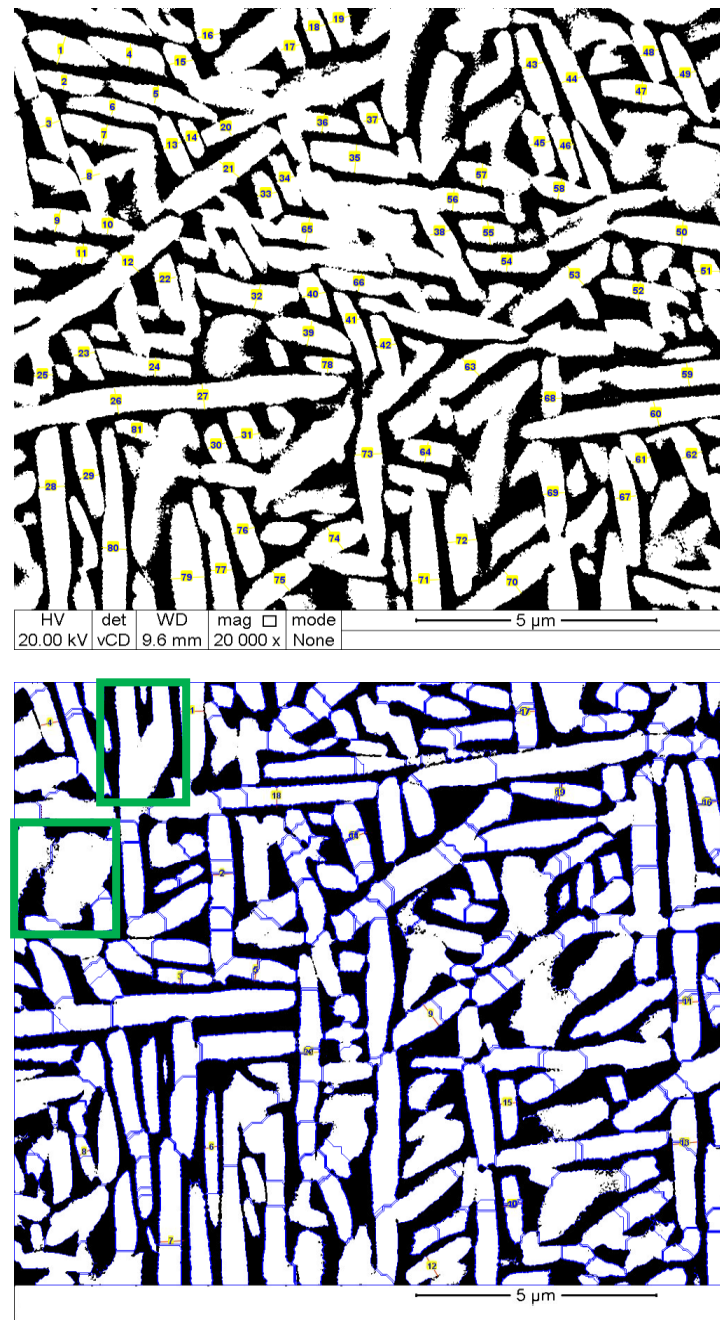


Figure 4.7: Manual measurement vs CLEMEX measurement

Manual measurement has the advantage of being able to determine which features are whole laths. However, the CLEMEX software is not always able to make that determination, especially with overlapping and irregular-shaped laths. Geometrical limits were included in the programme, to limit the routine to long-thin shapes. This has resulted in the features highlighted in green in Figure 4.7 to be automatically excluded from the measurements.

The routine is identical for all the images that have been run through it which removes any human bias from the results. In addition, all the CLEMEX results were compared to manual measurements of the same micrographs. In this case, 20 random laths were measured per ROI, and the average was

compared to the CLEMEX average. As can be seen in the example histogram in Figure 4.8, the manual and automated measurements give comparable average lath widths. In addition, a similar normal distribution can be seen for both methodologies. This technique was performed for each of the ROIs used in this study to ensure the CLEMEX valid was robust enough to provide accurate values across all the deposits.

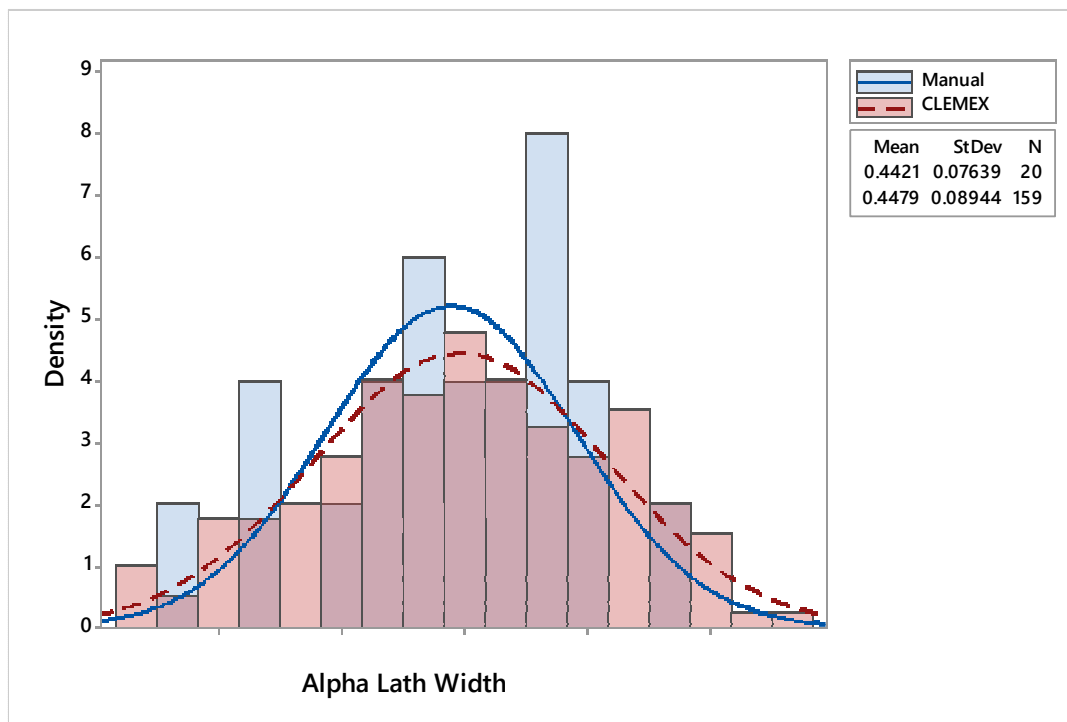


Figure 4.8: Histogram showing manual vs. automated (CLEMEX) measurements of alpha lath widths

4.4 CLEMEX results

Once the raw data had been processed, the results were plotted on a probability plot as shown in Figure 4.9.

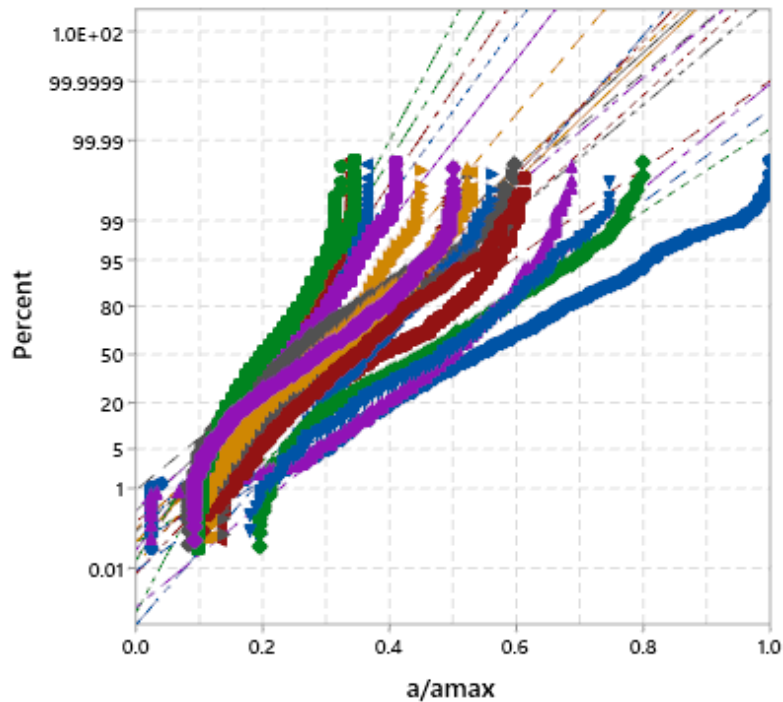


Figure 4.9: Probability plot for the alpha lath widths for all DoE specimens

The results plotted in Figure 4.9 show not only the large spread in alpha lath width across all the specimens but also within the specimens themselves. For example, the blue data points on the far right-hand side of the plot has the coarsest microstructure with the highest d_{50} and d_{90} values. However, this specimen also contains laths that have been measured at 20% the width of the largest lath. Each specimen has a bulk average, but this may be heavily skewed depending on where the measurements were taken in the build. To minimise this effect, several regions of interest were randomly selected during the imaging process to try and remove any bias and provide an accurate overview of each specimens microstructure.

The mean-size of the alpha-laths for each specimen is provided in Table 4.2, along with the number of individual measurements for each (N). This N value is the number of laths that were identified by the CLEMEX software after the SEM images were run through the routine and processing of the raw data.

Table 4.2: Statistics from probability plot

Mean	StDev	N	P	Energy density (E ₀ *)	Parameter set
0.2183	0.166	2051	<0.005		
0.2173	0.1305	681	<0.005	40	1
0.2173	0.1387	1745	<0.005		
0.2388	0.1098	1246	<0.005		
0.2601	0.108	865	<0.005		
0.2888	0.09543	918	<0.005	66	2
0.3662	0.1248	618	<0.005		
0.3283	0.09984	703	<0.005		
0.2046	0.05742	2059	<0.005		
0.2858	0.1067	1253	<0.005	66	3
0.2725	0.1004	874	<0.005		
0.2795	0.0765	1056	<0.005		
0.3303	0.1105	1544	<0.005		
0.31	0.09551	1121	<0.005	66	4
0.4686	0.07805	813	0.005		
0.3494	0.08637	1200	<0.005		
0.5414	0.06641	1560	<0.005		
0.3784	0.06109	1839	<0.005	109	5
0.455	0.04872	1295	<0.005		
0.4824	0.07033	1848	<0.005		

For clarity, it is easier to group the parameter sets according to the normalised energy density (E₀*) which is defined as $q^*/v^*l^*h^*$ as shown in Figure 4.10. Parameter set 5 had the highest energy input, and the mean values (which have been normalised against α^{max}) show that this has resulted in a coarser microstructure. This is most likely due to an excess of energy during the process which has caused additional re-heating of previously deposited material. This acts as a form of heat treatment, coarsening the microstructure. The builds with the lowest energy input (parameter set 1) had far less excess energy by comparison and as a result the alpha laths have not coarsened as much.

Parameter sets 2, 3 & 4 were deposited using the same energy density and so might be expected to have similar microstructures. The probability plots and the data from the table shows that parameter sets 2 and 4 have very similar lath widths, but parameter set 3 has an unusually fine microstructure. Although the energy densities were the same, the individual process inputs (velocity and hatch spacing etc.) used to achieve this were different. The layer height was kept consistent for all the builds so the differences between 2, 3 and 4 is the beam velocity and the hatch spacing. Parameter set 2 had the smallest hatch spacing ($1/h^*=1.65$). The increased overlap between adjacent tracks would be expected to increase the heat input and keep the cooling rates low resulting in a coarser

microstructure than 3 and 4. In reality however, parameter set 2 has a finer microstructure on average than parameter set 4. As can be seen from the probability plots there is quite a spread in the measurements within the same specimen and between specimens with identical process inputs. This variation may be hiding the true average, although the sample size used should be large enough to account for this. Instead, it may be that there is another factor influencing the microstructure. As mentioned previously, although the v^* and $1/h^*$ values differ between parameter sets 2, 3 and 4, the actual E_0^* values are the same. This implies that the same amount of energy is being provided per volume of material. The only difference between these parameter sets is the powder feed rate (PFR) that has been used. The potential effects of the powder feed on the energy input, microstructure and mechanical properties is discussed in Chapter 7.

The importance of quantifying the size of the microstructure is that it has a direct impact on the mechanical properties (particularly the ultimate tensile strength (UTS) and 0.2% yield stress). This will be discussed with the mechanical test results in Chapter 5.

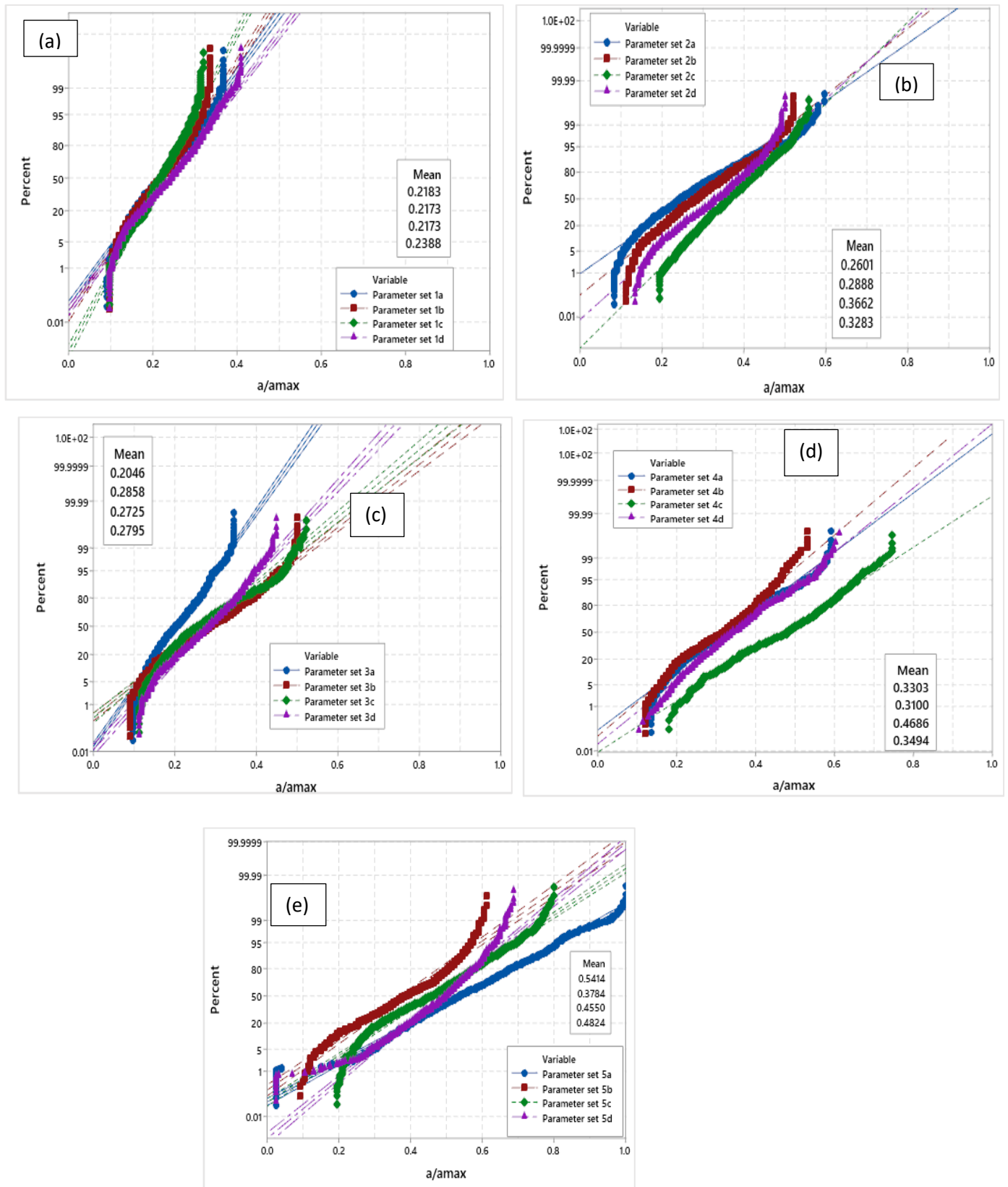


Figure 4.10: Probability plots for the five different parameter sets (a-e) showing alpha lath widths from the microscopy sections.

4.5 Bulk vs. localised section

In addition to ensuring that the CLEMEX routine is a suitable measurement methodology, how representative these small ROIs (chosen for their proximity to the machined tensile specimens) are of the bulk microstructure is also important. To address this, a specimen taken from the centre of the build also underwent microstructural assessment. Twenty SEM micrographs were collected at equal intervals down the specimen as shown in Figure 4.11, with the blue crosses indicating the start and end position.

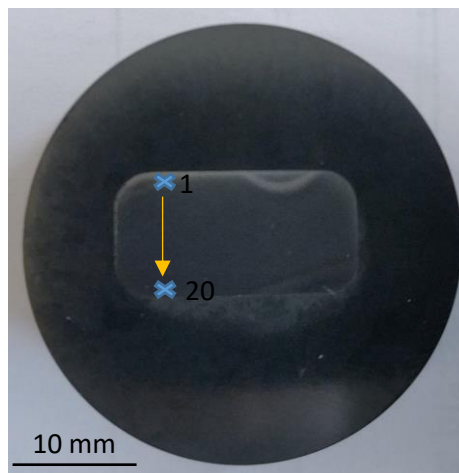


Figure 4.11: Bulk microscopy sample

The average normalised alpha lath widths for each of the twenty micrographs is plotted as a function of build position in Figure 4.12. As can be seen there is variation in the average lath width with a maximum (normalised) value of 0.79 and a minimum of 0.52. This is representative of the measurements taken from the localised samples from the same build. The overall average for the bulk is 0.38, compared to 0.43 for all the localised measurements. This is only a difference of only 0.05, meaning that the localised ROIs used to quantify the microstructure for comparison with process inputs and mechanical properties are reasonably representative of bulk microstructure even taking variation within the same build into account.

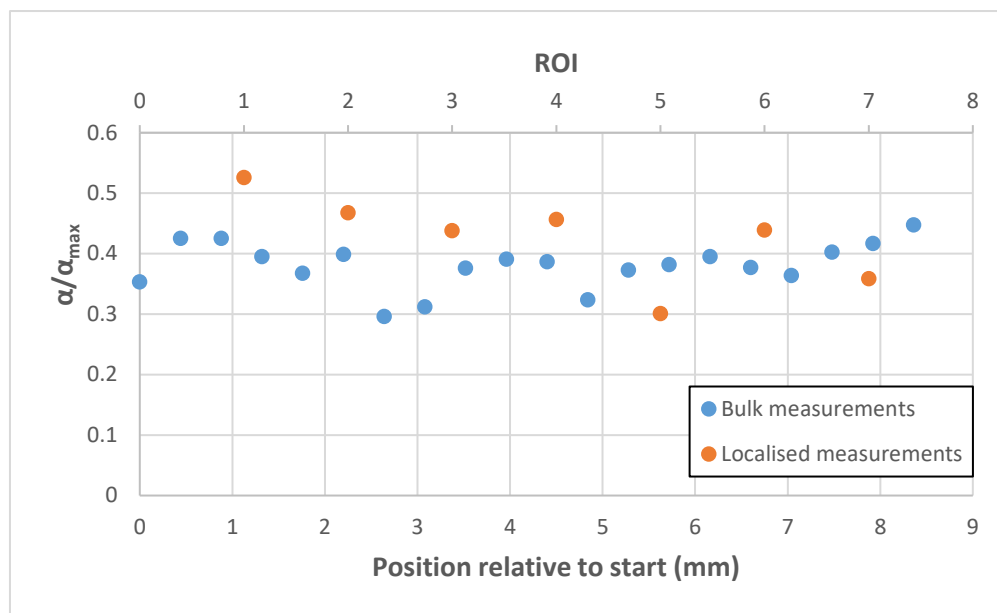


Figure 4.12: Normalised alpha lath widths in bulk sample

4.6 Effect of build height on microstructure

Some of the variations between tensile specimens may be as a result of build height. For each build, two tensile specimens were produced, one from the top of the build and one from the bottom near the substrate. It would be expected that the bottom of the build would have the finest microstructure since the substrate will act as a heat sink at the start of the build process. This would result in higher cooling rates and hence a finer microstructure.

In Figure 4.13, all the alpha lath width measurements are plotted as a function of build position rather than for each parameter set. Overall, the average lath width is very similar between the top and the bottom of the build. The bottom of the build has a larger spread in the data, but the smallest laths for each region are very similar. Since the build is only 30mm in height the difference in microstructure from the bottom to the top is not too pronounced. The bottom of the build may initially experience high cooling rates which leads to finer laths. However, the build, including the initial layers will retain heat during the deposition process which would lead to a coarsening of the microstructure. This may be why the bottom of the build sees more of a spread in the size of the microstructure compared to the top where the final layers will not be held at a high temperature for as long. This has been demonstrated by Qian et al (2005) [37], using thermocouples during deposition of Ti-6Al-4V revealed that the bottom and middle of the build undergo several heating cycles above the α -transus, which could have the effect of transforming any martensitic microstructure.

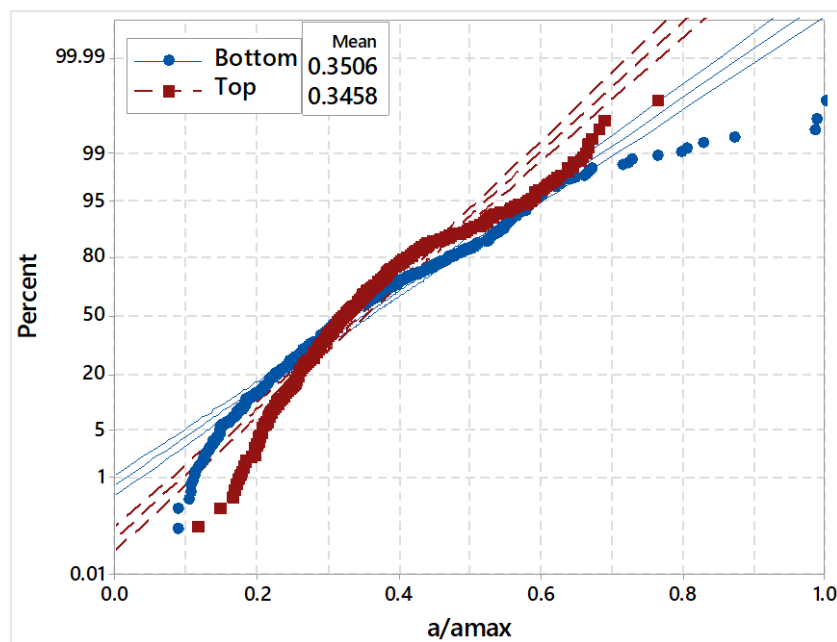


Figure 4.13: Probability plot showing the alpha lath widths as a function of build position

4.7 ICP-OES results

Samples from across the parameter sets 1-5 were sent to AMG Analytical in Rotherham, UK to undergo inductively coupled plasma optical emission spectroscopy (ICP-OES) to test specifically for aluminium content. The high energy densities being used to deposit the material could have led to the evaporation of some of aluminium. Nominally this is present at 6 wt% within the powder. Results from the analysis are given below in Table 4.3.

Table 4.3: Results from ICP-OES

Al content from ICP-OES (wt%)	Difference to baseline	Corresponding E_0^*
5.36	0.54	109
5.9	Baseline	-
5.39	0.51	109
5.59	0.31	66
5.02	0.88	40
5.17	0.73	66

The substrate which is made from forged Ti-6246 was also sent for analysis and gave a baseline value of 5.9 wt%. The DLD samples showed significant enough loss of Aluminium that the composition was

below the minimum wt% requirements [126]. In fact, only one of the builds has an acceptable Al content between 5.5 and 6.5 wt%. as indicated by the red lines. The highest loss was 0.88 wt% and from a build with the lowest energy input. Figure 4.14 appears to show that builds with higher energy densities have resulted in a lower loss of Al.

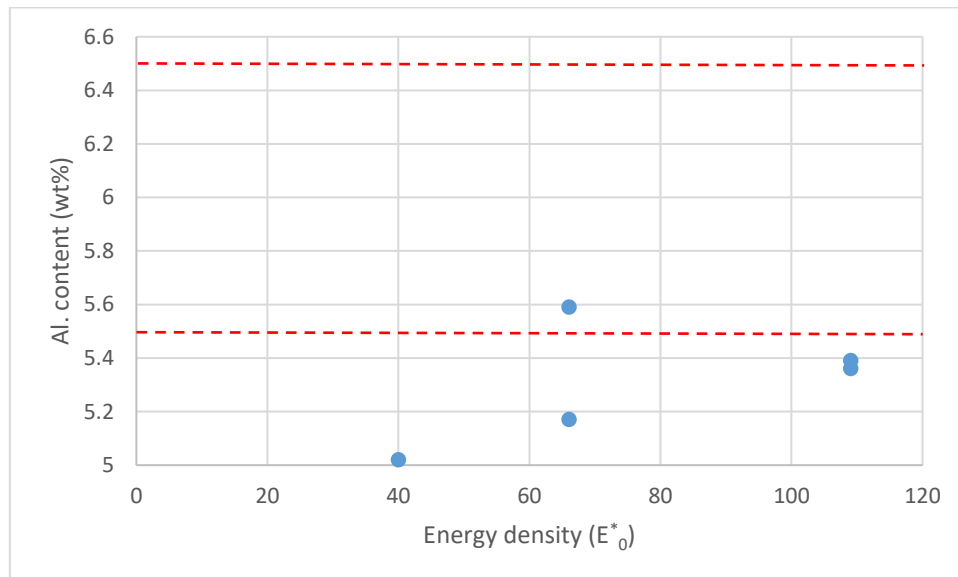


Figure 4.14: Al content as a function of energy density

Aluminium is an α -stabiliser and promotes the tensile strength of the material. This is evident in the tensile properties from the same build as the ICP-OES tested material. This build has a higher UTS and 0.2%YS values compared to the identical build ($E_0^*=66$) which has an Al content of 5.17 wt% as shown in Table 4.4: Effect of Al content on UTS properties.

Table 4.4: Effect of Al content on UTS properties

E_0^*	Al (wt%)	Normalised UTS
66		1
	5.59	0.98
	5.17	0.95
		0.94

4.8 3-D analysis of build quality using X-ray Computed Tomography

X-ray computed tomography (XCT) was performed on the tensile specimens to investigate the presence of build defects which may have affected the mechanical properties. Low resolution XCT was performed on the grip sections of the 20 DLD mini tensile specimens and additional high resolution XCT was performed on the grip and gauge section of one of the specimens (see Figure 4.15).



Figure 4.15: Schematic showing the regions of interest for the high resolution (left) and low resolution (right) XCT scans

4.8.1 Results & Discussion

As discussed in Chapter 3, the low resolution scans were performed using a Custom 320kV Bay machine and multiple grip sections could be scanned at once. The overall resolution limit meant that any features $< 25\mu\text{m}$ could not be detected with any confidence. Across the 20 grip sections, only a single pore was detected, the XCT reconstruction of this pore is shown in Figure 4.16. Since the 3-D size of this pore is only just above the resolution limit of the equipment, the irregular features produced by the reconstruction are unlikely to be real. The actual pore is likely to be more spherical and have an approximate diameter of $100\mu\text{m}$ which is large compared to the size of the lamellar microstructure. This is also likely to be on the upper limit of what we would expect from any gas pores from the powder and may instead be a result of the Argon gas feed used during deposition. However, since this pore was in the grip section well away from the fracture surface it would have had no effect on the mechanical properties of the build.

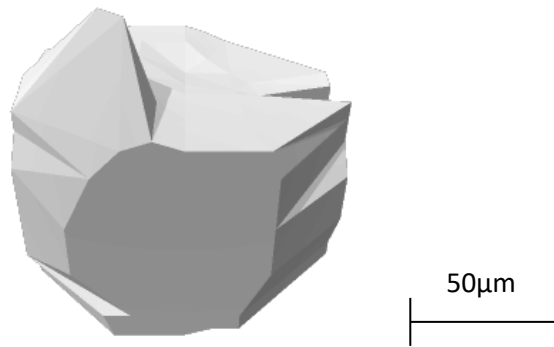


Figure 4.16: XCT reconstruction of pore detected in low resolution scans

There were no other detectable pores found in the low resolution scans, which does not necessarily mean that there were no more present, simply they were too small to be resolved.

A higher resolution scan was performed on the grip and the gauge section of the tensile that had the 100 μm pore to establish if there were any other smaller defects present. Interestingly, this specimen had an elongation to failure value of less than half that of both the other tensile taken from the same build and the two tensiles taken from the replicate build (same process parameters). The ductility of this specimen only just met the minimum requirements set by Rolls-Royce for Blisk repair.

These scans were performed on an Xradia Versa XCT and had a resolution limit of approximately 5 μm . There were no more additional pores within the grip section, meaning that this section was close to 100% dense (99.9999%). The high resolution scan of the gauge section was performed from the fracture surface down through the gauge for approximately 3 mm (see Figure 4.17), since this was the maximum volume that could fit the field of view. This high resolution scan only revealed the presence of three pores all with diameters of $\sim 20\mu\text{m}$, again resulting in almost 100% density. These pores were all roughly spherical in shape meaning they are likely the result of gas porosity from the powder used for the deposition.



Figure 4.17: XCT reconstruction of the high resolution scan of the gauge section. Fracture surface is at the top

4.9 Conclusions

The aim of this chapter was to provide both a qualification and a quantification of the DLD Ti-6246 microstructure. The typical solidification microstructure was found, as expected, to consist primarily of $\alpha+\beta$ lamellar. The typical size of the alpha-lath widths was sub $1\mu\text{m}$ with evidence of extremely fine dendritic microstructure at the very top of the build. This is likely due to the lack of re-melting and re-heating cycles in the last few layers meaning that the microstructure doesn't have a chance to coarsen. Between the bulk microstructure in the centre of the build and the top dendritic zone, there is a transition zone with a bi-lamellar microstructure. The typical primary alpha laths are observed but within the β -phase a very fine secondary α -phase can be seen at high magnification.

The CLEMEX software was used to create a routine capable of providing an automated method of measuring the size of α -lath widths. Over 4000 laths were analysed and measured per parameter set. The results revealed quite a large spread in lath width not only between different parameter sets, but between parameter sets with the same energy densities and even within the same builds. The general trend was found to be that as the energy density increases so does the average size of the laths. This is due to the excess energy provided by the laser beam meaning that a larger volume of material can remain at high temperature reducing the cooling rate and allowing time for the laths to coarsen.

Parameter sets 2, 3 and 4 had the same energy density per unit volume but had different microstructure sizes, with parameter set 3 being particularly fine. It is thought that the powder feed rate which is generally varied to keep layer height (l) constant may be having an affect since this is the only parameter that is different between the parameter sets.

XCT was used to analyse the quality of the build and to determine if the process window could produce defect free builds. Even at high resolution scans, only three pores could be detected. In addition, ICP-OES showed that there was no appreciable drop in aluminium content between the builds.

Both 2-D, in the form of SEM, and 3-D techniques, in the form of XCT, were used in this study to analyse the microstructure and build quality of the Ti-6246 deposits. Each of these techniques have their own advantages as well as limitations. SEM analysis is quicker, simpler and economical compared to XCT. It is a useful way to easily assess the solidification microstructure as well as highlight the presence of defects. However, it is limited to one region of interest at a time and the cross-section may not necessarily be representative of the bulk material.

In contrast, XCT imaging allows for the analysis of the bulk material but as well as being a more complex technique it is limited in resolution, meaning that smaller features may easily be missed.

Microstructural analysis and build quality

However, it is useful for determining if there are any specific issues with the deposition strategy or process parameters when narrowing down a process window.

In this case, neither the 2-D nor 3-D analysis showed evidence of significant build defects such as pores, cracks or lack of fusion. Overall, the lack of any significant defects close to the fracture surface in the tensile specimens, or in the builds generally, means that the chosen process parameters are optimised in terms of producing a near to fully dense build. It is also therefore unlikely that any reduced mechanical properties result from poor build quality. It is possible that there is micro-porosity present, which is below the resolution limit of both the Versa scans as well as the SEM.

5 Effect of process parameters on properties of Ti-6246 DLD

5.1 Introduction

This section will discuss the microstructural and mechanical results of the Ti-6246 DLD mini tensile specimens deposited using the RPM 557 using the parameters discussed in Chapter 3. The aim of these builds was to investigate the microstructural and mechanical response to changing the energy density of the builds. This was achieved by altering the hatch spacing and the velocity, the combinations of which were determined by a Design of Experiments (DoE) which is discussed here.

The results from the tensile tests are presented here in the form of responses within the DoE. The mechanical test results have been normalised against the minimum required values for DLD repair. Ideally, the results should have a value greater than or equal to the minimum values which gives a normalised result of (at least) 1. In the case of repair, it is important that the new material has comparable properties to the parent material. This is especially true for critical components, such as aerofoil blisks where Ti-6246 is commonly used, since there are strict material and mechanical requirements that must be matched if the part is to go (back) into service. Therefore, it is important that a process window can be identified whereby the mechanical properties of the DLD Ti-6246 material meets the requirements for such a component, and that the process is robust and repeatable. The mechanical response is plotted as a function of the DoE factors or process inputs $1/h^*$ and q^*/v^*l^* in order to create a response surface. Linear regression has also been used to create a model and a set of equations to define each response in terms of the factors.

By setting boundaries on the response surfaces based on the repair requirements, a suitable and optimised process window can be defined.

5.2 Investigating process space

It is common for the effects of process inputs to be investigated as a group rather than in isolation, since changing laser power will also alter the energy density for the build which may have consequences on the final component. Process maps such as the one compiled by Thomas et al (2016) [107] as shown in Figure 5.1 can be used to identify process windows. The process map shown in Figure 5.1 is based upon the work done by Ion et al (1992) [105] where the parameters are normalised

against the thermophysical properties of the material in question. A description of how these normalised parameters are calculated is given in Chapter 2.

Using normalised parameters means that the same map can be used to plot the results from separate experiments and for different materials and process parameters. The dashed lines in Figure 5.1 represent isopleths indicating constant energy density. Data points that fall on the same dotted line originate from deposits with identical energy densities, but using a different combination of hatch spacing and laser beam parameters. Currently, it is not clear that components deposited with identical energy densities necessarily have the same microstructures and hence mechanical properties.

Such process maps can be used to identify process windows i.e. the range of process parameters that will result in a robust fully-dense build for a given material, or can be used to predict and test optimised parameters. In the case of DLD of Ti-6246 there is very limited data to be found in literature with regards to ideal process parameters. However, a potential process window was identified based upon private communication by Rolls-Royce. The set-up for the DoE used to calculate the combinations of process parameters used for the Ti-6246 DLD mini tensile specimens is discussed in the following section.

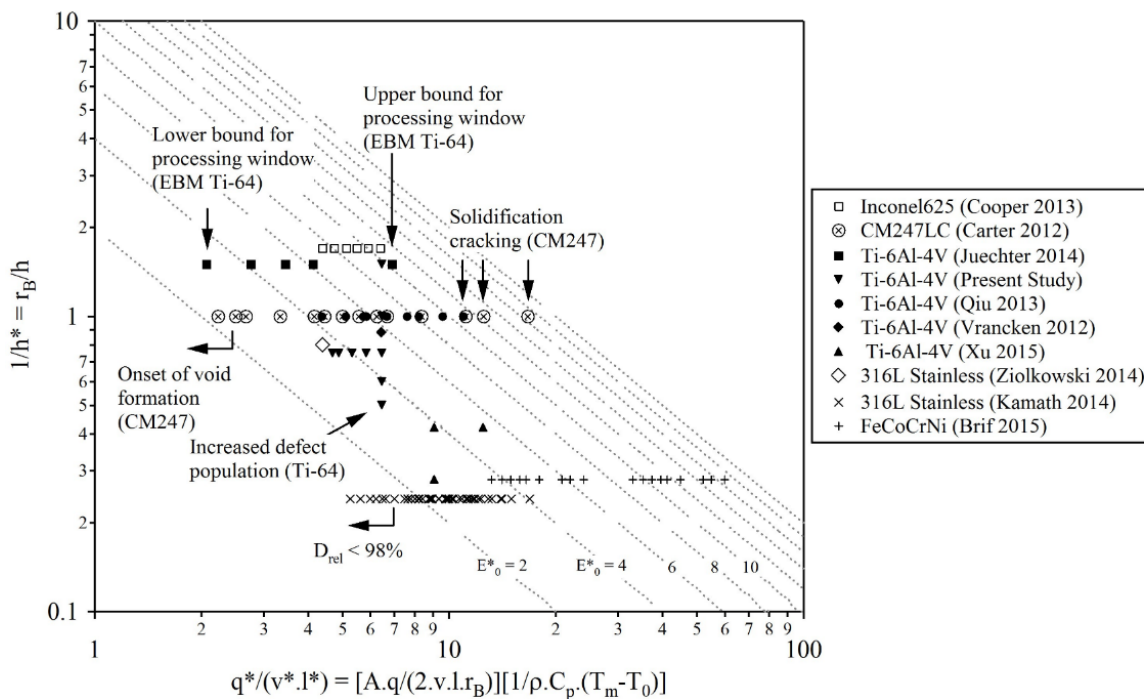


Figure 5.1: Normalised process map for DLD of different alloys [107]

5.2.1 Design of Experiments for Ti-6246 mini tensile process window

The method used to determine the combinations of process parameters used for the deposition of the mini tensile specimens was a 2-level factorial. This type of DoE is used to determine how different factors interact with one another and how this affects the measured responses. Outcomes of these experiments. Creating this process window and investigating the mechanical responses for each point will help to inform future experiments with the aim of optimising the process parameters for Ti-6246 DLD on the RPM 557. This is especially useful since, as mentioned previously, there is little to no data available for additively manufactured Ti-6246 in general.

Software package MiniTab® was used to create a 2-level factorial DoE to determine and assess a processing window for DLD of Ti-6246. The limits of the window defined here were based on previous work by Rolls-Royce that established a range of parameters that resulted in dense and defect-free builds. The purpose of this DoE is to quantify the effect process parameters have on key mechanical properties. Of secondary interest is the effect parameters have on microstructure (which does itself affect mechanical properties.) For simplicity the laser power and layer height were kept constant. Only laser velocity was used as a variable factor in order to alter the energy per unit volume (q^*/v^*l^*). The (inverse) hatch spacing ($1/h^*$) was identified as the second factor under investigation as in Figure 5.1.

The total number of experimental runs is defined by:

- Minimum and maximum of each factor
 - 4 points
- Centre-point
 - 4
- Replicates
 - 4 (not including centre-point)
- Total
 - 20

One of the main applications for Ti-6246 DLD is the repair of components such as compressor blisks, so it is important that the mechanical properties such as strength and ductility are not only comparable to the parent component, but that the process itself is robust enough to produce repeatable results. Therefore, having at least multiple replicates defined in the 2-level factorial is essential.

Table 5.1: DoE table showing experimental factors and the responses

Standard Order	Energy density	Hatch	UTS/UTS _{target}	YS/YS _{target}	%E/%E _{target}
1	40.21	1	1.006	1.118	0.96
2	40.21	1	1.033	1.121	1.6
3	40.21	1	0.996	1.122	0.92
4	40.21	1	0.973	1.105	0.8
5	65.88	1	0.97	1.051	1.9
6	65.88	1	1.028	1.101	1.7
7	65.88	1	0.966	1.052	2
8	65.88	1	1.015	1.083	1.7
9	40.21	1.65	0.987	1.113	0.84
10	40.21	1.65	1.008	1.122	0.96
11	40.21	1.65	1.037	1.112	1.7
12	40.21	1.65	1.031	1.116	1.4
13	65.88	1.65	0.953	1.071	1.1
14	65.88	1.65	1.006	1.076	2.4
15	65.88	1.65	0.966	1.064	2.8
16	65.88	1.65	0.957	1.065	2.4
17	53.045	1.325	0.989	1.125	0.7
18	53.045	1.325	0.986	1.096	1.3
19	53.045	1.325	1.028	1.113	1.5
20	53.045	1.325	1.045	1.114	1.3

5.3 Results & Discussion

The mini tensile specimen blocks were deposited according to the parameters given in Table 5.1 using the RPM 557 machine (as described in Chapter 3). For these experiments, the beam power, beam radius and layer height were all kept constant, with the beam velocity and hatch spacing being the two variable parameters being investigated. In addition to the 20 mini tensiles produced by DLD, there are also 5 non-DLD (forged) specimens for use as a baseline. All tensile specimens were machined using EDM and had gauge dimensions 12.7 x 3.2 x 2.54 mm with the total tensile bar length of 50.8 mm. All specimens underwent uniaxial tensile testing according to ASTM E-8(11) (see Chapter 3). The results of the non-DLD specimens are given in Table 5.2.

Table 5.2: Results from non-DLD tensile specimens

Specimen	UTS/UTS _{target}	0.2% YS/0.2% YS _{target}	%E/%E _{target}
1	1.012	1.006	2.7
2	0.981	1.033	0.38
3	0.996	0.973	2.3
4	1.004	1.005	1.8
5	1.005	1.004	2.2

5.3.1 Grubbs' Test

There is an obvious outlier in the non-DLD test results with specimen 2 having an abnormally low elongation to failure. To test whether this data point can indeed be defined statistically as an outlier and justify its removal from the data set, the Grubbs' test was performed on the elongation to failure data for the Non-DLD specimens. The equations used are shown below.

$$G = \frac{\bar{x} - x_{min}}{s} \quad (12)$$

$$G_{crit} = \frac{N - 1}{\sqrt{N}} \sqrt{\frac{t_{\alpha, N-2}^2}{N - 2 + t_{\alpha, N-2}^2}} \quad (13)$$

Eq. 12 calculates the G test statistic where \bar{x} is the mean of the data set, x_{min} is the minimum value (i.e. being tested as an outlier) and s is the standard deviation. The value calculated here is then compared to the G critical value defined by Eq. 13. Here, N is the number of data points which in this case is 5 and t is the critical value of a t-distribution with which can also be written as t_{crit} . If the value calculated in Eq. 12 is larger than G_{crit} ($G > G_{crit}$) then the data point can be rejected as an outlier.

Table 5.3 shows the values determined for the Grubb’s test of the elongation to failure data for the forged material.

Table 5.3: Table of inputs and calculated values for the Grubb's test

Parameter	Value
\bar{x}	9.38
x_{\min}	1.9
s	4.48
G	1.67
N	5
t_{crit}	4.54
G_{crit}	1.67

Performing this test reveals that $G=G_{\text{crit}}$, therefore the elongation to failure result for specimen 2 may be considered an outlier and will not be included in the results or discussion that follows.

5.3.2 Response surfaces

Using the results in Table 5.1, it is possible to perform a linear regression calculation to fit a model to the data.

Eqs.14-16 below describe the regression model that relates 0.2% yield stress, UTS and elongation to failure (responses) to the input factors (q^*/v^*l^* and $1/h^*$). The interaction between q^*/v^*l^* and $1/h^*$ is also taken into account as $q^*/v^*l^*h^*$. The symbols x, y and z in the equations below are q^*/v^*l^* , $1/h^*$ and $q^*/v^*l^*h^*$ respectively. The regression model is in coded factors and this means that the relative influence of each of the factors can be identified by the size of the coefficients.

As can be seen, the “x” factor has the largest coefficients across all three equations, implying that q^*/v^*l^* is the most significant factor. For both 0.2% YS and UTS, y and z coefficients suggest that these terms are largely insignificant. Since v^* is the only variable changing for the energy density, this is the dominant DLD process parameter. For %E, the hatch spacing appears to be of some significance.

$$0.2\%YS = 1.1 - 0.02x - 0.0009y - 0.00005z \quad (14)$$

$$UTS = 0.999 - 0.0131x - 0.0026y - 0.0085z \quad (15)$$

$$\%E = 1.5 + 0.4262x + 0.1262y + 0.0487z \quad (16)$$

An Analysis of Variance (ANOVA) can be performed in order to determine which of the factors has any statistical significance. This is determined by the F-value or alternatively the P-value and both are presented below in Table 5.4 for all three response models. The F-value is a measure of whether a term is associated with the selected response. This value is used to calculate the p-value which is a measure of the probability that the null hypothesis is valid. A p-value of <0.05 generally indicates that the term is statistically significant (disproves the null hypothesis), values >0.1 indicate that a term is not significant and that the null hypothesis may not necessarily be discounted. In the case of the UTS model, all of the p-values except q^*/v^*l^* are larger than 0.05. The overall UTS model p-value of 0.156 shows that there is a 15.6% chance that the model values could have occurred due to noise. By contrast, both the 0.2% YS and %E models show low p-values and hence are significant and the model can be used with confidence.

Effect of process parameters on properties of Ti-6246 DLD

Table 5.4: ANOVA results from the response models

Source	DF	Adj SS	Adj MS	F-Value	P-Value
Model (UTS)	3	0.004	0.001	1.99	0.156
Linear	2	0.003	0.001	1.99	0.170
q*/v* *	1	0.003	0.003	3.82	0.068
1/h*	1	0.000	0.000	0.15	0.701
2-Way Interactions	1	0.001	0.001	2.00	0.176
q*/v* *h*	1	0.001	0.001	2.00	0.176
Error	16	0.012	0.001		
Lack-of-Fit	1	0.001	0.001	1.18	0.294
Pure Error	15	0.011	0.001		
Total	19	0.016			
R ² = 27.19%					

Source	DF	Adj SS	Adj MS	F-Value	P-Value
Model (0.2% YS)	3	0.008	0.003	12.10	0.000
Linear	2	0.008	0.004	18.14	0.000
Energy density	1	0.008	0.008	36.23	0.000
Hatch	1	0.000	0.000	0.05	0.821
2-Way Interactions	1	0.000	0.000	0.02	0.897
Energy density*Hatch	1	0.000	0.000	0.02	0.897
Error	16	0.004	0.000		
Lack-of-Fit	1	0.001	0.001	6.56	0.022
Pure Error	15	0.003	0.000		
Total	19	0.012			
R ² = 69.41%					

Source	DF	Adj SS	Adj MS	F-Value	P-Value
Model (%E)	3	3.200	1.067	5.04	0.012
Linear	2	3.162	1.581	7.47	0.005
Energy density	1	2.907	2.907	13.74	0.002
Hatch	1	0.255	0.255	1.21	0.288
2-Way Interactions	1	0.038	0.038	0.18	0.677
Energy density*Hatch	1	0.038	0.038	0.18	0.677
Error	16	3.385	0.212		
Lack-of-Fit	1	0.447	0.447	2.28	0.152
Pure Error	15	2.938	0.196		
Total	19	6.585			
R ² = 48.60%					

The R-squared value is a measure of how well the data fits to the regression line and so the larger that value the better the fit. For the UTS model the R² value is 27.19% compared to 69.41% and 48.60% for the 0.2% YS and %E models respectively. Therefore, this suggest that the 0.2% YS model best fits the data and the UTS model is the weakest which is expected from the p-values.

5.3.3 0.2% YS model

Figure 5.2 shows the Pareto chart of standardized effects for the 0.2% YS response. This shows gives an indication of which factors have the largest effect on the response and the level of that effect. In this case, q^*/v^*l^* has the most significant effect. In addition it is shown that the other two factors are statistically insignificant since they fall below the reference line.

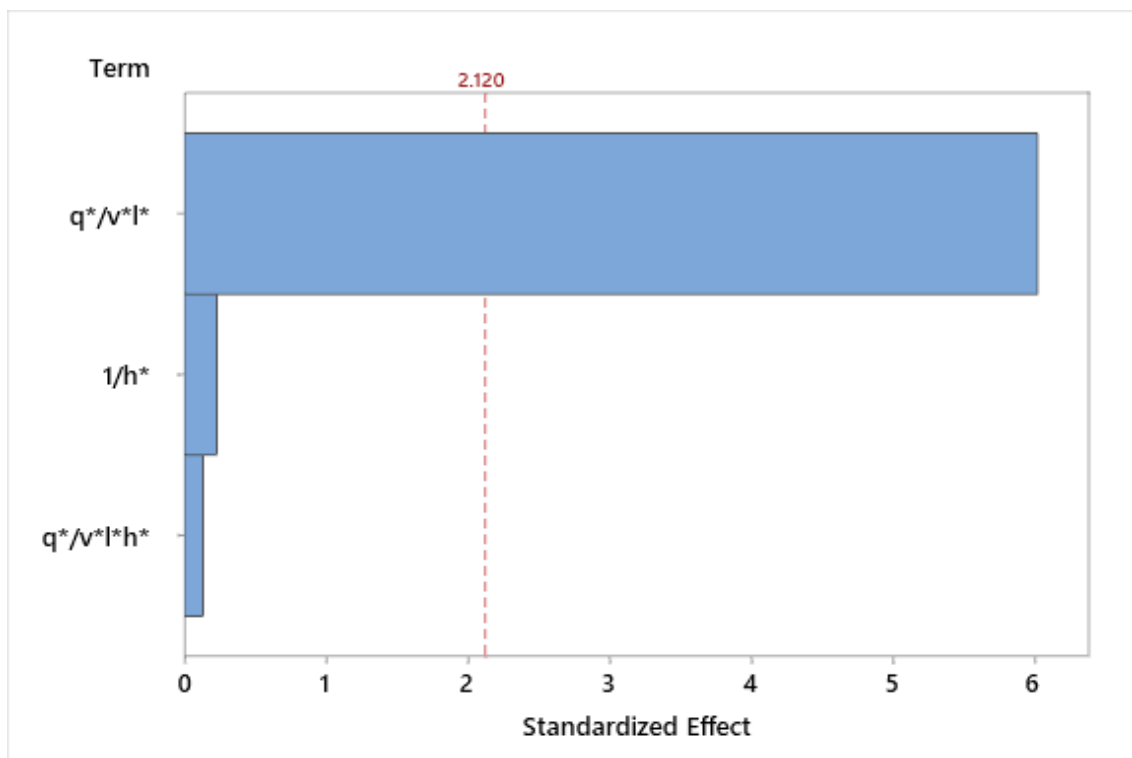


Figure 5.2: Pareto chart for 0.2%YS

The significance of q^*/v^*l^* over the other factors can also be seen in the response contour map in Figure 5.3. here it is clearly seen how the hatch spacing has little effect on the yield stress of the material. The contour map also suggests that in order to maximise the yield stress then q^*/v^*l^* should be reduced. However, within the process window investigated here the ratio of 0.2% YS_{actual} and 0.2% YS_{target} is always >1 meaning that the priority in adjusting process parameters should be on optimising UTS and ductility.

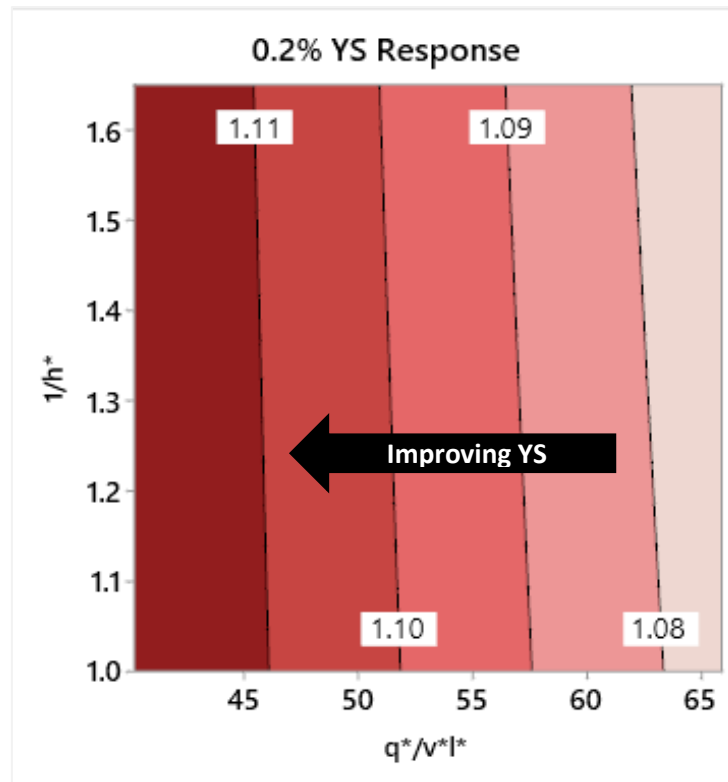


Figure 5.3: Response surface with contours showing constant 0.2% yield stress for the process window. The yield stress values shown are $0.2\%YS/0.2\%YS_{req}$

In terms of “real” parameters, an increase in beam velocity can be correlated to an increase in 0.2% yield stress. This could be explained by faster cooling rates at higher beam velocities which in produces finer microstructures. These fine microstructures often lead to high mechanical strengths due to the Hall-Petch effect.

5.3.4 %E model

Figure 5.4 shows the Pareto chart for the factors affecting %E response. Much like the 0.2% YS model, the most dominant factor is q^*/v^*I^* . The hatch spacing may have a slightly larger influence on the ductility than in the case of yield stress but is still statistically insignificant.

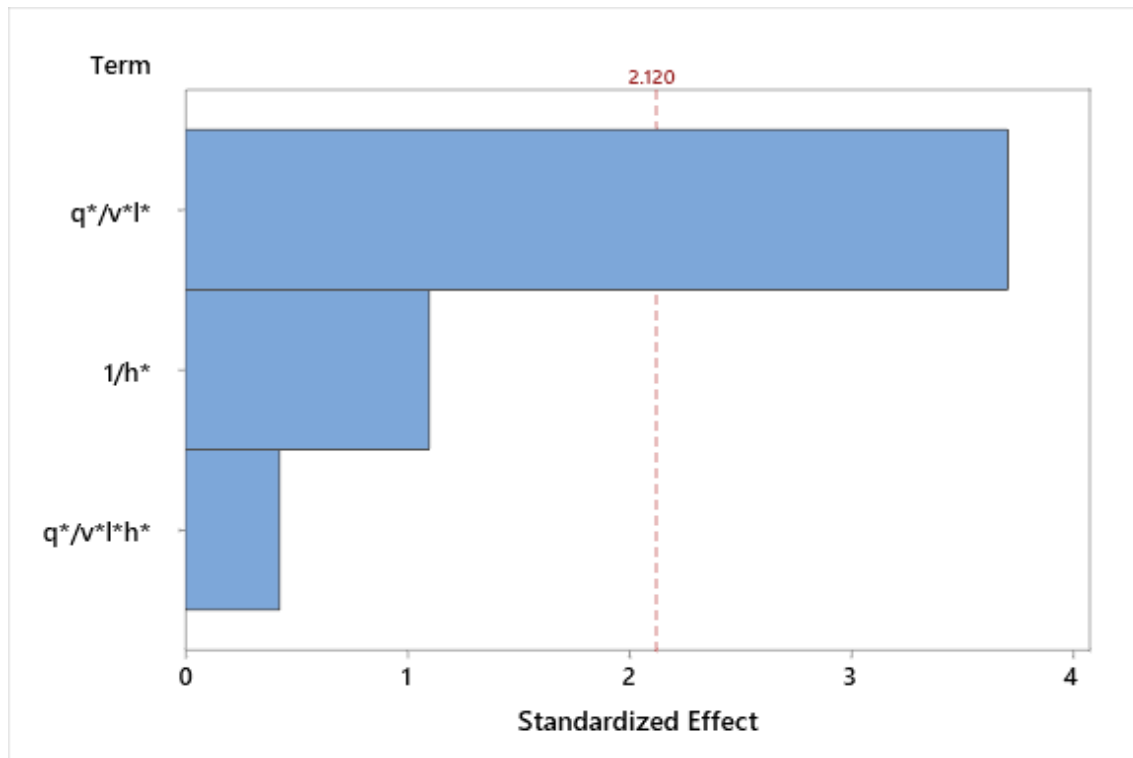


Figure 5.4: Pareto chart for %E response

Figure 5.5 shows the contour map for the %E response, as expected q^*/v^*l^* has the most affect but the minor influence of hatch spacing is shown in the slight curvature of the contour lines.. The blue circle in the bottom left-hand corner marks the position of the $\%E_{actual}/\%E_{target} = 1$ contour line. The area the left of this contour indicates the region where the elongation to failure results would be expected to fall below target requirements for Blisk repair.

In order to maximise the ductility of the deposited material, the right-hand side of the process window defined here would be most suitable. It is clear then from Figure 5.3 and Figure 5.5 that a compromise would have to be made between the yield stress and the ductility of the material. Moving towards the right of the process window results in improved ductility but also sees a decrease in the yield stress. However, as previously stated, the yield stress values are acceptable across the whole of the process window so there is scope for a shift to higher q^*/v^*l^* values.

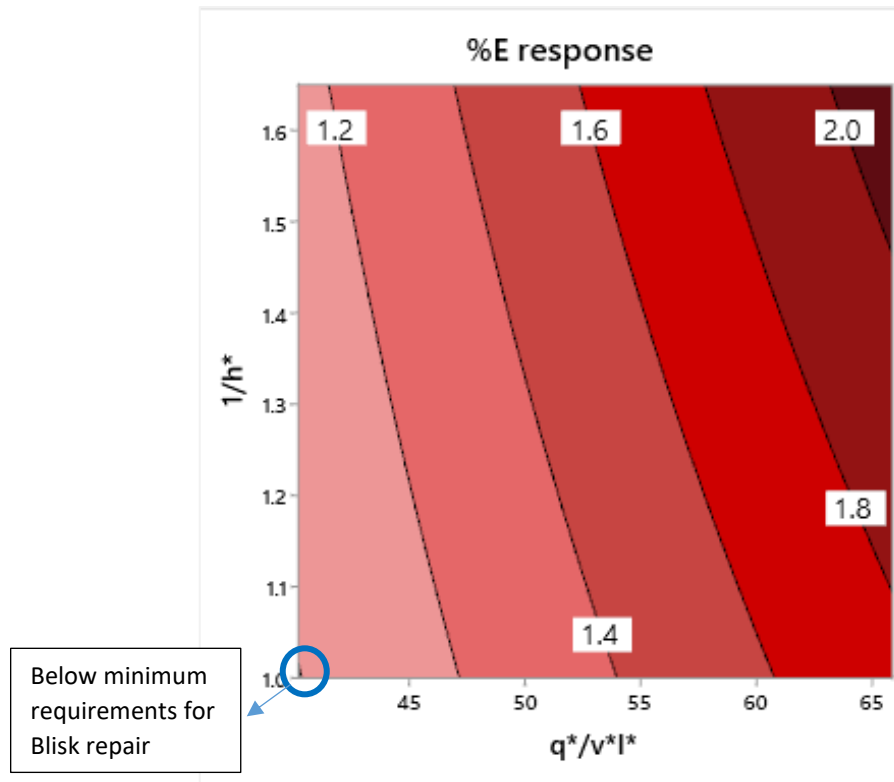


Figure 5.5: Response surface showing contours of constant %E for the process window. The elongation values shown are $\%E/\%E_{target}$. Blue circle indicates position of the $\%E/\%E_{target}=1$ contour line

5.3.5 UTS model

For completeness, the UTS model results have been included all results from the ANOVA table suggest that the model isn't statistically significant. The poorly fitting model may be due to the large variation in UTS results even within runs that have the identical factor levels. This is evident in Figure 5.6 where none of the factors are above the reference line. Interestingly, the q^*/v^*I^* appears to be the dominant factor as in the previous two models. Figure 5.7 shows the contour map for the UTS results, where there is a large area of the process window where the UTS target value has not been met. Although the poorly fitting model means that the positioning of the contour lines is incorrect, the general trends may still hold. Moving to higher q^*/v^*I^* results in an increased likelihood that the UTS falls below minimum requirements which is the same relationship as the 0.2% YS as might be expected.

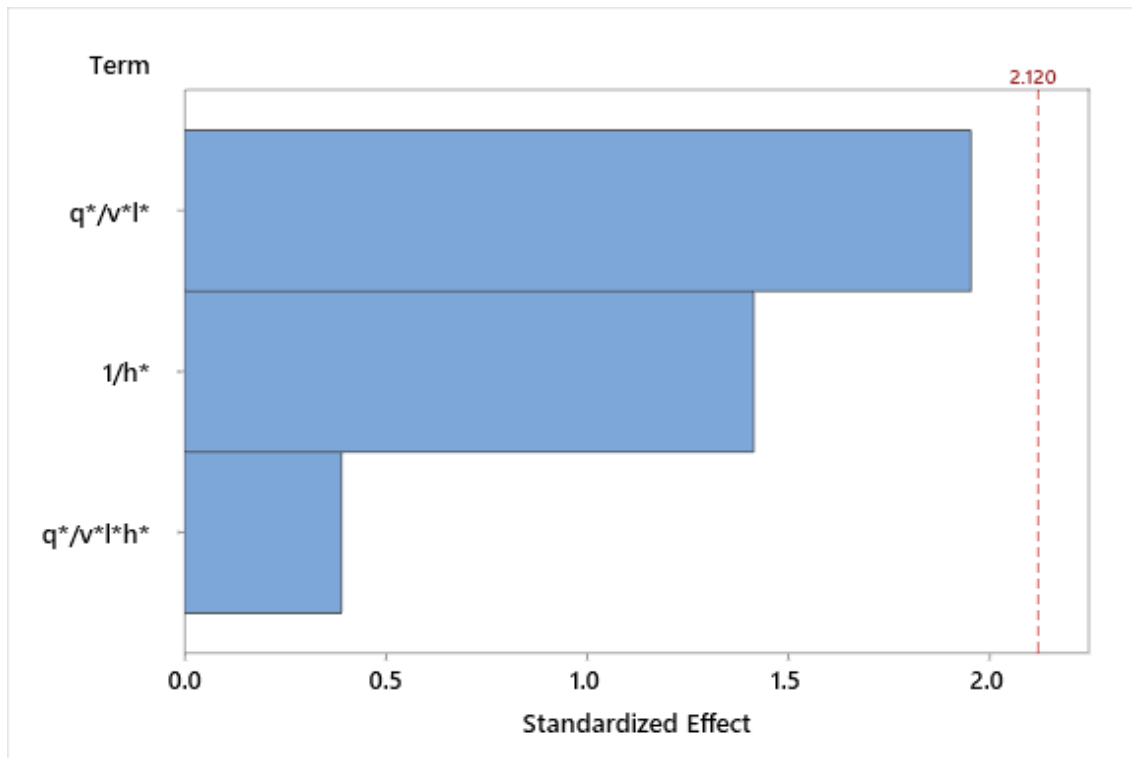


Figure 5.6: Pareto chart for UTS response

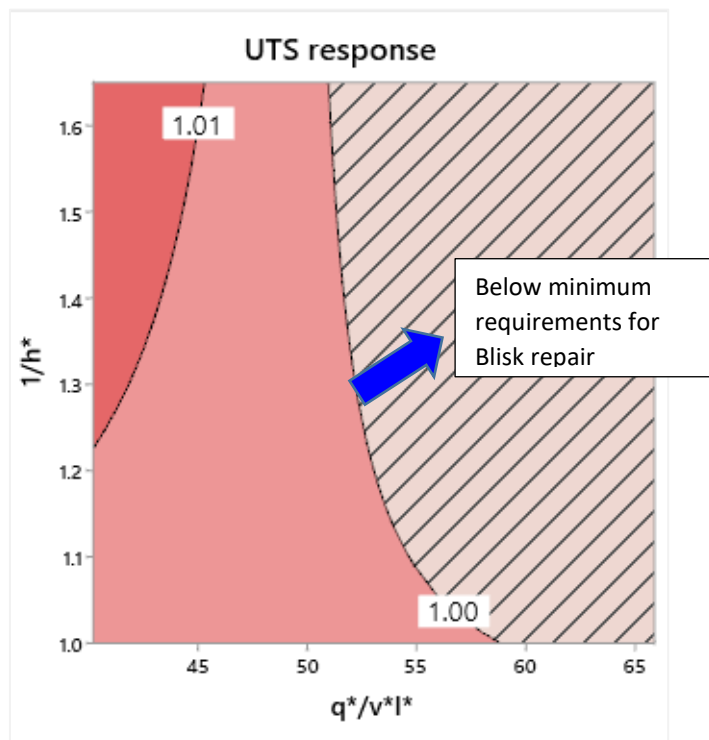


Figure 5.7: Response surface showing contours of constant UTS for the process window. The UTS values are defined as UTS/UTS_{target}

5.3.6 Optimisation

Ideally, all three of the mechanical responses would be optimised and be above the minimum requirements set for this application. For this DoE, the yield stress results are all well above the minimum requirements but the UTS and elongation results can often be low. Finding a combination of $1/h^*$ and q^*/v^*l^* values that will produce acceptable mechanical results is important if a Blisk repair process window is to be defined. Figure 5.8 shows the region of the current process window where the mechanical properties all meet target requirements. Only the contour lines for UTS, shown in red, and %E, shown in blue (bottom left-hand corner) are visible since all tensile specimens met minimum requirements for 0.2% yield stress. Only the contour lines for UTS, shown in red, and %E, shown in blue (bottom left-hand corner) are visible since all tensile specimens met minimum requirements for 0.2% yield stress.

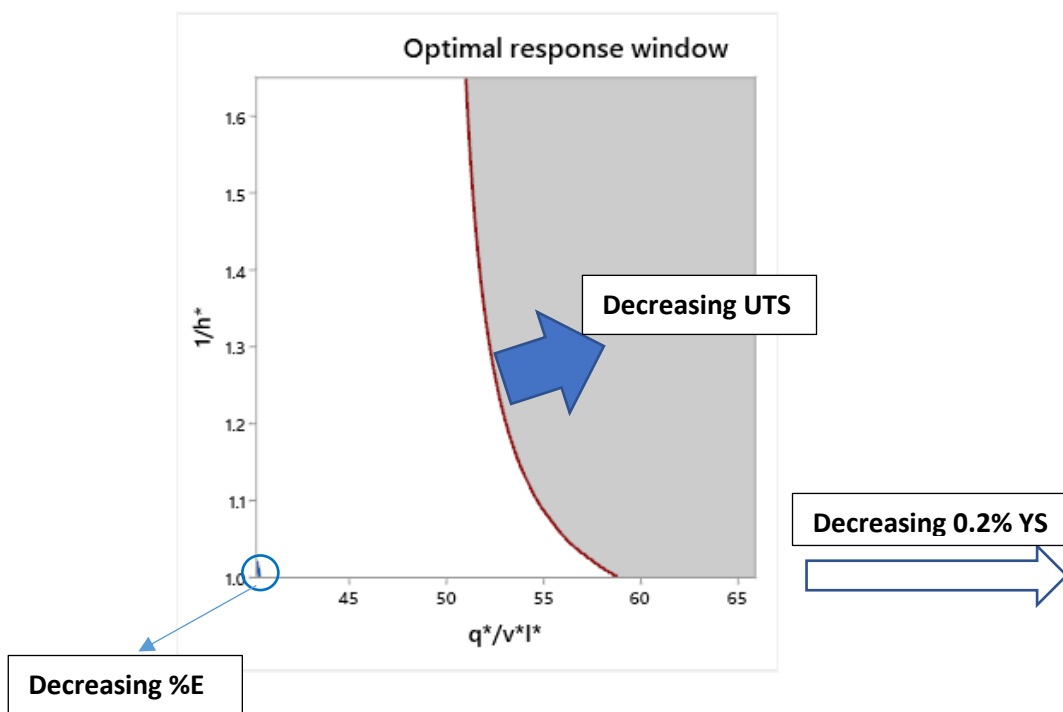


Figure 5.8: Contour plot to show regions of optimised mechanical responses

Regions where one or more of the responses do not meet minimum target requirements are shaded in grey. The white area shows the region where all three mechanical responses meet the set requirements. As is shown in this figure, decreasing $1/h^*$ (increase hatch spacing) generally improves the mechanical properties in question. As discussed previously, the hatch spacing has little to no effect on 0.2% yield stress. In addition, Figure 5.8 also suggests that q^*/v^*l^* should not be increased beyond what has been explored in this process window (~ 65) as this may lead to further reductions in UTS.

A recommendation would be to keep the value of q^*/v^*l^* used for the centre point of the DoE which is 53.045 constant. There is also scope to reduce q^*/v^*l^* slightly without dropping below the minimum requirement for material ductility. A reduction in q^*/v^*l^* can be achieved by reducing the beam power or increasing beam velocity or layer height. As has been shown in the above discussion, the hatch spacing has little affect on the mechanical properties compared to the energy density. However, an increase in hatch spacing would decrease build time which might be of importance for large Ti-6246 builds. It should be noted that any significant increase in the hatch spacing could lead to insufficient track overlap and cause build defects which would have a detrimental impact on mechanical properties .

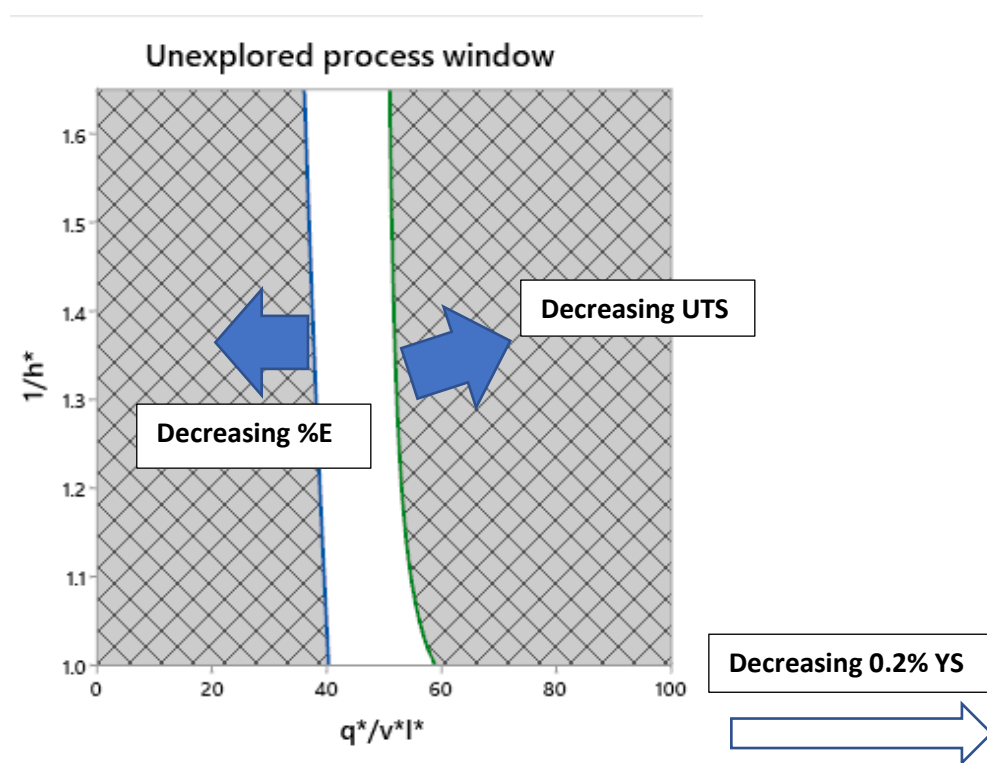


Figure 5.9: Contour plot showing "unexplored region" for potential Blisk repair process window with improved mechanical properties

5.3.7 Effect of build height on mechanical results

The possible effect of build height was considered with regards to effect on mechanical properties and is shown graphically in Figure 5.10.

Here probability plots show the mechanical responses as a function of build position, i.e. whether the results come from a tensile bar taken from the top or bottom of the build. The elongation to failure results reveal little difference between the top and bottom of the build. This contrasts with the UTS

results where there are two distinct populations. The tensiles from the top of the deposits have, on average, a higher UTS than those taken from the bottom of the build. However, it should be noted that the difference between the maximum and minimum UTS values across all the tensiles is small when compared to the difference between the maximum and minimum elongation values. Therefore, although there appears to be a build height effect, the overall size of these deposits is small enough that this has a limited effect on the UTS values. For larger deposits, this build height effect may become more significant.

In the case of 0.2% yield stress, the overall difference in average value is small enough to be negligible even though there does appear to be a slight difference between the data sets especially at low yield stress values. Much like the UTS results, the difference between maximum and minimum 0.2% yield stress values is not as significant as elongation to failure. It is interesting to note that the bottom tensiles appear to have two separate populations which is not true of the top tensiles. Four builds show low yield stress values and six show much larger yield stress values, with no builds in-between. The four with the lowest yield stress were deposited with the highest energy densities. The remaining six were deposited using either the mid or low energy density. Since yield stress is mostly affected by microstructure, it suggests that the difference between high and mid/low energy density has had a significant effect on the microstructure (as discussed in Chapter 4). The difference between the mid and low energy density regimes has little to no effect on the mechanical properties (and hence the microstructure) as shown in Figure 7.6.

Generally, it might be expected that that the bottom of the build would have slightly finer microstructure on average and hence result in higher UTS or 0.2% yield stress results. As discussed in Chapter 4, there is not a significant difference between the top and bottom of the build and as a result there is not a large difference in the mechanical properties. The position on the build from where the tensiles were taken does not appear to have had a significant effect on the mechanical properties. Again, this is most likely due to the size of the deposits which were only 30mm in height. For larger builds, there is a bigger difference in build conditions, between the top and bottom of the deposit which can have an effect on factors such as the cooling rate. This may lead to a more significant difference in mechanical properties between the top and bottom of a build.

Effect of process parameters on properties of Ti-6246 DLD

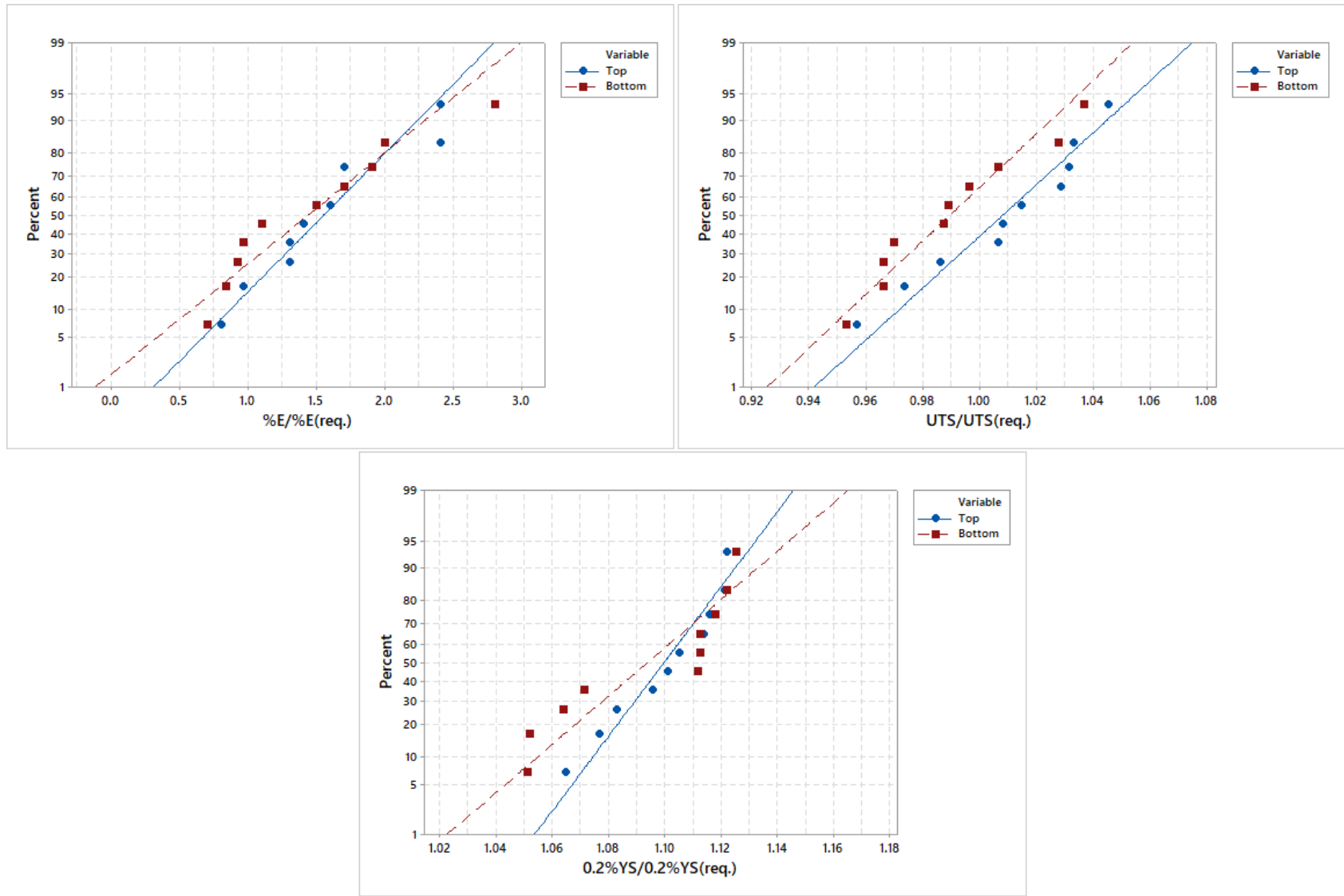


Figure 5.10: Probability plots showing the elongation to failure, 0.2% yield stress and UTS results as a function of build position

5.3.8 Microstructural effects on mechanical properties

There is a known relationship between the size of a materials microstructure and the strength of the material. This is known as the Hall-Petch relationship [127] and it is well-documented for conventionally processed materials such as those that have been wrought or cast. For titanium, the size of the alpha-phase has a measurable effect on the strength of the material and obeys the Hall-Petch relationship [128] (see Eq. 17). The Hall-Petch equation is given below where σ_y is the yield stress, σ_0 is a material constant and an indication of lattice resistance to dislocation motion, k_y is another material constant known as the strengthening coefficient and d is the size of the microstructural feature.

$$\sigma_y = \sigma_0 + \frac{k_y}{\sqrt{d}} \quad (17)$$

Xu et al (2015) [129] collated Hall-Petch data for Ti-6Al-4V (fabricated using SLM, EBM and conventional methods). The authors found that the relationship between yield strength and the inverse square root of the α -lath widths was mostly followed the Hall-Petch relationship. Although, as noted by Yang and Liu (2016) [130], this relationship does not always hold for dual-phase materials. However, the average α -lath width for each specimen was measured, and the inverse square root of the α -lath widths were plotted against the yield stress results for DLD Ti-6246 to reveal any possible relationship. The results are shown in Figure 5.11, where the finer microstructures (higher $(\alpha_{\text{lathwidth}}/\alpha_{\text{lathwidthmax}})^{-1/2}$ value) generally result in a greater 0.2% yield stress value. This shows that the Hall-Petch relationship still somewhat holds even for a two-phase alloy produced using DLD.

Effect of process parameters on properties of Ti-6246 DLD

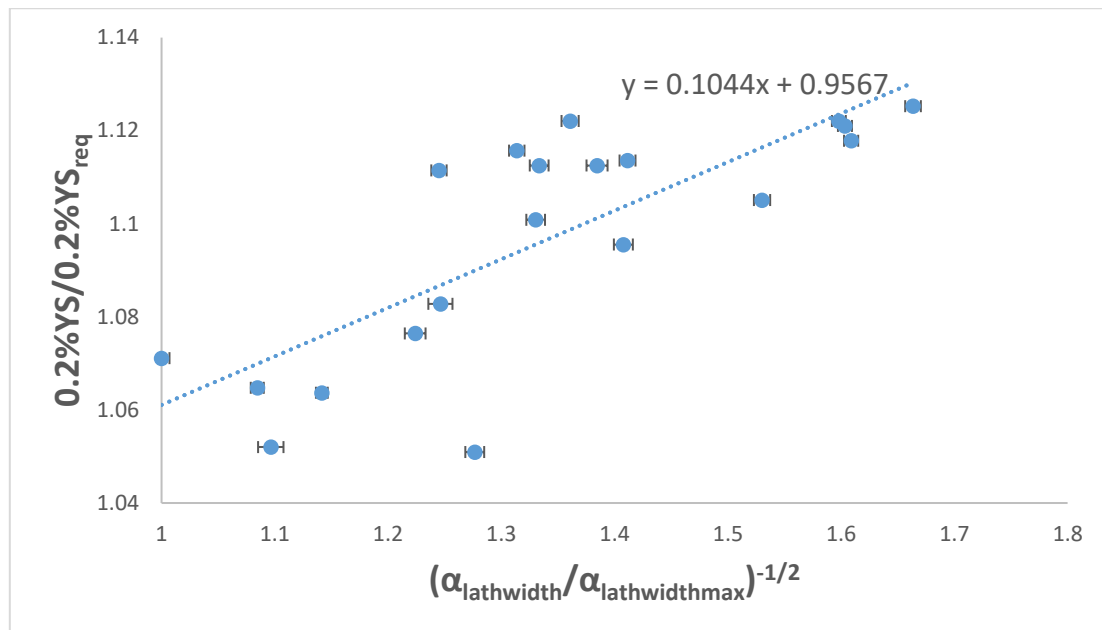


Figure 5.11: Hall-Petch type graph showing relationship between the inverse square root of the alpha lath widths and the 0.2% yield stress for Ti-6246 DLD

Using the Hall-Petch relationship and putting in terms of units, the strengthening coefficient k_y was found to be 2.71 MPa mm^{0.5} (0.0858 MPa m^{0.5}). There is not much data in literature with which to compare this to other than a value of 12.7 MPa mm^{0.5} for α -Ti [131], which is 4.5x that calculated using the DLD Ti-6246 tensile data. The most obvious difference being that Ti-6246 is a two-phase alloy, and the addition of the β -phase, which has a lower strength than the α -phase may reduce the overall strength and hence the value of k_y . Work undertaken by Semiatin and Bieler (2001) [128] gave values for the strengthening coefficient of Ti-6Al-4V between 0.02-0.05 MPa m^{0.5} which is much closer to the value calculated from Figure 5.11. This would be expected as Ti-6Al-4V also contains both α and β phase. The slightly higher value determined for Ti-6246 in this work is likely due to the finer α laths produced from DLD compared to the conventionally produced Ti-6Al-4V in the Semiatin and Bieler study.

It should be noted that the Hall-Petch relationship is mainly used for larger microstructures, the DLD microstructure is almost exclusively <1 μ m. So although the data appears to follow the same sort of relationship described by the Hall-Petch relationship, where small microstructures lead to higher strengths, the exact relationship is different.

Ghamarian et al (2016) [132] and Hayes et al (2017) [133] noted this discrepancy and developed an equation that takes into account additional factors such as solid solution strengthening, Taylor hardening and the effect of texture. They found that the contribution of the Hall-Petch effect due to the α -laths was less than 10%. The most important microstructural contribution was Taylor hardening, although this only held true when the α -laths were fine enough for this effect to occur. Additional importance is placed upon the volume fractions of the different phases and modes, such as α -laths and equiaxed α in the case of Ti-6Al-4V that was the focus of the study.

5.4 Conclusions

A 2-level factorial with two factors was set up using statistical software package MiniTab in order to assess the relationship between process inputs $1/h^*$ and q^*/v^*l^* and critical responses. The three responses analysed were the 0.2% yield stress, ultimate tensile stress (UTS) and elongation to failure (%E). Linear regression was used to fit the responses to the process inputs and in the case of 0.2% YS and %E, the models were found to be statistically significant. In both of these cases, it was q^*/v^*l^* which was the dominant factor and not $1/h^*$. Since the laser power and layer height were both kept constant throughout the DoE this means that laser velocity was found to influence the mechanical responses more than the hatch spacing. The response surfaces produced showed that there is a compromise to be made between maximising the 0.2% YS and the %E. Increasing q^*/v^*l^* (decreasing laser velocity) results in a decrease in the 0.2% YS and also the UTS. Conversely, decreasing q^*/v^*l^* decreases the %E. However, it should be noted that for the current process window, all of the tensile specimens met the minimum requirement for repair. Further optimisation of the process could be achieved by reducing q^*/v^*l^* slightly which could potentially reduce the cost of the process by reducing energy consumption. Alternatively, the hatch spacing could be increased which would speed up the process since fewer tracks would be required per layer.

It was also found that there was quite a variation in the tensile build results even between specimens deposited with the same parameters. However, this variation was also found to be present in the non-DLD forged specimens meaning that this variation is not necessarily unique to the DLD process. In the case of UTS, it is possible that this variation arises due to differences in build height. Specimens taken from the top of the build had on average a higher UTS value and hence more likely to meet minimum requirements. However, the other responses did not seem to be as affected by build height, at least for builds of this size.

Effect of process parameters on properties of Ti-6246 DLD

The relationship between microstructure and mechanical was also quantified using the inverse square root of the lath widths and the 0.2% YS which is analogous to the Hall-Petch relationship. It was found that as the size of the alpha laths decreased the yield stress increased linearly. This also allowed for a calculation of the strengthening coefficient k_y for Ti-6246. A value of $0.0858 \text{ MPa m}^{0.5}$ was determined and although a value for Ti-6246 could not be found in literature it is the same order of magnitude as that for Ti-6Al-4V of $0.02\text{-}0.05 \text{ MPa m}^{0.5}$ which could be found in literature.

6 Modelling the DLD process

6.1 Introduction

Modelling the DLD process is complex because of the multiple different length scales that can be considered [134]. For example, a micro-scale approach such as phase-field (PF) simulations can be used to model solid and liquid phases within a material as well as predict solidification microstructure. An example is Fallah et al (2012) [135] who used PF simulation to model dendritic growth across the solid-liquid interface during deposition of a Ti-Nb alloy. Such models can be highly accurate and can be applied to different materials and processes. However, they can be extremely complex and computationally expensive which limits the size of the model to only a few dendrites at most. In addition, they are limited to binary alloys only, which is not suitable for Ti-6246.

Other models such as those that use the Monte Carlo method or Cellular Automata are meso-scale models and predict material behaviour on a granular level. Application of these models to predict grain size has proven successful when compared against experimental results [136]. However, the models are limited when applied to AM processes. One of the failings is not fully capturing the effects of nucleation and hence may only predict formation and growth of columnar and not equiaxed grains. Such models may be suitable for welding or laser cladding [136] where only one layer is deposited. A different approach is required for more complex processes with multiple layers and thermal cycles.

The third length-scale incorporates the macro-scale models, which generally focus on the thermal field created by the laser (or electron beam) during the deposition process. The model developed during this work and described here in Chapter 6 is such a model. These macro thermal models often use either computational fluid dynamics (CFD) or finite element modelling (FEM) to provide information about the temperature field or cooling rate for example. Most of these models are fundamentally based on the work by Rosenthal for a point-heat source or Gaussian profile which are described below.

Baykasoglu et al (2018) [98] for example, have created a 3-D FE model for the LENS process (analogous to DLD). This model, much like the one discussed in this chapter, has been validated against experimental results. It differs, in that average α -lath width measurements from the build cross-sections are used as the validation method instead of melt pool depths. As was discussed in Chapter 4, the average lath width can be skewed heavily by the large range in lath sizes present in the same build. The authors have not addressed this issue which may have implications when trying to assess the influence of process parameters on microstructure or mechanical properties.

Modelling the DLD process

Kelly and Kampe (2004)[101] developed a two dimensional thermal model for thin wall deposition using Ti-6Al-4V. This model, therefore has a number of similarities to the work presented in this chapter. However, the authors limited their model to exploring the effect of laser traverse speed on the thermal properties of the build, in comparison to the model developed here for Rolls-Royce, which is adapted for normalised parameters so that it may be applied to different systems. In addition, Kelly and Kampe have not included a distributed heat-source (e.g. Gaussian) within their model which limits the accuracy of the results. The results themselves are mostly qualitative not quantitative and were only compared but not directly validated against experimental results.

Picasso et al (1994) [87] also used thermal modelling to determine the size of the melt pool during laser cladding. This model takes a different approach to most, as the thermal field aspect is coupled with a model for powder addition. However, unlike the model developed here for Rolls-Royce, Picasso et al only used the model to quantify power attenuation and did not explore the implications this might have on material properties or on an optimised process window.

Two thermal models were developed as part of this work to determine effects of the laser beam during the DLD process. Modelling the process in this way is useful to Rolls-Royce because it provides a straightforward way of testing and visualising the effects that altering process parameters has during deposition. Importantly, this model is validated directly with a build that is representative of the process and geometry of the commercial application in question. This distinguishes it from most models found in literature (micro, meso and macro) that do not consider any specific real-world application.

This model also works alongside the Design of Experiments approach to reduce the number of trials that need to be performed to define an optimal process window. In addition, this does not have to be limited to the current process space being investigated or the same alloy. This in turn reduces the amount of cost and resources to develop a deposition strategy for new alloys such as Ti-6246. The model discussed here and in Chapter 7 is also used to help quantify links between process parameters, microstructure and mechanical properties.

As discussed in section 2.5, there are many approaches to this. The following section details the methodologies used for the purposes of this research. The modelling work was performed using MATLAB™ and the code is given in Appendix D: MATLAB code.

The first approach was to treat the laser as a point heat-source in accordance with the work by Rosenthal [89] and used Eq. 18 below. Here q is the laser power (W), k the thermal conductivity (Wm^{-1})

Modelling the DLD process

$^1\text{K}^{-1}$), v the laser velocity (ms^{-1}), α the thermal diffusivity (m^2s^{-1}) and r is defined as $\sqrt{x^2 + y^2 + z^2}$ where x , y and z are positions with respect to the laser beam in Cartesian co-ordinates.

$$\Delta T = \frac{nq}{2\pi kr} e^{-\frac{v(x+r)}{2\alpha}} \quad (18)$$

The second model treats the laser beam as a Gaussian heat source, meaning that the radius of the laser is now taken into account. The temperature field is calculated using Eq. 19 [95].

$$\Delta T = \left[\frac{nq}{2\pi kv\sqrt{t(t+t_0)}} e^{-\frac{1}{4\alpha}\left(\frac{(z+z_0)^2}{t} + \frac{y^2}{t+t_0}\right)} \right] \quad (19)$$

Here there is the addition of t which is time (s), t_0 the heat flow time constant (s) defined as $r_b^2/4\alpha$, and characteristic length, z_0 (m).

Common to both equations is n which is normally defined as the absorption coefficient and is material dependent. However, in the case of the work presented here, n is treated as a fitting parameter to help calibrate the thermal model predictions with experimental results.

In both equations, the thermophysical properties are assumed to be temperature independent. This is common to a lot of similar models and is assumed in this work due to a lack of information on elevated temperature properties of Ti-6246 as well as lack of data on build temperature during DLD. However, since the models are calibrated against real builds, the effect the temperature has on the values of k and α is captured by “ n ” the fitting parameter.

Both the microstructural and mechanical properties of DLD builds are largely determined by the solidification conditions they have been subjected to. These conditions, are in turn, influenced by the process parameters used during the deposition of the builds. There are many studies that involve complex finite element modelling of the process in order to explain microstructural evolution and mechanical properties such as hardness and UTS with respect to specific processing conditions. However, these require a substantial amount of computational power and time to run, and the set-up of such models means that it may not always be easy or practical to change aspects of the model.

Modelling the DLD process

The purpose of the models described in this chapter is to provide an efficient and more straightforward way of exploring the effects of changing DLD process parameters. This can then be used to help predict the mechanical response to the process window. The approach taken here provides an easy route of adaptation for materials other than Ti-6246 making this a versatile model.

6.2 Calibration build deposition

As discussed in section 2.5, the parameter “ n ” in Eq. 5 is typically described as a measure of the absorptivity of the material, but for the purposes of this model it is being used as a calibration parameter. To determine the value of n , the melt pool depth (where $T=T_m$) predicted by the model was compared to a Ti-6246 DLD build. The build geometry was comparable to that of an IP compressor aerofoil blade.

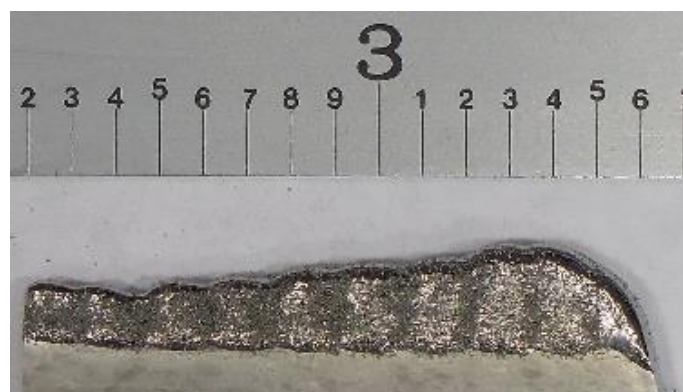
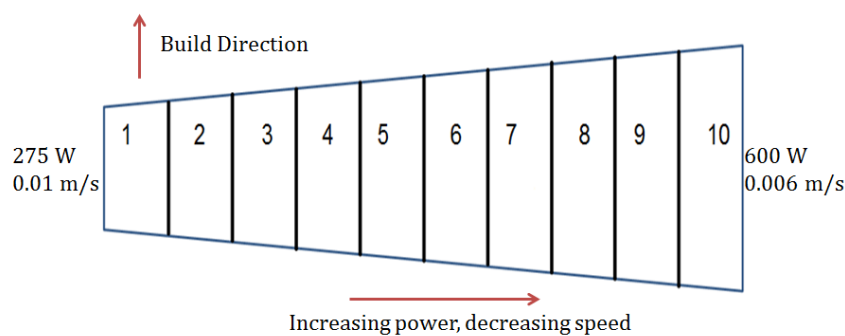


Figure 6.1: Schematic (top) of the different process input parameter sets for the deposition of the aerofoil-type build (bottom) used to calibrate both the Rosenthal and Gaussian heat source models. Note the scale is in inches for the bottom image.

The build was deposited with the RPM 557 and both the power and the velocity of the beam were varied along the length of the build as shown in Figure 6.3 . The resulting build was a combination of ten different line energy densities (q/v), with the final beam power and velocity having the nominal values of 600W and 5.9mms⁻¹ respectively. The line energy densities used during the deposition are given in Table 6.1.

Table 6.1: Build parameters used for the deposition of the aerofoil thin build

Process set	Line energy density [Jm⁻¹]
1	25000
2	32353
3	40860
4	48276
5	57500
6	66447
7	75000
8	83088
9	91406
10	101695

6.2.1 Optical microscopy of calibration build

The build was then prepared by sectioning and cold mounting ready for optical microscopy. The depth of the last laser pass was imaged using an Olympus BX-51 optical microscope as shown in Figure 6.2.

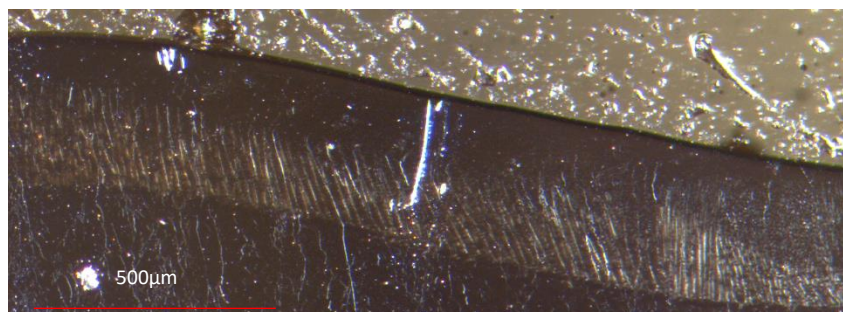


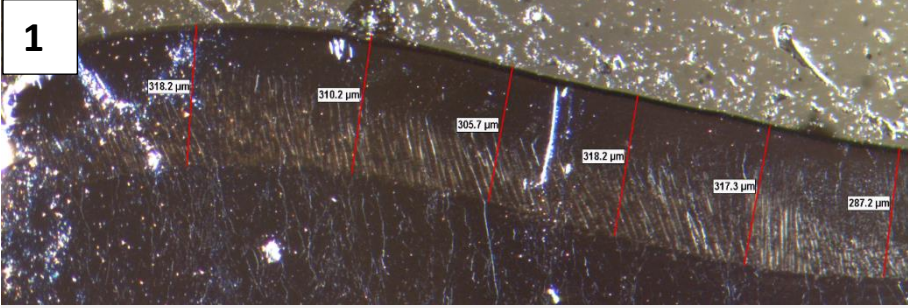
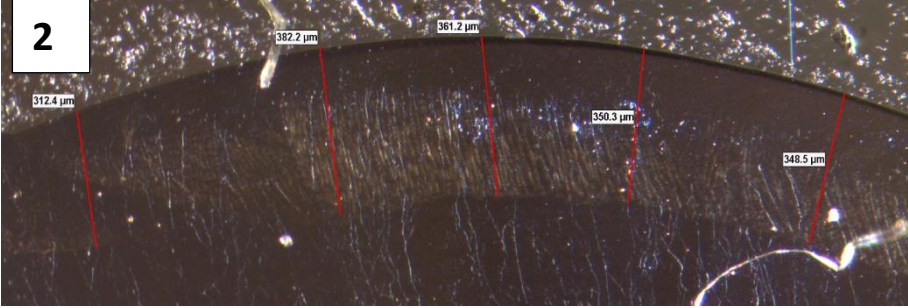
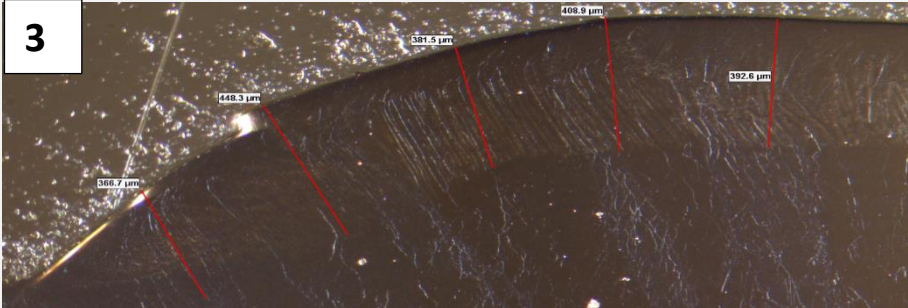
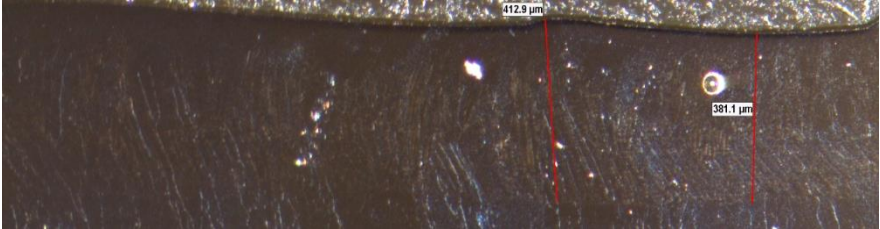
Figure 6.2: Optical image of top section of the Ti-6-2-4-6 MA aerofoil-type build showing the last laser pass

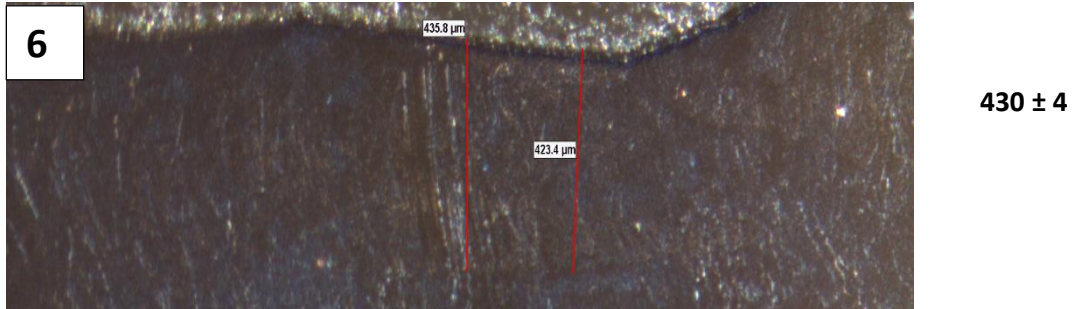
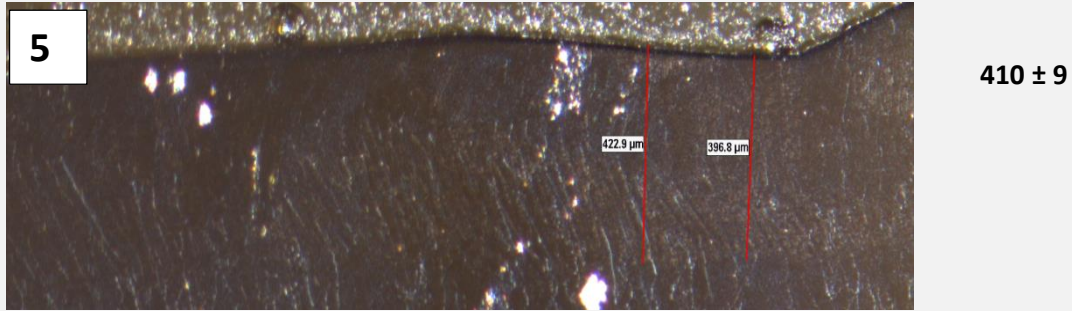
Modelling the DLD process

Multiple measurements of the melt depth were recorded for each parameter set in order to determine an average depth for each. This was achieved using the manual measurement tool in the image analysis software package, CLEMEX. Measurements were only possible for the first six parameter sets since the last four did not have clearly defined melt tracks that were suitable for measurement. Table 6.2 shows the optical micrographs for the first six parameter sets from the build that were used to calculate an average value for the maximum melt depth.

Modelling the DLD process

Table 6.2: Optical microscopy images of the aerofoil-type build with measurements of the depth of the melt pool generated by the last laser pass

Parameter Set	Average melt depth [μm]
	309 ± 6
	354 ± 14
	392 ± 14
	414 ± 16



6.2.2 Determining value of calibration factor “n”

Since parameter set 1 of the calibration build had the most clearly defined melt depth, this was used to determine the value of n in equations 4 and 5. The average depth for this parameter set was 309 μm and n was adjusted until the melt depth predicted by each model was in agreement with this. This resulted in n having values of 0.14 and 0.85 for the Rosenthal and Gaussian approaches respectively. Table 6.3 shows the comparison between melt depth predictions from the two thermal models and the experimentally determined depths using $n=0.14$ and $n=0.85$.

Modelling the DLD process

Table 6.3: Comparison between predicted and measured values for maximum melt pool depth for a Ti-6246 DLD build

Parameter Set	Rosenthal predicted depth [μm]	Gaussian predicted depth [μm]	Measured depth [μm]	Difference between predicted and measured [μm]
1	306	308	309 ± 6	1
2	356	343	354 ± 14	11
3	406	375	392 ± 14	17
4	444	401	414 ± 16	13
5	484	427	410 ± 9	17
6	526	450	430 ± 4	20

The absorptivity of Ti-6246 is not readily available in literature, however the absorptivity of Ti-6Al-4V is quoted as being between 0.39 and 0.51 depending on laser power and the presence of powder or not [137]. The low n value for the Rosenthal model is likely due to the large correction required from the temperature field tending to infinity at the laser centre.

6.3 Eagar & Tsai “Rosenthal” model

One of the methods of modelling the laser beam and its associated temperature field is to assume that the laser can effectively be modelled as a point heat-source. There is a large amount of literature detailing the methodologies behind this as discussed in section 2.5. However, the initial model developed as part of this work was based upon the solution to the semi-infinite Rosenthal equation [88] which is shown in Eq. 20.

$$\Delta T = \frac{n q}{2\pi k r} e^{-\frac{v(x+r)}{2\alpha}} \quad (20)$$

Modelling the DLD process

Here the change in temperature (ΔT) effected by the laser can be calculated from the thermophysical properties of the material the laser is incident upon. Table 1 lists the different variables required for the semi-infinite Rosenthal equation alongside their corresponding symbols from Eq. 20.

Table 6.4: List of parameters used in the semi-infinite Rosenthal equation

Symbol	Parameter/Description
T	Temperature [K]
n	Calibration factor
q	Laser power [W]
k	Thermal conductivity [$\text{Wm}^{-1}\text{K}^{-1}$]
r	Position in Cartesian co-ordinates [m], $\sqrt{x^2 + y^2 + z^2}$
v	Laser beam velocity [ms^{-1}]
x, y, z	Position in Cartesian co-ordinates [m]
α	Thermal diffusivity [m^2s^{-1}]

Both the thermal conductivity and the thermal diffusivity are material dependent and for Ti-6246 have the values of $7.7 \text{ Wm}^{-1}\text{K}^{-1}$ and $3.31 \times 10^{-6} \text{ m}^2\text{s}^{-1}$ respectively. Unlike the thermal conductivity, the thermal diffusivity was not available in literature for Ti-6246 but was instead calculated using Eq. 21.

$$\alpha = \frac{k}{\rho c_p} \quad (21)$$

The density (ρ) of Ti-6246 was taken to be 4650 kgm^{-3} and the specific heat capacity (c_p) was taken to be $500 \text{ Jkg}^{-1}\text{K}^{-1}$.

The laser power (q) and laser beam velocity (v) are process inputs that can be varied for each deposition, and x and r are the position with respect to the laser beam centre in Cartesian co-ordinates where r is $\sqrt{x^2 + y^2 + z^2}$. For simplicity, a 2-D model is being used so y is assumed to be 0 throughout.

6.3.1 Calibration results

From the calibration build, it was found that an n-value of 0.14 gave a reasonable fit to experimentally determined melt depth results, and this value is used for the work that follows. Figure 6.3 shows the predictions of melt depths made by the model compared to values obtained experimentally.

Modelling the DLD process

Parameter set 1 (see section 3.3) has the lowest energy density (Jm^{-1}) – here defined as q/v and parameter set 6 has the highest energy density (66278 Jm^{-1}). The first data point (lowest energy density) was used for calibration to determine a value of 0.14 for n , which was then assumed to be constant as the energy density of the builds increased.

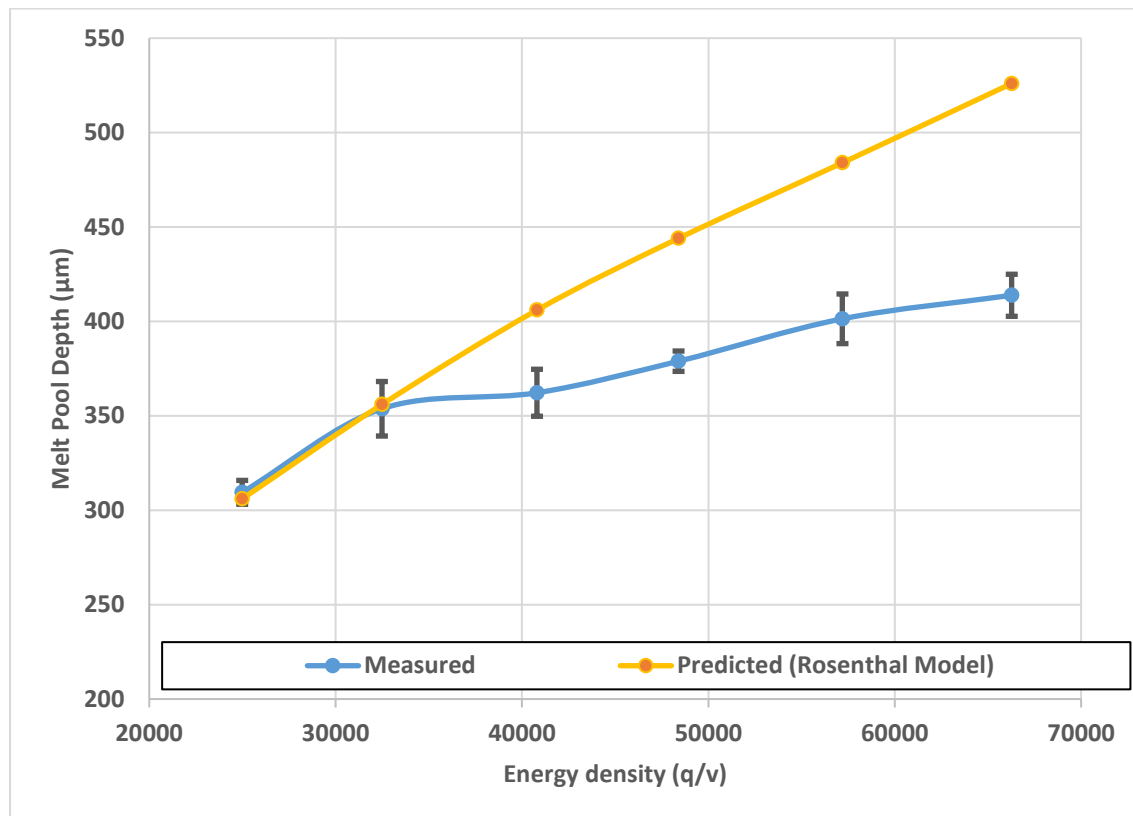


Figure 6.3: Comparison between experimentally measured melt depths for a Ti-6246 DLD build compared to predictions made by the Rosenthal thermal model with $n=0.14$

For a constant value of n , the Rosenthal model is in good agreement with experimental results for the four lowest energy density builds, with a maximum deviation of $30\mu\text{m}$. However, the model continues to predict ever deeper melt depths where experimental results show the depths plateau. The difference between predicted and measured melt depth for $(q/v)=66278\text{Jm}^{-1}$ is $96\mu\text{m}$ which is small compared to the size of the measured melt pool at 22% of the observed melt depth. Therefore, the Rosenthal model is still a reasonable fit in terms of the absolute depth of the melt pool but it does not take into account the slight plateau. As the energy density increases beyond approximately 67000Jm^{-1} , the discrepancy between model and experiment becomes more significant. This lack of agreement at higher energy densities may be as a result of calibrating the model against low energy density using

Modelling the DLD process

the Rosenthal equation which predicts an ever increasing melt pool depth. Therefore moving to higher energy density regimes means the calibration value becomes less realistic as in reality the depth of the melt pool does not appear to increase at the same rate. Additionally, the accuracy of the experimental measurements of the melt depths worsens as the energy density increases, as more of the previously deposited material is melted and distorts the shape of the last melt track. This makes it impossible to locate the bottom of the melt pool in some instances with any degree of confidence as shown in Figure 6.4.

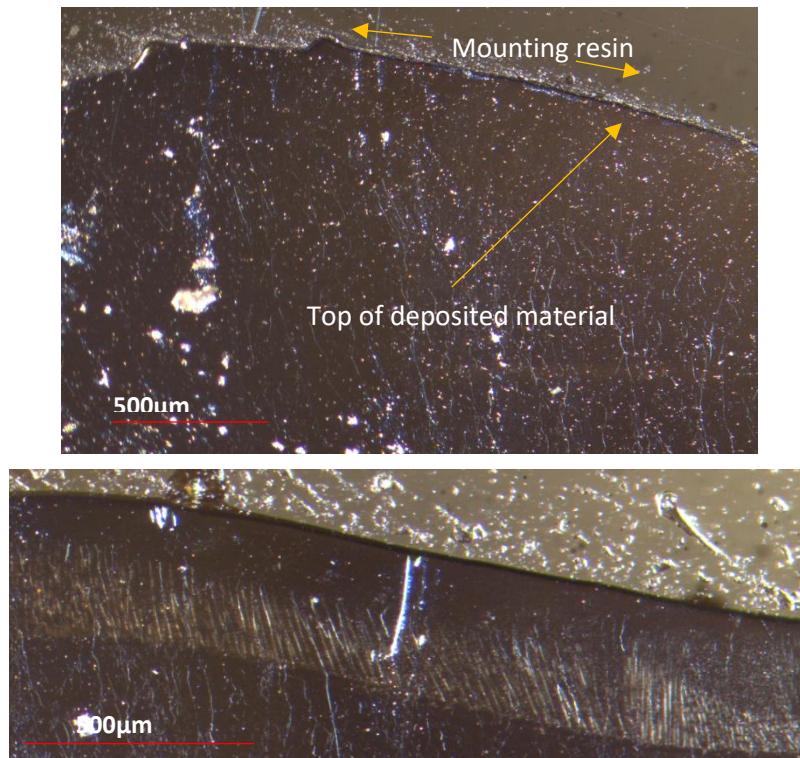


Figure 6.4: Optical micrograph of the top of calibration build deposited using an energy density of 101245 Jm^{-1} (top) and 24987 Jm^{-1} (bottom)

A possible solution would be to calibrate the model for each energy density. However, the increasing difficulty of defining the bottom of the melt pool may result in an inaccurate value for the calibration factor and may have no benefit over assuming a constant value over all energy input regimes.

6.3.2 Effects of process parameters

The temperature profile of a point heat-source type laser was produced in MATLAB™ using eq. 1 and a top-down view (x-y plane) is shown in . A side on view (x-z plane) is shown in Figure 6.6. Here the

Modelling the DLD process

laser beam is centred at (0,0) and is moving in the positive x-direction. The inner black line is the $T=T_m$ isotherm where T_m for Ti-6246 is 1948K. The outer black line is the β -transus isotherm at 1207K.

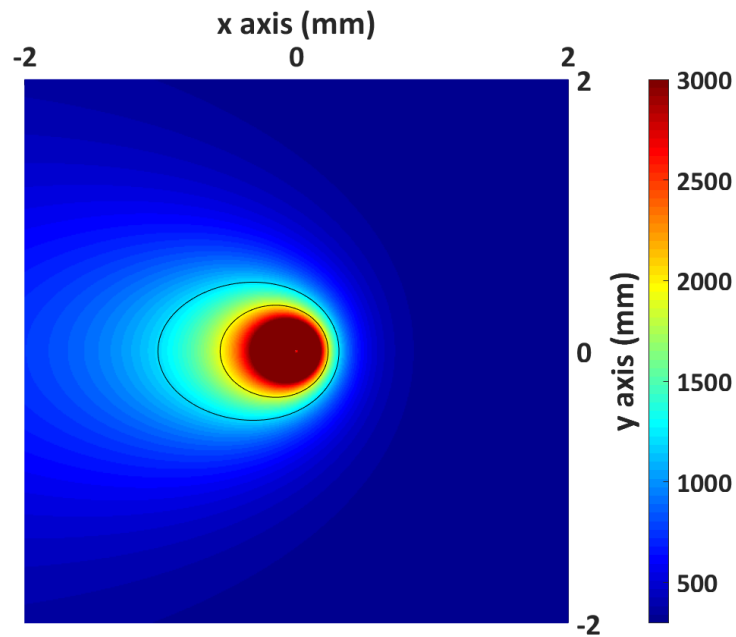


Figure 6.5: Temperature field generated by a point-heat source in the x-y plane. Laser centre at (0,0) moving in the positive x-direction. Laser power (q) – 400W, laser velocity (v) – 0.01ms⁻¹

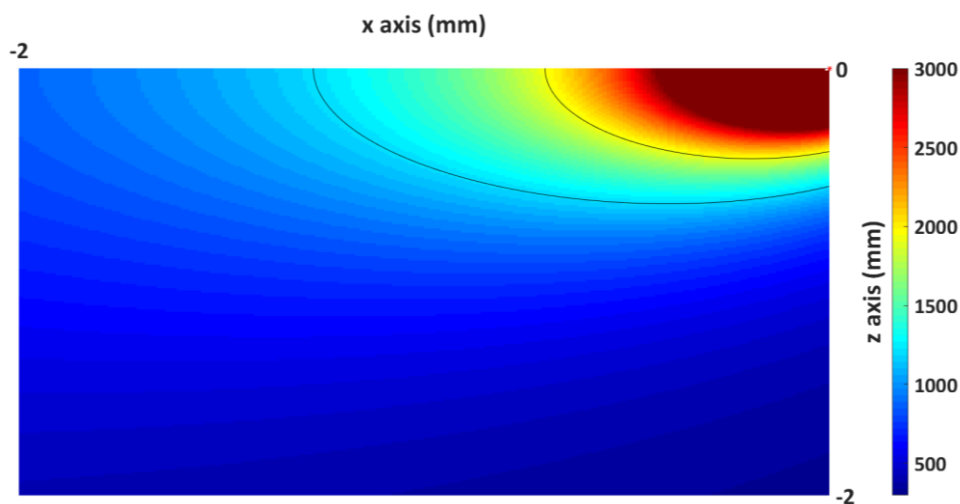


Figure 6.6: Temperature fields generated by the laser beam in the x-z plane. Laser beam moving in the positive x-direction. Laser power (q) – 400W, laser velocity (v) – 0.01ms⁻¹

The area bound by the inner line is above the melting temperature of Ti-6246 and hence is assumed to be liquid. Everything that is not bound by this isotherm is assumed to be below the melting temperature and hence not part of the melt pool. As can be seen in , the melt pool is stretched out

Modelling the DLD process

behind the laser so that the melt pool is oval in shape. Additionally, the temperature field extends in front of the laser beam, although in this case the isotherms become bunched up due to the motion of the laser in this direction. The outer contour line depicted in shows the position of the β -transus temperature of Ti-6246 ($T=1207\text{K}$). Although material in between the two contour lines is not part of the main melt pool, the temperature is above the β -transus and the extent of this area is still important in understand solidification microstructure. As the material cools below the β -transus it undergoes a transformation to α -phase. The position of this contour line with respect to depth below the material surface (see z-axis in Figure 6.6) is important since this reveals how much of the previously deposited material experiences multiple heating cycles above the β -transus temperature. This has an impact on the final pre-transformation microstructure of the MA build and hence has an effect on its mechanical properties.

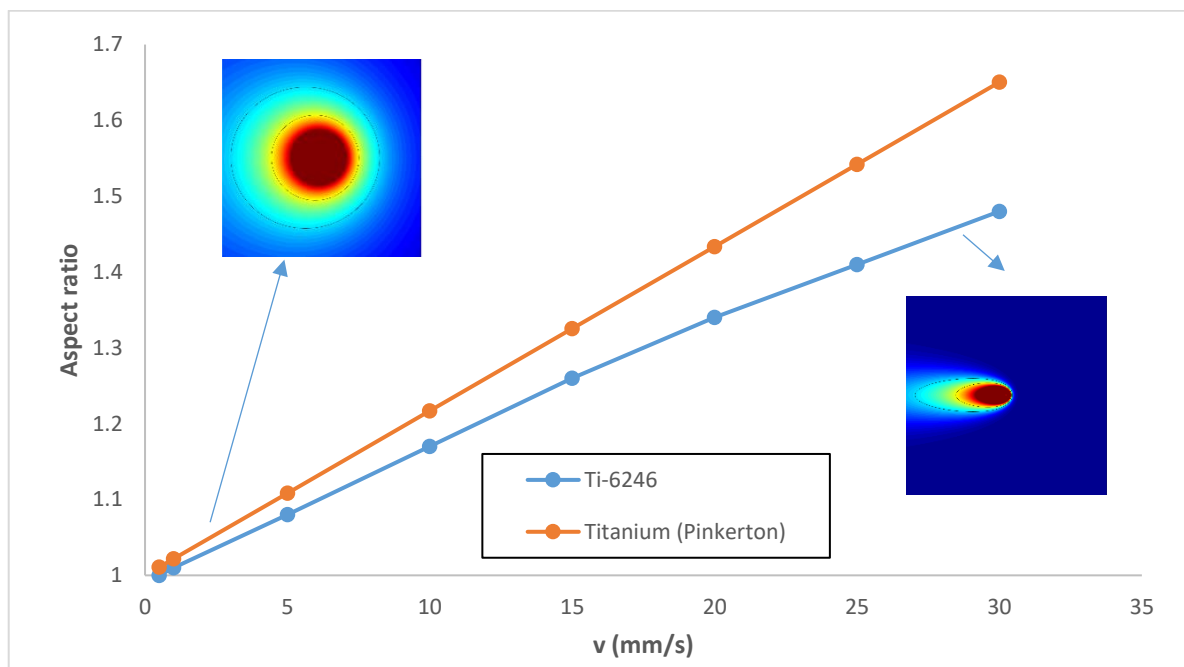


Figure 6.7: Relationship between the aspect ratio of the melt pool and the velocity of the laser beam

The aspect ratio of the melt pool as a function of laser velocity is shown in Figure 6.7. At low velocities the width and the length of the melt pool is almost equal, resulting in an almost circular melt pool with an aspect ratio of approximately 1. As the laser velocity increases, the shape of the melt pool becomes elongated. Although this increases the aspect ratio of the melt pool, the overall length of the melt pool remains fairly constant as the isotherms ahead of the beam become compressed. The aspect ratios for Ti-6246 DLD shown in Figure 6.7 are compared to predictions by Pinkerton and Li [86] for

Modelling the DLD process

titanium derived using Eq. 22 D and E are constants with values of 0.057 and -1.12 respectively, Q is the laser power and v is the laser velocity.

$$\textit{Aspect ratio} = 1 + (DQ + E)v \quad (22)$$

The aspect ratios are in reasonable agreement at lower beam velocities with the discrepancy likely coming from the differences in thermophysical properties such as melting temperature and thermal conductivity between Ti-6246 and pure titanium. The predictions of titanium using Eq. 22 give a higher aspect ratio for all beam velocities, meaning that the melt pool is more elongated than for Ti-6246.

Since Eq. 22 treats the y and z direction the same, it is simple to change the plane of the melt pool to the x-z plane as shown in Figure 6.6. The laser beam is still travelling in the positive x-direction but the other axis now indicates depth below the material surface.

As can be seen from Figure 6.5 and Figure 6.6, the material directly surrounding the laser beam is at a maximum temperature (as decided by the temperature scale) but quickly decays as a function of distance from the laser beam in both the y and z directions. This can be shown graphically as in Figure 6.8 where the temperature is plotted as a function of distance from the laser centre (x=0) in both the y and z directions. As can be seen, the top surface and the next section down, the maximum temperature is extremely high and is unrealistic for the DLD process. However, the temperature rapidly decreases to below the melting temperature (1948K) in 0.25mm. The maximum temperature and the area it extends over is largely dependent upon the process parameters being considered.

Modelling the DLD process

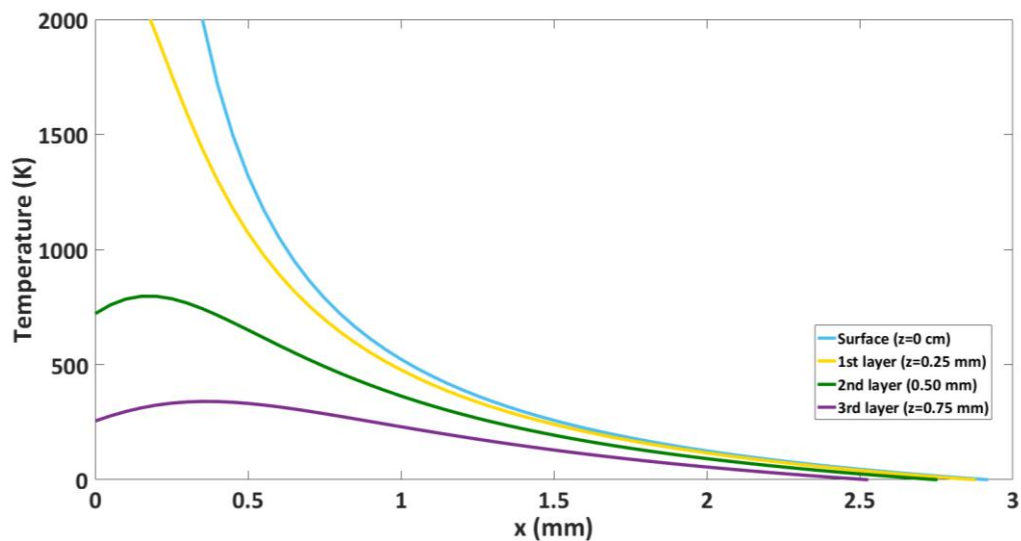


Figure 6.8: Temperature distribution as a function of transverse (y) distance from laser centre for a range of depths (z)

As mentioned previously, the depth of the β -transus contour can be measured as well as the actual melt pool depth. The melt pool depths and β -transus depths as a function of beam velocity is shown in Figure 6.9. As the beam velocity increases, the depth of these two regions decreases since the line energy density (q/v) decreases meaning that less power is incident on the material surface per unit length.

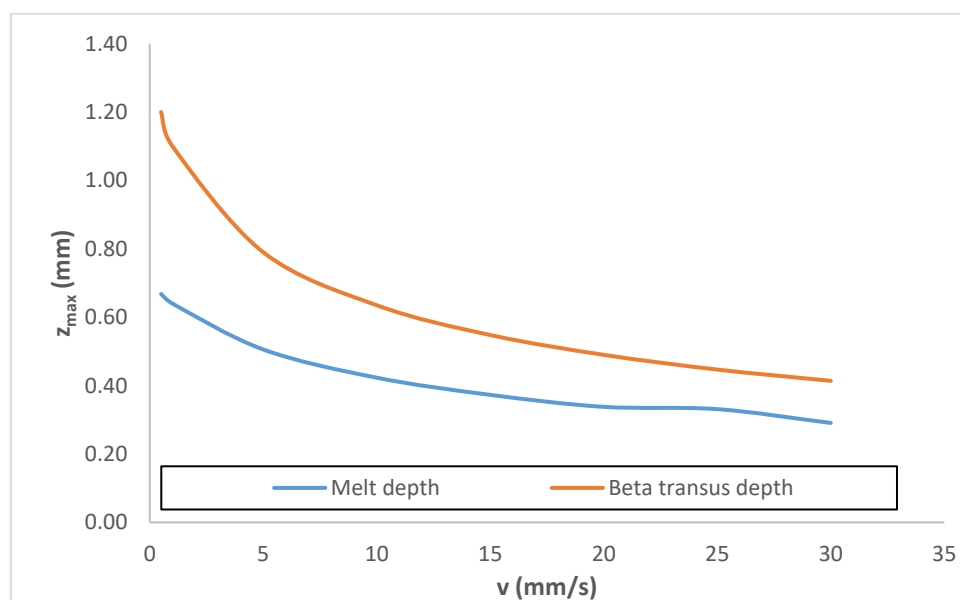


Figure 6.9: Relationship between melt pool depth (blue) and beta transus depth (orange) and beam velocity for constant laser power

6.3.3 Cooling rates

As well as calculating the temperature field, an estimation of the cooling rates can be determined using Eq. 23 [85], which is simply the time derivative of the expression in Eq. 22.

$$\frac{\delta T}{\delta t} = -v \left[\frac{x}{R^2} + \frac{v}{2\alpha} \left(1 + \frac{x}{R} \right) \right] T \quad (23)$$

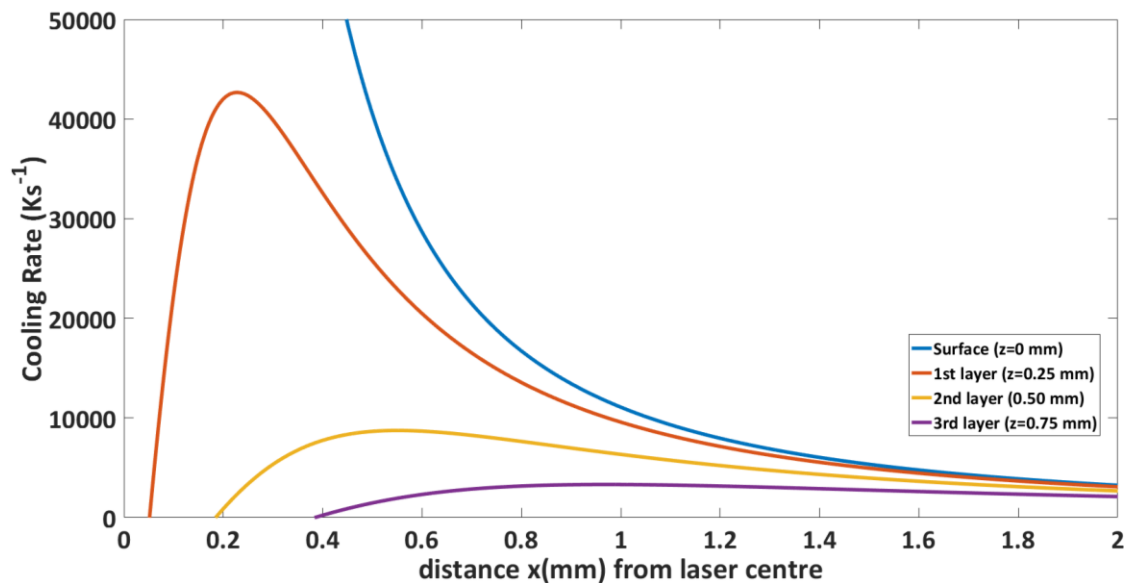


Figure 6.10: Cooling rates as a function of both depth below the surface (z) and transverse distance from laser centre (x) for the high velocity mini tensile builds

Figure 6.10, the cooling rate has been plotted as a function of distance in x from the laser centre (which is at $x=0$) for a range of depths below the material surface. The values for beam power (q) and beam velocity (v) were taken from the high velocity mini tensile deposits. Here it can be seen that the cooling rates at the surface of the material and in the next layer down are extremely high, but drop rapidly moving away from the laser centre. The peak cooling rate is offset from the laser since material at $x=0$ mm will be undergoing heating not cooling. Figure 6.10 also demonstrates the rapid drop-off in cooling rates for increasing z values. The peak cooling rate for 0.5mm below the surface is around 8000Ks^{-1} which is significant drop from the peak cooling rate of $4.3 \times 10^4 \text{Ks}^{-1}$ at 0.25mm below the surface.

Figure 6.11 shows how the cooling rates change moving along the T_m contour line which defines the outer limits of the melt pool. The cooling rate is 0Ks^{-1} at the bottom of the melt pool since material

Modelling the DLD process

just in front of this region is being heated (so has a negative cooling rate) and material behind this region is cooling. Moving towards the back of the melt pool (increasing x) the cooling rate rises to a maximum of between 0.8 and $1.4 \times 10^4 \text{Ks}^{-1}$ for the three different velocities. The highest beam velocity results in the highest cooling rate at the back of the melt pool, and there is a faster drop off in the cooling rate compared to the slower beam velocities. The significance of this is that the builds deposited using the high beam velocity experience cooling rates almost twice that of the lower velocity builds. This may have a quantifiable effect on the microstructure of these builds.

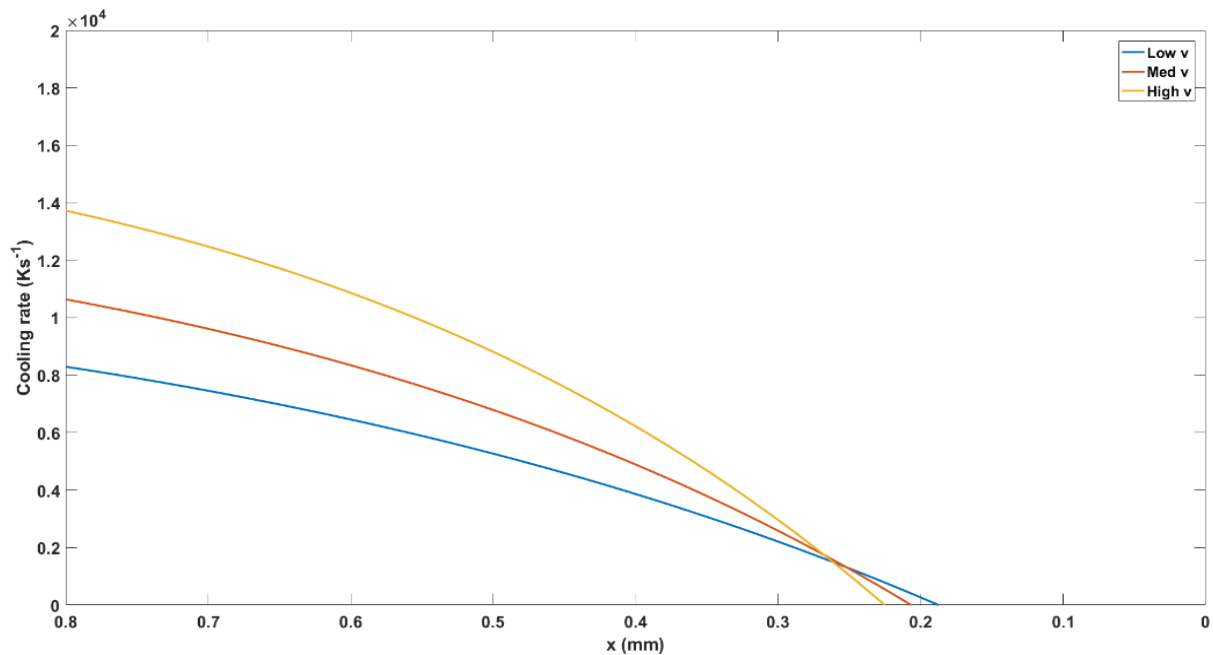


Figure 6.11: Cooling rates along the T_m contour using process parameters for mini tensile builds

6.3.4 Assumptions and limitations of the point heat-source model

The assumption of a constant calibration value is not the only limiting factor of the Rosenthal model. The most apparent limitation is modelling the laser beam as having an infinitely small radius. This causes the predicted temperatures at the laser centre to tend towards infinity, as shown in Figure 6.8.

Another assumption is that the thermophysical properties of Ti-6246 are not temperature dependent. The values for these properties have been taken at room temperature and not at the elevated temperatures that are present during the deposition process since they are not readily reported in literature. Changing these values as a function of temperature has an effect on the size of the melt pool generated by the laser beam. Since the elevated thermophysical properties of Ti-6246 could not

Modelling the DLD process

be established it was not possible to investigate the effect this would have. However, elevated temperature thermophysical properties of Ti-6Al-4V, another common aerospace alloy, are listed in literature and are given in Table 6.5. The effect on the melt pool morphology when changing these parameters is shown in Figure 6.12.

Table 6.5: Thermophysical properties for Ti-6Al-4V at room and elevated temperatures

Thermophysical property	Value at room temperature (298K)	Value at 0.5T_m (~974K)
Thermal conductivity [Wm ⁻¹ K ⁻¹]	6.7	12
Thermal diffusivity [m ² s ⁻¹]	2.88x10 ⁻⁶	3.39x10 ⁻⁶

Modelling the DLD process

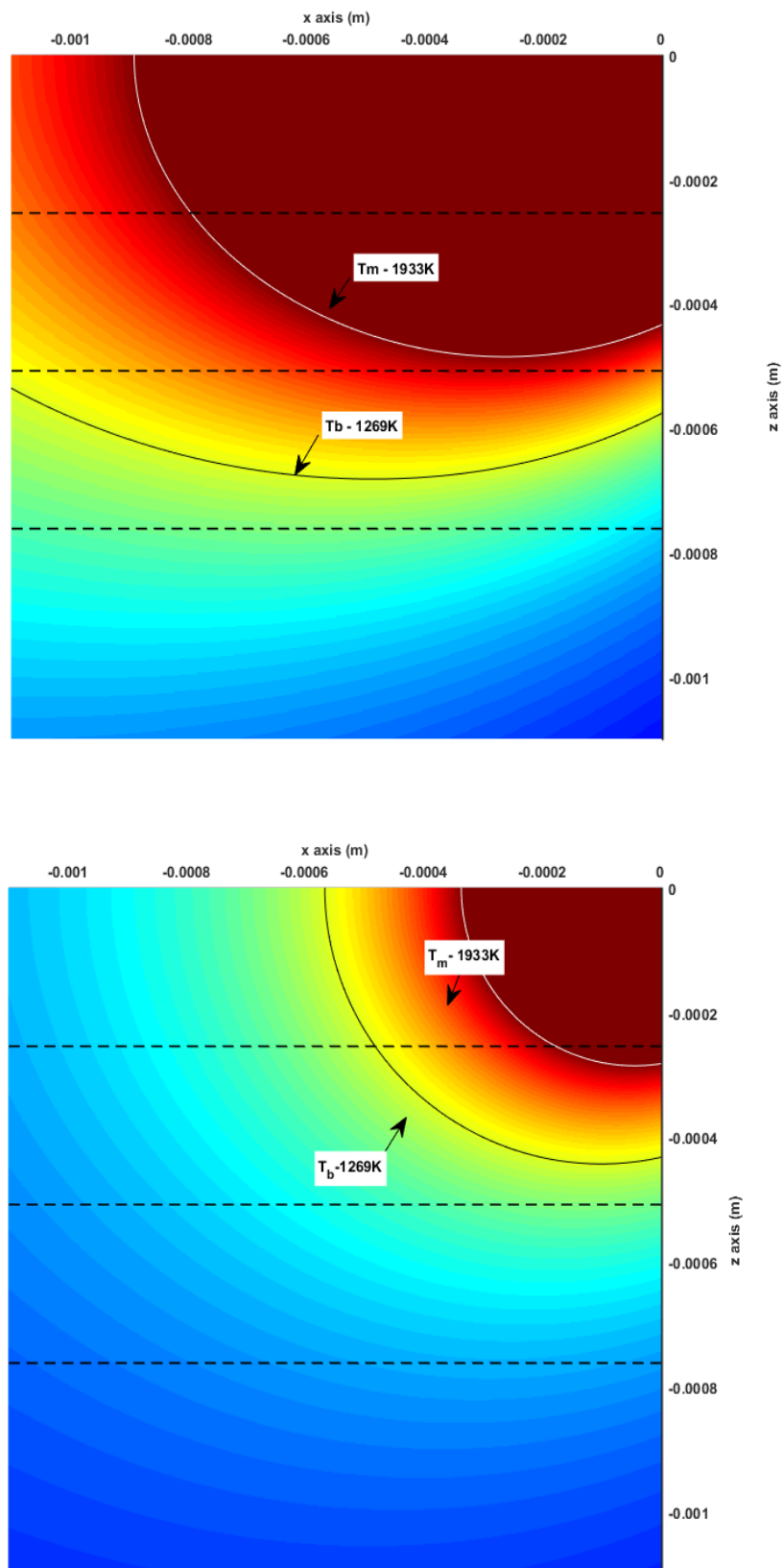


Figure 6.12: Comparison between using room temperature thermophysical properties (top) and elevated temperature properties (bottom) for Ti-6Al-4V

Modelling the DLD process

In Figure 6.12 the laser beam is centred at (0,0) and is moving in the positive x-direction. The inner contour line is the melting temperature isotherm at 1933K, and the outer contour line is the β -transus isotherm at 1269K. The dashed black lines represent previously deposited sequential layers using a typical layer height of 0.254mm.

Using elevated temperature properties results in a decreased melt pool area. Initially when using room temperature values, the melt pool penetrated approximately two of the previously deposited layers. Using elevated temperature properties, the melt pool only penetrates just over one layer. The amount of remelting and number of heating cycles the material undergoes has an effect on the quality of the build as well as the solidification microstructure. Therefore, knowing how far the melt pool penetrates into the workpiece is useful, not just the general relationship between melt depth and process parameters.

The third assumption is that the build temperature (T_0) remains constant throughout the deposition process, realistically, the build temperature will increase with time. At the start of the deposition process the build temperature is approximately at room temperature. However, this will increase rapidly. The initial layers deposited will have high cooling rates due to the substrate acting as a heat sink, keeping the build temperature fairly low. As the substrate heats up as more layers are deposited, the effectiveness of the heat sink will decrease and there will be a rise in the build temperature. Therefore, the assumption of $T_0=298\text{K}$ will only hold for the start of the process. Realistic build temperatures as a function of time during the Ti-6246 deposition process are not known. However, Figure 6.13 shows the difference in melt pool shape for a T_0 value of 298K (room temperature) and at $0.5T_m$ (974K). Here the increase in build temperature causes the melt pool to penetrate further into the build since a higher proportion of the material is above the melting temperature of Ti-6246 (1948K).

Another assumption is that there is no powder being added to the melt pool or interacting with the laser beam (i.e. the powder feed rate (PFR) is 0). Clearly, for the DLD process, powder is introduced to the melt pool which will have an effect on the power incident on the workpiece and on the melt pool itself. This assumption will be addressed in Chapter 7.1

These last three assumptions are not exclusive to the Rosenthal model and are also present in the Gaussian model discussed below.

Modelling the DLD process

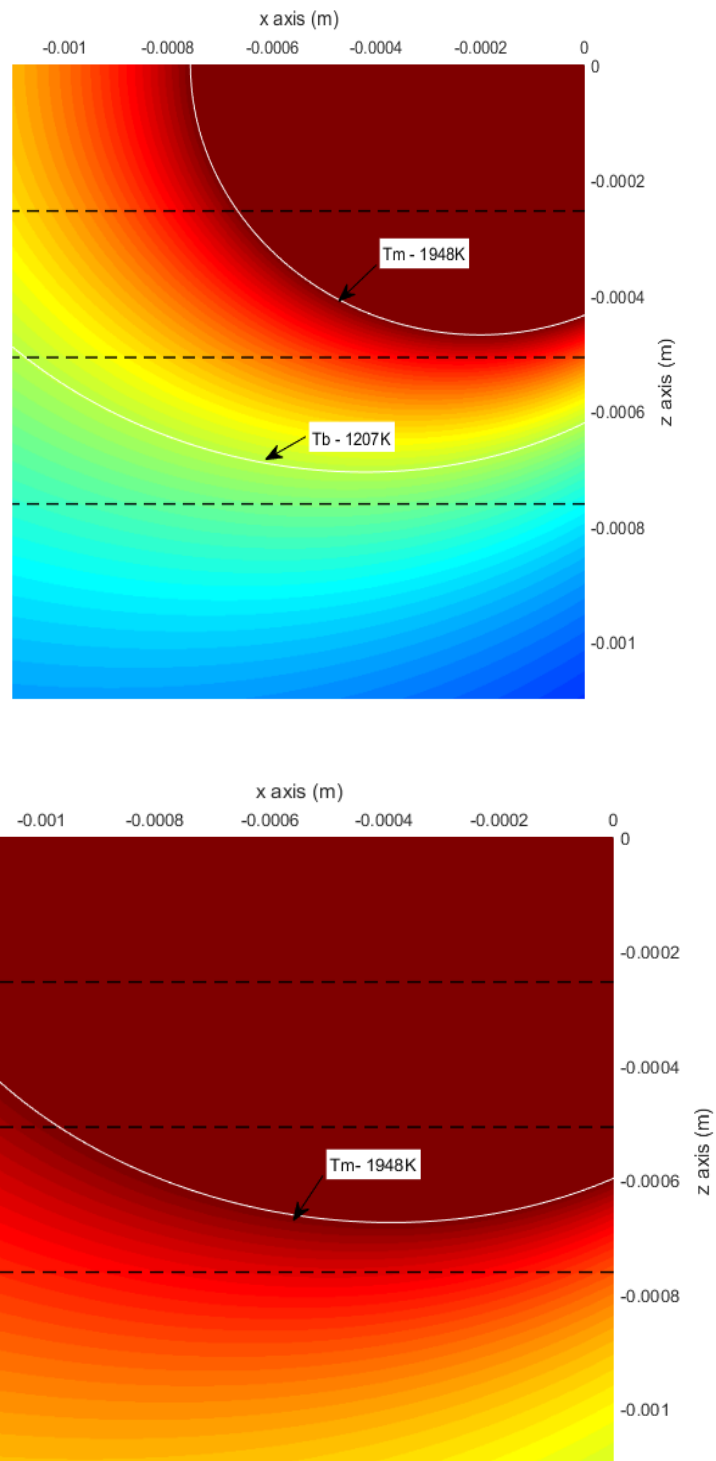


Figure 6.13: Comparison between assuming build temperature is at room temperature (top) and at an elevated temperature (bottom)

6.4 Development of Shercliff and Ashby Gaussian model

The most critical assumption inherent within the Rosenthal model is that it treats the laser as a point heat-source. The laser used during DLD is commonly in the Gaussian mode, meaning it has a defined beam radius. Therefore, a second thermal model was developed to assess the effects of this assumption. This was achieved by using the Gaussian line source equation shown in Eq. 24 and described by Shercliff and Ashby (1991) [95].

$$T = \left[\frac{nq}{2\pi kv\sqrt{t(t+t_0)}} e^{-\frac{1}{4\alpha}\left(\frac{(z+z_0)^2}{t} + \frac{y^2}{t+t_0}\right)} \right] + T_0 \quad (24)$$

The variables in Eq. 24 have the same definitions as those for the Rosenthal model with the additional parameters defined below in Table 6.

Table 6.6: Additional modelling parameters for Gaussian laser mode

Variable	Description
t	Time [s]
T ₀	Heat flow time constant [s]
x, y, z	Co-ordinates where the laser beam centre is at (0, 0, 0)
z ₀	Characteristic length [m]
r _B	Laser beam radius [m]

The methodology described by Shercliff and Ashby and utilised in this model is performed using dimensionless variables which have been defined in Chapter 3. The dimensionless forms of the variables are defined below in Eqs. 25-29.

Modelling the DLD process

Dimensionless temperature:

$$T^* = \frac{T - T_0}{T_m - T_0} \quad (25)$$

Dimensionless power:

$$q^* = \frac{nq}{r_b k (T_m - T_0)} \quad (26)$$

Dimensionless velocity:

$$v^* = \frac{v r_b}{\alpha} \quad (27)$$

Dimensionless co-ordinates (relative to beam centre):

$$x^* = \frac{x}{r_b}; \quad y^* = \frac{y}{r_b}; \quad z^* = \frac{z}{r_b} \quad (28)$$

Dimensionless time:

$$t^* = \frac{t}{t_0} \quad (29)$$

where t_0 is defined as $r_b^2/4\alpha$.

6.4.1 Calculating the value of characteristic length, z_0

The characteristic length is a parameter that prevents the temperature field from reaching infinity as it does when using the Rosenthal equation. This is achieved by assuming that the heat source (laser beam for this study) is incident on an imaginary surface that is a distance (z_0) above the actual

Modelling the DLD process

substrate surface [96]. The value of z_0 is dependent on the process parameters such as laser power and velocity and must be calculated each time one of these is changed. The method for determining the characteristic length is described below and follows the methodology set out by Shercliff and Ashby[95]. The MATLAB written to solve the following equations is given in Appendix C: MATLAB code.

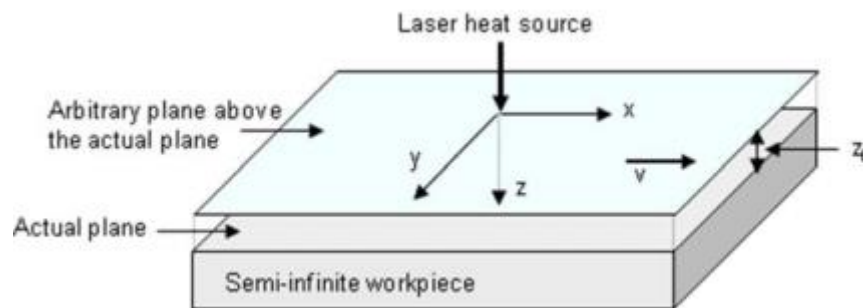


Figure 6.14: Schematic to show the position of the imaginary surface at a distance z_0 above the substrate surface[96]

Step 1: Calculating time to peak temperature (t_p^*)

Firstly the time to peak temperature must be calculated. This variable is the amount of time it takes for any given position (defined by x^* , y^* and z^*) to reach the maximum temperature. The equation given by Shercliff and Ashby is shown below in Eq. 30.

$$t_p^* = \frac{1}{4} \left[2(z^* + z_0^*)^2 - 1 + [4(z^* + z_0^*)^4 + 12(z^* + z_0^*)^2 + 1]^{\frac{1}{2}} \right] \quad (30)$$

Here z^* is set to 0 in order to calculate the time to peak temperature at the substrate surface, with z^* representing distance below the surface of the material.

Step 2: Calculating peak temperature (T_p^*)

The value of t_p^* was calculated for a range of z_0^* values and then inserted into Eq. 31 which is the dimensionless form of Eq. 24.. Here t^* has been substituted with t_p^* to give a range of values for the peak temperature. The values of q^* and v^* were fixed throughout for simplicity.

$$T_p^* = \frac{2q^*}{\pi v^*} e^{-\left[\frac{(z^*+z_0^*)^2}{t_p^*} + \frac{y^{*2}}{t_p^*+1}\right]} \sqrt{t_p^*(t_p^*+1)} \quad (31)$$

Step 3: Peak temperature approximation by the Bass equation

The peak temperature can also be calculated using an analytical solution known as the Bass equation (Eq. 32), which calculates the temperature field of a stationary Gaussian beam.

$$T_p^* = \left(\frac{1}{\pi}\right)^{\frac{3}{2}} q^* \tan^{-1}\left(\frac{8}{v^*}\right)^{\frac{1}{2}} \quad (32)$$

The fixed values chosen for q^* and v^* in Eq. 31 are also used here in the Bass equation. The MATLAB script then compared the results from both peak temperature equations and extracted the value of z_0^* where both equations gave the same value of T_p^* . As mentioned previously, the value of characteristic length is dependent on v^* and q^* , so must be recalculated when varying these parameter.

Once z_0^* has been determined it can be inserted into Eq. 31 which can be rearranged to make z^* the subject. To calculate the maximum melt depth ($z^*=z_m^*$), T_m substitutes T so that $T^*=1$. Therefore, z^* is now equivalent to the maximum melt depth, z_m^* , which is defined as the maximum depth below the surface where $T \geq T_m$. This value can be converted into the non-dimensionless form by substituting into and rearranging Eq. 24.

Before calibrating the Shercliff and Ashby Gaussian model, it was important to ensure that the equations and methodology described above had been implemented correctly. The first validation was to use MATLAB script to create a temperature contour plot analogous to that produced by Ahmed et al [96].

Modelling the DLD process

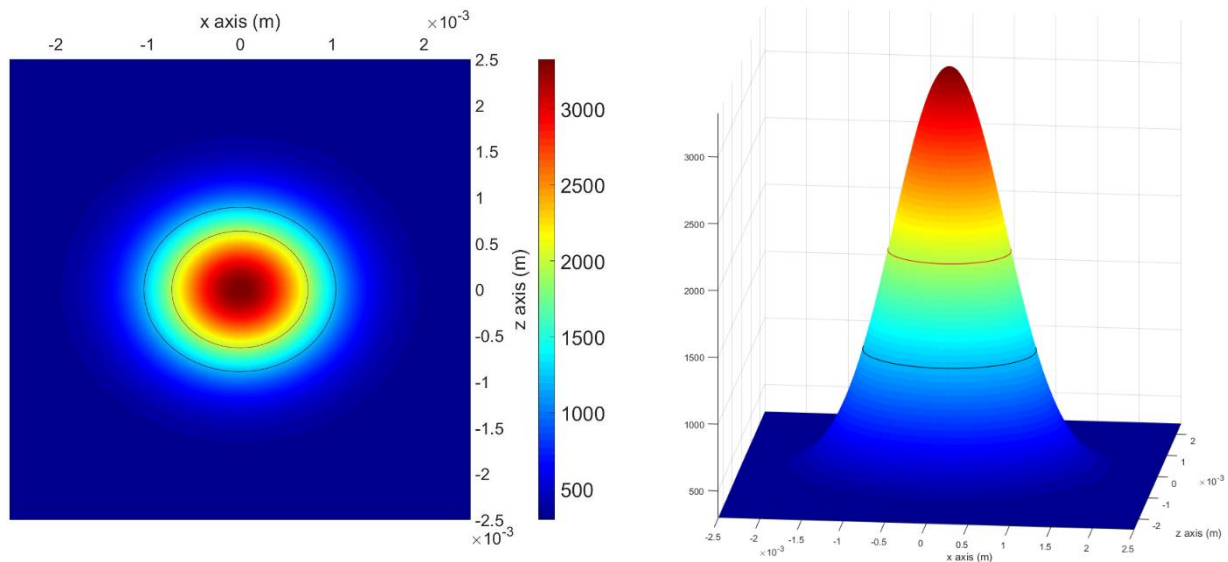


Figure 6.15: Temperature profile of the laser beam using Shercliff and Ashby model

As in the Rosenthal temperature profile, the colours indicate the temperature, the red contour line the position of the melting temperature isotherm at 1948K, and the black contour line the position of the β -transus at 1207K. The temperature profile does not tend to infinity at the laser centre, unlike the Rosenthal model, due to the calculation of z_0 .

The script was also validated by using it to recreate one of the master diagrams produced by Shercliff and Ashby [95] (see Appendix D: Master plot for validation). The authors used the equations and methodology to calculate the case depth, z_c^* , as a function of v^* and q^* for a 0.4% carbon steel.

6.4.2 Calibration results

The Gaussian model was calibrated in the same way as the Rosenthal model which is discussed at the start of this chapter. A value of 0.85 for the fitting parameter, n , was found to predict the correct melt depth for parameter set 1. As can be seen in Figure 6.16, the Gaussian model is a good fit to the experimentally determined melt depths over the full range of energy densities (parameter sets 1-6). Compared to the Rosenthal model, the Gaussian model has a shallower gradient for the melt depths, which is likely due to the less intense temperatures at the laser centre. The result of this is that the

Modelling the DLD process

maximum deviation from the experimental results is approximately $20\mu\text{m}$, compared to $96\mu\text{m}$ for the Rosenthal model.

It is worth noting that for the low energy density parameter sets (namely 1-3) the Rosenthal model is more representative of the experimental melt depths and it is only from parameter set 4 that the Gaussian model shows improvement over the Rosenthal model. It may be the case that for low energy densities, the Rosenthal form of the equation is more suitable.

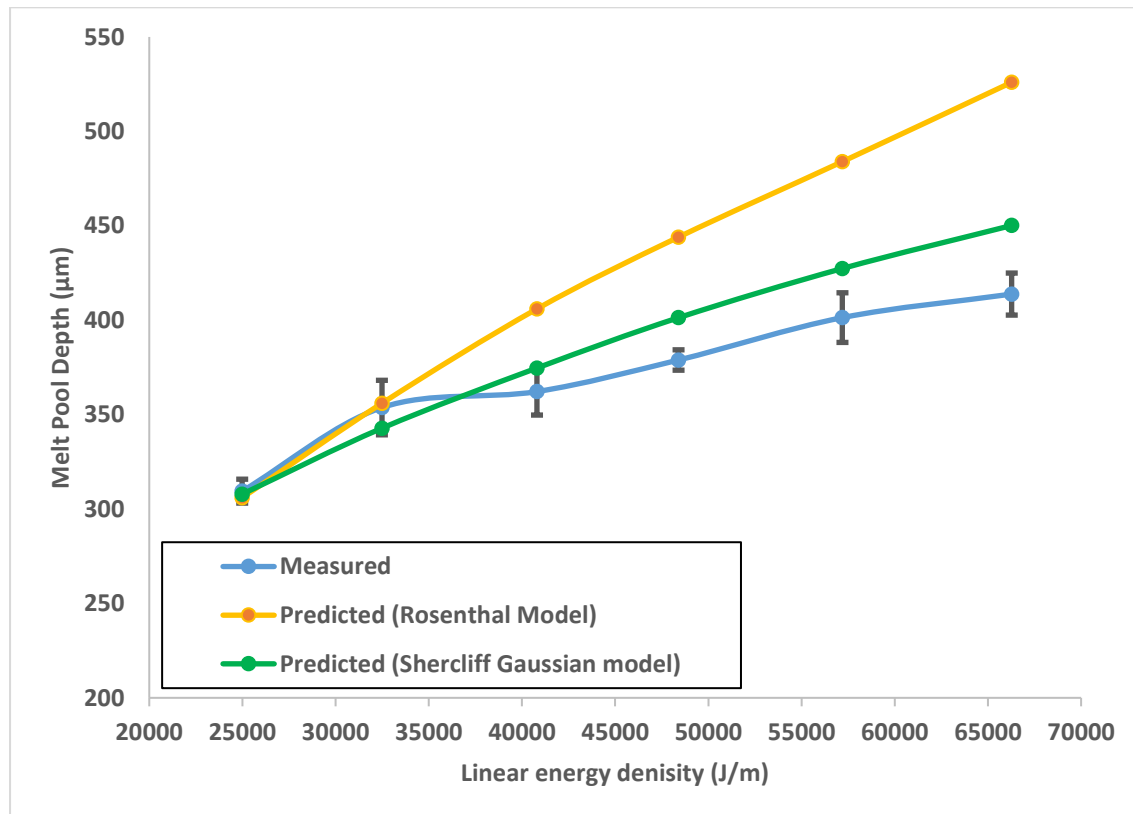


Figure 6.16: Comparison between melt depths predicted by the Gaussian and Rosenthal models and experimental results

6.4.3 Calculating melt depths for Ti-6246 DLD

The calibrated Gaussian model was then used to predict melt depths as a function of both laser velocity and power, using Ti-6246 DLD properties. The results are plotted in Figure 6.17 below with v given in terms of the dimensionless variable v^* . As would be expected, increasing the beam velocity results in a decrease in the melt pool depth since for a constant value of beam power, less energy is

Modelling the DLD process

incident on the material. An increase in the power of the beam (at constant v^*) has the opposite effect and produces a deeper melt pool due to an increase in energy incident on the material.

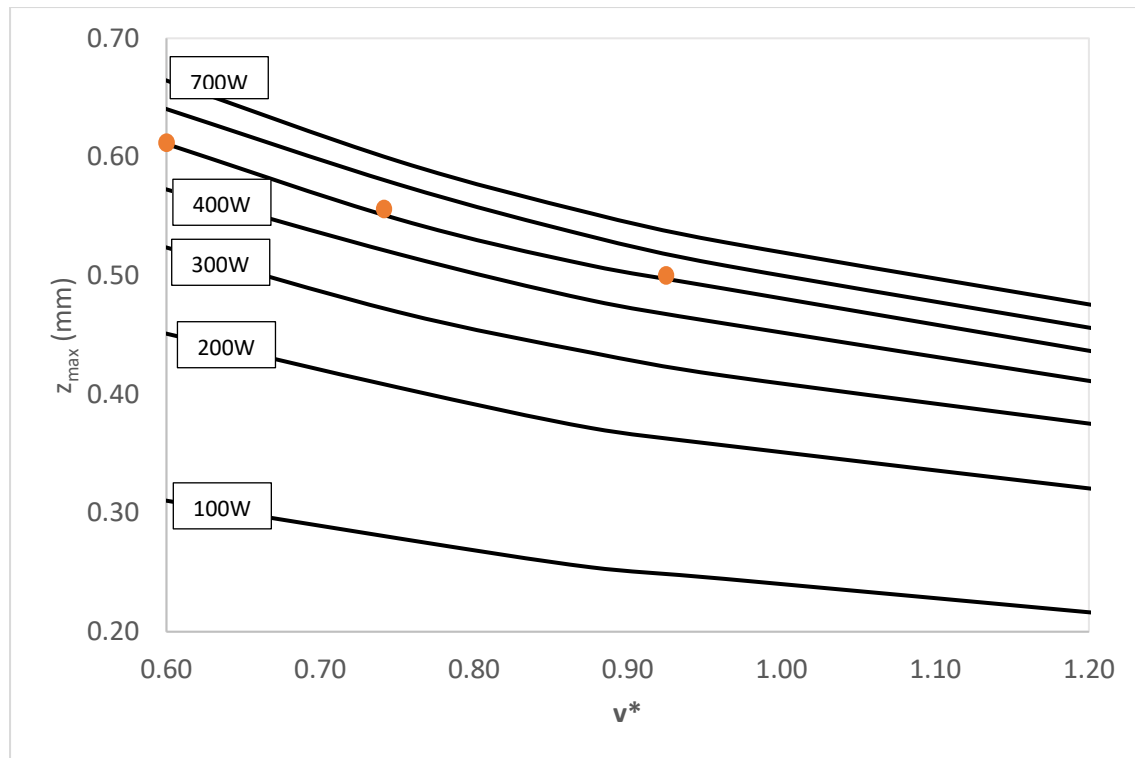


Figure 6.17: Maximum melt pool depth predicted by a Gaussian laser beam as a function of dimensionless laser velocity (v^*) for different laser powers

Figure 6.17 shows how the melt depth changes as a function of power and velocity. The dominant process parameter switches. Doubling laser power from 100W to 200W increases the depth of the melt pool by 0.14mm ($v^*=0.6$). Doubling v^* from 0.6 to 1.2 at 100W, decreases melt depth by 0.09mm. Therefore, the beam power slightly dominates the effect of changing beam velocity. At higher powers however, doubling power from 300W to 600W, increases melt depth by 0.12mm at $v^*=0.6$. By comparison, doubling the velocity from 0.6 to 1.2 at 300W results in the depth decreasing by 0.15mm. Overall, neither parameter overwhelmingly dominates over the other. The orange points on the graph show the values for v^* and the predicted melt depths for the mini tensile DoE. The Gaussian equation does not include a term that takes hatch spacing into account, we can see the change in overall melt depth for the different runs. The layer height (l) used during the mini tensile deposition was constant at 0.254mm. Therefore, Figure 6.17 suggests that each pass of the laser beam will melt between approximately 2-2.5 layers. Sufficient melting of the substrate and previously deposited layers is important in ensuring that there is good bonding between each subsequent layer and reduces the likelihood of defects. However, large melt depths can also lead to a higher level of dilution which can

Modelling the DLD process

lead to a reduction in mechanical properties. The effect of increasing the power has an ever declining effect on the melt depth as can be seen in Figure 6.17, where the lines start to get closer together. Conversely, the gradient of the lines increase gradually, indicating the effect of the velocity starting to dominate. This plot could be used to provide a sanity check for sensible parameters when setting up a new Design of Experiments in order to reduce the need for any unnecessary runs where, for example, $z < l$. An upper limit could also be set to prevent over-melting of the substrate.

6.5 Conclusions

Two different models were assessed to determine how well they could predict melt depths during a DLD process. The first model used the Rosenthal equation to calculate a temperature field. This has the advantage of being a fairly simplistic model that doesn't require too much computing power. However, its limitations are that it assumes that the radius of the laser beam is infinitely small. As shown in this chapter, this means that the temperature field tends to infinity close to the laser centre.

The second approach was to model the laser beam as a Gaussian profile, meaning that the laser beam has a defined radius. This model requires more computing power but removes the main downfall of the Rosenthal model. Both of the models assumed that the thermophysical properties were temperature independent and could be kept at a fixed value, and that the build temperature was fixed at 298K.

Both of the models were compared to a calibration build which was a thin-wall aerofoil-type build that was deposited using increasing values of linear energy density (q/v). For the deposition, layer height was fixed and both laser power (q) and velocity (v) were varied.

The melt depths were observed optically and measured so that they could be compared to model predictions. For both models, the absorption factor "n" was treated as a calibration or fitting parameter and was calibrated against the lowest energy density parameter set on the calibration build. The "n" value for the Rosenthal model was determined to be 0.14 and the model itself proved to be reasonable at predicting melt depths for the lowest linear energy density builds. However, as q/v increased the model began to deviate with a maximum deviation from observed values of approximately 100 μ m. This was 22% of the total melt pool depth and hence quite significant. The Gaussian model by comparison was found to have an "n" value of 0.85 and was found to be good at

Modelling the DLD process

predicting melt depths for the full range of q/v values. The maximum deviation for this model was only $20\mu\text{m}$.

Although both models were found to be accurate at low linear energy densities, the Gaussian model proved to be superior as this increased and hence worth the additional computational time it takes to generate the results. This model will therefore be used to calculate the melt depths in the following chapter and the results can be assumed to be reasonably accurate.

7 Powder effects and Melt Pool Saturation

In addition to any powder-jet laser beam interactions, which were shown to be negligible for the DoE process parameters, the effect the powder particles may have on the melt pool are also important. The following section looks at defining the melt pool saturation level (MPSL) which is the ratio between the material addition from the powder feed rate and the size of the “capture area” generated by the laser beam. The capture area is determined using the calibrated melt depths from the Gaussian model whose development is discussed in Chapter 6.4. The size of this area is a function of the laser velocity, power and the size of the beam radius. The amount of powder captured by the melt pool per unit time is determined by the PFR and an assumed powder capture efficiency of 20%.

7.1 Investigating the effects of powder feed rate

Many thermal models of the DLD process focus on the effects of changing parameters such as beam power, beam velocity and beam radius on melt pool morphology. As discussed in Chapter 2, the effects of the powder addition aspect of DLD is often ignored and the powder feed rate (PFR) is often adjusted in order to keep layer height consistent throughout the build. The repercussions of changing the PFR on aspects such as the attenuation of the laser beam and the effect on the melt pool conditions are not usually considered.

This chapter explores the potential effect of powder feed rate on the deposition process, by quantifying the effect of the powder-jet laser beam interactions and the effect of PFR on the melt pool itself. This is achieved by using the Gaussian heat source model discussed in Chapter 4 to quantify the relationship between powder feed rate and energy density. In turn this can be used to quantify relationships between process parameters, microstructure and mechanical properties.

7.1.1 Powder particle influences on beam power

In laser cladding, where a thin layer of material is deposited onto a substrate, the powder feed rate is often regarded as a key process parameter. Liu et al (2005)[138] for example, calculated the amount of laser power attenuated by powder particles during a laser cladding process. Although laser cladding

Powder effects and Melt Pool Saturation

utilises a much higher PFR than DLD, their work investigated a wide range of feed rates, and the concept is identical for the two processes. Additionally, Shah et al (2011) [45] also investigated the effects of changing PFR, with the focus on how this alters the geometry of the melt pool. They found that increasing the feed rate resulted in an increase in the size of the melt pool area.

In the work performed by Picasso et al (1994) [87] the authors describe a series of equations to quantify the overall effect of the powder-jet laser beam interaction during laser cladding. This is shown below in eq. 33 and eq. 34. The description of the parameters used are given in Table 7.1. Most of these are machine settings that are determined by the user and optimised for different materials and build geometries.

$$P_w = P_l \left\{ \beta_w \left(1 - \frac{P_{at}}{P_l} \right) + \eta_p \beta_p \frac{P_{at}}{P_l} \left[1 + (1 - \beta_w) \left(1 - \frac{P_{at}}{P_l} \right) \right] \right\} \quad (33)$$

Where:

$$\frac{P_{at}}{P_l} = \frac{\dot{m}_p}{2\rho r_j r_p v_p \cos(\theta_j)} \quad (34)$$

Table 7.1: Table listing parameters used in calculating powder-laser beam interactions for Ti-6246 DLD

Variable	Value
Beam power – P_l	300-700 W
Workpiece absorption – β_w	0.37-0.42[137]
Powder capture efficiency – η_p	0.2
Powder feed rate – \dot{m}_p	0.3-5 GPM
Density of Ti-6246 - ρ	4650 kgm ⁻³

Powder effects and Melt Pool Saturation

Beam radius – r_l	$\sim 5 \times 10^{-4}$ m
Powder radii – r_p	22-75 μ m
Velocity of powder – v_p	~ 14 ms ⁻¹
Radius of powder jet – r_j	$\sim 2 \times 10^{-3}$ m
Angle of powder jet – θ_j	65°

Table 7.1 describes the parameters from eq. 33-34 and also gives typical values for these parameters for DLD of Ti-6246. For the following calculations, the workpiece absorption is assumed to be 0.4 and is also assumed to remain constant throughout the deposition process. The powder capture efficiency can be dependent on a variety of factors such as the type of powder nozzle used and can be as low as 7% [139]. A value of 12% was found for DLD of Ti-6Al-4V [140] and for the purposes of this work, a worst case scenario of 10% capture efficiency is assumed. The radius of the powder particles had a range between 22-75 μ m the mid-point was taken.

7.1.2 Initial attenuation by powder particles in laser beam

The first stage was to calculate the initial power loss due to powder particles interacting with the laser beam before they reach the melt pool. This power loss, denoted by P_{at} , can be determined by a slight rearrangement of eq. 34 (see Eq. 35). The amount power that is attenuated as a function of powder feed rate is shown below in

$$P_{att} = \frac{P_l m_p}{2\rho r_j r_p v_p \cos(\theta)} \quad (35)$$

As would be expected, as the powder feed rate increases the amount of laser power that is attenuated increases as well. This is due to an increase in the powder jet density which in turn increases the number of powder particles interacting with the laser beam per unit time. These powder particles absorb some of the laser power in-flight, resulting in the loss of power at the substrate surface. As can be seen in Figure 7.1, the fraction of power that has been lost is between 5-15W at the highest powder feed rate which is of the order of 2%. This is not hugely significant, and indeed is far less than power

Powder effects and Melt Pool Saturation

loss due to reflection from the workpiece. As the PFR is increased this effect becomes more and more substantial. However, unlike laser cladding where the PFR can be around 20g/min, DLD is usually far lower and so from Figure 7.2 it is clear that it is unlikely to have a major effect on the amount of power reaching the melt pool. Hence, the shadowing effect of the powder particles has little to no contribution towards the 0.85 value for the calibration factor inherent in the Gaussian model.

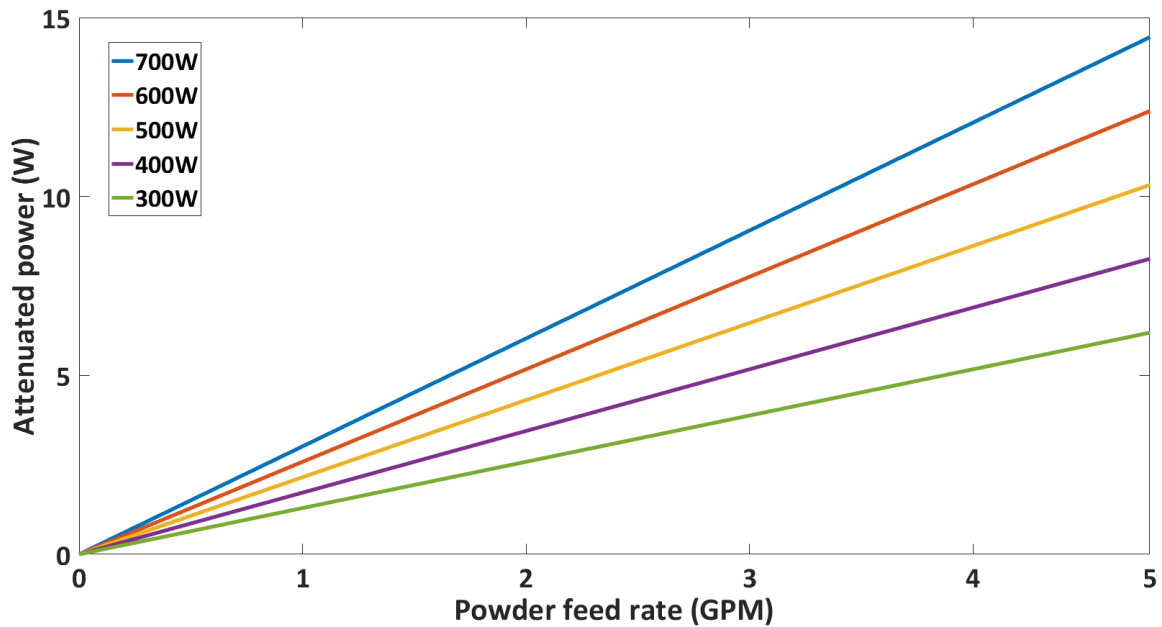


Figure 7.1: Graph showing the relationship between powder feed rate and attenuated power as a function of laser power

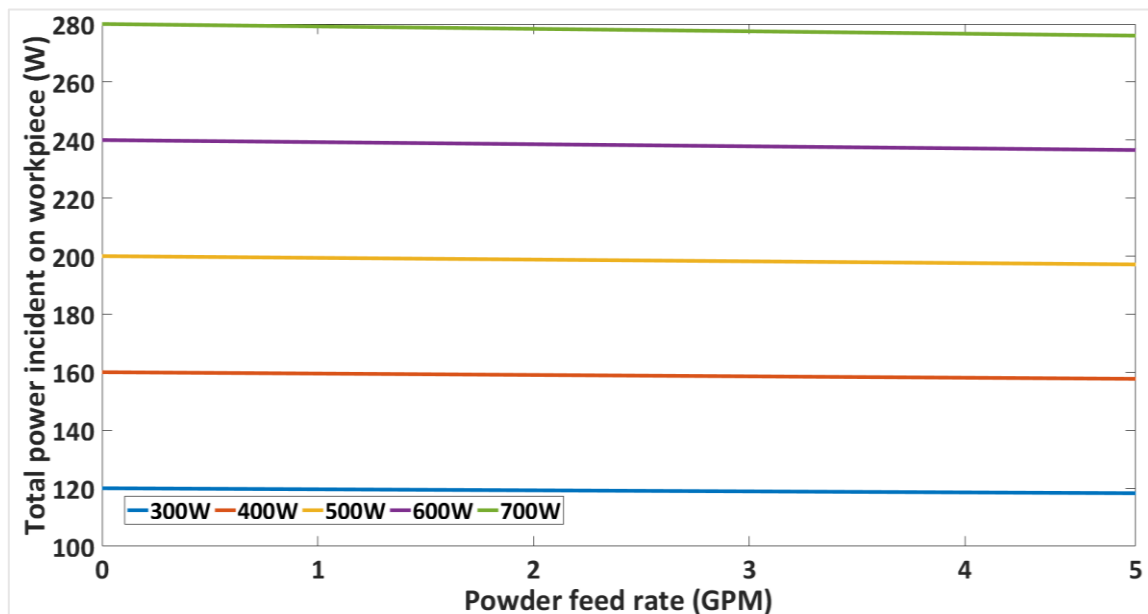


Figure 7.2: Graph to show the relationship between powder feed rate and total workpiece absorption

Powder effects and Melt Pool Saturation

Since the results in Figure 7.2 show that power loss due to powder-laser beam effects is small at the PFRs shown, it is clear that the source of the majority of the power loss is due to reflectivity of the workpiece. Therefore, the effect of the powder can mostly be ignored, with its contribution to the calibration factor “n” essentially 0. Instead the efficiency of workpiece absorption is the critical parameter. This is significantly different to the results given by Picasso, where the effect of the powder-beam interactions results in up to 500W of power being attenuated. The major difference between the work presented here and that by Picasso et al, is that their work is for laser cladding and hence the powder feed rates involved are ~20-30 times higher than that used for DLD. The reduced density of the powder jet means there are considerably less powder particles to interfere with the laser beam.

The powder feed rates used for the deposition of the mini tensile specimens were all $\geq 1\text{g/min}$. From the figures above, it is clear that the PFR could be increased by a factor of 5 and still potentially have little to no effect on the power incident on the workpiece. Increasing the powder feed rate could also be accompanied by an increase in the laser velocity (to keep constant layer height) which would decrease the build time. Therefore, one of the constraining factors for how quickly a build can be deposited will be the powder feed rate and how much of the laser beam is being attenuated. If the laser power decreases significantly then this could result in lack of fusion defects if not enough of the previous layer is re-melted. The powder-jet laser beam interactions calculated above can help inform the upper limits of the PFR so that the build is not being affected.

7.2 Melt pool saturation

The methodology described above is based on laser cladding which typically uses high powder feed rates and is restricted to single layers. As such, the powder-jet and laser beam interactions are the focus of the study by Picasso et al. However, for DLD the laser parameters such as the beam radius are smaller than for laser cladding, and melt depth is also a key parameter since DLD is multi-layer deposition. Using the Gaussian model to predict melt depths based on DLD process parameters, a new method for assessing the potential effects of powder feed are defined by a melt pool saturation level (MPSL)

7.2.1 Laser melting capability

The amount of energy (Q) required to melt a mass of material (m) can be calculated using Eq. 36.

$$Q = mc\Delta T + mL \quad (36)$$

Here Q is the energy (J), m is the mass of material (kg), c is the specific heat capacity ($\text{Jkg}^{-1}\text{K}^{-1}$), ΔT is the change in temperature and L is the latent heat of fusion Jkg^{-1} . In the case of Ti-6246 DLD, the minimum ΔT is the difference between the initial build temperature and the melting point of Ti-6246 (1948K). The power of the laser (q) can be substituted for Q and the equation can be rearranged (Eq. 37) to determine the amount of mass that can be melted per second for a given laser power.

$$m^{upper} = \frac{q}{(c\Delta T + L)} \quad (37)$$

Figure 7.3 shows the maximum mass (gmin^{-1}) that can be melted using different laser powers. It is assumed that the material is being heated up from the initial build temperature (298K) to the melting temperature of Ti-6246 (1948K). Since the latent heat of fusion of Ti-6246 is not readily available in literature, a value of 360 kJkg^{-1} for Ti-6Al-4V was used instead.

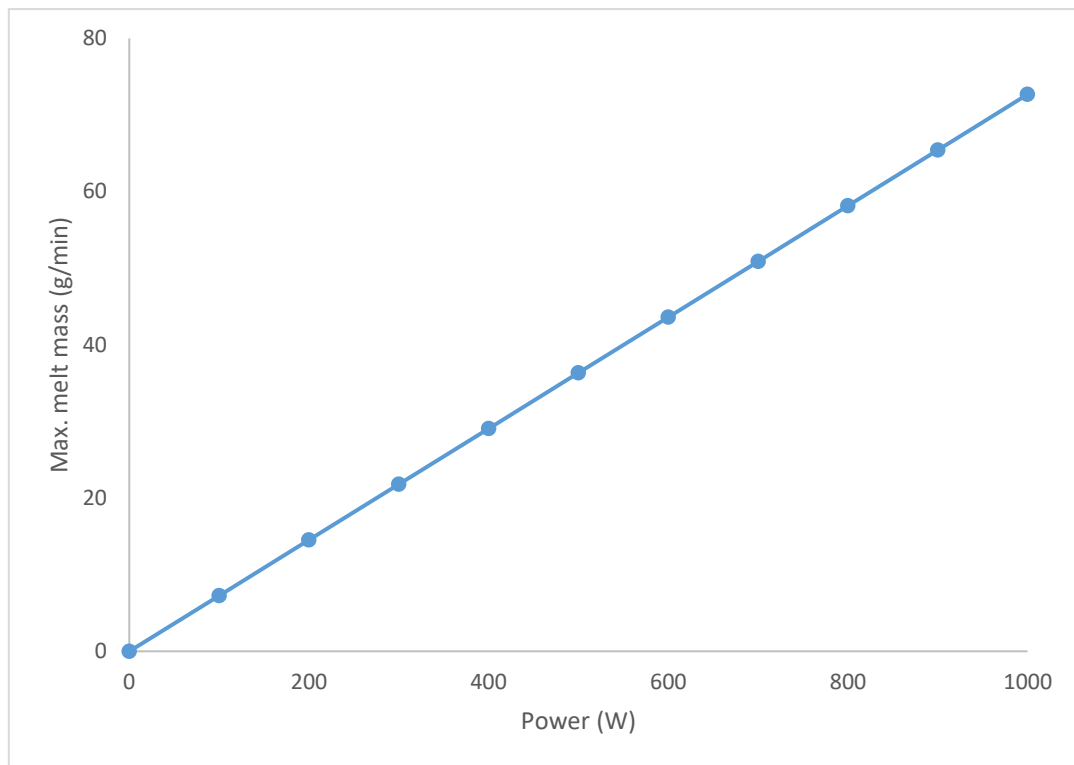


Figure 7.3: Graph showing maximum mass of Ti-6246 that can be melted per second for different laser powers

The melting temperature is the minimum temperature the material must be heated to during the DLD process for full consolidation of the powder. However, during the DLD process and as shown with the Gaussian model developed in Chapter 6.4, the peak temperatures are far in excess of T_m . Therefore, ΔT in Eq.37 is much greater than is assumed for Figure 7.3. If we assume an average peak temperature (T_p) of 14,000K then more energy is required to raise the temperature of the material to this value. As shown in Figure 7.4, this results in significantly less material per second reaching this peak temperature (two orders of magnitude) when compared to Figure 7.3. Again, T_0 is assumed to be 298K which is an exaggerated case. Although Figure 7.4 extends infinitely, in reality the substrate being deposited onto is not infinite in size and hence there is a limit to the maximum mass of material being melted. In addition, using high laser powers can lead to over-melting of the substrate and any previously deposited layers which can cause an effect known as key-holing. This is where the melt pool shape transforms from a semi-circular geometry to a deeper, longer geometry or a “key-hole” [141]. This is problematic for DLD since it indicates an excess energy density and leads to the formation of pores.

Powder effects and Melt Pool Saturation

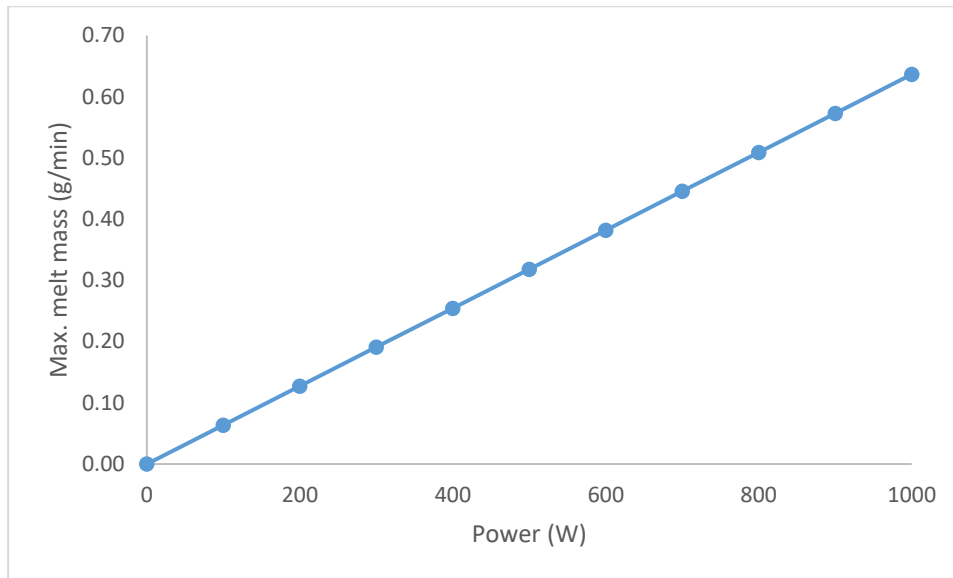


Figure 7.4: Graph showing maximum mass of Ti-6246 raised to T_p per second for different laser powers

For the DLD process, m^{upper} is a combination of the material from the powder feed and the previously deposited material (i.e. workpiece) that is being melted by the laser as described in Eq.38.

$$m^{upper} = m_p^{max} + m_{deposit} \quad (38)$$

Therefore, the maximum PFR (m_p^{max}) for a given laser power can be calculated by subtracting the mass of the previously deposited material being re-melted from the total mass as defined by Eq.39.

$$m_p^{max} = m^{upper} - m_{deposit} \quad (39)$$

The term $m_{deposit}$ (i.e. mass of deposit material being re-melted) can be calculated using the Gaussian model melt depth predictions from Chapter 6.4 and the following assumptions:

1. The laser beam generates a spherical melt pool
2. The melt pool is centred on the surface of the previously deposited layer
3. Material that is bound by the $T=T_m$ isotherm as shown in yellow in Figure 7.5 is liquid.

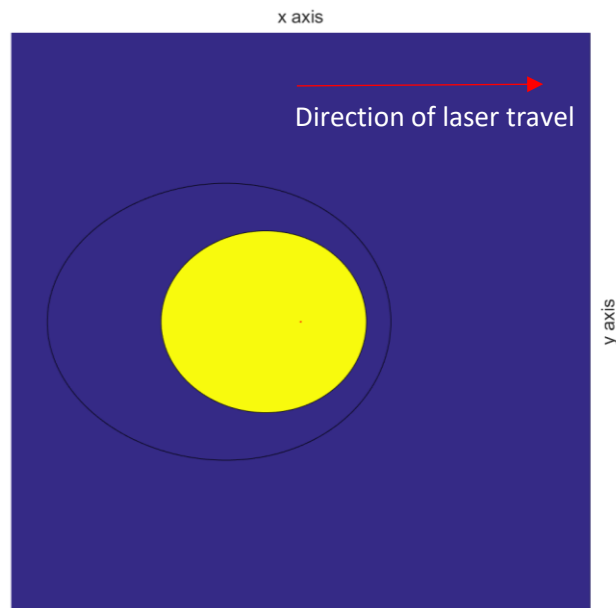


Figure 7.5: Powder capture area (yellow) bounded by the $T=T_m$ isotherm

Figure 7.5 shows how the shape of the melt pool on the surface of the workpiece is slightly elongated. Its exact geometry is dependent on laser velocity and power. However, the portion of the melt pool that is capturing powder is, for the most part, directly below the laser centre. It is assumed that the tail-end of the melt pool can therefore be excluded from the calculations, making the powder capture area circular.

Using assumptions 1 and 2, the surface area of the melt pool can be calculated from the melt depth (z_m), using Eq. 40.

$$\pi z_m^2 \quad (40)$$

Multiplying the area by the velocity (v) of the laser beam results in a melt volume per second which can then be multiplied by the density (ρ) of Ti-6246 to calculate a mass per second (kg s^{-1}) as shown in Eq. 41.

$$\pi z_m^2 v \rho \quad (41)$$

Powder effects and Melt Pool Saturation

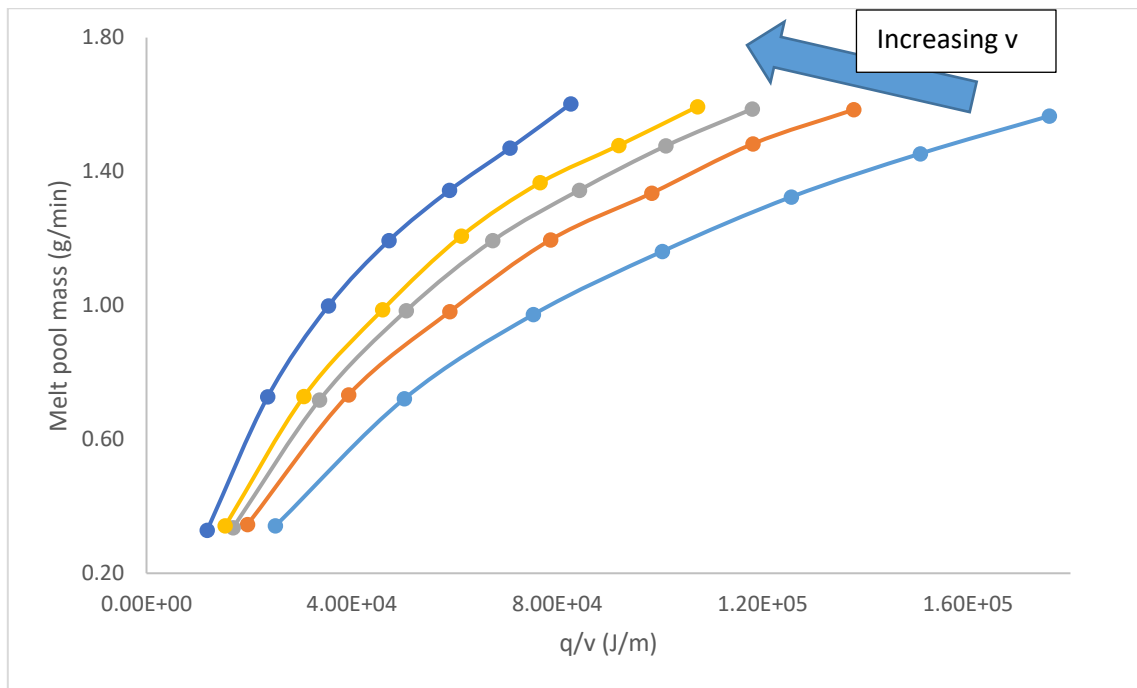


Figure 7.6: Graph showing the relationship between q/v energy density and amount of material melted per second

Figure 7.6 shows the results from Eq. 41 plotted against energy density for a range of beam velocities. For a given beam velocity, an increase in q/v (i.e. increasing beam power) the mass of material being melted also increases. This is as expected since the depth of the melt pool increases with laser power due to more energy available to be absorbed by the substrate material.

Equation 39 can therefore be rearranged and written as:

$$m_p^{max} = m^{upper} - \pi z_m^2 v \rho \quad (42)$$

7.2.2 Calculating the MPSL

The ratio between the actual mass melted by the laser (powder feed and previously deposited layers) and the total melting capacity of the laser is defined by this work as the melt pool saturation level (MPSL). This can be written as:

$$MPSL = \frac{(\pi z_m^2 v \rho + n_p m_p)(c_p \Delta T + L)}{q} \quad (43)$$

This is also depicted in Figure 7.7 where laser parameters such as speed and power are identical between the two images, and the only variable is the powder feed rate. This means that the terms such as q and $\pi z_m^2 v_p$ are the same and m_p is the only parameter affecting the MPSL. Figure 7.7a shows a low PFR resulting in a low MPSL compared to Figure 7.7b where a higher PFR is being used with the same laser parameters.

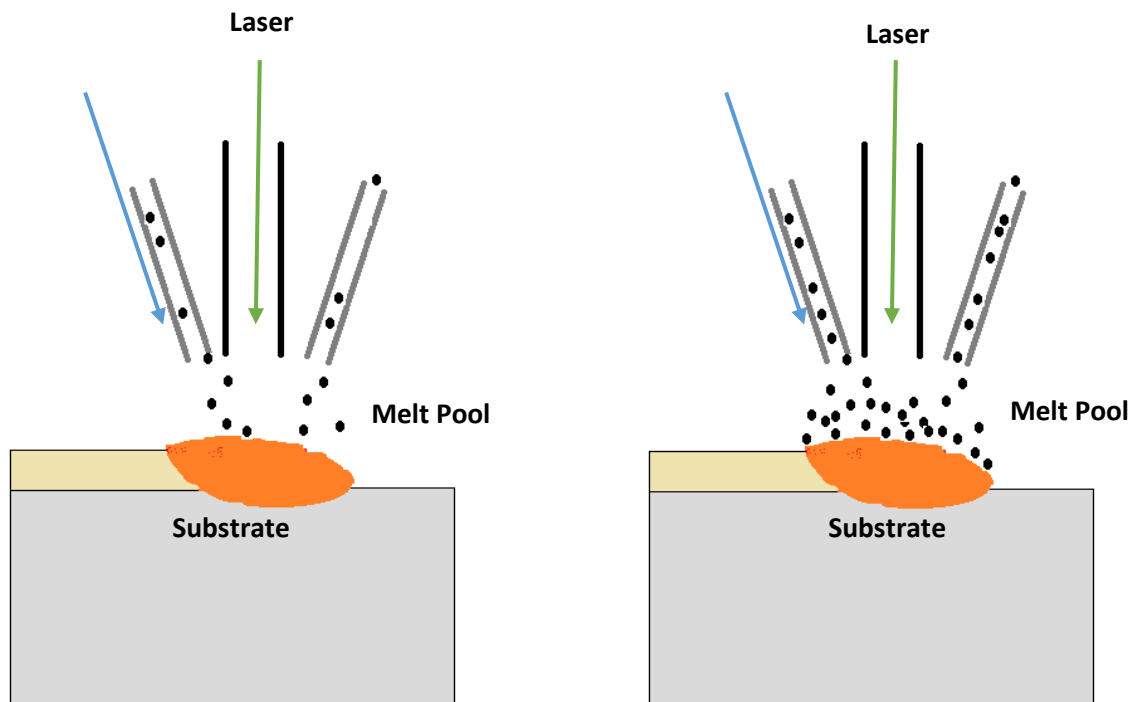


Figure 7.7: Comparison between (a) low melt pool saturation (left) and (b) high melt pool saturation (right)

The melt pool is defined as fully (100%) saturated when the mass of material being melted; which is a combination of powder from the powder-jet and previously deposited material, is equal to the melting capacity of the laser (m^{upper}). This is true when $n_p m_p^{\text{actual}} = m_p^{\text{max}}$. A value of MPSL above 100% indicates that more material is being fed into the melt pool than can be melted by the laser power and hence cannot be fully consolidated. This can lead to build defects, poor surface quality or in the worst case scenario, build failure. If the build is to be robust and fully dense then the ratio between aspirational feed rate and actual feed rate needs to be controlled.

Applying this to the mini tensile DoE builds gives the results plotted in Figure 7.8. As shown, the highest MPSL is for parameter set 1 with a value of 4.3%. This indicates that within the process window being explored in this work, the melting capacity of the laser is far in excess of the material being added to

Powder effects and Melt Pool Saturation

the process each layer. This is in agreement with the results from the Picasso et al. methodology where the PFR appears to have little effect on the laser beam. This is to be expected since this is not a laser cladding process where large amounts of material have to be deposited in a single layer.

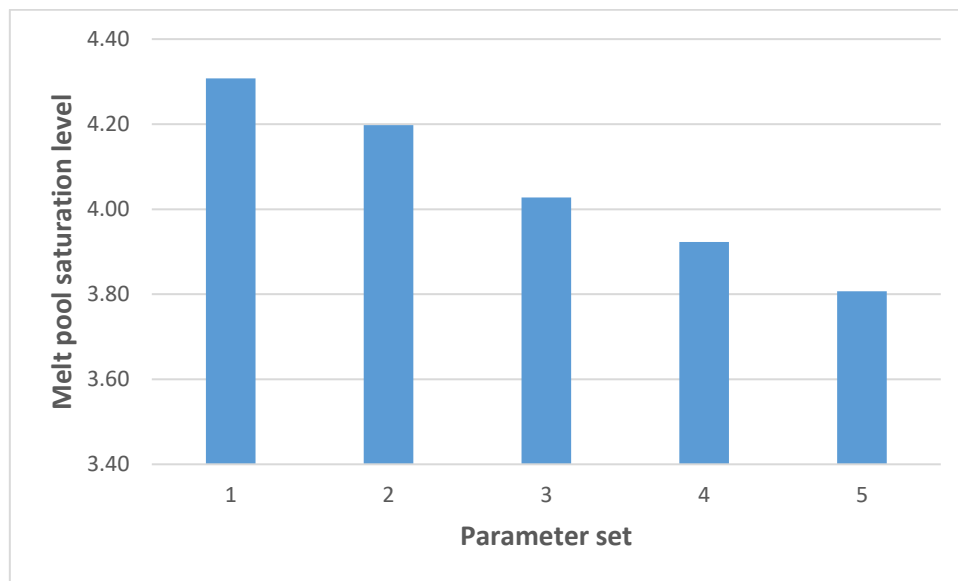


Figure 7.8: Melt pool saturation levels for mini tensile DoE parameter sets

7.3 Aspirational powder feed rate

A powder feed rate that results in a 100% MPSL defines an upper limit for this process parameter. However, it is just as important to define a lower limit on the PFR if the process is to be stable and consistent throughout the build.

The lower limit can be defined by the following equation:

$$m_p^{low} = lhv\rho \quad (44)$$

Here l and h are the pre-defined layer height (m) and hatch spacing (m) respectively, v and ρ are as defined previously. The size of the layer height and hatch spacing should follow the rules set out by Picasso et al. in order to ensure a good quality build with a low amount of porosity. In this case, the

Powder effects and Melt Pool Saturation

layer height and hatch spacing should be approximately (and not exceed) $2/3r_b$. Following this rule, the volume of material that needs to be deposited every second is:

$$lhv = \frac{4}{9}r_b^2v \quad (45)$$

Multiplying the volume in Eq. 45 by the density of the material, the mass per second that needs to be deposited can be determined. Since the material is delivered via the powder feed, this value can be defined as the aspirational powder feed rate. Note that in addition to multiplying by the density, the right-hand side of the equation has also been divided by the powder capture efficiency. If the process is 100% efficient i.e. all powder from the powder-jet is delivered into the melt pool then $n_p=1$.

$$m_p^{aspirational} = \frac{\frac{4}{9}r_b^2v\rho}{n_p} \quad (46)$$

The aspirational PFR can be compared to the m^{upper} term defined previously to identify two regimes as shown in Eqs. 47-48:

$$\frac{q}{c\Delta T + L} \times \frac{1}{m_p^{asp}} > 1 \quad (47)$$

$$\frac{q}{c\Delta T + L} \times \frac{1}{m_p^{asp}} < 1 \quad (48)$$

In the first regime, there is an excess of energy. The laser is providing more energy per second than is required to melt the powder delivered by the *aspirational* PFR (m_p^{asp}). In the second regime, the laser power is providing insufficient energy to melt all the powder delivered at the *aspirational* PFR. This

Powder effects and Melt Pool Saturation

would lead to inconsistent layer height and potentially increase the likelihood of lack of fusion defects and pores. Ideally, the ratio would be approximately equal to or slightly in excess of 1 in order to account for fluctuations in the process such as a change in powder capture efficiency. The case where the ratio is $\gg 1$ is also not ideal as the power being used is far in excess of what is required which could not only result in evaporation of some of the elements but would also be an inefficient and expensive (in terms of energy consumption) process. In Eq. 46, the aspirational PFR that is required to deposit layers of a consistent layer height and with a fixed hatch spacing was defined. This figure should always be $\leq m^{\text{upper}}$ as defined in Eqs. 47-48, otherwise the mass of powder being delivered is larger than what the laser beam is capable of melting.

Equation 44 can be used to calculate the lower limit for the powder feed rate required for each of the five different parameter sets used in the DoE. The ratio between the delivered “actual” powder feed rate with an assumed capture efficiency of 20% and the ideal PFR required for consistent layer heights can be determined. If the ratio has a value of 1 (100%) then exactly enough powder is being introduced to the melt pool to build up the set layer height. Results for the DoE builds are presented below in Figure 7.10. Results show that parameter set 2 is the only one that has a PFR higher than the aspirational PFR (117%), which could result in a slight overbuild. However, this is likely to average out over the entire build since the capture efficiency is unlikely to remain fixed at exactly 20%. Taking into account fluctuations in the powder capture efficiency, parameter set 3 is likely also delivering at roughly m_p^{asp} . Parameter sets 4 and 5 appear to be significantly below m_p^{asp} at 74% and 72% respectively.

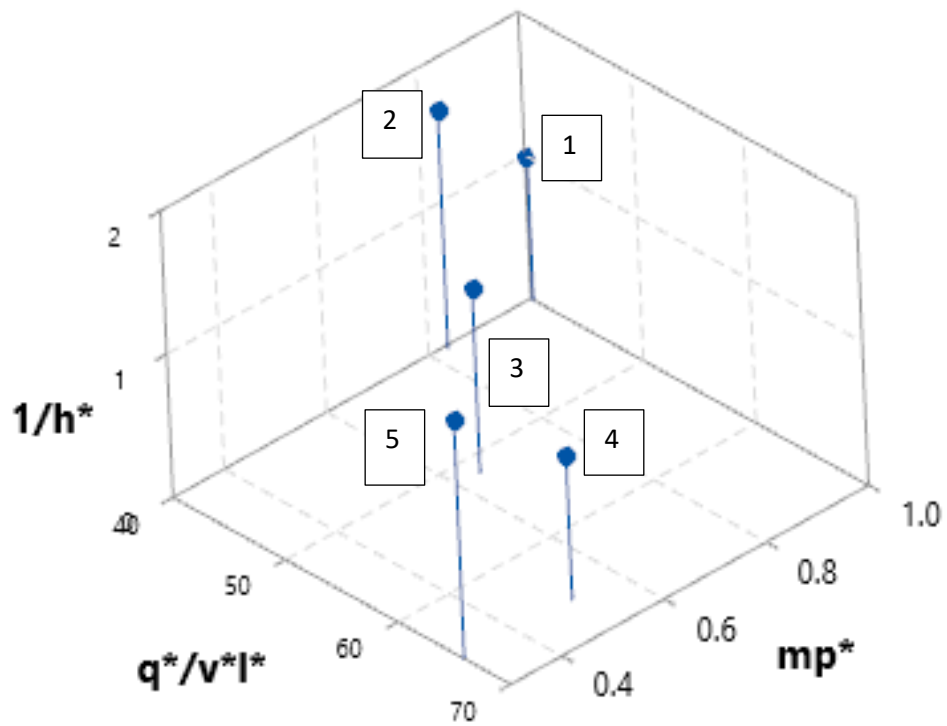


Figure 7.9: 3-D process map for the Ti-6246 DLD mini tensile builds including the PFR

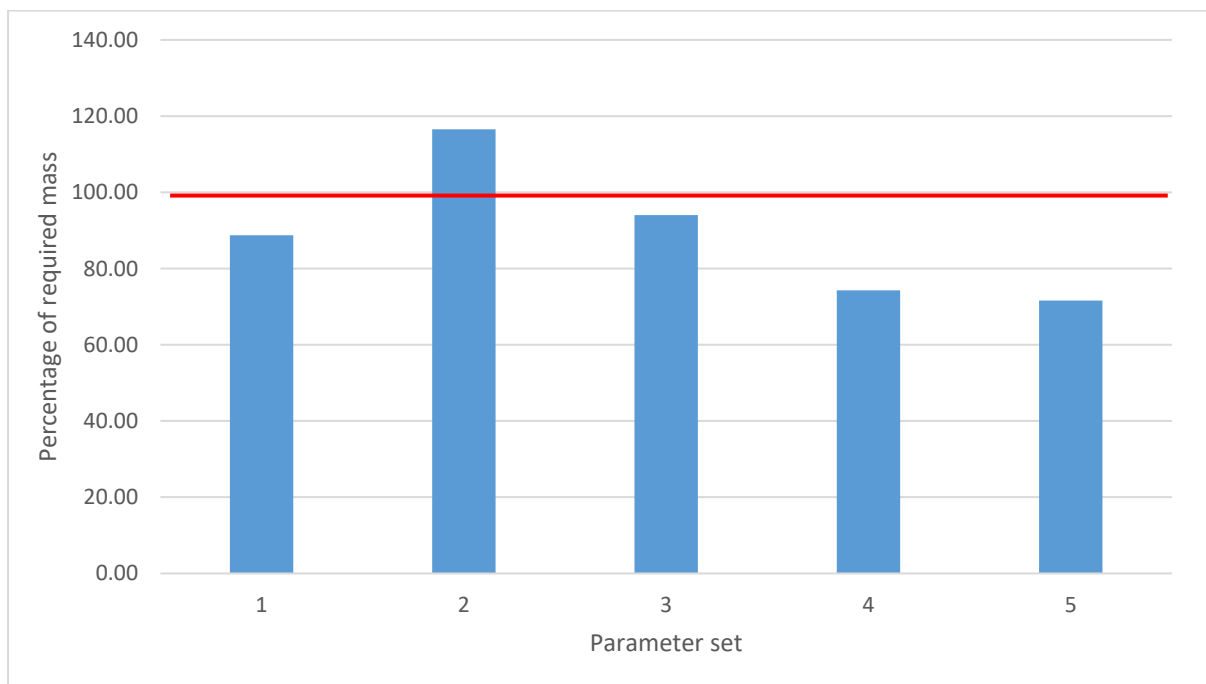


Figure 7.10: Percentage of "ideal" or required mass of powder delivered to the melt pool

7.3.1 Effect of aspirational feed rate on mini tensile DoE

The fraction of required mass for each of the builds is an important factor in explaining the differences in microstructure and mechanical properties between parameter sets. Results from Chapter 5 show how q^*/v^*l^* is the dominant factor affecting mechanical response. However, when taking into account energy density (E^*) which is defined as $q^*/v^*l^*h^*$, then parameter sets 2, 3 and 4 are identical. The only difference between them is the PFR and hence the ratio presented in Figure 7.10.

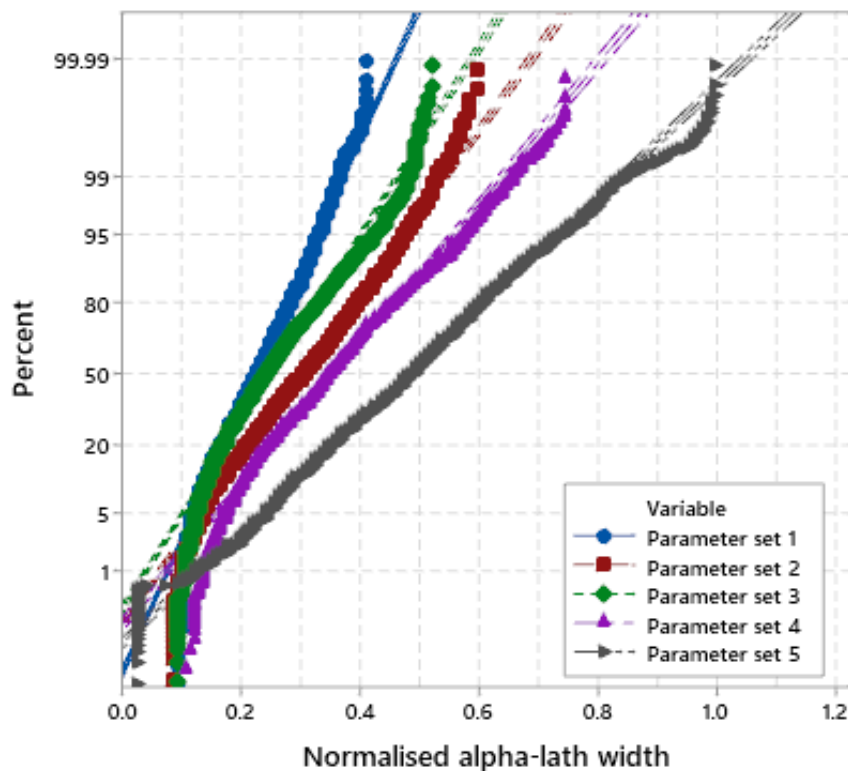


Figure 7.11: Probability plot of alpha lath widths grouped by DoE parameter sets

Figure 7.11 shows the relationship between the size of the alpha lath widths and the fraction of m_p^{asp} . The general trend from parameter set 1 to 5 is a coarsening of the microstructure. This is most likely related to the increasing linear energy density q^*/v^*l^* affecting the cooling rate. Parameter sets 2, 3 and 4 have the same $q^*/v^*l^*h^*$ values and it would reasonably be expected that they would have the same average microstructure. However, as can be seen in Figure 7.11, parameter set 3 (green) has an unusually fine microstructure as indicated by the d_{50} value of 0.25, almost equal to that of parameter set 1. As shown in Figure 7.10, parameter set 3 was delivering a mass of powder significantly below the aspirational PFR. This may have resulted in inconsistent layer heights and insufficient track overlap due to the reduced amount of powder which would have affected the cooling rates. The differences

Powder effects and Melt Pool Saturation

in microstructure size is shown visually in Figure 7.12. It can be clearly seen that the microstructure for parameter set 3 (Figure 7.12c) is much finer than all but the final image which has the same average lath width. It is important to note, however, that the range of alpha lath widths even within the same build can be quite large. As can be seen in Figure 7.11, for the same parameter set, the difference between the largest and smallest lath can be significant and equivalent around $1\mu\text{m}$ to most extreme case. This difference is significant especially when considering the average size of most of the laths.

The effect that the reduced relative PFR has had on parameter set 5 is not as clear. In Figure 7.11, the d_{50} value indicates that this parameter set produces coarse microstructure rather than the fine microstructure of parameter set 3. However, there is a small population of alpha-laths at the very bottom end of the scale which could be an indicator. This parameter set also shows the greatest spread between largest and smallest alpha laths.

Powder effects and Melt Pool Saturation

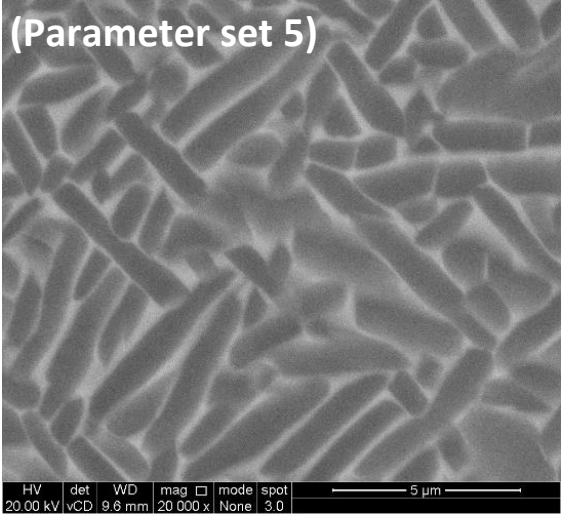
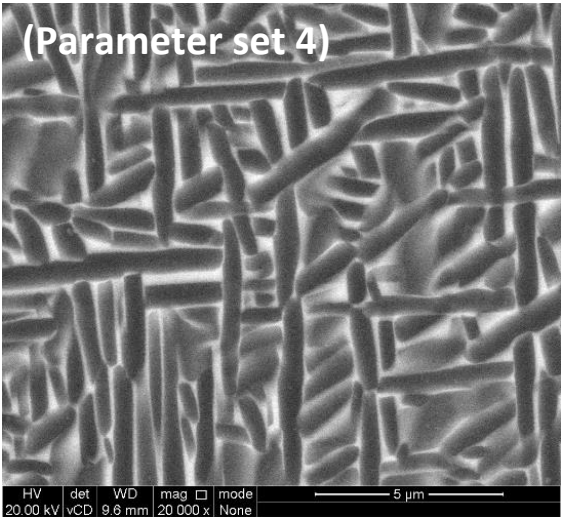
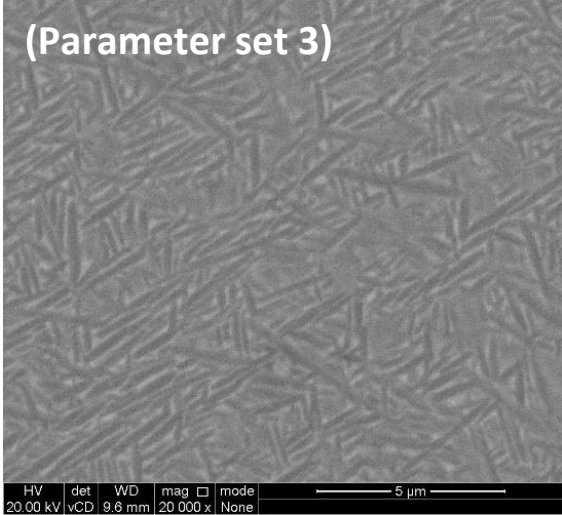
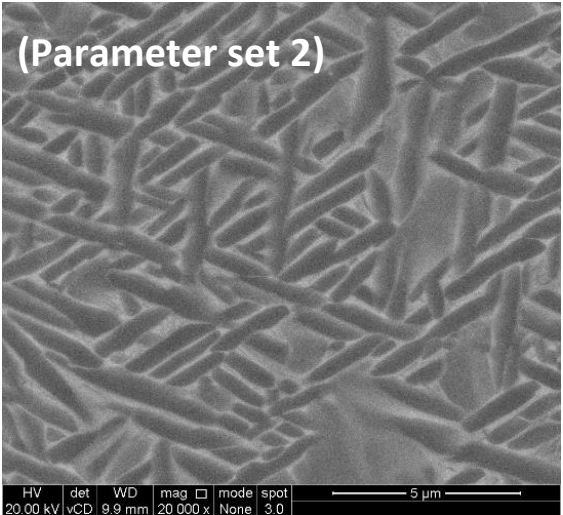
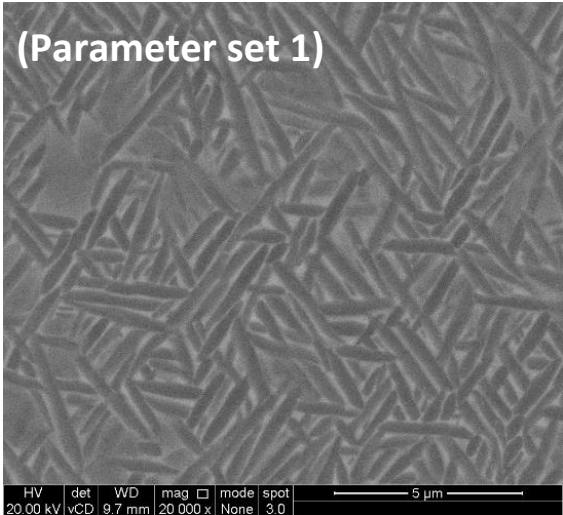


Figure 7.12 (a-e): Typical micrographs showing the alpha laths for five different MPSLs. (a) 23%, (b) 38%, (c) 48%, (d) 61% and (e) 74%

Powder effects and Melt Pool Saturation

On top of the microstructural effects, the fraction of the aspirational PFR might also be expected to affect the mechanical properties of the deposits. Figure 7.13 shows the relationship between the fraction of aspirational PFR and the 0.2% yield stress of the DoE mini tensile specimens. The blue data points indicate results from each of the 20 separate tensiles and the orange data points provide the average for each parameter set. It is quite clear that the size of the microstructure dominates the yield stress. Parameter set 3 which has one of the finest microstructures also has a high average 0.2% yield stress. This is not unexpected since as discussed in Chapter 5 there is a known relationship between the size of the microstructure and the mechanical properties from the Hall-Petch. However, as stated above, parameter sets 2, 3 and 4 have the same overall E^* value and it would therefore be expected that the microstructure and hence mechanical properties would all be similar. Figure 7.13 shows that parameter set 4 actually has a lower yield stress response than 2 and 3 which cannot be explained by the E^* value used for deposition. The only difference between these three sets of data is the PFR used. In the case of parameter set 4, the PFR is significantly below the aspirational PFR which appears to have had a detrimental affect on the yield stress. The same is true for parameter set 5 as well. The three parameter sets closest to m_p^{asp} have the highest average 0.2% yield stress.

Looking at the average results, there also appears to be a step in between parameter sets 4 and 2, where there is a sudden increase in the average yield stress. Lack of data between these points makes it impossible to tell whether this is a gradual increase or not. There does appear to be a plateau in the yield stress at approximately 90% of m_p^{asp} , and the lack of scatter in results compared to the other data sets, suggests that this may be real. When operating at or above the aspirational PFR, the deposit is building in a stable and consistent manner meaning that the build defects should be minimised hence optimising the response. It might be expected that if ever higher PFRs compared to m_p^{asp} were to be used (150%, 200% etc), then a dip in the mechanical response may be a result due to overbuilding of the layers that cannot be compensated for.

Powder effects and Melt Pool Saturation

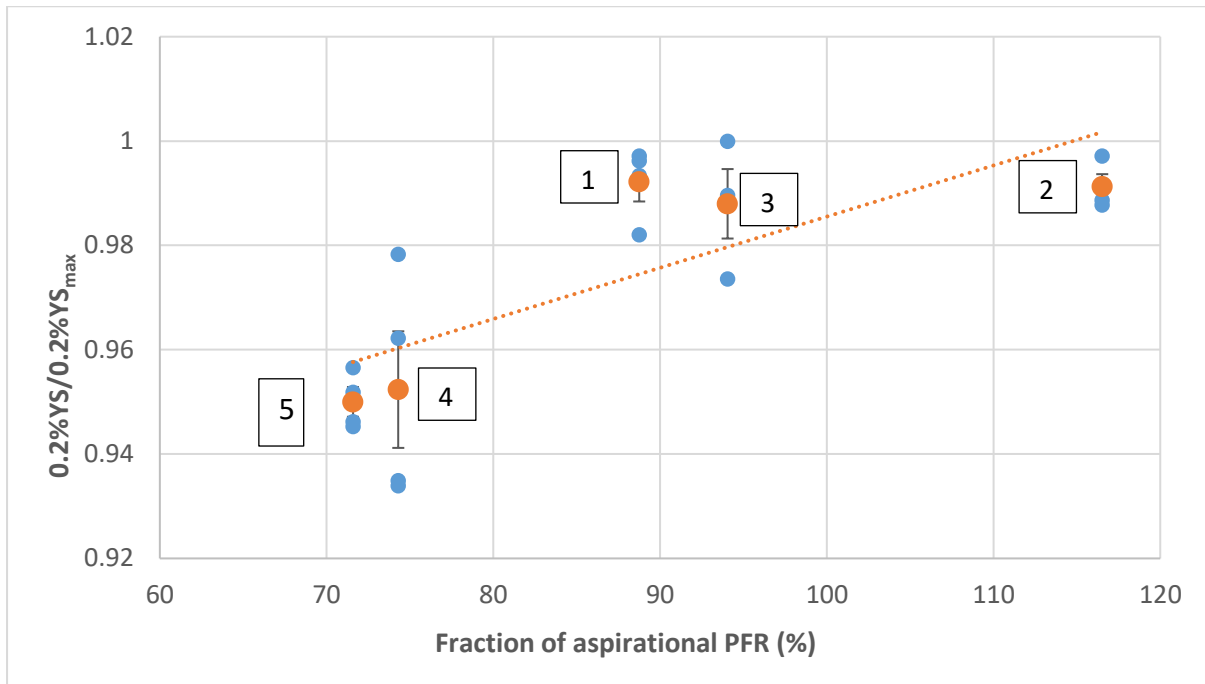


Figure 7.13: Relationship between the 0.2% Yield Stress and the fractional of aspirational PFR used

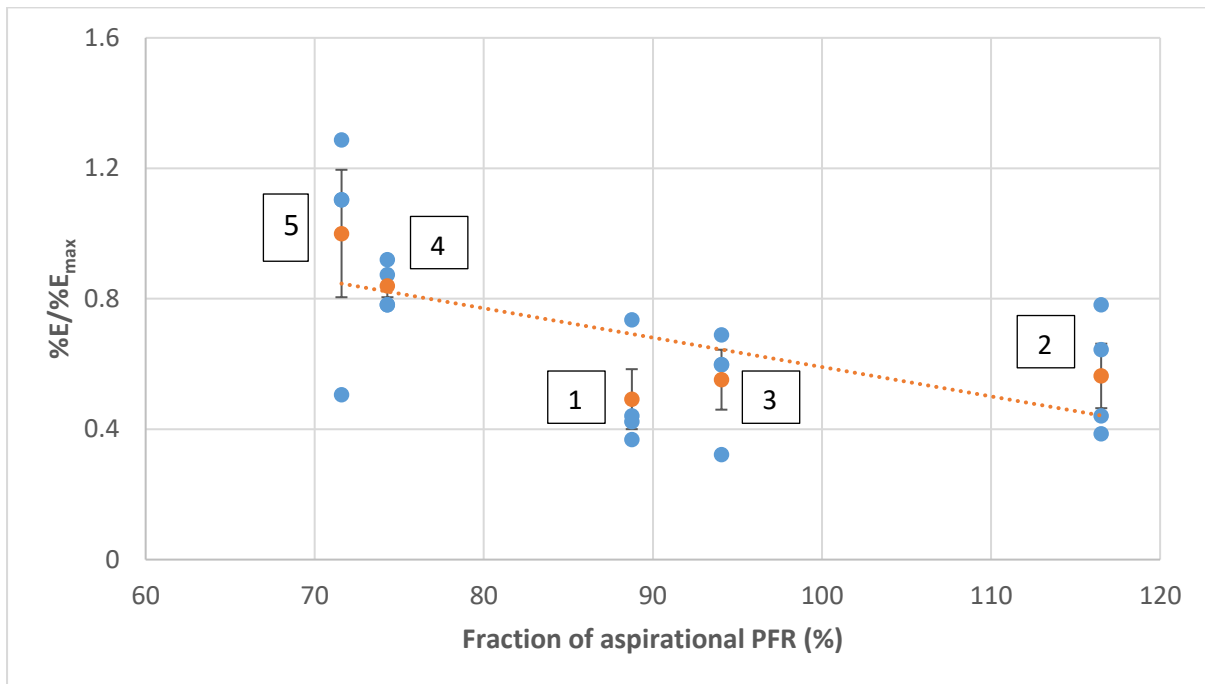


Figure 7.14: Relationship between fraction of aspirational PFR and ductility

Figure 7.14 shows the relationship between the fraction of aspirational PFR and the ductility (as indicated by the elongation to failure). Opposite to the trend shown in Figure 7.13, there is an overall downwards trend in %E as the aspirational PFR is approached. There is also a slight step-change in %E between parameter sets 4 and 1. Although this seems more gradual than the corresponding step in

Powder effects and Melt Pool Saturation

Figure 7.13, the spread in %E on the y-axis is larger than 0.2% YS, making this a more pronounced change.

7.4 Conclusions

The results from the Picasso-based model reveals that due to the low number density of particles in the powder-jet, the powder-laser beam interactions attenuate less than 15W of the total laser power even in the worst case scenario. For this reason, the powder-jet effects on the total power absorbed by the workpiece are assumed to be negligible.

The Picasso model mostly focuses on the powder-jet laser beam interactions and so a new parameter was defined which was the melt pool saturation level (MPSL). This is the ratio between the total melting capacity of the laser and the actual amount of material being melted. This later term is comprised of the powder injected into the melt pool by the powder feed and also the amount of already deposited material being re-melted. Much as in the case of the Picasso model, for the process window defined in this study, the saturation of the melt pool which extremely small at less than 5%.

However, this MPSL and the melting capacity of the laser does set an upper limit on the PFR which is useful to know when looking to optimise the process. Although, for DLD where PFRs are usually quite low (compared to laser cladding) this may not be too much of an issue unless PFR is significantly raised and the laser power is reduced.

A lower limit on the powder feed rate was also defined by setting an aspirational PFR. This is determined by the layer height, hatch spacing and laser velocity. From previous chapters it was shown that the PFR for each of the parameter sets may be affecting the mechanical responses since not everything could be explained using $q^*/v^*l^*h^*$. A general trend was found where as the aspirational PFR is approached, the yield stress increases to maximum and then plateaus as the PFR continues to increase beyond m_p^{asp} . The opposite is true for the elongation to failure which sees a decrease the closer to the aspirational PFR.

8 Conclusions & Future Work

The conclusions from this work are best separated into four different sections. The first concerns the qualification and quantification of the Ti-6246 DLD microstructure. The second concerns the results from the uniaxial tensile tests and the resulting response surfaces produced using linear regression. The modelling of the temperature field using both the Rosenthal and Gaussian definition for the laser beam is the third set of conclusions. Lastly, the investigation into assessing effects of the powder feed rate and the definition of both upper and lower limits to the PFR which can be used to help optimise the process window.

8.1 Ti-6246 DLD Microstructure

- The typical microstructure for Ti-6246 manufactured using direct laser deposition (DLD) consists of an $\alpha+\beta$ lamellar microstructure
- A robust automated method of measuring the size of the α -laths was determined by creating a unique routine using CLEMEX software on back-scattered SEM images taken of the microstructure
- The α -lath widths were mostly $<1\mu\text{m}$ in width throughout the bulk of the builds although there was evidence of dendritic microstructure at the top of the build. This means that all repairs should be over-built to allow for machining (as expected). The fine microstructure is a result of the high cooling rates for DLD process.
- In addition to the dendritic microstructure, a transition zone was found directly underneath the dendritic region. This transition zone is characterised by a bi-lamellar microstructure where extremely fine secondary α -laths can be observed within the β -phase in-between the primary α -laths. Again, this has implications for the amount of overbuild required for machining.
- Although there is significant variation in lath width even within the same specimen, generally as the energy density increase so does the lath width. This is likely due to the excess power providing extra energy to heat previously deposited material, slowing down the cooling rate and hence allowing the microstructure to coarsen.

Conclusions & Future Work

- Builds with identical energy densities showed variations in microstructure, implying that there are other process inputs not being taken into account. The only variable between such parameter sets is the powder feed rate.
- Effects of build height were shown to be limited which is due to the small size of the deposits. It may be that larger builds will have a larger degree of variation between the top and the bottom of the build.
- The process window defined in this work is capable of consistently producing fully-dense and defect-free builds as shown by the XCT results (and SEM). This implies that the mechanical properties will not be influenced by the presence of pores (for example).
- Aluminium loss due to evaporation was shown to be minimal if not negligible. Again implying this will not affect the mechanical properties of the specimens.

8.2 Mechanical properties and response surfaces

- Mechanical testing of the DLD Ti-6246 deposits showed a fair amount of variation even between builds deposited using the same process parameters. This highlights the inherent variability of such a process which is likely due to the large amount of variables that can be adjusted or controlled.
- Variation in the mechanical properties is not exclusive to the DLD material. The baseplate material which is forged Ti-6246 also shows a degree of variation
- Mechanical testing shows that the DLD Ti-6246 shows results that are reasonably comparable to forged material and can reach minimum requirements for DLD repair even in the non-heat treated state.
- Linear regression performed on the mechanical test results produced models to map responses to the process inputs. The model for the 0.2% YS and the %E had p-values <0.05 meaning they were statistically significant. The UTS model was not found to be statistically significant due to the high amount of noise in the data.
- The response surfaces and linear regression revealed that the beam velocity had the most effect on mechanical properties, particularly the yield stress. The hatch spacing had very little effect on the 0.2% yield stress of the material or the %E.
- Response surfaces show how a decrease in q^*/v^*l^* increases the 0.2% yield stress and a decrease in the %E.

Conclusions & Future Work

- The process can be optimised by reducing $1/h^*$ (increasing hatch spacing). This would speed up the process and shouldn't have too much affect on the mechanical properties. Alternatively, the velocity could be increased slightly to achieve the same increase in productivity. The power could also be slightly reduced which would decrease the energy consumption.

8.3 Point heat source and Gaussian models

- The calibration of the parameter "n" in both the Rosenthal and Gaussian temperature field equations allows for a good predictive model for melt depths in both cases for a range of process parameters. The calibration factor (if assumed to be constant) was 0.14 and 0.85 for the Rosenthal and Gaussian models respectively
- The point heat source model is a reasonable thermal model of the laser beam temperature field for Ti-6246 at low line energy densities. However, at higher energies, the level of calibration is unsuitable and there starts to be ever increasing discrepancy between modelled and predicted melt depths.
- The point heat source equation makes reasonable predictions about the temperature field far from the laser beam but tends to infinity at the laser beam centre.
- The Gaussian model takes into account the tendency for the temperature field to approach infinity by the calculation of a characteristic height. For this reason the melt pool depth predictions are more accurate than the point heat source model.
- Both of the models have limitations in the form of the thermal physical properties which are assumed to remain constant and have been taken at room temperature. Similarly, the build temperature was assumed to be constant at 298K.
- Neither of the models take into account the effects of the powder feed.

8.4 Powder effects and PFR limits

- A calculation of the effects of the powder-jet laser beam interaction shows that only a small percentage of power is lost due to the shading effects of the powder particles. This is down to the low powder feed rates and hence the low density of the powder-jet. Increasing the PFR,

Conclusions & Future Work

for example to speed up the deposition process, may result in a more significant attenuation effect.

- A melt pool saturation level (MPSL) has been determined. This is the ratio between the total melting capacity of the laser and the actual amount melted during the process. The amount melted during the process is a combination of the powder delivered by the powder jet and the substrate melting. Much like the Picasso model, for the tensile deposits, the MPSL was found to be almost negligible at no more than 5% in all cases.
- The MPSL can be used as an upper limit when altering the powder feed rate during optimisation. If the velocity of the laser is increased, then the PFR would usually be increased accordingly. Additionally, increasing the PFR could be a way of increasing the productivity of the process by depositing more material per unit time.
- An aspirational powder feed rate was defined as a lower limit on the PFR during optimisation. This is determined by the layer height, hatch spacing and laser beam velocity.
- The aspirational PFR should always be less than the total laser melting capacity. Between these two values is the PFR processing window.
- DoE parameter sets 1, 2 and 3 were deposited at close to the aspirational PFR. These three parameter sets had the finest microstructures and may explain why parameter set 3 is so much finer than parameter set 4 which was deposited with the same E^* ($q^*/v^*l^*h^*$).
- Deposits operating significantly below the aspirational PFR show a markedly lower 0.2% YS than those deposited at close to the aspirational PFR.

8.5 Further work

8.5.1 Testing conditions

Current study: Room temperature mechanical properties of Ti-6246 DLD material was comparable to parent material and certain combinations of the process parameters explored met requirements set by Rolls-Royce for repair application.

Future work: In the case of compressor blisks, the fatigue properties of the component are important. Fatigue tests would be useful to test the performance of the DLD material and compare to results from parent material. In addition, elevated temperature tests (tensile) could be performed on the samples

Conclusions & Future Work

to see how the properties are affected by non-room temperature testing which is more representative of in-service conditions.

8.5.2 Assessment of optimisation recommendations

Current study: The current process window can produce dense and defect-free Ti-6246 DLD material.

Future work: Linear regression and response surface analysis indicate that the current process window could be further optimised, not in terms of mechanical properties but in terms of productivity and energy-consumption. This is of interest when scaling up this repair technology for industrial and commercial use. This can be achieved by decreasing beam power or increasing beam velocity. The effect this has on build quality still needs to be considered to ensure good mechanical properties. In addition to this, the values determined for the upper and lower limits for PFR should also be explored.

8.5.3 Expansion of the thermal model for elevated temperatures

Current study: A thermal model based on a Gaussian laser source was developed and used to predict melt pool depths and hence define a new parameter – melt pool saturation level (MPSL).

Future work: Although the results from the thermal model developed in this study was validated against a real build, the value used for T_0 was 298K (room temperature) which is not an accurate representation of the real DLD process. Determination of a more accurate build temperature would help to improve the model being used. This could be achieved by placing thermocouples underneath the substrate to measure the build temperature for the duration of a deposit. A new value for T_0 could also help to inform new values for thermophysical properties such as thermal diffusivity and conductivity which were assumed to be temperature independent.

8.5.4 Quality assurance

Current study: Both 2-D (SEM) and 3-D (XCT) analysis techniques were used to assess the build quality of the DLD deposits. Both methods agreed that the builds were consistently dense and free of any major defects such as large pores or cracks.

Future work: To gain confidence in the DLD repair process and the chosen process parameters, thorough investigation into the condition of the build is required for quality assurance purposes. However, once adopted as a commercial repair technique, XCT is an expensive and potentially unnecessary step. Investigation into correlating results from NDT techniques including ultrasonic, eddy current, dye penetrant and surface profiling with porosity levels could be valuable as simple quality assessment tools.

Conclusions & Future Work

8.5.5 Additional process parameters

Current work: The process window explored in this study looked at the effect of changing energy density (by varying v^*), hatch spacing ($1/h^*$) and powder feed rate (PFR).

Future work: Additional parameters that could be investigated include but are not limited to; laser power, gas flow rates, shielding gases (Ar, He etc), laser spot size and Ti-6246 particle size distribution.

References

References

- [1] M. Peters, J. Kumpfert, C.H. Ward, C. Leyens, Titanium alloys for aerospace applications, *Adv. Eng. Mater.* (2003). <https://doi.org/10.1002/adem.200310095>.
- [2] H. Qi, M. Azer, a. Ritter, Studies of Standard Heat Treatment Effects on Microstructure and Mechanical Properties of Laser Net Shape Manufactured INCONEL 718, *Metall. Mater. Trans. A.* 40 (2009) 2410–2422. <https://doi.org/10.1007/s11661-009-9949-3>.
- [3] F. Liu, X. Lin, C. Huang, M. Song, G. Yang, J. Chen, W. Huang, The effect of laser scanning path on microstructures and mechanical properties of laser solid formed nickel-base superalloy Inconel 718, *J. Alloys Compd.* 509 (2011) 4505–4509. <https://doi.org/10.1016/j.jallcom.2010.11.176>.
- [4] B.E. Carroll, T. a. Palmer, A.M. Beese, Anisotropic tensile behavior of Ti–6Al–4V components fabricated with directed energy deposition additive manufacturing, *Acta Mater.* 87 (2015) 309–320. <https://doi.org/10.1016/j.actamat.2014.12.054>.
- [5] S.S. Al-Bermani, An Investigation into Microstructure and Microstructural Control of Additive Layer Manufactured Ti-6Al-4V by Electron Beam Melting, (2011) 238. <http://etheses.whiterose.ac.uk/14694/1/555712.pdf>.
- [6] M. Whittaker, Titanium in the Gas Turbine Engine, *Adv. Gas Turbine Technol.* 4 (2011). <https://doi.org/10.5772/21524>.
- [7] T. Aina, C.O. Folayan, G.Y. Pam, Influence of Compression Ratio on the Performance Characteristics of a Spark Ignition Engine, *Adv. Appl. Sci. Res.* 3 (2012) 1915–1922. <http://www.imedpub.com/articles/influence-of-compression-ratio-on-the-performance-characteristics-of-a-sparkignition-engine.pdf>.
- [8] H.M. Flower, Microstructural development in relation to hot working of titanium alloys, *Mater. Sci. Technol.* 6 (1990) 1082–1092. <https://doi.org/10.1179/026708390790189984>.
- [9] C. Leyens, M. Peters, Titanium and Titanium Alloys, 2003. <https://doi.org/10.1002/3527602119>.
- [10] I. Polmear, D. StJohn, J.-F. Nie, M. Qian, I. Polmear, D. StJohn, J.-F. Nie, M. Qian, Light Alloys: Metallurgy of the light metals, in: *Light Alloy.*, Butterworth-Heinemann, 2017: pp. 369–460. <https://doi.org/10.1016/B978-0-08-099431-4.00007-5>.

References

- [11] W.G. Burgers, On the process of transition of the cubic-body-centered modification into the hexagonal-close-packed modification of zirconium, *Physica*. 1 (1934) 561–586.
[https://doi.org/10.1016/S0031-8914\(34\)80244-3](https://doi.org/10.1016/S0031-8914(34)80244-3).
- [12] J.B. Newkirk, A.H. Geisler, Crystallographic aspects of the beta to alpha transformation in titanium, *Acta Metall.* 1 (1953). [https://doi.org/10.1016/0001-6160\(53\)90113-8](https://doi.org/10.1016/0001-6160(53)90113-8).
- [13] N. Stanford, P.S. Bate, Crystallographic variant selection in Ti-6Al-4V, *Acta Mater.* 52 (2004) 5215–5224. <https://doi.org/10.1016/j.actamat.2004.07.034>.
- [14] D. Rugg, M. Dixon, F.P.E. Dunne, Effective structural unit size in titanium alloys, *J. Strain Anal. Eng. Des.* 42 (2007) 269–279. <https://doi.org/10.1243/03093247JSA273>.
- [15] G.A. Sargent, K.T. Kinsel, A.L. Pilchak, A.A. Salem, S.L. Semiatin, Variant selection during cooling after beta annealing of Ti-6Al-4V ingot material, *Metall. Mater. Trans. A Phys. Metall. Mater. Sci.* 43 (2012) 3570–3585. <https://doi.org/10.1007/s11661-012-1245-y>.
- [16] P.S. Davies, B.P. Wynne, W.M. Rainforth, M.J. Thomas, P.L. Threadgill, Development of microstructure and crystallographic texture during stationary shoulder friction stir welding of Ti-6Al-4V, *Metall. Mater. Trans. A Phys. Metall. Mater. Sci.* 42 (2011) 2278–2289.
<https://doi.org/10.1007/s11661-011-0606-2>.
- [17] a. a. Antonysamy, J. Meyer, P.B. Prangnell, Effect of build geometry on the β -grain structure and texture in additive manufacture of Ti6Al4V by selective electron beam melting, *Mater. Charact.* 84 (2013) 153–168. <https://doi.org/10.1016/j.matchar.2013.07.012>.
- [18] S.S. Al-Bermani, M.L. Blackmore, W. Zhang, I. Todd, The origin of microstructural diversity, texture, and mechanical properties in electron beam melted Ti-6Al-4V, *Metall. Mater. Trans. A Phys. Metall. Mater. Sci.* 41 (2010) 3422–3434. <https://doi.org/10.1007/s11661-010-0397-x>.
- [19] G. Lütjering, J.C. Williams, *Titanium : Engineering Materials and Processes*, Ed. SPRINGER. second edi (2007) 1–442. <https://doi.org/10.1007/978-3-540-73036-1>.
- [20] B. Ralph, *Titanium alloys: An atlas of structures and fracture features*, 2008.
<https://doi.org/10.1016/j.matchar.2007.01.007>.
- [21] K. Firm, R. Boyer, G. Welsch, *Materials Properties Handbook: Titanium Alloys*, 1994.
<https://doi.org/http://www.sciencedirect.com/science/article/pii/S0045782504000313>.

References

- [22] G. Wang, Z. Chen, J. Li, J. Liu, Q. Wang, R. Yang, Microstructure and Mechanical Properties of Electron Beam Welded Titanium Alloy Ti-6246, *J. Mater. Sci. Technol.* 34 (2018) 570–576. <https://doi.org/10.1016/j.jmst.2016.10.007>.
- [23] S. Yang, H. Brokmeier, Z.Y. Zhong, M. Jiang, N. Schell, Characterization of phase transformation of Ti-6246 through thermal treatments using high energy synchrotron X-Ray radiation, (n.d.) 2–3.
- [24] B. Cantor, H. Assender, P. Grant, *Aerospace Materials, Ser. Mater. Sci. Eng.* (2001) 556. <https://doi.org/10.1108/eb037525>.
- [25] A.M.M. García, BLISK Fabrication by Linear Friction Welding, *Adv. Gas Turbine Technol.* 365 (2011) 411–435. <https://doi.org/10.5772/2127>.
- [26] F.C. Campbell, *Manufacturing Technology for Aerospace Structural Materials*, in: *Manuf. Technol. Aerosp. Struct. Mater.*, Elsevier, 2006: pp. 211–272. <https://doi.org/http://dx.doi.org/10.1016/B978-185617495-4/50006-8>.
- [27] M. Jackson, R.J. Dashwood, L. Christodoulou, H.M. Flower, Isothermal subtransus forging of Ti-6Al-2Sn-4Zr-6Mo, *J. Light Met.* 2 (2002) 185–195. [https://doi.org/10.1016/S1471-5317\(02\)00044-5](https://doi.org/10.1016/S1471-5317(02)00044-5).
- [28] J. Donachie, J. M, *Titanium – A Technical Guide*, ASM Int. 2nd Ed. 55 (2000) 1023–1026. <https://doi.org/10.1016/j.scriptamat.2006.08.010>.
- [29] T. Ahmed, H.J. Rack, Phase transformations during cooling in $\alpha+\beta$ titanium alloys, *Mater. Sci. Eng. A.* 243 (1998) 206–211. [https://doi.org/10.1016/S0921-5093\(97\)00802-2](https://doi.org/10.1016/S0921-5093(97)00802-2).
- [30] T.F. Broderick, A.G. Jackson, H. Jones, F.H. Froes, The effect of cooling conditions on the microstructure of rapidly solidified Ti-6Al-4V, *Metall. Trans. A.* 16 (1985) 1951–1959. <https://doi.org/10.1007/BF02662396>.
- [31] L. Thijs, F. Verhaeghe, T. Craeghs, J. Van Humbeeck, J.P. Kruth, A study of the microstructural evolution during selective laser melting of Ti-6Al-4V, *Acta Mater.* 58 (2010) 3303–3312. <https://doi.org/10.1016/j.actamat.2010.02.004>.
- [32] Y. Fan, W. Tian, Y. Guo, Z. Sun, J. Xu, Relationships among the Microstructure, Mechanical Properties, and Fatigue Behavior in Thin Ti6Al4V, *Adv. Mater. Sci. Eng.* 2016 (2016). <https://doi.org/10.1155/2016/7278267>.

References

- [33] P.L. Blackwell, A. Wisbey, Laser-aided manufacturing technologies; their application to the near-net shape forming of a high-strength titanium alloy, *J. Mater. Process. Technol.* 170 (2005) 268–276. <https://doi.org/10.1016/j.jmatprotec.2005.05.014>.
- [34] G. Lütjering, Influence of processing on microstructure and mechanical properties of (α + β) titanium alloys, *Mater. Sci. Eng. A.* 243 (1998) 32–45. [https://doi.org/10.1016/S0921-5093\(97\)00778-8](https://doi.org/10.1016/S0921-5093(97)00778-8).
- [35] I. Gibson, D.W.D.W. Rosen, B. Stucker, *Additive Manufacturing Technologies: Rapid Prototyping to Direct Digital Manufacturing*, 2009. <https://doi.org/10.1007/978-1-4419-1120-9>.
- [36] Y. Tian, D. Mcallister, H. Colijn, M. Mills, D. Farson, M. Nordin, S. Babu, Rationalization of Microstructure Heterogeneity in INCONEL 718 Builds Made by the Direct Laser Additive Manufacturing Process, *Metall. Mater. Trans. A.* 45A (2014) 4470–4483. <https://doi.org/10.1007/s11661-014-2370-6>.
- [37] L. Qian, J. Mei, J. Liang, X. Wu, Influence of position and laser power on thermal history and microstructure of direct laser fabricated Ti–6Al–4V samples, *Mater. Sci. Technol.* 21 (2005) 597–605. <https://doi.org/10.1179/174328405X21003>.
- [38] R. Engeli, T. Etter, S. Hövel, K. Wegener, Processability of different IN738LC powder batches by selective laser melting, *J. Mater. Process. Technol.* 229 (2016) 484–491. <https://doi.org/10.1016/j.jmatprotec.2015.09.046>.
- [39] J. Kummailil, C. Sammarco, D. Skinner, C.A. Brown, K. Rong, Effect of select LENS™ processing parameters on the deposition of Ti-6Al-4V, *J. Manuf. Process.* 7 (2005) 42–50. [https://doi.org/10.1016/S1526-6125\(05\)70080-3](https://doi.org/10.1016/S1526-6125(05)70080-3).
- [40] R.R. Dehoff, M.M. Kirka, W.J. Sames, H. Bilheux, a. S. Tremsin, L.E. Lowe, S.S. Babu, Site specific control of crystallographic grain orientation through electron beam additive manufacturing, *Mater. Sci. Technol.* 000 (2014) 1743284714Y.000. <https://doi.org/10.1179/1743284714Y.0000000734>.
- [41] E. Soylemez, J.L. Beuth, K. Taminger, Controlling Melt Pool Dimensions over a Wide Range of Material Deposition Rates in Electron Beam Additive Manufacturing, *Proc. 2010 Solid Free. Fabr. Symp.* (2010) 571–582. <http://utwired.engr.utexas.edu/lff/symposium/proceedingsArchive/pubs/Manuscripts/2010/>

References

- 2010-48-Soylemez.pdf.
- [42] H.P. Tang, M. Qian, N. Liu, X.Z. Zhang, G.Y. Yang, J. Wang, Effect of Powder Reuse Times on Additive Manufacturing of Ti-6Al-4V by Selective Electron Beam Melting, *Jom*. 67 (2015) 555–563. <https://doi.org/10.1007/s11837-015-1300-4>.
- [43] M. Gharbi, P. Peyre, C. Gorny, M. Carin, S. Morville, P. Le Masson, D. Carron, R. Fabbro, Influence of various process conditions on surface finishes induced by the direct metal deposition laser technique on a Ti-6Al-4V alloy, *J. Mater. Process. Technol.* 213 (2013) 791–800. <https://doi.org/10.1016/j.jmatprotec.2012.11.015>.
- [44] a J. Pinkerton, L. Li, An analytical model of energy distribution in laser direct metal deposition, *Proc. Inst. Mech. Eng. Part B J. Eng. Manuf.* 218 (2004) 363–374. <https://doi.org/10.1243/095440504323055498>.
- [45] K. Shah, A.J. Pinkerton, A. Salman, L. Li, Effects of melt pool variables and process parameters in laser direct metal deposition of aerospace alloys, *Mater. Manuf. Process.* 25 (2010) 1372–1380. <https://doi.org/10.1080/10426914.2010.480999>.
- [46] S. Bontha, N.W. Klingbeil, P. a. Kobryn, H.L. Fraser, Thermal process maps for predicting solidification microstructure in laser fabrication of thin-wall structures, *J. Mater. Process. Technol.* 178 (2006) 135–142. <https://doi.org/10.1016/j.jmatprotec.2006.03.155>.
- [47] L. Costa, R. Vilar, T. Reti, a. M. Deus, Rapid tooling by laser powder deposition: Process simulation using finite element analysis, *Acta Mater.* 53 (2005) 3987–3999. <https://doi.org/10.1016/j.actamat.2005.05.003>.
- [48] X. Wu, J. Liang, J. Mei, C. Mitchell, P.S. Goodwin, W. Voice, Microstructures of laser-deposited Ti-6Al-4V, *Mater. Des.* 25 (2004) 137–144. <https://doi.org/10.1016/j.matdes.2003.09.009>.
- [49] X. Zhao, J. Chen, X. Lin, W. Huang, Study on microstructure and mechanical properties of laser rapid forming Inconel 718, *Mater. Sci. Eng. A.* 478 (2008) 119–124. <https://doi.org/10.1016/j.msea.2007.05.079>.
- [50] W.E. King, A.T. Anderson, R.M. Ferencz, N.E. Hodge, C. Kamath, S.A. Khairallah, A. Rubenchik, Laser powder bed fusion additive manufacturing of metals ; physics , computational , and materials challenges, 041304 (2016) 1–53. <https://doi.org/10.1063/1.4937809>.
- [51] W.J. Sames, K. a. Unocic, R.R. Dehoff, T. Lolla, S.S. Babu, Thermal effects on microstructural

References

- heterogeneity of Inconel 718 materials fabricated by electron beam melting, *J. Mater. Res.* 29 (2014) 1920–1930. <https://doi.org/10.1557/jmr.2014.140>.
- [52] N. Tepylo, X. Huang, P.C. Patnaik, Laser-Based Additive Manufacturing Technologies for Aerospace Applications, *Adv. Eng. Mater.* 21 (2019) 1–35. <https://doi.org/10.1002/adem.201900617>.
- [53] D.D. Gu, W. Meiners, K. Wissenbach, R. Poprawe, Laser additive manufacturing of metallic components: materials, processes and mechanisms, *Int. Mater. Rev.* 57 (2012) 133–164. <https://doi.org/10.1179/1743280411Y.0000000014>.
- [54] M. Gäumann, C. Bezençon, P. Canalis, W. Kurz, Single-crystal laser deposition of superalloys: Processing-microstructure maps, *Acta Mater.* 49 (2001) 1051–1062.
- [55] T. Amine, J.W. Newkirk, F. Liou, Investigation of effect of process parameters on multilayer builds by direct metal deposition, *Appl. Therm. Eng.* 73 (2014) 498–509. <https://doi.org/10.1016/j.applthermaleng.2014.08.005>.
- [56] N. Hrabe, T. Quinn, Effects of processing on microstructure and mechanical properties of a titanium alloy (Ti-6Al-4V) fabricated using electron beam melting (EBM), part 1: Distance from build plate and part size, *Mater. Sci. Eng. A.* 573 (2013) 264–270. <https://doi.org/10.1016/j.msea.2013.02.064>.
- [57] N. Hrabe, T. Quinn, Effects of processing on microstructure and mechanical properties of a titanium alloy (Ti-6Al-4V) fabricated using electron beam melting (EBM), Part 2: Energy input, orientation, and location, *Mater. Sci. Eng. A.* 573 (2013) 271–277. <https://doi.org/10.1016/j.msea.2013.02.065>.
- [58] C. Zhong, J. Liu, T. Zhao, T. Schopphoven, J. Fu, A. Gasser, J.H. Schleifenbaum, Laser Metal Deposition of Ti6Al4V—A Brief Review, *Appl. Sci.* 10 (2020) 764. <https://doi.org/10.3390/app10030764>.
- [59] A. Dass, A. Moridi, State of the art in directed energy deposition: From additive manufacturing to materials design, *Coatings.* 9 (2019) 1–26. <https://doi.org/10.3390/COATINGS9070418>.
- [60] S. Kaierle, A. Barroi, C. Noelke, J. Hermsdorf, L. Overmeyer, H. Haferkamp, Review on Laser Deposition Welding: From Micro to Macro, *Phys. Procedia.* 39 (2012) 336–345. <https://doi.org/10.1016/j.phpro.2012.10.046>.

References

- [61] S.M. Yusuf, S. Cutler, N. Gao, Review: The impact of metal additive manufacturing on the aerospace industry, *Metals (Basel)*. 9 (2019). <https://doi.org/10.3390/met9121286>.
- [62] L. Xue, Laser consolidation - A one-step manufacturing process for making net-shaped functional aerospace components, *SAE Tech. Pap.* (2006). <https://doi.org/10.4271/2006-01-3163>.
- [63] R. Liu, Z. Wang, T. Sparks, F. Liou, J. Newkirk, Aerospace applications of laser additive manufacturing, in: *Laser Addit. Manuf. Mater. Des. Technol. Appl.*, 2017. <https://doi.org/10.1016/B978-0-08-100433-3.00013-0>.
- [64] M. Zenou, L. Grainger, Additive manufacturing of metallic materials, in: *Addit. Manuf.*, 2018. <https://doi.org/10.1016/b978-0-12-812155-9.00003-7>.
- [65] M. Heilemann, J. Beckmann, D. Konigorski, C. Emmelmann, Laser metal deposition of bionic aluminum supports: Reduction of the energy input for additive manufacturing of a fuselage, *Procedia CIRP*. 74 (2018) 136–139. <https://doi.org/10.1016/j.procir.2018.08.063>.
- [66] W. Xue, B.V. Krishna, A. Bandyopadhyay, S. Bose, Processing and biocompatibility evaluation of laser processed porous titanium, *Acta Biomater*. 3 (2007) 1007–1018. <https://doi.org/10.1016/j.actbio.2007.05.009>.
- [67] J. Verwimp, M. Rombouts, E. Geerinckx, F. Motmans, Applications of laser clad WC-based wear resistant coatings, *Phys. Procedia*. 12 (2011) 330–337. <https://doi.org/10.1016/j.phpro.2011.03.042>.
- [68] L. Quintino, Overview of coating technologies, in: *Surf. Modif. by Solid State Process.*, 2014. <https://doi.org/10.1533/9780857094698.1>.
- [69] V. Ocelík, N. Janssen, S.N. Smith, J.T.M. De Hosson, Additive Manufacturing of High-Entropy Alloys by Laser Processing, *Jom*. 68 (2016) 1810–1818. <https://doi.org/10.1007/s11837-016-1888-z>.
- [70] T.M. Yue, H. Zhang, Laser cladding of FeCoNiCrAlCuSi_{0.5} high entropy alloys on AZ31 Mg alloy substrates, *Mater. Res. Innov.* 18 (2014) S2624–S2628. <https://doi.org/10.1179/1432891714Z.000000000530>.
- [71] D. Patra Karmakar, G. Muvvala, A.K. Nath, Effect of scan strategy and heat input on the shear strength of laser clad Stellite 21 layers on AISI H13 tool steel in as-deposited and heat

References

- treated conditions, *Surf. Coatings Technol.* 384 (2020).
<https://doi.org/10.1016/j.surfcoat.2019.125331>.
- [72] M. Brandt, *Laser Additive Manufacturing Materials, Design, Technologies, and Applications.*, Elsevier Science, 2016.
- [73] B.C. Oberländer, E. Lugscheider, Comparison of properties of coatings produced by laser cladding and conventional methods, *Mater. Sci. Technol. (United Kingdom)*. 8 (1992) 657–665. <https://doi.org/10.1179/mst.1992.8.8.657>.
- [74] A. Calleja, I. Taberner, A. Fernández, A. Celaya, A. Lamikiz, L.N. López De Lacalle, Improvement of strategies and parameters for multi-axis laser cladding operations, *Opt. Lasers Eng.* 56 (2014) 113–120. <https://doi.org/10.1016/j.optlaseng.2013.12.017>.
- [75] A.S. Khanna, S. Kumari, S. Kanungo, A. Gasser, Hard coatings based on thermal spray and laser cladding, *Int. J. Refract. Met. Hard Mater.* 27 (2009) 485–491.
<https://doi.org/10.1016/j.ijrmhm.2008.09.017>.
- [76] J.M. Wilson, C. Piya, Y.C. Shin, F. Zhao, K. Ramani, Remanufacturing of turbine blades by laser direct deposition with its energy and environmental impact analysis, *J. Clean. Prod.* 80 (2014) 170–178. <https://doi.org/10.1016/j.jclepro.2014.05.084>.
- [77] K. Ramani, D. Ramanujan, W.Z. Bernstein, F. Zhao, J. Sutherland, C. Handwerker, J.K. Choi, H. Kim, D. Thurston, Integrated sustainable life cycle design: A Review, *J. Mech. Des. Trans. ASME*. 132 (2010) 0910041–09100415. <https://doi.org/10.1115/1.4002308>.
- [78] C. Piya, J.M. Wilson, S. Murugappan, Y. Shin, K. Ramani, Virtual repair: Geometric reconstruction for remanufacturing gas turbine blades, *Proc. ASME Des. Eng. Tech. Conf.* 9 (2011) 895–904. <https://doi.org/10.1115/DETC2011-48652>.
- [79] E.M. Birger, G. V. Moskvitin, A.N. Polyakov, V.E. Arkhipov, Industrial laser cladding: Current state and future, *Weld. Int.* 25 (2011) 234–243.
<https://doi.org/10.1080/09507116.2010.540880>.
- [80] M. Hedges, N. Calder, Near net shape rapid manufacture & repair by LENS, in: *Cost Eff. Manuf. via Net-Shape Process, Meet. Proc. RTO-MP-AVT-139*. 2 (2006) 13.
- [81] A.J. Pinkerton, W. Wang, L. Li, Component repair using laser direct metal deposition, *Proc. Inst. Mech. Eng. Part B J. Eng. Manuf.* 222 (2008) 827–836.

References

- <https://doi.org/10.1243/09544054JEM1008>.
- [82] Q. Liu, Y. Wang, H. Zheng, K. Tang, H. Li, S. Gong, TC17 titanium alloy laser melting deposition repair process and properties, *Opt. Laser Technol.* 82 (2016) 1–9.
<https://doi.org/10.1016/j.optlastec.2016.02.013>.
- [83] T. Petrat, B. Graf, A. Gumenyuk, M. Rethmeier, Laser metal deposition as repair technology for a gas turbine burner made of inconel 718, *Phys. Procedia.* 83 (2016) 761–768.
<https://doi.org/10.1016/j.phpro.2016.08.078>.
- [84] S. Bontha, N.W. Klingbeil, P. a. Kobryn, H.L. Fraser, Effects of process variables and size-scale on solidification microstructure in beam-based fabrication of bulky 3D structures, *Mater. Sci. Eng. A.* 513–514 (2009) 311–318. <https://doi.org/10.1016/j.msea.2009.02.019>.
- [85] H.E. Cline, T.R. Anthony, Heat treating and melting material with a scanning laser or electron beam, *J. Appl. Phys.* 48 (1977) 3895–3900. <https://doi.org/10.1063/1.324261>.
- [86] A.J. Pinkerton, L. Li, Modelling the geometry of a moving laser melt pool and deposition track via energy and mass balances, *J. Phys. D. Appl. Phys.* 37 (2004) 1885–1895.
<https://doi.org/10.1088/0022-3727/37/14/003>.
- [87] M. Picasso, C.F. Marsden, J.D. Wagniere, A. Frenk, M. Rappaz, A Simple but Realistic Model for Laser Cladding, *Metall. Mater. Trans. B.* 25B (1994) 281–291.
- [88] T.W. Eagar, N.S. Tsai, Temperature fields produced by traveling distributed heat sources, *Weld. J.* 62 (1983) 346–355.
- [89] D. Rosenthal, The Theory of Moving Sources of Heat and Its Application to Metal Treatments - Part I, *Trans. ASME.* 68 (1946) 849–862.
- [90] D. Rosenthal, The Theory of Moving Sources of Heat and Its Application to Metal Treatments - Part II, *Trans. ASME.* 68 (1946) 863–866.
- [91] R.B. Bird, W.E. Stewart, E.N. Lightfoot, *Transport Phenomena*, 2002.
- [92] MatWeb; Material Property Data, Titanium Ti-6Al-2Sn-4Zr-6Mo (Ti-6-2-4-6) STA-1, (n.d.).
<http://www.matweb.com/search/DataSheet.aspx?MatGUID=21a38a6ffc2e4932b857de46683d77a6&ckck=1> (accessed October 7, 2018).
- [93] N.T. Nguyen, A. Ohta, K. Matsuoka, N. Suzuki, Y. Maeda, Analytical Solutions for Transient

References

- Temperature of Semi-Infinite Body Subjected to 3-D Moving Heat Sources, *Weld. Res. Suppl.* 1 (1999) 265–274. e:%5CBIBLIO%5CArticles%5CSolution_transient-temp-3D-moving-heat-source_Nguyen_1999.pdf.
- [94] M.F. Ashby, K.E. Easterling, The transformation hardening of steel surfaces by laser beams-I. Hypo-eutectoid steels, *Acta Metall.* 32 (1984). [https://doi.org/10.1016/0001-6160\(84\)90175-5](https://doi.org/10.1016/0001-6160(84)90175-5).
- [95] H.R. Shercliff, M.F. Ashby, The prediction of case depth in laser transformation hardening, *Metall. Trans. A.* 22 (1991) 2459–2466. <https://doi.org/10.1007/BF02665012>.
- [96] N. Ahmed, K.T. Voisey, D.G. McCartney, Investigation into the effect of beam shape on melt pool characteristics using analytical modelling, *Opt. Lasers Eng.* 48 (2010) 548–554. <https://doi.org/10.1016/j.optlaseng.2009.12.013>.
- [97] S. Li, H. Xiao, K. Liu, W. Xiao, Y. Li, X. Han, J. Mazumder, L. Song, Melt-pool motion, temperature variation and dendritic morphology of Inconel 718 during pulsed- and continuous-wave laser additive manufacturing: A comparative study, *Mater. Des.* 119 (2017) 351–360. <https://doi.org/10.1016/j.matdes.2017.01.065>.
- [98] C. Baykasoglu, O. Akyildiz, D. Candemir, Q. Yang, A.C. To, Predicting microstructure evolution during directed energy deposition additive manufacturing of Ti-6Al-4V, *J. Manuf. Sci. Eng.* 140 (2018) 1–11. <https://doi.org/10.1115/1.4038894>.
- [99] G. Vastola, G. Zhang, Q.X. Pei, Y.W. Zhang, Modeling the Microstructure Evolution During Additive Manufacturing of Ti6Al4V: A Comparison Between Electron Beam Melting and Selective Laser Melting, *Jom.* 68 (2016) 1370–1375. <https://doi.org/10.1007/s11837-016-1890-5>.
- [100] Y. Fan, P. Cheng, Y.L. Yao, Z. Yang, K. Eglund, Effect of phase transformations on laser forming of Ti-6Al-4V alloy, *J. Appl. Phys.* 98 (2005). <https://doi.org/10.1063/1.1944202>.
- [101] S.M. Kelly, S.L. Kampe, Microstructural evolution in laser-deposited multilayer Ti-6Al-4V builds: Part II. Thermal Modeling, *Metall. Mater. Trans. A.* 35 (2004) 1869–1879. <https://doi.org/10.1007/s11661-004-0094-8>.
- [102] V. Manvatkar, A. De, T. DebRoy, Spatial variation of melt pool geometry, peak temperature and solidification parameters during laser assisted additive manufacturing process, *Mater. Sci. Technol.* 31 (2015) 924–930. <https://doi.org/10.1179/1743284714Y.0000000701>.

References

- [103] D.T. Swift-hook, A.E.F. Gick, Penetration Welding with Lasers, *Weld. Res. Suppl.* (1973) 492–499.
- [104] M. Davis, P. Kapadia, J. Dowden, W.M. Steen, C.H.G. Courtney, Heat hardening of metal surfaces with a scanning laser beam, *J. Phys. D. Appl. Phys.* 19 (2000) 1981–1997. <https://doi.org/10.1088/0022-3727/19/10/024>.
- [105] J.C. Ion, H.R. Shercliff, M.F. Ashby, Diagrams for laser materials processing, *Acta Metall. Mater.* 40 (1992) 1539–1551. [https://doi.org/10.1016/0956-7151\(92\)90097-x](https://doi.org/10.1016/0956-7151(92)90097-x).
- [106] A. Vasinonta, J.L. Beuth, M.L. Griffith, A Process Map for Consistent Build Conditions in the Solid Freeform Fabrication of Thin-Walled Structures, *J. Manuf. Sci. Eng.* 123 (2001) 615. <https://doi.org/10.1115/1.1370497>.
- [107] M. Thomas, G.J. Baxter, I. Todd, Normalised model-based processing diagrams for additive layer manufacture of engineering alloys, *Acta Mater.* 108 (2016) 26–35. <https://doi.org/10.1016/j.actamat.2016.02.025>.
- [108] Y.M. Wang, T. Voisin, J.T. McKeown, J. Ye, N.P. Calta, Z. Li, Z. Zeng, Y. Zhang, W. Chen, T.T. Roehling, R.T. Ott, M.K. Santala, P.J. Depond, M.J. Matthews, A. V. Hamza, T. Zhu, Additively manufactured hierarchical stainless steels with high strength and ductility, *Nat. Mater.* 17 (2018) 63–70. <https://doi.org/10.1038/NMAT5021>.
- [109] RPM Innovations Inc., Laser deposition systems, (n.d.). <https://www.rpm-innovations.com/laser-deposition-systems.html>.
- [110] D.R. Cox, N. Reid, *The Theory of the Design of Experiments*, 2002. <https://doi.org/10.1002/sim.1089>.
- [111] R.L. Plackett, J.P. Burman, *The Design of Optimum Multifactorial Experiments*, *Biometrika.* (1946) 305–325.
- [112] ASTM, Norma E8/e8M-11, Standard Test Methods for Tension Testing of Metallic Materials 1, *Am. Soc. Test. Mater. Handb.* (2009) 1–27. <https://doi.org/10.1520/E0008>.
- [113] J.I. Goldstein, D.E. Newbury, J.R. Michael, N.W.M. Ritchie, J.H.J. Scott, D.C. Joy, *Scanning Electron Microscopy and X-Ray Microanalysis*, Springer, 2017. <https://doi.org/10.1007/978-1-4939-6676-9>.
- [114] Nancscience.com, Scanning Electron Microscopy, (n.d.).

References

- <https://www.nanoscience.com/techniques/scanning-electron-microscopy/>.
- [115] S.S.K. B, A Review on Inductively Coupled Plasma Optical Emission Spectrometry (Icp-Oes) with a Special Emphasis on its Application, *Der Pharm. Lett.* 9 (2017) 44–54.
<https://doi.org/10.1039/c39920001222>.
- [116] Thermo Fisher, Inductively Coupled Plasma Optical Emission Spectroscopy (ICP-OES) Information, (n.d.).
- [117] M.M. Rahman, S.B. Khan, H.M. Marwani, A.M. Asiri, K.A. Alamry, Selective Iron(III) ion uptake using CuO-TiO₂ nanostructure by inductively coupled plasma-optical emission spectrometry, *Chem. Cent. J.* 6 (2012) 1. <https://doi.org/10.1186/1752-153X-6-158>.
- [118] N. Velitchkova, O. Veleva, S. Velichkov, N. Daskalova, Possibilities of high resolution inductively coupled plasma optical emission spectrometry in the determination of trace elements in environmental materials, *J. Spectrosc.* 1 (2013).
<https://doi.org/10.1155/2013/505871>.
- [119] E.N. Landis, D.T. Keane, X-ray microtomography, *Mater. Charact.* 61 (2010) 1305–1316.
<https://doi.org/10.1016/j.matchar.2010.09.012>.
- [120] J.P. Kruth, M. Bartscher, S. Carmignato, R. Schmitt, L. De Chiffre, A. Weckenmann, Computed tomography for dimensional metrology, *CIRP Ann. - Manuf. Technol.* 60 (2011) 821–842.
<https://doi.org/10.1016/j.cirp.2011.05.006>.
- [121] M. Neikter, P. Åkerfeldt, R. Pederson, M.L. Antti, Microstructure characterisation of Ti-6Al-4V from different additive manufacturing processes, *IOP Conf. Ser. Mater. Sci. Eng.* 258 (2017).
<https://doi.org/10.1088/1757-899X/258/1/012007>.
- [122] A. Saboori, D. Gallo, S. Biamino, P. Fino, M. Lombardi, An Overview of Additive Manufacturing of Titanium Components by Directed Energy Deposition: Microstructure and Mechanical Properties, *Appl. Sci.* 7 (2017) 883. <https://doi.org/10.3390/app7090883>.
- [123] B. Baufeld, O. Van Der Biest, R. Gault, K. Ridgway, Manufacturing Ti-6Al-4V components by Shaped Metal Deposition: Microstructure and mechanical properties, *IOP Conf. Ser. Mater. Sci. Eng.* 26 (2011). <https://doi.org/10.1088/1757-899X/26/1/012001>.
- [124] R.S. Sandala, Deformation Mechanisms of Two-Phase Titanium Alloys, Phd Thesis. (2012).
- [125] P.C. Collins, B. Welk, T. Searles, J. Tiley, J.C. Russ, H.L. Fraser, Development of methods for the

References

- quantification of microstructural features in $\alpha + \beta$ -processed α/β titanium alloys, *Mater. Sci. Eng. A*. 508 (2009) 174–182. <https://doi.org/10.1016/j.msea.2008.12.038>.
- [126] TIMETAL (R), Ti-6Al-2Sn-4Zr-6Mo data sheet, 2000.
- [127] B. E. O. Hall, The Deformation and Ageing of Mild Steel: III Discussion of Results, *Proc. Phys. Soc. Sect. B*. 64 (1951) 747.
- [128] S.L. Semiatin, T.R. Bieler, The effect of alpha platelet thickness on plastic flow during hot working of Ti-6Al-4V with a transformed microstructure, *Acta Mater.* 49 (2001) 3565–3573. [https://doi.org/10.1016/S1359-6454\(01\)00236-1](https://doi.org/10.1016/S1359-6454(01)00236-1).
- [129] W. Xu, M. Brandt, S. Sun, J. Elambasseril, Q. Liu, K. Latham, K. Xia, M. Qian, Additive manufacturing of strong and ductile Ti-6Al-4V by selective laser melting via in situ martensite decomposition, *Acta Mater.* 85 (2015) 74–84. <https://doi.org/10.1016/j.actamat.2014.11.028>.
- [130] D. Yang, Z. Liu, Quantification of Microstructural Features and Prediction of Mechanical Properties of a Dual-Phase Ti-6Al-4V Alloy, *Materials (Basel)*. 9 (2016) 1–14. <https://doi.org/10.3390/ma9080628>.
- [131] R.C. Picu, A. Majorell, Mechanical behavior of Ti-6Al-4V at high and moderate temperatures - Part II: Constitutive modeling, *Mater. Sci. Eng. A*. 326 (2002) 306–316. [https://doi.org/10.1016/S0921-5093\(01\)01507-6](https://doi.org/10.1016/S0921-5093(01)01507-6).
- [132] I. Ghamarian, B. Hayes, P. Samimi, B.A. Welk, H.L. Fraser, P.C. Collins, Developing a phenomenological equation to predict yield strength from composition and microstructure in β processed Ti-6Al-4V, *Mater. Sci. Eng. A*. 660 (2016) 172–180. <https://doi.org/10.1016/j.msea.2016.02.052>.
- [133] B.J. Hayes, B.W. Martin, B. Welk, S.J. Kuhr, T.K. Ales, D.A. Brice, I. Ghamarian, A.H. Baker, C. V. Haden, D.G. Harlow, H.L. Fraser, P.C. Collins, Predicting tensile properties of Ti-6Al-4V produced via directed energy deposition, *Acta Mater.* 133 (2017) 120–133. <https://doi.org/10.1016/j.actamat.2017.05.025>.
- [134] J.H.K. Tan, S.L. Sing, W.Y. Yeong, Microstructure modelling for metallic additive manufacturing: a review, *Virtual Phys. Prototyp.* 15 (2020) 87–105. <https://doi.org/10.1080/17452759.2019.1677345>.

References

- [135] V. Fallah, M. Amoozezaei, N. Provatas, S.F. Corbin, A. Khajepour, Phase-field simulation of solidification morphology in laser powder deposition of Ti-Nb alloys, *Acta Mater.* 60 (2012) 1633–1646. <https://doi.org/10.1016/j.actamat.2011.12.009>.
- [136] S. Mishra, T. DebRoy, Measurements and Monte Carlo simulation of grain growth in the heat-affected zone of Ti-6Al-4V welds, *Acta Mater.* 52 (2004) 1183–1192. <https://doi.org/10.1016/j.actamat.2003.11.003>.
- [137] F. Lia, J. Park, J. Tressler, R. Martukanitz, Partitioning of laser energy during directed energy deposition, *Addit. Manuf.* 18 (2017) 31–39. <https://doi.org/10.1016/j.addma.2017.08.012>.
- [138] J. Liu, L. Li, Y. Zhang, X. Xie, Attenuation of laser power of a focused Gaussian beam during interaction between a laser and powder in coaxial laser cladding, *J. Phys. D: Appl. Phys.* 38 (2005) 1546–1550. <https://doi.org/10.1088/0022-3727/38/10/008>.
- [139] C. Katinas, W. Shang, Y.C. Shin, J. Chen, Modeling Particle Spray and Capture Efficiency for Direct Laser, *ASME 2017 12th Int. Manuf. Sci. Eng. Conf.* (2017) 1–10.
- [140] C. Katinas, S. Liu, Y.C. Shin, Self-Sufficient Modeling of Single Track Deposition of Ti–6Al–4V With the Prediction of Capture Efficiency, *J. Manuf. Sci. Eng.* 141 (2018) 011001. <https://doi.org/10.1115/1.4041423>.
- [141] R. Cunningham, C. Zhao, N. Parab, C. Kantzos, J. Pauza, K. Fezzaa, T. Sun, A.D. Rollett, Keyhole threshold and morphology in laser melting revealed by ultrahigh-speed x-ray imaging, *Science* (80-.). (2019). <https://doi.org/10.1126/science.aav4687>.

9 Appendix A: CLEMEX routine

01 Clear => All
02 Set Process Frame to 0,0 1124x971 μm

Position 0, 0 pixels

Size 1024 x 885 pixels

Display frame : don't change

Pause on run : yes

[]

03 Gray Threshold
BPL1 range 108.. 133
04 Closing CIRC x2 => BPL1 Extend
05 Trap 10x10, BPL1 -> None
06 Separate SQR => BPL1
07 Object Measures (BPL1) -> OBJM1
Length
Main Length
Width
Breadth

End of Field

10 Appendix B: Pareto Charts

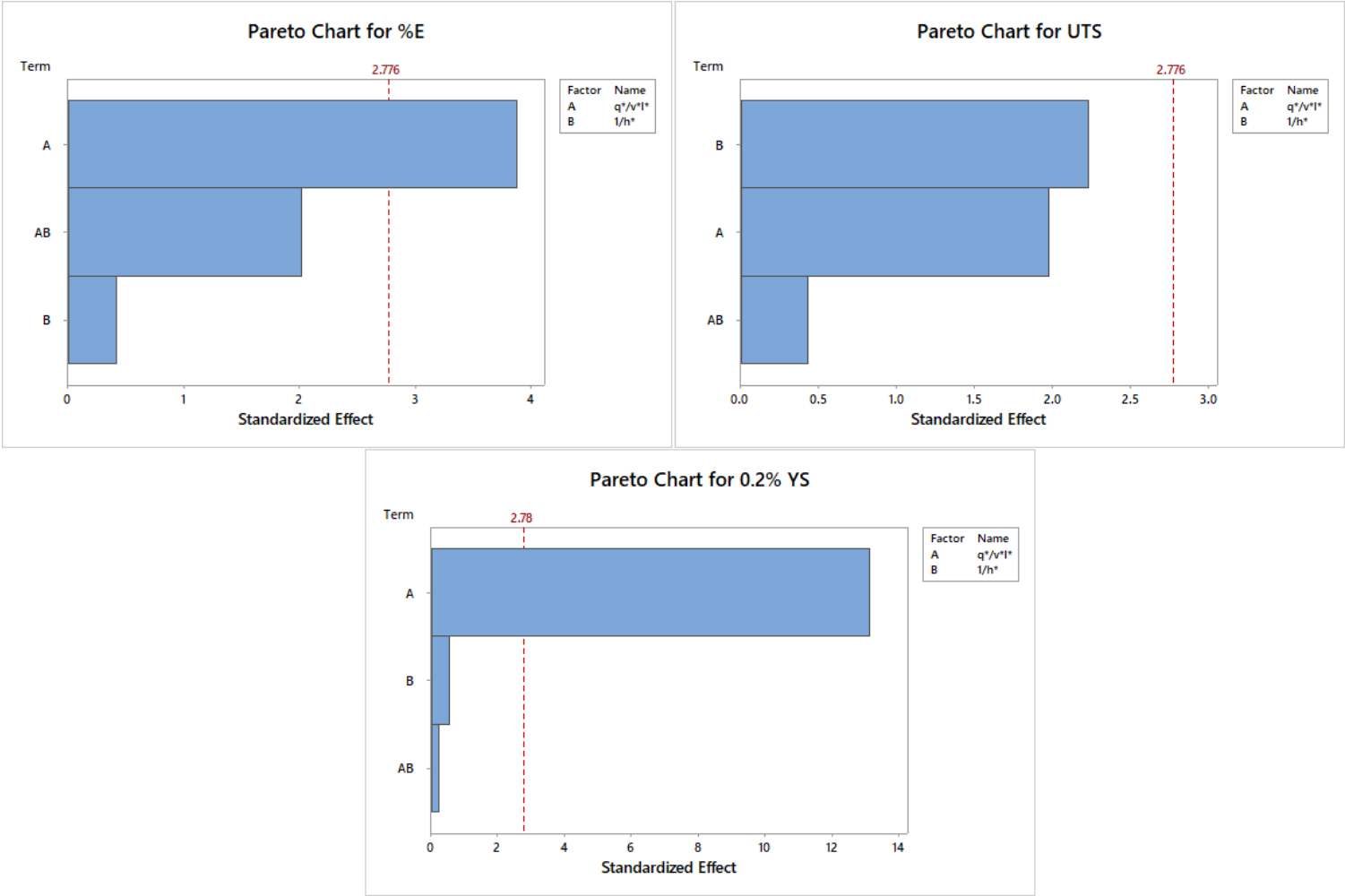


Figure 10.1: Pareto Effect Chart for %E, UTS and 0.2% YS to show standardised effects of $q^*v^*l^*$ and $1/h^*$

11 Appendix C: MATLAB code

```

%% ROSENTHAL EQUATION
%% MATERIAL PARAMETERS%

T0=298;      % Initial Build Temp in K
k=7.7;      % Thermal Conductivity - Wm^-1K^-1
a=3.31E-6;  % Thermal Diffusivity - m^2s^-1
n=0.14;     % Absorption coefficient/calibration factor
q=275;     % Power in W
v=0.0110058; % Beam velocity in ms^-1
Tm=1948;    % Melting temp - K
Tb=1207;    % Beta Transus temperature - K

% Define layer height for representation on plot %

layer=-2.54E-4; % Layer height for build - m
layer2=2*layer; % 2nd Layer
layer3=3*layer; % 3rd Layer
layer4=4*layer;
layer5=5*layer;
layer6=6*layer;

%% GEOMETRY VECTORS%

TmContour=[Tm, Tm];
TbContour=[Tb, Tb];

% y is assumed to be 0 throughout (2-D model)

step=1e-5; % step size for x and z - smaller step size = more accurate
xmin=-0.005;
xmax=0.005;

zmin=-0.005;
zmax=0.005;

x=[xmin:step:xmax];
z=[zmin:step:zmax];

%% CREATE MESHGRID%

[X,Z]=meshgrid(x,z); % co-ordinate matrix

%ROSENTHL EQUATION%

T=((n.*q)/(2.*pi.*k.*(sqrt((X.^2)+(Z.^2))))).*(exp((-v.*(X+(sqrt((X.^2)+(Z.^2)))))/(2.*a))))+T0;

```

Appendix C: MATLAB code

```
%% PLOTTING%

figure(1)

surf(X,Z,T)
set(surf(X,Z,T), 'LineStyle', 'none') % Turn off the mesh lines as it
dominates plot
colormap jet
colorbar
hold on

[C1,H1]=contour3(x,z,T,TmContour, 'black'); % Contour 3 allows the contour
lines to show over the surface plot

[C2,H2]=contour3(x,z,T,TbContour, 'black');

plot(0,0, 'r*'); % laser centre

view(2)

axis([xmin xmax zmin zmax]);

set(gca, 'XAxisLocation', 'top');
set(gca, 'YAxisLocation', 'right');
%legend('Melting temp contour - 1948K', 'Location', 'southwest');
% legend('Contour 1 - 773K', 'Contour 2 - 1073K', 'Contour 3 - Melting temp
1948K');
title('Plot of temperature contours using Rosenthal Solution');

% Create xlabel
xlabel('x axis (m)');

% Create ylabel
ylabel('z axis (m)');

% Set the colour bar limits
set(gca, 'CLim', [298 3000]);

%% MELT DEPTH %%
%%

C1melt=C1; % Makes a copy of C1
C1melt(:,1) = []; % Deletes first column of C1melt
C1meltz=C1melt(2,:); % Copies row 2 of C1melt into C1meltz
C1meltx=C1melt(1,:); % Copies row 1 of C1melt into C1meltx
meltdepth=abs((min(C1meltz))); % Finds the minimum value i.e. max melt
depth

C2melt=C2; % Makes a copy of C2
C2melt(:,1) = []; % Deletes first column of C2melt
C2meltz=C2melt(2,:); % Copies row 2 of C2melt into C2meltz
C2meltx=C2melt(1,:); % Copies row 1 of C2melt into C2meltx
betadepth=abs((min(C2meltz)));

%% Melt pool length %%
```

Appendix C: MATLAB code

```
C1meltxmax=max(C1meltx);
meltlength=abs((min(C1meltx)))+C1meltxmax;
C2meltxmax=max(C2meltx);
betalength=abs((min(C2meltx)))+C2meltxmax;

%% aspect ratio %%

aspect=meltlength/(2*meltdepth);

%%
%% COOLING RATES AND TEMPERATURE DISTRIBUTIONS %%
%%

% INPUT PARAMETERS -- NOTE NON-SI UNITS %

spe_heat=2.325; %specific heat per unit vol - J/cm^3/C

D=0.0331; %thermal diffusivity in cm^2/s
V=1.10058; %velocity of laser scan 0.847 cm/s

%%
%% COOLING RATE VS DISTANCE %%
%%

figure(2)

for z=0:0.0254e-2:0.0762e-2 %layer thickness is 0.0254 cm
x=-1e-2:0.0001e-2:0; %Example value for x co-ordinate in cm

r=sqrt((x.^2)+(z.^2)); %definition of r assuming that y=0

T=((n.*q)./(2.*pi.*k.*r)).*(exp((-v.*(x+r))/(2.*a)))+T0;

C_rate=-v.*((x./(r.^2))+ ((v./(2.*a)).*(1+(x./r)))).*T; % Cooling rate
equation

% PLOT COOLING RATE %

plot(abs(x),C_rate) %Plot the cooling rate (y) against x (x)
xlabel('distance x(m) from laser centre');
ylabel('Cooling Rate (Ks^{-1})');
title('Cooling Rates for different layer depths as a function of distance
from the laser');
axis([0 0.3 0 40000]);

hold on

end
legend('Surface (z=0 cm)', '1st layer (z=0.0254 cm)', '2nd layer (0.0508
cm)', '3rd layer (z=0.0762 cm)', 'Location', 'west');
```

Appendix C: MATLAB code

```
%%
%% COOLING RATE ALONG TM CONTOUR %%

figure (11)

r=sqrt((Clmeltx.^2)+(Clmeltz.^2)); %definition of r for the contour line

T=1948; % For Tm contour

C_rateTm=-v.*((Clmeltx./(r.^2))+ ((v./(2.*a)).*(1+(Clmeltx./r)))).*T; %
Cooling rate equation

plot(Clmeltz,C_rateTm)

hold on

% % PLOT COOLING RATE %
%
% plot(abs(x),C_rate) %Plot the cooling rate (y) against x (x)
% xlabel('distance x(m) from laser centre');
% ylabel('Cooling Rate (Ks^{-1})');
% title('Cooling Rates for different layer depths as a function of distance
from the laser');
% axis([0 0.3 0 40000]);
%
%
% hold on
%
% end
% legend('Surface (z=0 cm)', '1st layer (z=0.0254 cm)', '2nd layer (0.0508
cm)', '3rd layer (z=0.0762 cm)', 'Location', 'west');

%% TEMPERATURE DISTRIBUTION VS DISTANCE %%
%%
figure (3)

for z=0:0.0254:0.0762

x=-1:0.0001:0; %Example value for x co-ordinate in cm

r=sqrt((x.^2)+(z.^2)); %definition of r assuming that y=0

T=((n.*q)/(spe_heat.*D.*2.*pi.*r)).*(exp((-V.*(x+r))/(2.*D)));
%Rosenthal eq for temperature

% PLOT TEMPERATURE DISTRIBUTION %

plot(abs(x), T-273) %Plot the temperature(y) against x (x)
```

Appendix C: MATLAB code

```
hold on

end

title('Plot of temperature distribution for different layer depths as a
function of distance from the laser');

% Create xlabel
xlabel('x (cm)');

% Create ylabel
ylabel('Temperature (K)');

axis([0 0.3 0 2200]);
legend('Surface (z=0 cm)', '1st layer (z=0.0254 cm)', '2nd layer (0.0508
cm)', '3rd layer (z=0.0762 cm)', 'Location', 'west');

%%
%% TIME VS. COOLING RATES %%
%%
figure (4)

for z=0.0309; %layer thickness is 0.0254 cm

x=-2:0.0001:0; %Example value for x co-ordinate in cm

%z=0; %depth in the material in cm

r=sqrt((x.^2)+(z.^2)); %definition of r assuming that y=0

T=((n.*q)./(spe_heat.*D.*2.*pi.*r)).*(exp((-V.*(x+r))/(2.*D)))+273;
%Rosenthal eq for temperature

C_rate=-V.*(x./(r.^2))+ ((V./(2.*D)).*(1+(x./r))).*T; %Cooling rate
equation

t=-x/V; % Calculation for time have added minus sign to get distance
correct

Tkelvin=T-273;
% PLOT COOLING RATE %

plot(t,Tkelvin) %Plot the cooling rate (y) against x (x)
xlabel('time (s)');
ylabel('Temperature (K)');

xlim([0 2]);

ylim([0 2200]);

hold on
```

Appendix C: MATLAB code

```
end

legend('Surface (z=0 cm)', '1st layer (z=0.0254 cm)', '2nd layer (0.0508 cm)', '3rd layer (z=0.0762 cm)', 'Location', 'west');

%%
%% COOLING RATE VS. TIME %%
%%
figure(5)

for z=0.0309 %layer thickness is 0.0254 cm

x=(0.0181*V):0.000001:1; %Example value for x co-ordinate in cm

%z=0; %depth in the material in cm

r=sqrt((x.^2)+(z.^2)); %definition of r assuming that y=0

T=((n.*q)./(spe_heat.*D.*2.*pi.*r)).*(exp((-V.*(x+r))/(2.*D)));
%Rosenthal eq for temperature

C_rate=-V.*((x./(r.^2))+ ((V./(2.*D)).*(1+(x./r)))).*T; %Cooling rate equation

t=x/V; % Calculation for time have added minus sign to get distance correct

% PLOT COOLING RATE %

plot(t,C_rate) %Plot the cooling rate (y) against x (x)

% Create xlabel
xlabel('time (s)');

% Create ylabel
ylabel('Cooling Rate (Ks^{-1})'); % or C/s

xlim([0 2]);
ylim([0 8000]);

hold on

end

legend('Surface (z=0 cm)', '1st layer (z=0.0254 cm)', '2nd layer (0.0508 cm)', '3rd layer (z=0.0762 cm)', 'Location', 'west');

maxCR=max(C_rate);
averagecr=nanmean(C_rate);

%% AREA WITHIN CONTOUR TM %%
```


Appendix C: MATLAB code

```
%%  
  
contourarea=polyarea(C1meltx,C1meltz);  
C1melttran=transpose(C1melt);  
shp=alphaShape(C1melttran); % need to transpose C1melt first then just run  
this section  
contourperimeter=perimeter(shp);  
Contourcircle=(4*pi*contourarea)/((contourperimeter)^2);  
%%  
  
figure (7)  
hold on  
plot(C2meltx, C2meltz, 'black')  
plot(C1meltx, C1meltz)  
  
%%  
%% AREA WITHIN BETA TRANSUS  
  
contourareabeta=polyarea(C2meltx,C2meltz);  
C2melttran=transpose(C2melt);  
shpbeta=alphaShape(C2melttran);  
contourperimeterbeta=perimeter(shpbeta);  
Contourcirclebeta=(4*pi*contourareabeta)/((contourperimeterbeta)^2);  
  
%% ANGLE AT BACK OF MELT POOL %%  
  
meltback=(min(C1meltx)); % x co-ordinate of back of melt pool  
idxmeltback=find(C1meltx==meltback); % position in array of meltback  
idxmeltbackplusstep=idxmeltback+3; % Next cell number along  
C1meltzangle=C1meltz(idxmeltbackplusstep); % corresponding number in z  
tanangle=(step*3)/abs(C1meltzangle);  
anglemeltback=tand(tanangle);
```

Appendix C: MATLAB code

```
function [zcdim] = SAE_model2(vdim)
%% SCRIPT FOR THE GAUSSIAN melt depths

% Input arguments
% vdim : Dimensionless beam velocity v* (for qdim=8 vdim should be ~0.1 -->
10 )

%% DEFINITIONS %%
q=275;
n=0.85;
rb=2e-4;
k=7.7;
Tm=1948;
T0=298;
qdim=(n.*q)./(rb.*k.*(Tm-T0)); % Dimensionless beam power q* 68.57
zdim=0; % Dimensionless z co-ordinate z*
ydim=0; % Dimensionless y co-ordinate - max melt depth when 0 y*
% rb=35e-6; % IN718
% Thermal conductivity 7.7
% k=20.8; % IN718
a=3.31e-6; % Thermal diffusivity 3.31e-6
% a=4.9e-6; % IN718
% For fig 1. Tp*=1 --> Tp=A1 1948
% Tm=1609; %IN718
% Start temp
% Absorption efficiency

rb2=rb^2;
t0=rb2/(4*a); % Heat flow time constant

%% STEPPING THROUGH: EQNS--> 4, 3, 7A %%
%% STEP 1 (EQ.4) %%
%%
z0dim=0.001:1e-3:10;
tpdim=0.25.*(2.*(z0dim).^2-1+(4.*(z0dim).^4+12.*(z0dim).^2+1).^(1/2)));
%t_p*

%% STEP 2 (EQ.3) %%
%%
tdim=tpdim;
Tdim=((2./pi).*(qdim./vdim))./((tdim.*(tdim+1)).^(1/2)).*(exp(-
((z0dim).^2)./tdim)); %T*

%% STEP 3 (EQ.7A) %%
%%
bassTpdim=(1/pi)^(3/2)*qdim*(atan((8./vdim).^(1/2))); % radians %

%% FIND WHERE Tdim AND bassTpdim GIVE THE SAME VALUE (DEPENDENT ON STEP
SIZE OF Z0dim PREVIOUSLY DETERMINED) %%
%%
```

Appendix C: MATLAB code

```
Tpdiff=abs(Tdim-bassTpdim);

val=0; % Value to find within Tpdiff matrix
matdiff=abs(Tpdiff-val);
[idx idx]=min(matdiff); % index of the closest value (to 0)
closest=Tpdiff(idx); % closest value

%% FIND Z0DIM THAT CORRESPONDS TO THE CROSSOVER BETWEEN THE TWO EQUATIONS
%%

fz0dim=z0dim(idx);

%% PLUG INTO REARRANGEMENT OF EQ 3 (z* is now the subject and is z_c* (case
depth))
%% FIRST PART OF EQ. %%

tpdim2=tpdim(idx);
%Tpdim2=Tdim(idx);

logtop=((tpdim2.*(tpdim2+1)).^(1/2)); % swapped Tpdim2 (T_p*) to 1
logbot=(2./pi).*(qdim./vdim);
logfrac=logtop./logbot;
logsolve=log(logfrac);
%% SECOND PART OF EQ. %%

insqrt=-tpdim2.*logsolve;

sqrtsolve=sqrt(insqrt);

%% CALCUALTE ZCDIM (z_c*) AND PLOT ZC* VS. V* %%

zcdim=sqrtsolve-fz0dim;

end

%
%

%
% end
```

Appendix C: MATLAB code

```
% Build vdim vector
vdim = [1.63 1.5 1.38 1.28 1.19 1.13];
rb=4.89e-4;      % Beam radius 4.89x10-4
%vdim=linspace(0.1,10,30); % For a range of values of vdim

% Initialise zcdim to be same size as vdim
zcdim = zeros(size(vdim));
% loop over all vdim values
for i = 1:length(vdim)
    zcdim(i) = SAE_model2(vdim(i)); % Change to SAE_model2 for generic
version
end

%produce plot (loglog instead of plot for log scale)
figure(1)
loglog(vdim,zcdim)
ylabel 'z_c*';
xlabel 'v*';

%show values of zcdim
zcdim;
zcreal=zcdim.*rb;
zm=(zcreal.*0.8023)+(61.563e-6);

hold on
```

12 Appendix D: Master plot for validation

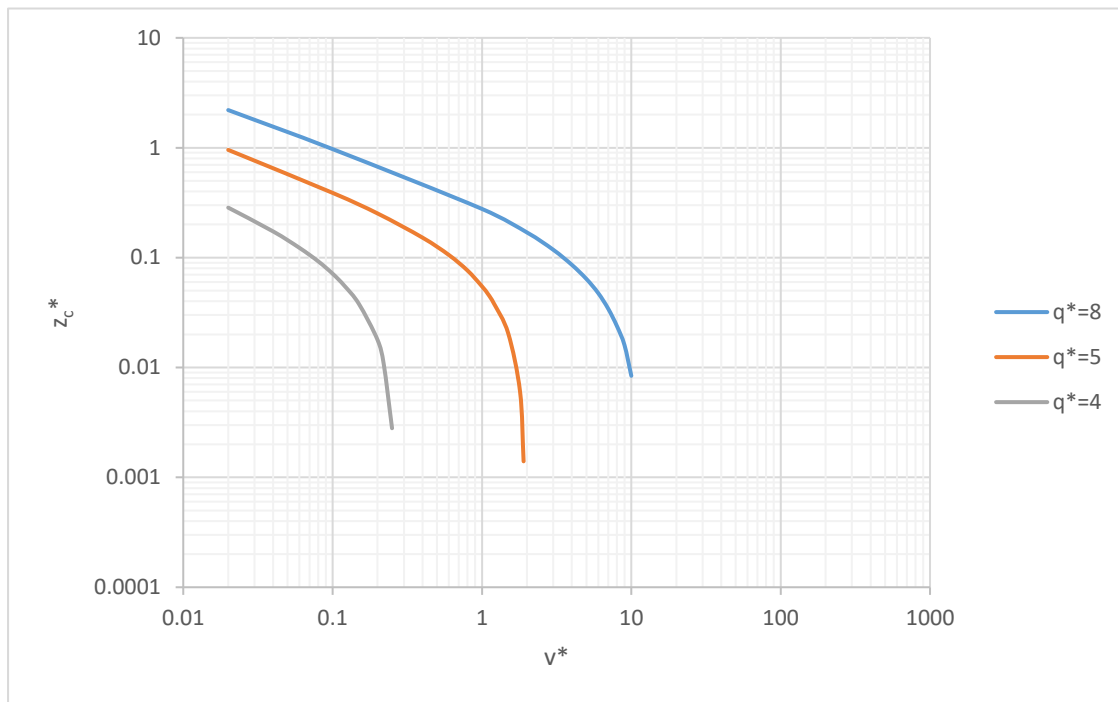


Figure 12.1: Recreation of the master plot by Shercliff and Ashby.